




2020

## EFFECTS OF HYDROLOGIC VARIATIONS ON HYDRAULIC AND DEFORMATIONAL CHARACTERISTICS OF UNSATURATED SOILS

Majid Mahmoodabadi

University of Kentucky, majid.mahmoodabadi@uky.edu

Author ORCID Identifier:

 <https://orcid.org/0000-0002-2454-3670>

Digital Object Identifier: <https://doi.org/10.13023/etd.2020.338>

[Right click to open a feedback form in a new tab to let us know how this document benefits you.](#)

### Recommended Citation

Mahmoodabadi, Majid, "EFFECTS OF HYDROLOGIC VARIATIONS ON HYDRAULIC AND DEFORMATIONAL CHARACTERISTICS OF UNSATURATED SOILS" (2020). *Theses and Dissertations--Civil Engineering*. 100. [https://uknowledge.uky.edu/ce\\_etds/100](https://uknowledge.uky.edu/ce_etds/100)

This Doctoral Dissertation is brought to you for free and open access by the Civil Engineering at UKnowledge. It has been accepted for inclusion in Theses and Dissertations--Civil Engineering by an authorized administrator of UKnowledge. For more information, please contact [UKnowledge@lsv.uky.edu](mailto:UKnowledge@lsv.uky.edu).

## **STUDENT AGREEMENT:**

I represent that my thesis or dissertation and abstract are my original work. Proper attribution has been given to all outside sources. I understand that I am solely responsible for obtaining any needed copyright permissions. I have obtained needed written permission statement(s) from the owner(s) of each third-party copyrighted matter to be included in my work, allowing electronic distribution (if such use is not permitted by the fair use doctrine) which will be submitted to UKnowledge as Additional File.

I hereby grant to The University of Kentucky and its agents the irrevocable, non-exclusive, and royalty-free license to archive and make accessible my work in whole or in part in all forms of media, now or hereafter known. I agree that the document mentioned above may be made available immediately for worldwide access unless an embargo applies.

I retain all other ownership rights to the copyright of my work. I also retain the right to use in future works (such as articles or books) all or part of my work. I understand that I am free to register the copyright to my work.

## **REVIEW, APPROVAL AND ACCEPTANCE**

The document mentioned above has been reviewed and accepted by the student's advisor, on behalf of the advisory committee, and by the Director of Graduate Studies (DGS), on behalf of the program; we verify that this is the final, approved version of the student's thesis including all changes required by the advisory committee. The undersigned agree to abide by the statements above.

Majid Mahmoodabadi, Student

Dr. L. Sebastian Bryson, Major Professor

Dr. Timothy Taylor, Director of Graduate Studies

EFFECTS OF HYDROLOGIC VARIATIONS ON HYDRAULIC AND  
DEFORMATIONAL CHARACTERISTICS OF UNSATURATED SOILS

---

DISSERTATION

---

A dissertation submitted in partial fulfillment of the  
requirements for the degree of Doctor of Philosophy in the  
College of Engineering  
at the University of Kentucky

By  
Majid Mahmoodabadi  
Lexington, Kentucky  
Director: Dr. L. Sebastian Bryson, Professor of Civil Engineering  
Lexington, Kentucky  
2020

Copyright © Majid Mahmoodabadi 2020  
<https://orcid.org/0000-0002-2454-3670>

## ABSTRACT OF DISSERTATION

### EFFECTS OF HYDROLOGIC VARIATIONS ON HYDRAULIC AND DEFORMATIONAL CHARACTERISTICS OF UNSATURATED SOILS

Constitutive models that can provide useful insight into the deformational mechanism induced by hydrologic variations are vital for design and analysis of structures where unsaturated regime predominates. An accurate description of unsaturated soils' behavior not only requires a vigorous constitutive model, but essentially is achievable using real-time mechanical (e.g. small-strain shear modulus) and hydrologic data sets. The main objective of this research was to develop a robust constitutive scheme that is compatible to quick fluctuations in hydrologic conditions.

The first step towards accomplishing this aim involved proposing a novel methodology to estimate the small-strain shear modulus with respect to the variations in net normal stress and matric suction. Fundamental of the proposed scheme was established on the inverse relationship between the small-strain shear modulus and soil-water characteristic curve (SWCC). The model proved to be highly reliable in estimating real-time values of the small-strain shear modulus along several loading and hydrologic scenarios.

Furthermore, a dependable and robust constitutive scheme, identified as SFG model was selected and further modified to simulate hydraulic characteristics and elastoplastic deformations of the unsaturated soils as direct responses to isotropic/triaxial loads and hydrological variations. The modifications involved reformation of hysteresis and elastic shear strain components of the original model. The modified-SFG model was fitted against several case studies representing various hydrologic conditions. The model successfully reproduced hydro-mechanical characteristics of the studied soils. More significantly, the modified-SFG model offers possibility of a real-time simulating of hydro-mechanical behavior of unsaturated soils with respect to rainfall and evapotranspiration events.

Likewise, in this dissertation, long-term hydrologic variations within the soil's body was simulated under transient infiltration framework. Correlation between various parts of hydrologic data was used to estimate different components of hydrological dataset. The transient infiltration model was subsequently coupled with the modified-SFG scheme and hydro-mechanical behaviors of an unsaturated hillslope was incrementally simulated with respect to hydrologic variations. The outcome of this study provides geotechnical engineers with a capability of estimating the deformational behavior of unsaturated soils,

particularly stability of hillslopes, under various real-time rainfall and evapotranspiration conditions, and thus aids effectual risk assessments and construction managements.

**KEYWORDS:** Unsaturated Soil, Constitutive Model, Small-Strain Shear Modulus, Hydro-Mechanical Simulation, Hydrologic Variation, SFG Model.

---

Majid Mahmoodabadi

---

July 20, 2020

Date

EFFECTS OF HYDROLOGIC VARIATIONS ON HYDRAULIC AND  
DEFORMATIONAL CHARACTERISTICS OF UNSATURATED SOILS

By  
Majid Mahmoodabadi

L. Sebastian Bryson  
\_\_\_\_\_  
Director of Dissertation

Timothy Taylor  
\_\_\_\_\_  
Director of Graduate Studies

July 20, 2020  
\_\_\_\_\_  
Date

## ACKNOWLEDGMENTS

I would like to express my deep and sincere gratitude to my academic advisor, Dr. L. Sebastian Bryson for invaluable guidance and motivation throughout the course of this study. I am extremely thankful for the opportunity that he has offered me, especially in the most vulnerable period of my life. It was a great honor to work and study under his supervision. I would also like to thank him for his friendship, empathy, and great sense of humor.

I extend my gratitude to all my committee members, Dr. M. Kalinski, Dr. E. Woolery, and Dr. K. Pennell for their support during my PhD studies. I also thank all faculty, staff, and graduate students at the Department of Civil Engineering for their help, kindness and friendship.

Special thanks are given to my wife, parents and sister who have been wonderful sources of motivation and inspiration. Their support and love have strengthened me during the time of this work and in my entire lifetime.

Finally, very deep gratitude goes to my dear friends, Mehrooz Mehrizi, Mohammad Rezaee and Omid Omid, who are like brothers to me. Without their support, this work would not have been possible.

## TABLE OF CONTENTS

<b>ACKNOWLEDGMENTS .....</b>	<b>III</b>
<b>LIST OF TABLES .....</b>	<b>VI</b>
<b>LIST OF FIGURES .....</b>	<b>VII</b>
<b>CHAPTER 1. INTRODUCTION.....</b>	<b>1</b>
1.1 Soil's State .....	1
1.2 Problem Statement.....	3
1.3 Conceptual Overview.....	5
1.4 Objective .....	6
1.5 Contents of Dissertation.....	8
<b>CHAPTER 2. PAPER 1 .....</b>	<b>11</b>
2.1 Introduction.....	11
2.2 Available Equations for Estimating the Small-Strain Shear Modulus.....	12
2.3 Coupled Hydraulic and Mechanical Behavior of Unsaturated Soil.....	13
2.4 General Mechanical Behavior Theory for Unsaturated Soils Based on Matric Suction Stress State.....	16
2.4.1 Soil-Water Characteristic Curve Modification.....	22
2.4.2 Volumetric Adjustment of the Soil-Water Characteristic Curve .....	27
2.5 Proposed Small-Strain Shear Modulus Model.....	28
2.5.1 Performance Evaluation of the Proposed Small-Strain Shear Modulus Prediction Equation .....	30
2.5.2 Performance of the Proposed Model at Constant Net Normal Stress .....	31
2.5.3 Performance of the Proposed Model at Various Net Normal Stresses.....	36
2.5.4 Performance of the Proposed Model at Constant Suction.....	39
2.5.5 Sensitivity of the Proposed Model to the Parameter $m_i$ .....	42
<b>CHAPTER 3. PAPER 2 .....</b>	<b>43</b>
3.1 Introduction.....	43
3.2 An Overview of the Original SFG Model.....	45
3.2.1 Volumetric Strain .....	45
3.2.2 Yield Curve and Hardening Laws .....	47
3.2.3 Shear Strength .....	50
3.2.4 Incremental Stress-Strain Over Shearing Phase.....	51
3.3 Modified-SFG Model.....	53
3.3.1 Hysteresis Behavior.....	53



3.3.2	Shear Modulus Model .....	58
3.3.3	Performance Evaluation of the Modified-SFG model Over Shearing Phase ...	65
<b>CHAPTER 4.</b>	<b>PAPER 3 .....</b>	<b>72</b>
4.1	Introduction.....	72
4.2	Framework Used for Developing Modified-SFG Model.....	74
4.2.1	Modifying Hysteresis Function .....	74
4.2.2	Modifying Elastic Shear Strain Component.....	76
4.3	Modeling Hydro-Mechanical Behavior of Unsaturated Soils by Means of the Modified-SFG Model.....	78
4.3.1	Field Methodology and Hydrologic Observations .....	78
4.3.2	Hydro-Mechanical Simulation .....	81
4.4	Framework Used for Developing an Infiltration Model.....	86
4.4.1	Transient Infiltration.....	87
4.4.2	Simulation of Infiltration Process.....	88
4.5	Coupled Modified-SFG and Infiltration Model.....	95
<b>CHAPTER 5.</b>	<b>SUMMARY AND CONCLUSION .....</b>	<b>99</b>
APPENDIX A	SWCC modeling.....	101
APPENDIX B	SWCCs modificaiton .....	108
APPENDIX C	SWCCs of the literature soils used for validating the small-strain shear modulus model .....	115
APPENDIX C.1	Original SWCCs.....	116
APPENDIX C.2	Modified SWCCs .....	123
APPENDIX D	SWCCs of the literature soils used for validating the modified-SFG model .....	129
APPENDIX E	Shear Wave velocity measurment using bender element system	133
APPENDIX F	Predictive models developed for the small-strain shear modulus of unsaturated soils .....	160
APPENDIX G	Acquiring hydraulic and mechanical data associated with the Sharing Stage.....	168
APPENDIX H	Hydrus software.....	170
<b>REFERENCES.....</b>		<b>184</b>
<b>VITA.....</b>		<b>195</b>

LIST OF TABLES

Table 2.1 SWCC fitting parameters for three literature soils used to show inverse relationship between the SWCC and small-strain shear modulus ..... 18

Table 2.2. Geotechnical index properties for fourteen soils used in proposed equations. 31

Table 2.3 Literature soils used for performance evaluation of the proposed small-strain shear modulus prediction model ..... 32

Table 2.4 Fitting parameters for the modified SWCCs and small-strain shear modulus equation..... 35

Table 3.1 Parameters used to predict the small-strain shear modulus under varying net normal stress ..... 62

Table 3.2 Geotechnical index properties for two soils utilized for verification purposes 65

Table 3.3 Parameters used for simulating hydro-mechanical behavior of Pearl Clay..... 67

Table 3.4 Model parameters used for simulating hydro-mechanical behavior of Speswhite Kaolin ..... 69

Table 4.1 Depth of hydrologic sensors at the Doe Run and Herron Hill sites..... 79

Table 4.2 Geotechnical properties of the monitoring sites ..... 79

Table 4.3 Value of parameters used for hydro-mechanical simulations..... 81

Table 4.4 Original hydraulic parameters with optimized SWCC parameters ..... 94

Table 4.5 Measured and predicted hydrologic data for Herron Hill slope ..... 95

Table 4.6 Parameters used to describe hydro-mechanical behavior of the Herron Hill by the predicted hydrologic data..... 96

## LIST OF FIGURES

Figure 1.1 Land slide problem in unsaturated condition, (a) several features of an unsaturated hillslope (modified after Rahardjo et al. 2019), (b) a disastrous landslide.....	2
Figure 1.2 Conceptual Framework .....	8
Figure 2.1 SWCC and normalized shear modulus for three literature soils, (a) clayey soil (Sawangsurriya et al., 2009), (b) silty soil (Khosravi et al., 2018a), and (c) sandy soil (Takkabutr, 2006) .....	17
Figure 2.2 Time of first arrival over drying process (data from Dong and Lu, 2016a)...	20
Figure 2.3 SWCC modification for three literature soils, (a) clayey soil (Sawangsurriya et al., 2009), (b) silty soil (Khosravi et al., 2018a), and (c) sandy soil (Takkabutr, 2006)...	26
Figure 2.4 Adjusted and original SWCC curves with normalized shear modulus curve at net normal stress of 600 kPa for silty soil (Khosravi et al., 2018a).....	28
Figure 2.5 Measured and predicted small-strain shear modulus values at constant net normal stress: (a) Denver Bentonite, Red Lake Falls Lean Clay-2 and Sand-Kaolin; (b) Concrete Sand and MN Road Lean Clay-1; (c) Anaheim Clayey Sand and Red Wing Silt ; (d) SG-1 and DI TH23 Slopes Fat Clay.....	33
Figure 2.6 Measured and predicted small-strain shear modulus data for four literature soils at several net normal stresses, (a) Rock Flour at $P = 0.69$ kPa, (b) Rock Flour at $P = 138$ kPa, (c) Completely Decomposed Tuff at $P = 110$ kPa, (d) Completely Decomposed Tuff at $P = 300$ kPa, (e) F-75 Silica Sand at $P = 3.5$ kPa, (f) F-75 Silica Sand at $P = 12$ kPa, (g) Bonny Silt-1 at $P = 150$ kPa, (h) Bonny Silt-1 at $P = 200$ kPa .....	37
Figure 2.7 Measured and predicted small-strain shear modulus for three literature soils at several matric suctions. (a) Bonny Silt-2 at matric suction = 50 kPa and initial void ratio = 0.85 (b) Bonny Silt-3 at matric suction = 60 kPa and initial void ratio = 0.66, c) Ottawa Sand at matric suction = 70 kPa.....	41
Figure 2.8 Evaluate sensitivity of the proposed model to the value of parameter $m_i$ . (a) DI TH23 Slopes Fat Clay, (b) Bonny Silt-2 .....	42
Figure 3.1 Degree of saturation versus suction.....	53
Figure 3.2 Simulation of hydro-mechanical behavior of an unsaturated soil, (a) isotropic deformation under $s = 200$ kPa, (b) effective degree of saturation with respect to mean net normal stress .....	58
Figure 3.3 SWCC and normalized shear modulus curve for silty soil.....	59
Figure 3.4 Measured and predicted normalized shear modulus data for the Completely Decomposed Tuff at, (a) $\bar{p} = 110$ kPa and (b) $\bar{p} = 300$ kPa .....	63
Figure 3.5 Change of preconsolidation stress with suction .....	64
Figure 3.6 Stress paths for triaxial shear tests on Pearl Clay.....	66
Figure 3.7 Measured and predicted results of triaxial compression test on Pearl Clay, (a) volumetric strain versus deviatoric stress, (b) deviatoric stress versus effective degree of	

saturation, (c) shear strain versus deviatoric stress, (d) axial strain versus deviatoric stress .....	68
Figure 3.8 Stress paths for triaxial shear tests on Speswhite kaolin .....	69
Figure 3.9 Measured and predicted results of triaxial compression test on Speswhite kaolin consolidated to $p = 100$ kPa. (a) Volumetric strain versus deviatoric stress, (b) Deviatoric stress versus effective degree of saturation, (c) Shear strain versus deviatoric stress, (d) Axial strain versus deviatoric stress .....	70
Figure 3.10 Measured and predicted results of triaxial compression test on Speswhite kaolin consolidated to $p = 150$ kPa. (a) Volumetric strain versus deviatoric stress, (b) Deviatoric stress versus effective degree of saturation, (c) Shear strain versus deviatoric stress, (d) Axial strain versus deviatoric stress .....	71
Figure 4.1 Overview of monitoring sites, (a) Doe Run, (b) Herron Hill .....	79
Figure 4.2 Seasonal hydrologic-rainfall data for monitoring sites, (a) cumulative and daily rainfall at Doe Run, (b) degree of saturation and pressure head at Doe Run, (c) cumulative and daily rainfall at Herron hill, (d) degree of saturation and pressure head at Herron hill .....	80
Figure 4.3 Simulated hydro-mechanical behavior of the Herron Hill, (a) volumetric strain versus deviatoric stress, (b) degree of saturation versus shear strength, (c) axial strain versus deviatoric stress, (d) volumetric strain versus shear strain. ....	83
Figure 4.4 Changes in factor of safety with a reduction in degree of saturation at the Herron Hill site .....	86
Figure 4.5 Hydrologic data for Doe Run at depth of 30 cm, (a) seasonal volumetric water content and pressure head (b) in-situ SWCC .....	88
Figure 4.6 Simulated and in-situ data along main drying segment for Doe Run at depth of 30 cm, (a) inverse simulation of pressure head, (b) inverse and optimized simulation of volumetric water content.....	91
Figure 4.7 Simulated and measured pressure head for monitoring sites, (a) pressure head data for Doe Run at depth of 30 cm, (b) degree of saturation data for Doe Run at depth of 30 cm, (c) pressure head data for Doe Run at depth of 70 cm, (d) degree of saturation data for Doe Run at depth of 70 cm, (e) pressure head data for Herron Hill at depth of 100 cm, (f) degree of saturation data for Herron Hill at depth of 100 cm .....	93
Figure 4.8 Hydro-mechanical behavior of the Herron Hill site simulated by the measured and predicted hydrologic data, (a) deviatoric stress versus volumetric strain, (b) degree of saturation versus shear strength, (c) deviatoric stress versus axial strain, (d) volumetric strain versus shear strain .....	97
Figure 4.9 Simulated mechanical behavior of Herron Hill slope at a specific deviatoric stress (a) pressure head versus volumetric strain, (b) pressure head versus axial strain ..	98

## CHAPTER 1. INTRODUCTION

### 1.1 Soil's State

State of a soil is totally governed by the nature of fluids occupying porous spaces. An unsaturated state is formed due to the presence of both air and water inside soil's voids. A key feature associated with unsaturated state is the degree of saturation less than unity as the porous areas are partially filled by the water. A variably saturated soil converts to a saturated soil if all air molecules are replaced by the water. State transformation occurs over a wetting process that causes a gradual increase in degree of saturation. On the other hand, a gradual decrease in degree of saturation leads to a state transition from saturated to unsaturated. The state condition of a typical soil in the environment is a direct proportion of seasonal hydrologic variations, that are manipulated by evapotranspiration and rainfall events.

Hydraulic and mechanical behaviors of the soils are significantly affected by the soils' state alternation. Giving an example, an initially unsaturated soil may experience enormous volumetric strain, referred to as wetting collapse phenomenon, if the degree of saturation increases. A natural or man-made structure standing on an unsaturated layer may be extensively damaged due to dramatic volume changes. In terms of shear strength, an elevation in degree of saturation (reduction in matric suction) resulting from rainfall into hillslopes may trigger slope slide, which indicates a substantial loss of shear strength. Mechanical properties of unsaturated soils can be distinctively different with different hydraulic paths (Sheng et al., 2008a; Baum et al 2010). Consequently, interaction between the mechanical and hydraulic responses is an important feature of the unsaturated soils. Figure 1.1 schematically illustrates a common dilemma associated with the unsaturated environment. Until recently, most investigation focused on the effect of positive pore pressure on land slides, however literature studies have reported a great number of hillslope failures in presence of negative pore pressure, which indeed is a typical feature of the unsaturated regimes.

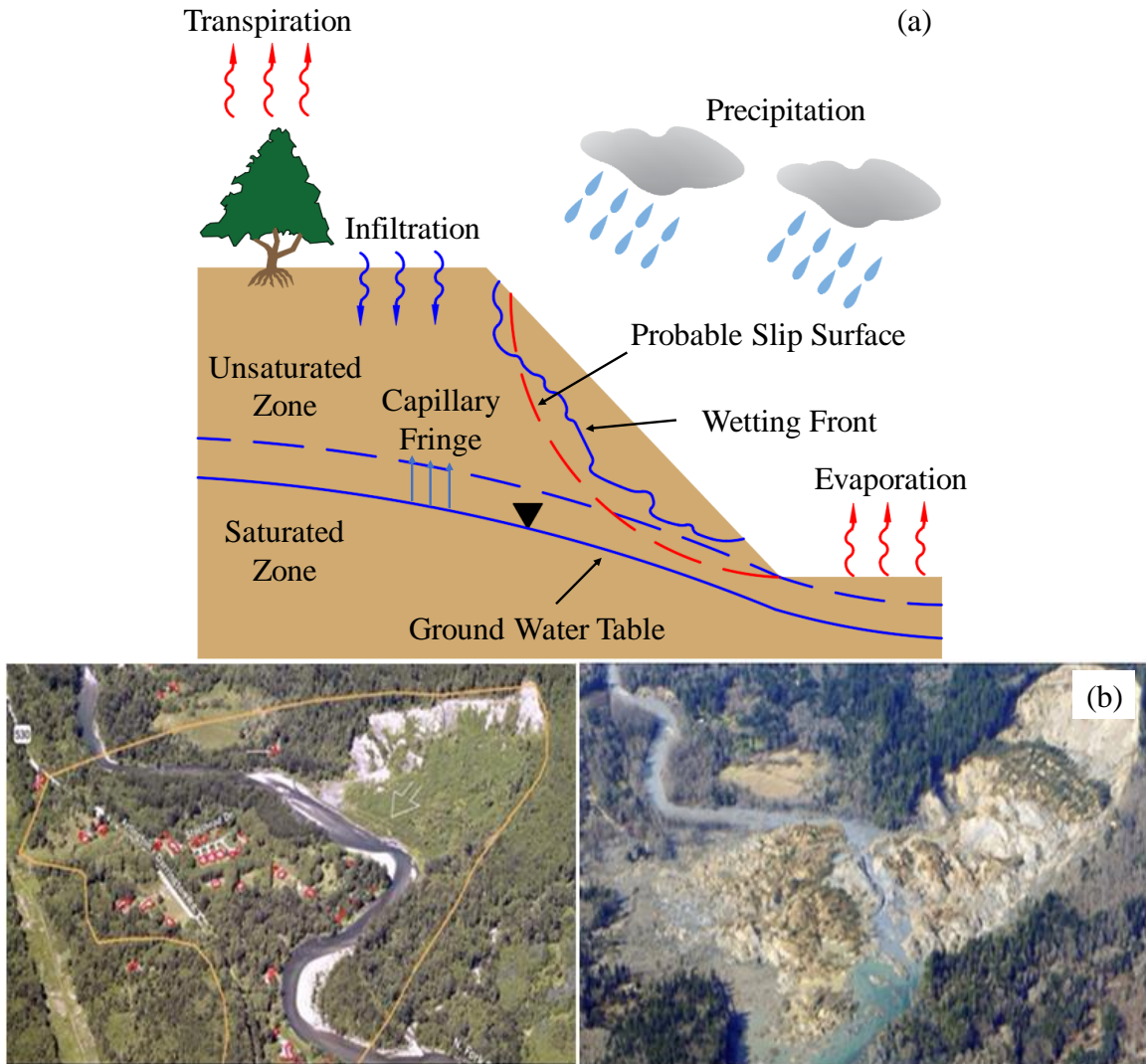


Figure 1.1 Land slide problem in unsaturated condition, (a) several features of an unsaturated hillslope (modified after Rahardjo et al. 2019), (b) a disastrous landslide

Since an unsaturated hillslope is subjected to cyclic wetting and drying throughout its lifetime, a precise insight of the hydro-mechanical behavior of variably saturated soils is of significant in engineering practice. An efficient and timely risk management requires an accurate and realistic description of soil's behavior under the hydrologic variations. In other words, lack of adequate and clear understanding of soil deformational behavior may lead to a catastrophic failure, massive destruction and fatalities (Figure 1.1).

Deformational-load analysis could be reasonably accomplished with use of appropriate and precise constitutive laws/models. A constitutive model is generally formulated by coupling hypothetical fundamentals with experimental observations. Results

obtained by a constitutive model is later compared with the data collected from laboratory testing in order to assess validity of the proposed model. In particular, a constitutive model can be utilized as a powerful simulation tool to describe skeletal deformation and hydrologic hysteresis of variably saturated soils with respect to applying load and seasonal variations. Thus, the constitutive model provides real-time or near real time insight about hydro-mechanical features of the soils.

## 1.2 Problem Statement

Constitutive laws that can describe the mechanical and hydraulic properties of partially saturated soils are essential for in-depth understanding of the behavior of these soils and for the design of infrastructure where unsaturated condition prevails. However, developing robust and reliable constitutive models for multiphase soils remains one of the greatest problems in geomechanics (Zhou, 2011). A typical constitutive law employs several parameters to model deformation and hydraulic characteristics of an unsaturated soil. A series of parameters govern volumetric deformations, while a group of which address shear strains induced by triaxial loads. Thus, pre-determination of the involving parameters is crucial for designing and simulation purposes.

Small-strain shear modulus is a dynamic property of the soil that describes relationship between shear stress and shear strain and is an important parameter for design and analysis of soil response to such dynamic loads as earthquake, traffic and wind (Ghayoomi et al., 2017). The small-strain shear modulus is identical to stiffness of the soil and corresponds to a small-strain range. Due to minimal interparticle slippage within the small stress-strain range, deformational behavior of the soil adopts an elastic condition (Atkinson and Salfors, 1991; Hardin and Kalinski, 2005). Therefore, the small-strain shear modulus mostly associates with the elastic deformation and represents the slope of the linear portion of a shear strain-shear stress curve (Khosravi, 2011). Within the soil's structure, solid grains share surficial contacts with water, which indeed functions as a resilient medium. Hydrologic variations, as of particular synonyms to cyclic drying and wetting, directly influence the amount of water content in the porous spaces, and hence control wetted area around the solid particles. Any fluctuation in water content leads to a subsequent change in particle-particle interaction force, which in turn yields a variation in

the small-strain shear modulus. This restrictive variation hinders application of a constant small-strain shear modulus for describing deformational behavior of the unsaturated soils over periodic wetting and drying seasons. Remarkably, direct measurement of the small-strain shear modulus demands time-consuming and expertise sensitive laboratory testing. Due to quick fluctuations in hydrologic conditions, on-time determination of the small-strain shear modulus that represents the current hydrologic condition sounds to be absolutely unfeasible. Thus, a real-time hydro-mechanical simulation of the unsaturated soils requires a prompt and accurate prediction of the small-strain shear modulus.

Unsaturated soils science so far is identified as the most challenging discipline in geomechanics due to arduous principles and complicated laboratory experiments (Perez-Ruiz, 2009). A satisfactory constitutive model should be complete in the sense that the material behavior is modeled for all stress and strain paths; it should be possible to obtain the model parameters through a reasonable number of tests; and the model should be founded upon physical principles of the soil response to applied stress or strain (Leong et al., 2003). In addition, a reliable unsaturated constitutive law must be able to address three substantial behaviors associated to hydrologic and loading variations, as volume change, shear strength and hydraulic hysteresis.

In context of unsaturated constitutive laws, the prime elastoplastic scheme was proposed on 1990, and it has since been followed by a multitude of constitutive models. These models, though using different experimental curves for the soil behavior and presented in different stress spaces, largely fall in the same framework of original model and can be considered as its variants (Sheng et al., 2004). Constitutive laws proposed for the unsaturated soils are normally an extension of the Modified Cam Clay model, which was originally derived to govern deformational behavior of the saturated soils. Therefore, unsaturated constitutive laws reduce to the Modified Cam Clay model when degree of saturation reaches the unity. Although the most developed schemes can replicate such essential aspects of the unsaturated soils' behavior, very few constitutive frameworks can provide realistic and coherent descriptions of the volumetric deformation, shear strength, and hydraulic behavior of the unsaturated soils (Zhou and Sheng, 2009). This shortcoming highlights an absolute necessity to a steady and vigorous constitutive law for hydro-mechanical simulations.



Environmental conditions extremely influence internal stress state in soil's body, which in turn controls load-deformational responses of the soil. (Godt et al., 2009; Bittelli et al., 2012; Lu and Godt, 2013; Suradi et al., 2014, Chen et al., 2018). Within a specific load range, failure mechanism may be expedited or delayed depending on the hydrologic characteristics of the soil. Even if a dependable and robust constitutive model is available, an accurate and timely hydro-mechanical simulation requires adequately on-time hydrologic data sets. In this case, the unsaturated constitutive model employs hydrologic data set as input and yields hydro-mechanical simulations as output. The general simulation framework is established on a coupled relationship between hydraulic variables and stress variables.

Since an unsaturated hillslope encounters cyclic rainfall and evapotranspiration events within the entire lifetime, an accurate estimation of the hydrologic data at any time elapse is the most critical step in simulations. Acquiring precise and immediate hydrologic data entails extensive in-situ monitoring and data acquisition over several seasons, which are successively supplemented by data analysis and identification of probable errors. However, a specific hillslope may collapse during hydrologic measurements, especially when intensive rainfalls excessively elevate the pore-water pressure inside the porous areas of the hillslope. This issue restricts application of a long-term in-situ hydrologic data for attaining a realistic description of soil's behavior.

Development of constitutive relationships that can explain and reproduce major hydro-mechanical features of the unsaturated soils as a function of variations in hydrologic conditions has been a critical problem in recent years. It should be noted that the discussed issues and shortcomings have set up firm barriers against development of a vigorous and accurate constitutive model for the mentioned purpose.

### 1.3 Conceptual Overview

Basically, the elastic shear strain is a significant component utilized for describing deformational behavior of unsaturated soils. This study believes that an accurate prediction of the small-strain shear modulus with respect to hydrologic variations greatly contributes to a real-time estimation of the elastic shear strain of the soil. In addition, hydraulic and deformational simulations are essentially reflections of the soil responses to the hydrologic

and loading conditions. Reliable and appropriate hydro-mechanical simulations become attainable with use of a robust and vigorous constitutive law. A great number of models existing in the literature with pros and cons. A selection criterion can be applied to evaluate all models and filter out that/those scheme(s) satisfying the selection criterion. To acquire a precise hydro-mechanical simulation, the selection criterion can be established on the ability of the constitutive model(s) to successfully address volume change, shear strength and hydraulic hysteresis of the unsaturated soils. The selected constitutive model can be finalized upon being thoroughly studied, subjected to modifications (if needed) and conformed with adequate experimental data. In addition, this study hypothesizes that prediction of the hydrologic data yields future hydrologic characteristics of the soil in advance. This approach provides a real-time hydrologic insight over a wide range of time elapses. A reliable and steady constitutive law coupled with the immediate hydrologic and small-strain shear modulus data allows a real-time description of hydro-mechanical behavior of unsaturated soils with respect to variations in hydrologic conditions.

#### 1.4 Objective

The ultimate aim of this research is to provide geotechnical engineers with a capability to estimate the initial state of an unsaturated soil and to later evaluate and predict the deformational behavior of the soil under various real-time hydrologic conditions. The research serves to extend the current “science” of the unsaturated soil mechanics along consecutive steps as follows:

Develop fundamental structure of the small-strain shear modulus prediction schemes and propose a state-of-the-art model that can be used for predicting the small-strain shear modulus with respect to the seasonal variations. Accordingly, the study assesses reliability and uniqueness of the developed model in accordance to several types of soils and over different state and stress conditions.

Evaluate available unsaturated constitutive laws consistent with their ability in describing crucial soil’s behaviors identified as volumetric change induced by isotropic consolidation, shear strength and hydraulic hysteresis. Then, select the most reliable and robust constitutive model best satisfying the mentioned criterion. Identify any plausible drawback(s) associated with the selected model and impose required modification(s),

which indeed finalize(s) the constitutive model for the simulation purposes. The modified constitutive law subsequently is coupled with the predictive model proposed for the small-strain shear modulus. Combination serves to predict the entire hydro-mechanical behavior of the unsaturated soils over sharing phase. This approach is identified as a coupled/combined constitutive- small-strain shear modulus framework. The model allows to generate multiple stress-strain schemes of a soil with respect to seasonal variations as there is no need to measure the small-strain shear modulus respective to each hydrologic condition.

Advance principles addressing hydraulic phenomenon within the soil's structure and develop a model to predict long-term hydrological characteristics of the unsaturated soils as a response to regional rainfall and evapotranspiration events. Development of a vigorous and coherent predictive model that can reproduce hydrological features of the unsaturated soils requires observational data sets accurately reflecting hydrologic behavior of the soil over several seasons. Accordingly, long-term hydrologic field measurements will be conducted on several physiographic sites. Hydrologic dataset essentially represents a full set of soil-water characteristic curve, which indeed is structured of different main and scanning parts. This study seeks to find an interrelationship between several segments of the hydrologic data and develop a predictive model based upon this correlation. This approach greatly contributes anticipation of the long-term hydrologic characteristics of the unsaturated soils by means of a short-term in-situ hydrologic data. Ultimately, incorporate predictive model formulated for the hydrologic variations with the coupled/combined constitutive-small-strain shear modulus framework and predict hydro-mechanical characteristics of the unsaturated soils with respect to variable hydrological conditions.

The proposed research is a high-rewards proposition that equips geotechnical discipline with a prediction model by which incremental deformation of unsaturated soils can be monitored in real-time. Hence, the model provides early warning of any potential collapses and contributes a more effectual risk management planning. Based on the suitability of using constitutive models to describe hydro-mechanical behavior of unsaturated soils and based on the current necessities to predict the small-strain shear modulus and hydrologic data, a comprehensive framework can be developed. The conceptual framework envisioned for this research is shown on Figure 1.2.

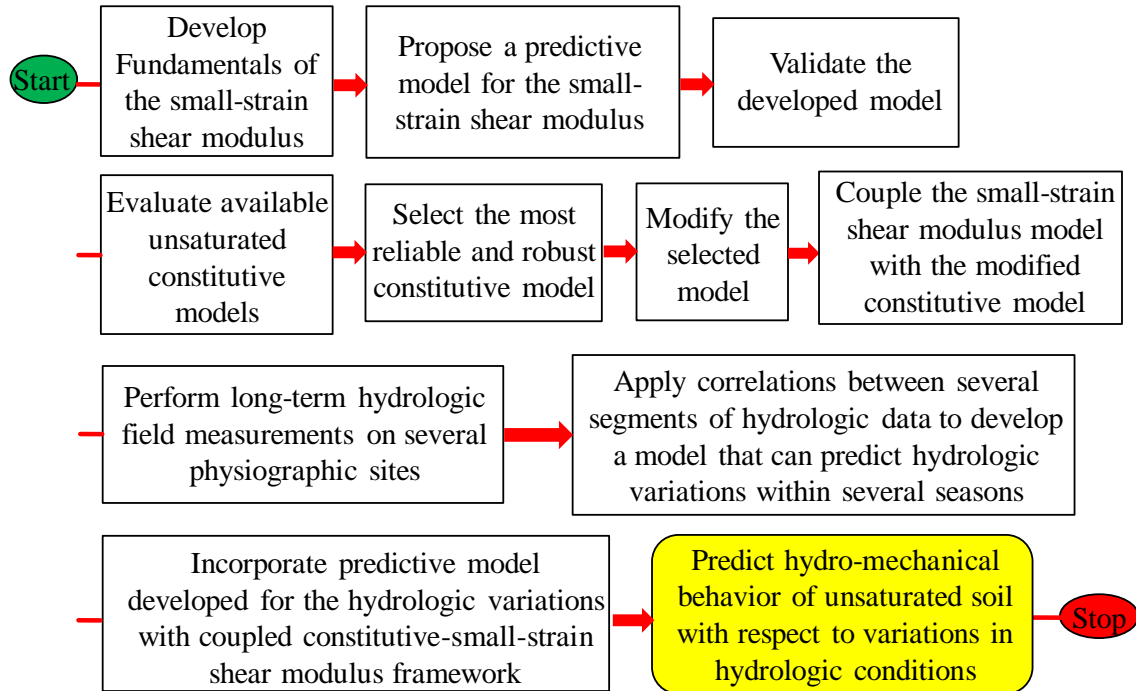


Figure 1.2 Conceptual Framework

## 1.5 Contents of Dissertation

Chapter 1- is the introduction presenting the soil's state, problem statement, conceptual overview and objectives of the research.

Chapters 2–4 consist of prepared papers and the contents in verbatim.

- Chapter 2- proposes a novel methodology that predicts the small-strain shear modulus of the unsaturated soils as a function of state conditions and stress state. The small-strain shear modulus is a complex function of the state conditions (e.g. degree of saturation), and stress states (e.g. pre-consolidation stresses). For the unsaturated soils, the variations of the state conditions at a given stress state are captured by the soil-water characteristic curve (SWCC). This paper presents a general methodology to predict the small-strain shear modulus of unsaturated soils based on an inverse relationship between the small-strain shear modulus and SWCC. Data from this study reveals that the SWCC and small-strain shear modulus do not exactly mirror each other. Thus, the original SWCC is subjected to a modification process. The SWCC is a function of initial soil state (e.g. initial void ratio). Therefore, a change in void

ratio induced by changing net normal stress leads to a change in SWCC. Thus, the modified SWCC is adjusted for the net normal stresses different than the original net normal stress. Finally, a small-strain shear modulus prediction equation is developed based on the modified SWCC. The proposed equation consists of four fitting parameters, which are estimated directly from the modified SWCC. The developed model shows to be applicable to numerous case studies for various net normal stresses and over a large range of matric suctions. The proposed approach reduces the amount of laboratory testing required to determine the small-strain shear modulus of the unsaturated soils.

*Mahmoodabadi, M. and Bryson, L. S., 2020. Direct Application of the Soil-Water Characteristic Curve to Estimate the Shear Modulus of Unsaturated Soils. Submitted to International Journal of Geomechanics.*

- Chapter 3- Studies a vigorous constitutive model originated to address coupled elastoplastic deformations and hydraulic characteristics of the unsaturated soils as a function of isotropic and triaxial loads. The model, referred to as SFG, reforms some fundamentals of the unsaturated soils' behavior to deal with (i) the change of yield stress with the suction, (ii) the volumetric deformation of slurry soil over drying process, and (iii) a transition from saturated state to the unsaturated state. However, literature frameworks suffer from inadequate capabilities to address the mentioned issues. According to the literature studies, the SFG model has been fitted to several case studies and demonstrates greater ability to model the yield stress projection, consolidation behavior, and shear strength of unsaturated soils than the most existing models. However, two deficiencies are associated with the SFG model. Hysteresis function utilized for describing the water content-volume change relationship is surrounded by a significant uncertainty. Also, the SFG model utilizes the small-strain shear modulus to estimate the elastic shear strain. As discussed earlier, measurement of the small-strain shear modulus demands a great amount of time and expertise. To overcome these obstacles, the original SFG model is imposed to two modifications. Initially, the water content-volume change relation is redefined, then the predictive model proposed for the small-strain shear modulus is introduced to the original SFG model. Performance of the modified model to

predict hydro-mechanical behavior of the unsaturated soils is assessed using several literature cases. Satisfactory prediction results firmly confirms applicability of the modified-SFG model to simulate hydro-mechanical behavior of unsaturated soils over several loading and hydrological scenarios.

*Mahmoodabadi, M. and Bryson, L. S., 2020. Constitutive Model for Describing the Fully Coupled Hydro-Mechanical Behavior of Unsaturated Soils. Submitted to International Journal of Geomechanics.*

- Chapter 4- Simulates hydrological cycles throughout the unsaturated sublayer regime applying transient infiltration phenomenon, which in fact governs water flow within the soils' body. A variety of analytical and numerical models are available to simulate water transient movement along the vadose zone, and hence estimate the seasonal hydrologic data. Analytical solutions are only compatible to coarse-grained soils, while the numerical solutions well suit a variety of materials. In this study, the Hydrus, the most utilized software operating under the finite element algorithm is utilized to simulate hydrologic variations during 2 years for two monitoring sites within the state of Kentucky. This paper presents a general infiltration methodology that can be used to predict the long-term hydrologic characteristics of the sublayer by using only the short-term hydrologic data. More significantly, this approach provides possibility of describing hydrologic behavior of the soil for upcoming years. Also, the proposed infiltration model is incorporated with the modified-SFG model and incremental hydro-mechanical behavior of the soils is simulated over different hydrologic events. This step accomplishes the objective of this research as provides geotechnical engineers with an invaluable tool to make more realistic estimations of soil responses to varying hydrologic conditions.  
*Mahmoodabadi, M. and Bryson, L. S., 2020. Prediction of Coupled Hydro-Mechanical Behavior of Unsaturated Soils Based on Seasonal Variations in Hydrologic Conditions. Submitted to Canadian Geotechnical Journal.*

Chapter 5- Conclusions: This chapter briefly presents the findings and conclusions of the research prescribed in the papers, Chapters 2-4.

## **Direct Application of the Soil-Water Characteristic Curve to Estimate the Shear Modulus of Unsaturated Soils**

### 2.1 Introduction

The small-strain shear modulus of soils is a key parameter in the design of geotechnical systems and in the analysis of the soil-structure response for earth and earth-supported infrastructure (Dong et al., 2018; Ngoc et al., 2019). The small-strain shear modulus is defined as the shear modulus of soils at strain levels less than 0.001 percent and is thus often referred in literature as the small-strain shear modulus. The small-strain shear modulus is not unique to a specific soil type. The small-strain shear modulus is a complex function of the state conditions (e.g. void ratio, degree of saturation) and stress states (e.g. in situ stresses, pre-consolidation stresses) (Mancuso et al., 2002; Rong and McCartney, 2017). Thus, it is crucial to consider the variations of the stress states and moisture conditions when choosing an appropriate small-strain shear modulus for analysis and design.

Variations of the state conditions for unsaturated soils at a given stress state are captured by the soil-water characteristic curve (SWCC). The SWCC describes the variation of the water content with respect to matric suction ( $u_a - u_w$ ), where matric suction is defined as the difference between pore air pressure,  $u_a$  and pore water pressure,  $u_w$ . The SWCC reflects the grain size distribution and the pore void volume within a soil mass. Thus, the SWCC provides a conceptual and interpretive tool to elucidate the behavior of unsaturated soils (Vanapalli and Fredlund, 2000). Changes in the matric suction correspond to changes in the contact stress between soil particles. Therefore, inter-particle stress of an unsaturated soil is defined by the matric suction. Consequently, matric suction directly contributes to the mechanical responses of unsaturated soils, such as stiffness and shear strength (Lu, 2016; Dong et al., 2018).

Several experimental studies (Ng and Yung, 2008; Sivakumar et al., 2013; Lu and Kaya, 2014; Ng and Zhou, 2014; Morales et al., 2015; Khosravi et al., 2018b, Ngoc et al., 2019) have shown that the small-strain shear modulus of unsaturated soils varies nonlinearly with matric suction and degree of saturation. These and similar research efforts

have tended to produce empirical or semi-empirical methods for estimating the small-strain shear modulus for unsaturated soils. However, the greater implication of these efforts is that the small-strain shear modulus is a direct function of the SWCC. Predicting the unsaturated small-strain shear modulus directly from a SWCC eliminates the need to perform advanced laboratory test procedures that require costly testing equipment. Unfortunately, few rigorous mathematical models exist that describe the direct relationship between small-strain shear modulus and SWCC.

This study presents a unique methodology by which the small-strain shear modulus of a soil can be predicted directly from the SWCC. Because the SWCC reflects soil type, state conditions, and stress states, the proposed methodology produces a small-strain shear modulus model that inherently considers these aspects as well.

## 2.2 Available Equations for Estimating the Small-Strain Shear Modulus

Several deterministic models (e.g. Sawangsuriya et al., 2009; Oh and Vanapalli, 2014; Han and Vanapalli, 2016; Dong et al., 2016; Suzuki et al., 2018; Khosravi et al., 2018b; Ngoc et al., 2019) have been proposed to predict the small-strain shear modulus of unsaturated soils. The aforementioned models all use various fitting parameters to estimate the small-strain shear modulus. The most common approach to estimate the fitting parameters is to optimize the fitting parameters via minimizing the least squared difference between the measured and the predicted values. A principal limitation for fitting parameters obtained by the least squared optimization is that the parameters do not represent a unique solution; meaning that different combinations of fitting parameters can produce the same results. Nevertheless, some researchers provide empirical relations between the fitting parameters and material properties and stress states (e.g. Oh and Vanapalli, 2014) or relate the fitting parameters to one of the fitting parameters of SWCC via empirical equations (e.g. Dong, et al., 2016) or formulate the fitting parameters based on standard compaction energy and material properties (e.g. Sawangsuriya et al., 2009). Other researchers (e.g. Han and Vanapalli, 2016; Khosravi et al., 2018b; Ngoc et al., 2019) only present the fitting parameters that resulted from the least squared optimization process but do not provide relationships between the fitting parameters and physical behavior. Because the fitting parameters for these types of equations are not linked to any physical behavior, the small-



strain shear modulus equations tend to be valid only for the types of soils and testing conditions in which the equations were developed.

As discussed earlier, the SWCC is influenced by the soil type, initial state conditions (i.e. initial void ratio), change in the stress states (i.e. net normal stress), and hysteresis. Thus, the SWCC reflects the full range of stress states and conditions for a specific unsaturated soil. If it is assumed that the fitting parameters associated with SWCC have physical meaning, then relating the small-strain shear modulus mathematically to the SWCC will eliminate the empirical nature of the fitting parameters associated with the available small-strain shear modulus equations. The implication of this assumption is that there will be an overall reduction in empiricism required in estimating the small-strain shear modulus.

If it is also assumed that a given SWCC equation adequately describes volume change and hysteresis, then a small-strain shear modulus equation directly related to the SWCC will inherently consider these factors as well. This approach overcomes deficiencies associated with the existing models. The intention of this study is to develop a predictive small-strain shear modulus model that is mathematically derived from SWCC, in order to better reflect the physical behavior of an unsaturated soil. The secondary objective of this study is that the predictive model will calculate or estimate the small-strain shear modulus with a minimal amount of optimization.

### 2.3 Coupled Hydraulic and Mechanical Behavior of Unsaturated Soil

Desorption behavior of a given soil is mostly related to capillary force. Based on the Young (1805) equation, water in a meniscus tube is in tension with the tube. Also, the water-tube tension is inversely proportional to tube diameter; meaning the tension decreases as the diameter of tube increases. The void spaces of a given soil can be considered as meniscuses tubes, therefore tension between water and surface of solid particles (considered as edge of tube) decreases as the size of voids increases. Thus, water desorption occurs faster in a soil containing larger pores (e.g. sand). In addition, a soil having a variety of pores sizes (e.g. clay) desorbs water more gradual than a soil having uniform pore sizes (Hillel, 1998). Thus, the size of the voids fully controls the desorption

behavior (i.e. drying shape) of SWCC (Lu and Likos, 2004). Furthermore, the size of the voids is directly influenced by particle size distribution.

In contrast, adsorption process involves several complex intermolecular force interactions, most notably including van der Waals attraction, electric double-layer interaction, etc. These forces are directly controlled by the surface area (Tuller et al., 1999; Lu and Khorshidi, 2015). The surface area is inversely related to the size of particles, i.e. a soil mostly containing fine grains (e.g. clay) have higher total surface area than a soil made of coarse particles (e.g. sand) (Tuller et al., 1999). Therefore, the lower surface area in coarse soils induces smaller intermolecular force interactions, which in turn causes a higher adsorption rate. Since both size of voids and surface area are dependent on the particle size, it can be deduced that there is a direct correlation between the size of particles and shape of drying and wetting SWCCs (Yang and You, 2013; Chang et al., 2017).

The fitting parameters associated with the van Genuchten (1980) model have physical meanings. In addition, the model is applicable to most all the soil textures (Yang and You, 2013). Thus, this model can be considered as the most reliable SWCC equation. The van Genuchten (1980) model is given as,

$$S_e = \left[ 1 + \left( \frac{s}{\alpha} \right)^n \right]^{-m} \quad (2.1)$$

where,  $S_e$  = effective degree of saturation =  $(\theta - \theta_r) / (\theta_s - \theta_r)$ ;  $\theta$  = volumetric water content;  $\theta_r$  = residual volumetric water content;  $\theta_s$  = saturated volumetric water content;  $s$  = matric suction;  $\alpha$ ,  $n$  and  $m$  = fitting parameters reflecting the air entry value, the slope at the inflection point of the SWCC, and the curvature of the SWCC near the residual point, respectively. Benson et al. (2014) reported correlations between fitting parameters of van Genuchten (1980) model and particle size distribution of the soils. The parameters  $\alpha$  and  $n$  are correlated respectively to coefficient of uniformity,  $C_u = d_{60}/d_{10}$  and center of the particle size distribution,  $d_{50}$ . Both parameters decrease with an increase in  $C_u$ . However, an increase in  $d_{50}$  leads to an increase in  $\alpha$  while a reduction in  $n$ .

As previously mentioned, the behavior of the SWCC is dependent on the initial state (i.e. initial void ratio). Therefore, changes in the void ratio result in the formation of

a new SWCC. For drained loading (whether drained via pore air or pore water), changes to the net normal stress lead to changes to the void ratio. Consequently, a SWCC developed at a given initial state may not be used to describe the mechanical behavior of a soil over several net normal stresses. Thus, the SWCC corresponding to the initial conditions must be adjusted in concert with changes to void ratio. Gallipoli et al. (2003) proposed a modified van Genuchten (1980) model to shift the SWCC based on the changes in void ratio associated with an applied net normal stress. The Gallipoli et al. (2003) model assumed that the shift in the SWCC could be quantified by replacing the  $\alpha$  parameter in the van Genuchten (1980) model with an equivalent expression as,  $\alpha = \omega/e^\psi$ . The Gallipoli et al. (2003) model is given as,

$$S_e = \left[ 1 + \left( \frac{e^\psi s}{\omega} \right)^n \right]^{-m} \quad (2.2)$$

where  $e$  = void ratio;  $n$  and  $m$  = the van Genuchten (1980) fitting parameters;  $\psi$  and  $\omega$  = model parameters associated with the rate at which the air entry suction changes with void ratio and the position of the SWCC relative to the current void ratio, respectively. In general, the  $n$  and  $m$  parameters control the shape of the SWCC and the  $\psi$  and  $\omega$  parameters control position of the SWCC as a function of changing net normal stresses. The fitting parameters and model parameters are determined by minimizing the least squared difference between the measured and predicted data at a typical void ratio. SWCCs can be generated over various net normal stresses by keeping the value of the optimized parameter constant and changing void ratio in accordance to the net normal stress. Since the Gallipoli (2003) model originated from van Genuchten (1980) model and can produce SWCCs over various net normal stresses, it will be used throughout this study. The variation of the void ratio as a function of net normal stress can be estimated using a constitutive model, e.g. Barcelona Basic Model developed by Alonso et al. (1990). A constitutive model predicts void ratio as a function of net normal stress from parameters and equations describing the mechanical behavior of the soil over the consolidation process. Thus, if values of void ratios are accurately estimated by the constitutive model, SWCCs can be generated over various net normal stress conditions.

## 2.4 General Mechanical Behavior Theory for Unsaturated Soils Based on Matric Suction Stress State

Several researchers (e.g. Dong et al., 2016; Xu and Zhou, 2016) have shown that SWCC and small-strain shear modulus project on inverse trend. This behavior is demonstrated in Figure 2.1. In the figure, the SWCC and the normalized shear modulus ( $G_N = G_{0,unsat} / G_{0,sat}$ ) (where  $G_{0,unsat}$  is defined as the small-strain shear modulus at a specific matric suction and  $G_{0,sat}$  is small-strain shear modulus at saturation condition) are plotted for a clayey, silty, and sandy soil. Figure 2.1 shows that the normalized shear modulus, as a function of matric suction, progresses as the proportional negative of the SWCC. The reason behind of this trend will be discussed later.

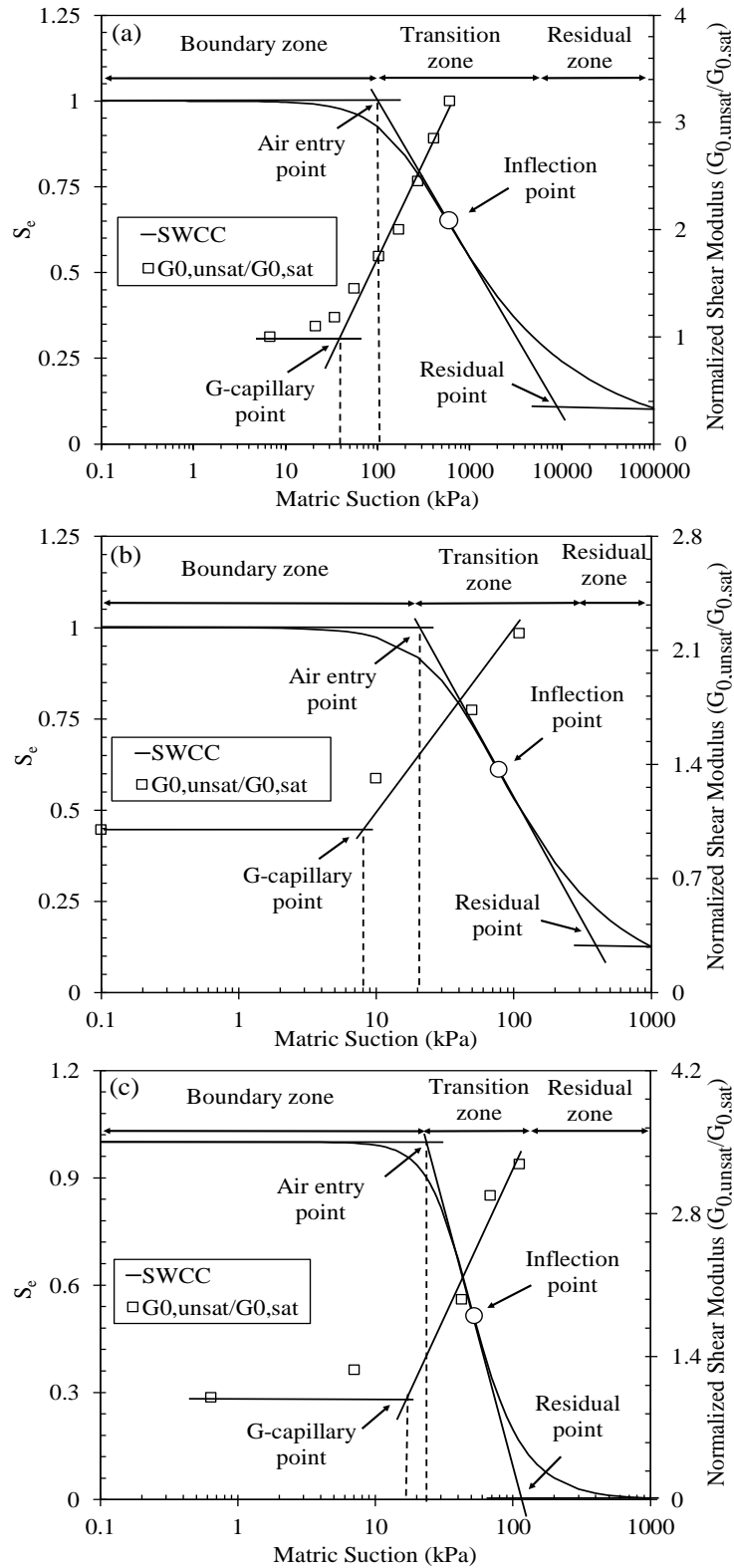


Figure 2.1 SWCC and normalized shear modulus for three literature soils, (a) clayey soil (Sawangsuriya et al., 2009), (b) silty soil (Khosravi et al., 2018a), and (c) sandy soil (Takkabutr, 2006)

In addition, fitting parameters utilized to create the SWCC for each soil are presented on Table 2.1. The trend of  $\psi$ ,  $\omega$ ,  $n$  and  $m$  reflects the grain size of the material, which directly controls the tension force between solid particles and water molecules. For Red Lake Falls Lean Clay-2, Bonny Silt-1 and Ottawa Sand, the  $\alpha$  values (i.e. van Genuchten (1980) model parameter) resulted from corresponding  $e$ ,  $\psi$  and  $\omega$  values of 200.0, 42.49, and 40.0, respectively. From capillarity, it is known that as particle size increases, the tension force between solid particles and water molecules decreases. Thus, water drainage commences in lower magnitudes of the suction which leads to a reduction in air entry point and consequently the  $\alpha$  parameter. Also, a low water-solid tension force results in a higher rate of adsorption and desorption within the soil structure that elevates the  $n$  value. The weaker water-solid tension force in coarse soils causes the SWCC of a coarse-grained material to change over a smaller range of matric suction compared to that of fine grain soils. This causes the SWCC of fine materials to be flatter as it must change over wider range of matric suction. Therefore, the  $m$  value is smaller for fine materials than coarse soils.

Table 2.1 SWCC fitting parameters for three literature soils used to show inverse relationship between the SWCC and small-strain shear modulus

Reference	Soil Name	Parameters for Gallipoli SWCC model					Modified Parameters	
		$e$	$\psi$	$\omega$	$n$	$m$	$\psi_i$	$\omega_i$
Sawangsurriya et al. (2009)	Red Lake Falls Lean Clay-2	0.60	3.71	30.05	1.45	0.25	2.97	7.94
Khosravi et al. (2018a)	Bonny Silt-2	0.85	3.44	23.96	1.78	0.37	3.28	6.72
Takkabutr (2006)	Ottawa Sand	0.56	1.22	19.65	3.03	0.58	0.81	12.26

According to Vanapalli and Fredlund (2000), the wetted contact area between soil particles decreases with an increase in soil suction. This phenomenon contributes to the changes in the skeleton stress and hence the small-strain shear modulus of the soil. As discussed previously, the water content-suction relationship within the soil is well interpreted by SWCC. The curve consists of three distinct regions including boundary, transition and residual zones. Due to effect of suction on skeleton stress, it is presumed that the small-strain shear modulus increases with matric suction in the same fashion that water

content decreases with matric suction. In reality, the small-strain shear modulus continuously increases with suction as it peaks at the residual point, but the value of the small-strain shear modulus minimally changes when suction exceeds the residual point (Schnellmann et al., 2015; Han and Vanapalli, 2016). As a result, it should not be expected that the SWCC and normalized shear modulus curve will exactly mirror each other.

To better demonstrate differences between the SWCC and normalized shear modulus data, two tangent lines are drawn on the SWCC and normalized shear modulus data. One line is tangent on the transition region of and the other is tangent on the capillary region. Intersection of these lines create a break point, which are identifiable on the SWCC and normalized shear modulus data (Figure 2.1). The break point associated with the SWCC is the air entry point. In this study, the break point on the normalized shear modulus data is arbitrary called G-capillary point. As can be observed in the Figure 2.1, the air entry point and the G-capillary point are not aligned. Upon passing the air entry and G-capillary points, the slopes of the SWCC (e.g. for clayey soil,  $\Delta S_e / \Delta(u_a - u_w) \approx 0.0006$ ) and normalized shear modulus data (e.g. for clayey soil,  $\Delta G_N / \Delta(u_a - u_w) \approx 0.003$ ) are also different. Thus, the normalized shear modulus data does not mirror the SWCC.

To better understand the reason behind the difference between the SWCC and normalized shear modulus data, the methodology used to estimate the small-strain shear modulus must be considered. Shear wave propagation in soils is commonly used to estimate the small-strain shear modulus of saturated and unsaturated soils. The small-strain shear modulus values can be estimated by Equation 2.3 as follows,

$$G_{\max} = \rho \cdot v_s^2 = \rho \cdot \left(\frac{L}{t}\right)^2 \quad (2.3)$$

where  $\rho$  = bulk mass density of the soil;  $v_s$  = shear wave velocity;  $L$  = shear wave travel distance; and  $t$  = shear wave propagation time. If the bulk mass density of the soil is defined based on the total mass and total volume of the sample, Equation 2.3 can be extended and given by

$$G_{\max} = \frac{m_s + m_w}{V_s + V_v} \cdot \left(\frac{L}{t}\right)^2 = \frac{m_s + m_w}{1 + e} \cdot \left(\frac{L}{t}\right)^2 \quad (2.4)$$

where  $m_s$  = mass of solid particles;  $m_w$  = mass of water;  $V_s$  = volume of solid particles; and  $V_v$  = volume of void. Assuming the solid particles are incompressible, then the value of  $V_s$  can be given as a unit volume equaled to 1, and therefore the  $V_v$  is equal to the void ratio,  $e$ . Regarding Equation 2.4, the small-strain shear modulus is proportional to the soil structure which is defined by the void ratio,  $e$  and the length of the sample,  $L$ . Normally, the SWCC is generated by assuming that the overall volume of the soil specimen does not change as matric suction increases (Fredlund and Houston, 2013). Both the SWCC and the normalized shear modulus curve are presumed to be subject to the same assumption. Therefore, the total volume of the sample is assumed to be constant during the measurements of the small-strain shear modulus over several suction values. The constant volume is an indicator of no change in void ratio. For a sample with a fixed length and a constant mass of solid particles, the change in the small-strain shear modulus is only controlled by the change in gravimetric water content, represented by the mass of water,  $m_w$ , and the shear wave propagation time,  $t$ .

Dong and Lu (2016a) investigated the effect of matric suction,  $s = u_a - u_w$  on shear wave velocity,  $v_s$  of the unsaturated soils. These researchers used the time of first arrival over the sample length to evaluate the effects of matric suction on the shear wave velocity, Figure 2.2. Shown data were collected during drying process of the soil.

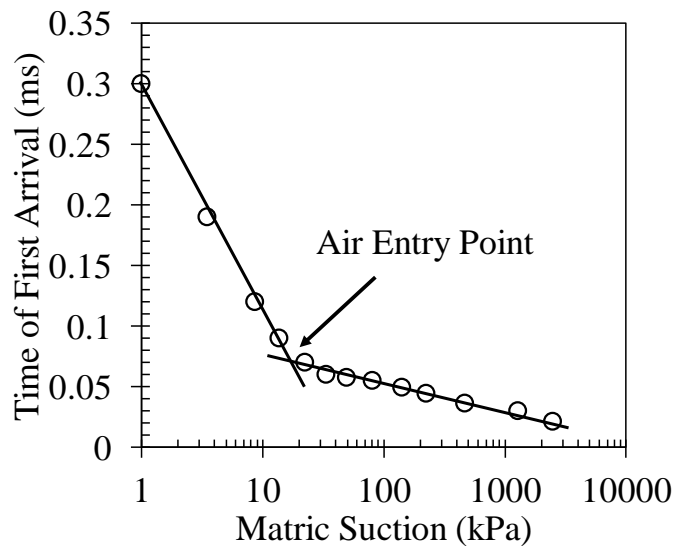


Figure 2.2 Time of first arrival over drying process (data from Dong and Lu, 2016a)



As can be observed on the figure 2.2, an increase in matric suction (i.e. decrease in water content) leads to a decrease in the shear wave travel time. This behavior is due to the inter-particle contact force that is governed by suction stress,  $\sigma^s$  given by

$$\sigma^s = S_e (u_a - u_w) \quad (2.5)$$

An increase in the suction stress results in an increase in the inter-particle contact force and a consequent decrease in shear wave travel time (Dong and Lu, 2016a). The effective degree of saturation represents the mass of water in the soil at different levels of matric suction. Since suction stress and effective degree of saturation are proportionally related, it can be deduced that the suction stress and the mass of water are also related.

Considering the SWCC, the mass of water minimally changes with matric suction,  $\Delta m_w / \Delta (u_a - u_w) \approx 0$  before air entry point. Referring to Equation 2.4, the small-strain shear modulus is directly and inversely proportional to the water content and the shear wave travel time, respectively. This relationship can be expressed in terms of incremental change as,  $\Delta G_0 \propto (\Delta m_w / \Delta t^2)$ . In the boundary region, the small-strain shear modulus is mostly controlled by the shear wave travel time due to a minimal change of the mass of water with suction. In addition, the shear wave travel time changes with matric suction,  $\Delta t / \Delta (u_a - u_w)$  before the air entry point, as illustrated on the Figure 2.2. The change of shear wave travel time with matric suction results in the small-strain shear modulus increase before the value of applied suction reaches the air entry value. This explains why the air entry point of the SWCC and the G-capillary point of the normalized shear modulus curve are not aligned.

Within the transition zone, the rate of water drainage increases that causes the differential effective degree of saturation increases such that  $\Delta S_{e,transition} > \Delta S_{e,boundary}$ . Considering the differential suction stress,  $\Delta \sigma^s = \Delta S_e \cdot \Delta (u_a - u_w)$ , it is expected that the changing rate of suction stress to be different before and after G-capillary point. Different rates of suction stress change and direct proportionality of the small-strain shear modulus to suction stress cause two distinct rate of small-strain shear modulus increase to be observed. Since all small-strain shear modulus values are normalized based on a constant small-strain shear modulus, the normalized shear modulus data also trends differently

before and after the G-capillary point. This completely confirms the trend shown on the figure 2.1. Within transition zone, the matric suction changes from air entry to a maximum value corresponding to the residual state of the soil (e.g. 10,000 kPa for fine-grained materials). Corresponding to this matric suction range, the effective degree of saturation,  $S_e$  varies from almost 1 to a value very close to 0. Thus, the matric suction changes at a higher rate than the effective degree of saturation. This means that the changing rate of the suction stress is mostly influenced by the changing rate of matric suction than the effective degree of saturation. Thus, the suction stress also varies in faster rates than the effective degree of saturation, along the drying process. Due to the direct relationship between the small-strain shear modulus and suction stress, it is completely normal that the small-strain shear modulus changes quicker within a specific suction interval. The difference between changing rate of the effective degree of saturation and normalized shear modulus shown on the Figure 2.1 exactly relies on the explained phenomenon. Given that the air entry point and G-capillary point are different, as well as the slope of SWCC and normalized shear modulus data at the transition zone is also different, a direct prediction of the small-strain shear modulus from the SWCC is problematic. Thus, to facilitate direct prediction, the original SWCC must be shifted/ modified such that the air entry point and the G-capillary point moves towards each other. In addition, the difference between the slope of the normalized shear modulus data and SWCC must be diminished by an offsetting approach, such as the one taken by Dong and Lu (2016b). In their approach, the authors correlated suction stress curve and the small-strain shear modulus by means of an offsetting factor. Due to the direct relationship between suction stress and suction, it is expected that the slope of the normalized shear modulus data and SWCC to be offset as well. As another example, Hoyos et al. 2015 estimated the small-strain shear modulus of a silty sand by means of an offsetting factor that correlates the small-strain shear modulus to the matric suction.

#### 2.4.1 Soil-Water Characteristic Curve Modification

The proposed process for modifying the original SWCC involves shifting the curve along the matric suction axis, through three steps:

1. Identify the inflection point of the original SWCC (Figure 2.1).

2. Identify the exact value of air entry suction of the original SWCC.
3. Postulate the air entry point of the original SWCC as an inflection point of the shifted SWCC. Then, generate a curve passing through the postulated point.

The inflection point of the original SWCC is determined by taking the second derivative of the Gallipoli (2003) model (i.e. Equation 2.2). The root of the second derivative gives the suction at the inflection point. The second derivative of the Equation 2.2 in effective degree of saturation-logarithmic matric suction space is given as,

$$\frac{d^2 S_e}{d(\log s)^2} = \frac{\ln(10) \cdot \left[ 1 + \left( \frac{e^{\psi} s}{\omega} \right)^n \right]^{-m} \cdot \left[ m^2 \cdot n^2 \cdot \left( \frac{e^{\psi} s}{\omega} \right)^{2n} - m \cdot n^2 \cdot \left( \frac{e^{\psi} s}{\omega} \right)^n \right]}{s \left[ \left( \frac{e^{\psi} s}{\omega} \right)^{2n} + 2 \left( \frac{e^{\psi} s}{\omega} \right)^n + 1 \right]} = 0 \xrightarrow{\text{Root}} s_{\text{inf}} \quad (2.6)$$

where  $s_{\text{inf}}$  = suction at the inflection point. The air entry value is often estimated graphically from the SWCC by obtaining the intersections of the tangent of the saturation portion of curve and the tangent of the transition portion of the curve. However, the exact value of air entry suction can be estimated from the slope of tangent line at the inflection point of the curve. The slope of the tangent line at the inflection point is calculated by imposing the first derivative on the Equation 2.2 as follows:

$$Slp_{ii} = \frac{dS_e}{d(\log s_{\text{inf}})} = -\ln(10) \cdot m \cdot n \cdot \left( \frac{e^{\psi} s_{\text{inf}}}{\omega} \right)^n \cdot \left[ 1 + \left( \frac{e^{\psi} s_{\text{inf}}}{\omega} \right)^n \right]^{-m-1} \quad (2.7a)$$

where  $Slp_{ii}$  = slope of line tangent at the inflection point of the SWCC. If the tangent line at the inflection point is extended towards the maximum effective degree of saturation, ( $S_e = 1.0$ ), and if it is assumed that a horizontal line can be drawn from the maximum effective degree of saturation, the tangent line and horizontal line intersects at a point corresponding to the air entry point. In essence, the slope of tangent line between the inflection point and air entry point equals to the ratio of the differential effective degree of saturation to the differential matric suction

$$Slp_{ii} = \frac{(S_{e_{aev}} - S_{e_{\text{inf}}})}{[\log(s_{\text{inf}}) - \log(s_{aev})]} \quad (2.7b)$$

Consequently, the matric suction at the air entry point can be estimated mathematically as,

$$\log(s_{aev}) = \log(s_{inf}) - \frac{Se_{aev} - Se_{inf}}{Slp_{ii}} \quad (2.8)$$

where  $s_{aev}$  = air entry suction;  $Se_{aev}$  = effective degree of saturation at the air entry point which equals unity;  $Se_{inf}$  = effective degree of saturation at the inflection point, which is obtained by inputting  $s_{inf}$  into the Equation 2.2. The third step of SWCC modification involves shifting the original curve along the suction axis, so that the air entry point of SWCC approaches the G-capillary point of the normalized shear modulus curve. Benson et al. (2014) suggested that the air entry point is mostly related to the  $\alpha$  parameter of van Genuchten (1980) equation. Considering Gallipoli (2003) equation and relationship between  $\alpha$ ,  $\psi$  and  $\omega$ , the air entry point based on Gallipoli (2003) model is related to  $\psi$  and  $\omega$ . Thus, the SWCC can be shifted by changing  $\psi$  and  $\omega$  while keeping  $m$  and  $n$  unchanged.

The SWCC shifting distance corresponds to the distance between the air entry point of the SWCC and the G-capillary point of the normalized shear modulus curve. However, the exact location of the G-capillary point of the normalized shear modulus curve is unknown, thus the shifting distance is unknown as well. The only known values are the inflection and air entry points of the original SWCC. Based on the observations (Figure 2.1) and the previous discussion about the effect of mass of water and shear wave travel time on the small-strain shear modulus, the G-capillary point of the normalized shear modulus curve is positioned on the “wet” (i.e. left) side of air entry point of the original SWCC. Thus, the original SWCC must be shifted towards the left. In  $Se - \log s$  space, if an arbitrary matric suction is selected that is smaller than the inflection point of the original SWCC, then the SWCC is passed through the selected point, the generated SWCC will be at the left side of the original SWCC. Considering two known parameters of the original SWCC, the air entry point is always smaller than the inflection point. Thus, setting the inflection point of the shifted curve equal to the air entry point of the original SWCC results in the generation of the shifted SWCC on the left side of the original SWCC. The shifted SWCC will have a smaller air entry point than the original SWCC and will be closer to the

G-capillary point of the small-strain shear modulus curve. Therefore, it is assumed that setting the inflection point of the shifted SWCC equal to the air entry point of the original SWCC will result in a decrease of distance between air entry point of the SWCC and G-capillary point of the normalized shear modulus curve. Thus, the matric suction corresponding to the air entry of the original SWCC is inserted into the Equation 2.6 and parameters  $\psi$  and  $\omega$  are changed so that the second derivative equals zero. In this approach, new values are obtained for  $\psi$  and  $\omega$ , thus Equation 2.2 is redefined for a modified SWCC as follows:

$$Se_i = \left[ 1 + \left( \frac{e_i^{\psi_i} s}{\omega_i} \right)^n \right]^{-m} \quad (2.9)$$

where  $Se_i$  = modified effective degree of saturation;  $e_i$  = void ratio of the soil corresponding to the original net normal stress;  $\psi_i$  and  $\omega_i$  = fitting parameters of the modified SWCC that are different from the original parameters;  $n$  and  $m$  = fitting parameters of the modified SWCC curve that are the same as the original parameters. The entire modified SWCC is generated via inputting arbitrary values of matric suction into the Equation 2.9. The performance of the shifting process is demonstrated in Figure 2.3. The figure comparatively shows the change in distance between the air entry point of SWCC and the G-capillary point of the normalized shear modulus curve via the modification process. While the intent of the shifting process was not to exactly align the air entry value of SWCC to a point with the G-capillary point of the normalized shear modulus curve, the shifting process served the purpose of better aligning the SWCC and the normalized shear modulus curve. Therefore, the behavior of the normalized shear modulus is more proportional to the inverse of SWCC, which facilitates the predictions of the unsaturated small-strain shear modulus directly from the SWCC.

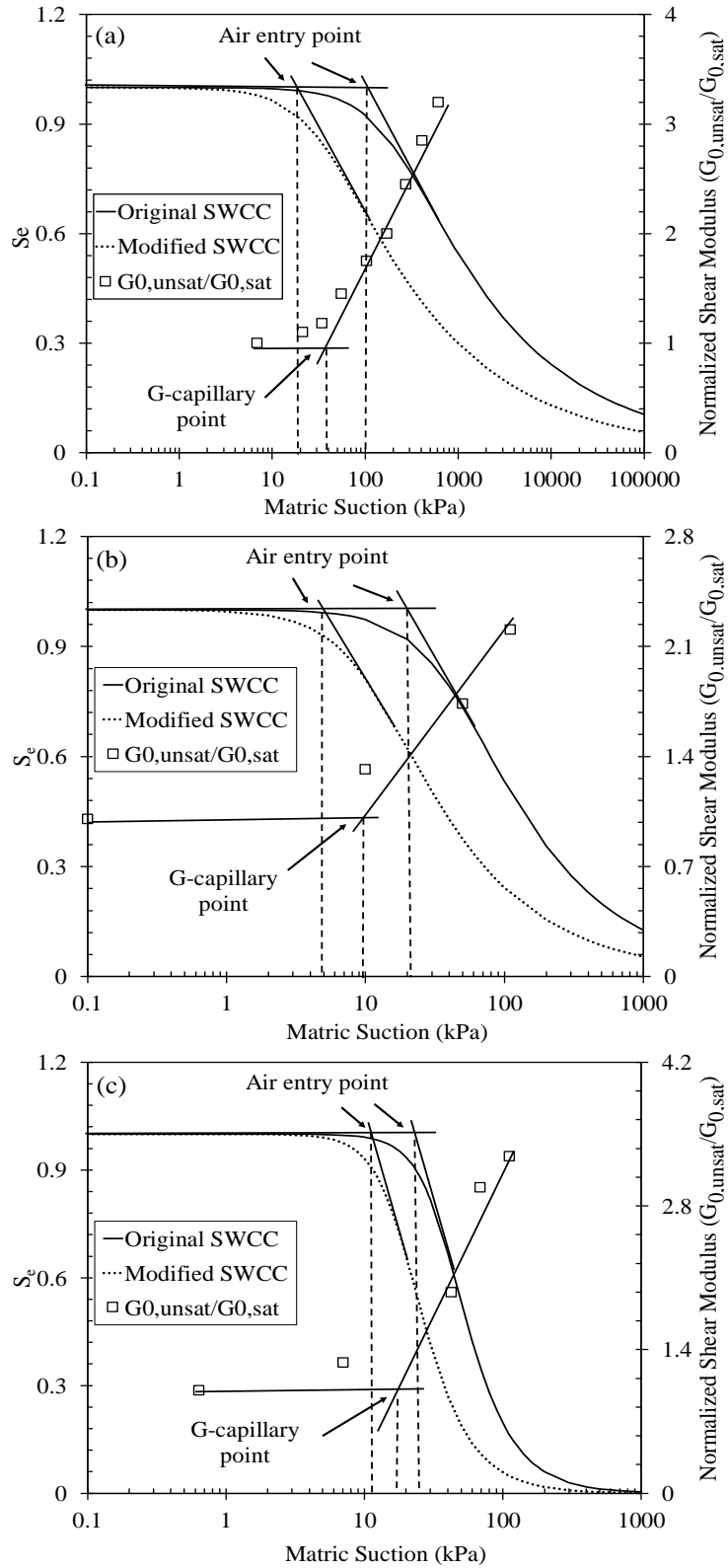


Figure 2.3 SWCC modification for three literature soils, (a) clayey soil (Sawangsuriya et al., 2009), (b) silty soil (Khosravi et al., 2018a), and (c) sandy soil (Takkabutr, 2006)

Referring back to Table 2.1, the value of  $\psi_i$  and  $\omega_i$  are less than  $\psi$  and  $\omega$  for three literature soils which indicates an smaller air entry value for the modified SWCC as compared with the original SWCC. It should be noted that  $n$  and  $m$  are held constant over SWCC modification process. The modified SWCC represents a water content-matric suction relationship at a given net normal stress that is considered the initial or original net normal stress. For field loading conditions, an unsaturated soil undergoes changes in the net normal stress. Changes in the net normal stress result in volume change (i.e. changes to the void ratio). Thus, a single modified SWCC would not be applicable for all net normal stresses. A solution for dealing with this issue requires adjustment of the modified SWCC to vary over a range of void ratios.

#### 2.4.2 Volumetric Adjustment of the Soil-Water Characteristic Curve

The Gallipoli et al. (2003) model can be used to address the changes of the SWCC with respect to the void ratio. Equation 2.9 is adjusted to reflect changes in the void ratio that corresponds to the change in net normal stress (whether the changes result in higher or lower void ratios). In this case, the fitting parameters of the Equation 2.9 are kept constant and the original void ratio is changed to the value corresponding to the different net normal stress. For the adjusted curve, the effective degree of saturation is calculated via setting arbitrary values for the matric suction. The SWCC adjustment process is synonymous to generating a modified SWCC at a net normal stress differing from the original net normal stress using the modified SWCC of the original net normal stress.

The SWCC adjustment procedure is explained in more detail using an example. Consider the silty soil shown on Figure 2.1. The small-strain shear modulus was measured for the soil over a net normal stress,  $P$  of 600 kPa. The original SWCC of the soil at net normal stress of 40 kPa is available. Parameters of the original SWCC at  $P$  of 40 kPa are  $e_i = 0.85$ ,  $\psi = 3.44$ ,  $\omega = 24.00$ ,  $n = 1.78$  and  $m = 0.37$ . The intention is to generate the modified SWCC at  $P$  of 600 kPa using the original SWCC at  $P$  of 40 kPa. Figure 2.4 shows the original SWCC and the normalized shear modulus curve for the soil at  $P$  of 600 kPa. Initially, the original SWCC at  $P$  of 40 kPa was modified, which led to attaining  $\psi_i = 3.28$  and  $\omega_i = 6.72$  from Equation 2.9. The parameters  $n$  and  $m$  are remained

unchanged. The SWCC adjustment is then performed by changing the value of void ratio in Equation 2.9 (which currently corresponds to  $P$  of 40 kPa) to the void ratio corresponding to  $P$  of 600 kPa. This process results in formation of the modified SWCC at  $P$  of 600 kPa. Figure 2.4 also illustrates the modified SWCC at  $P$  of 600 kPa which has an air entry point very close to G-capillary point of the normalized shear modulus curve at  $P$  of 600 kPa. The distance between air entry point of the original SWCC and the G-capillary point at  $P$  of 600 kPa is approximately 10 kPa, while the distance between air entry point of the modified SWCC and G-capillary point of the normalized shear modulus curve at the same net normal stress is almost 2 kPa. The adjustment method provides the ability to decrease the distance between the air entry point of original SWCC and the G-capillary point of normalized shear modulus curve at different net normal stresses, using only the original SWCC corresponding to the initial net normal stress.

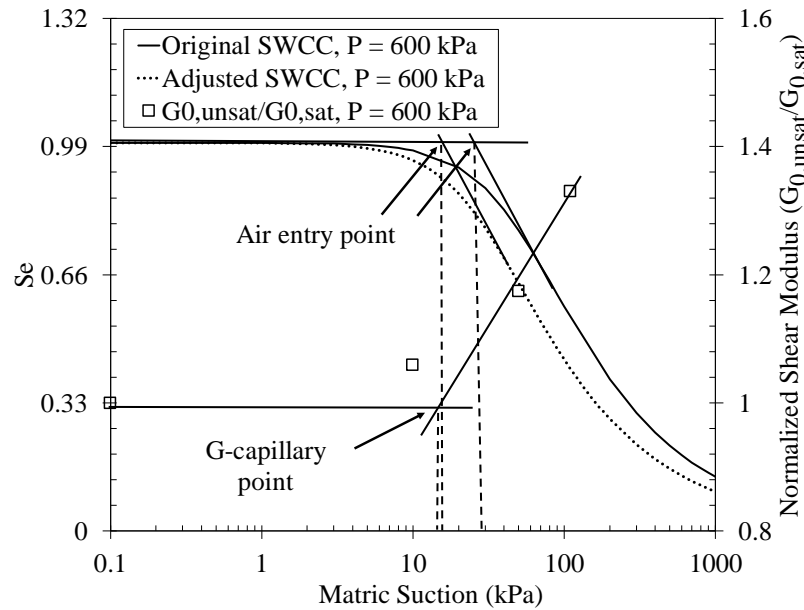


Figure 2.4 Adjusted and original SWCC curves with normalized shear modulus curve at net normal stress of 600 kPa for silty soil (Khosravi et al., 2018a)

## 2.5 Proposed Small-Strain Shear Modulus Model

The inverse projection of the SWCC and the normalized shear modulus data is the basis for the small-strain shear modulus prediction model. Having modified the SWCC, a prediction model can be developed based on the Equation 2.9 that will estimate the normalized shear modulus over various void ratios. The modified SWCC and the normalized shear modulus curve have different concavities along the entire matric suction



range and different slope in the transition zone, as shown on the Figure 2.3. The slope is associated with the parameter  $n$ . As discussed earlier, the slope difference must be offset, which means the parameter  $n$  needs to be changed. Literature data show that the ratio of the slope of normalized shear modulus  $\Delta G_N/\Delta s$  to the slope of the SWCC  $\Delta S_e/\Delta s$  in some cases is very small and for some soils is quit high. This reveals that this ratio varies in a large range. Thus, offsetting the slopes by changing parameter  $n$  cause this parameter to be changed in a wide range. Also, changing parameter  $n$  is synonymous to optimizing this parameter. However, the goal of this study is to predict the small-strain shear modulus of the unsaturated soils by the least amount of parameter optimization. Therefore, the parameter  $n$  is kept unchanged and the difference between the slope of SWCC and the normalized hear modulus data were offset by using parameter  $m$ . The reason behind of selecting  $m$  for offsetting  $n$  is discussed later. The concavity simply depends on the sign of power coefficient, parameter  $m$ . Therefore, Equation 2.9 may be inversed by changing the sign of parameter  $m$  but keeping the same value. The parameters  $\psi_i$ ,  $\omega_i$  and  $n$  stay unchanged in both sign and magnitude as they are associated with the air entry point and the slope in the transition zone. Consequently, the proposed small-strain shear modulus prediction model is expressed as follows:

$$f = \frac{G_{0,unsat}}{G_{0,sat}} = \left[ 1 + \left( \frac{e_i^{\psi_i} s}{\omega_i} \right)^{n_i} \right]^{m_i} \quad (2.10a)$$

$$G_{0,unsat} = G_{0,sat} \cdot \left[ 1 + \left( \frac{e_i^{\psi_i} s}{\omega_i} \right)^{n_i} \right]^{m_i} \quad (2.10b)$$

Equation 2.10 is denoted as the main predictive model proposed for the small-strain shear modulus. To make clearer contrast between the modified SWCC equation (Equation 2.9) and the small-strain shear modulus prediction equation, the  $\psi_i$ ,  $n$  and  $m$  parameters are purposely denoted as  $\psi'_i$ ,  $n_i$  and  $m_i$ . Upon SWCC modification, the air entry point of the shifted SWCC is dragged towards the G-capillary point of the normalized shear modulus data, but these points are not exactly aligned (Figures 2.3 and 2.4). Thus, the value of  $\psi'_i$  used in Equation 2.10 does not exactly equal  $\psi_i$  used in Equation 2.9. As explained previously, the slope of the SWCC and normalized shear modulus differ, as well. To predict

the normalized shear modulus, there is no option but setting  $\psi'_i$  equal to the  $\psi_i$  and  $n$  equal to  $n_i$  then changing  $m_i$  to compensate/offset for the divergence between both  $\psi'_i$  and  $\psi_i$  and between  $n$  and  $n_i$ . This approach diminishes the number parameter optimization from three to one. The difference between  $m_i$  and  $m$  was small in most cases. This observation is an indication that more research is needed into the process of aligning the air entry point of the SWCC to the G-capillary point of the normalized shear modulus curve and finding a relationship between  $n$  and  $n_i$ . In the interim, setting  $m_i$  equal to  $m$  provides satisfactory results.

#### 2.5.1 Performance Evaluation of the Proposed Small-Strain Shear Modulus Prediction Equation

The performance of the proposed small-strain shear modulus prediction models was evaluated using fourteen soils found in literature. The geotechnical properties of the fourteen soils are given in Table 2.2. The evaluation soils represent a variety of soils types ranging from coarse grain (i.e. sands ranging from well graded to clayey sand) to fine grain (i.e. silts and clays ranging from low plasticity to high plasticity) soils. The soil samples were evaluated based on their stress state and state conditions during the small-strain shear modulus measurement tests. Accordingly, the soils were separated into three groups: (1) samples tested only under a constant net normal stress over a range of matric suction; (2) samples tested over various net normal stresses and matric suctions; (3) samples tested under a constant matric suction but various net normal stresses. Each group of soil samples and the associated discussions are presented in the subsequent sections.

Table 2.2. Geotechnical index properties for fourteen soils used in proposed equations

Reference	USCS	PI (%)	Sand (%)	Silt (%)	Clay (%)	MDD (kN/m <sup>3</sup> )
Khosravi et al. (2010)	SW	N/A	99	1	0	17.5
Lee et al. (2007)	SW	N/A	82.4	1.3	0	19.91
Takkabutr (2006)	SP	N/A	98	2	0	15.35
Picornell and Nazarian (1998)	SP	N/A	100	0	0	16.48
Hippley (2003)	ML	N/A	27	71	2	16
Khosravi and McCartney (2012)	ML <sup>1</sup>	4	16.1	69.9	14	16.5
Khosravi et al. (2016)	ML <sup>2</sup>	4	16.1	69.9	14	16.5
Khosravi et al. (2018a)	ML <sup>3</sup>	4	16.1	69.9	14	16.5
Ng et al. (2009)	ML	14	24	72	4	17.3
Sawangsurriya et al. (2009)	SC	14	59	23	18	18.5
	ML	11	11.9	82.4	5.7	17.9
	CL	24	8.9	63.8	27.3	15.8
	CL	9	36.3	45.3	14.5	17.7
	CH	52	3.1	21.2	75.2	14.4
Dong and Lu (2016b)	CH	73	2	8	90	N/A
Ngoc et al. (2019)	SC	9.8	75	18	7	N/A

Note: PI is plasticity index; Sand, Silt and Clay represent fractional weight of sand, silt and clay per total weight of the soil sample, respectively; G<sub>s</sub> is specific gravity; MDD is the maximum dry density; OMC is the optimum moisture content.

<sup>1, 2, 3</sup> Same soil, but they were compacted at different initial dry densities and tested under different net normal stresses.

### 2.5.2 Performance of the Proposed Model at Constant Net Normal Stress

Nine individual evaluation soils were used for assessing the proposed small-strain shear modulus prediction model at constant net normal stress. These soils are denoted herein as the First group of soils. Table 2.3 presents fitting parameters corresponding to the original Gallipoli (2003) SWCC equation for the First group of evaluation soils.

Table 2.3 Literature soils used for performance evaluation of the proposed small-strain shear modulus prediction model

Group	Reference	Soil Name	Original Gallipoli SWCC model parameters				
			$e_i$	$\psi$	$\omega$	$n$	$m$
First	Picornell and Nazarian (1998)	Concrete Sand	0.75	0.11	0.84	2.80	0.32
	Lee et al. (2007)	SG-1	0.31	1.05	3.85	1.29	0.17
First	Sawangsurriya et al. (2009)	Anaheim Clayey Sand	0.37	1.49	16.92	1.48	0.27
		Red Wing Silt	0.51	3.03	7.53	1.03	0.75
		MN Road Lean Clay-1	0.48	4.03	10.51	1.44	0.24
		Red Lake Falls Lean Clay-2	0.60	3.71	30.05	1.45	0.25
		DI TH23 Slopes Fat Clay	1.15	5.22	519.74	1.77	0.23
	Dong and Lu (2016b)	Denver Bentonite	2.21	6.08	4989.5	2.04	0.11
	Ngoc et al. (2019)	Sand-Kaolin <sup>d</sup>	0.33	2.59	7.15	2.68	0.18
		Sand-Kaolin <sup>w</sup>	0.33	1.51	4.63	46.73	0.002
Second	Hippley (2003)	Rock Flour	0.49	2.12	2.21	23.2	0.02
	Ng et al. (2009)	Completely Decomposed Tuff	0.57	3.15	13.06	2.34	0.33
	Khosravi et al. (2010)	F-75 Silica Sand	0.61	0.76	1.64	33.82	0.11
	Khosravi et al. (2012)	Bonny Silt-1 <sup>d</sup>	0.53	1.54	5.06	18.04	0.01
		Bonny Silt-1 <sup>w</sup>	0.53	0.81	2.20	8.46	0.01
Third	Khosravi et al. (2018a)	Bonny Silt-1	0.85	3.44	24.00	1.78	0.37
	Khosravi et al. (2016)	Bonny Silt-2	0.66	2.83	4.34	3.41	0.08
	Takkabutr (2006)	Ottawa Sand	0.56	1.22	19.65	3.03	0.58

Note:  $e_i$  is the void ratio at original net normal stress.

<sup>d, w</sup> stand for drying and wetting, respectively.

To predict the small-strain shear modulus of unsaturated soils, initially Equation 2.9 was employed to generate the modified SWCC at constant net normal stresses. Then, the small-strain shear modulus was predicted by means of Equation 2.10. The performance results of the proposed small-strain shear modulus model are shown in Figure 2.5. The figure shows the measured values of the small-strain shear modulus for all soils as well as the predicted small-strain shear modulus data. In some cases, the name of the soil sample has been shortened to fit inside the figure's legend.

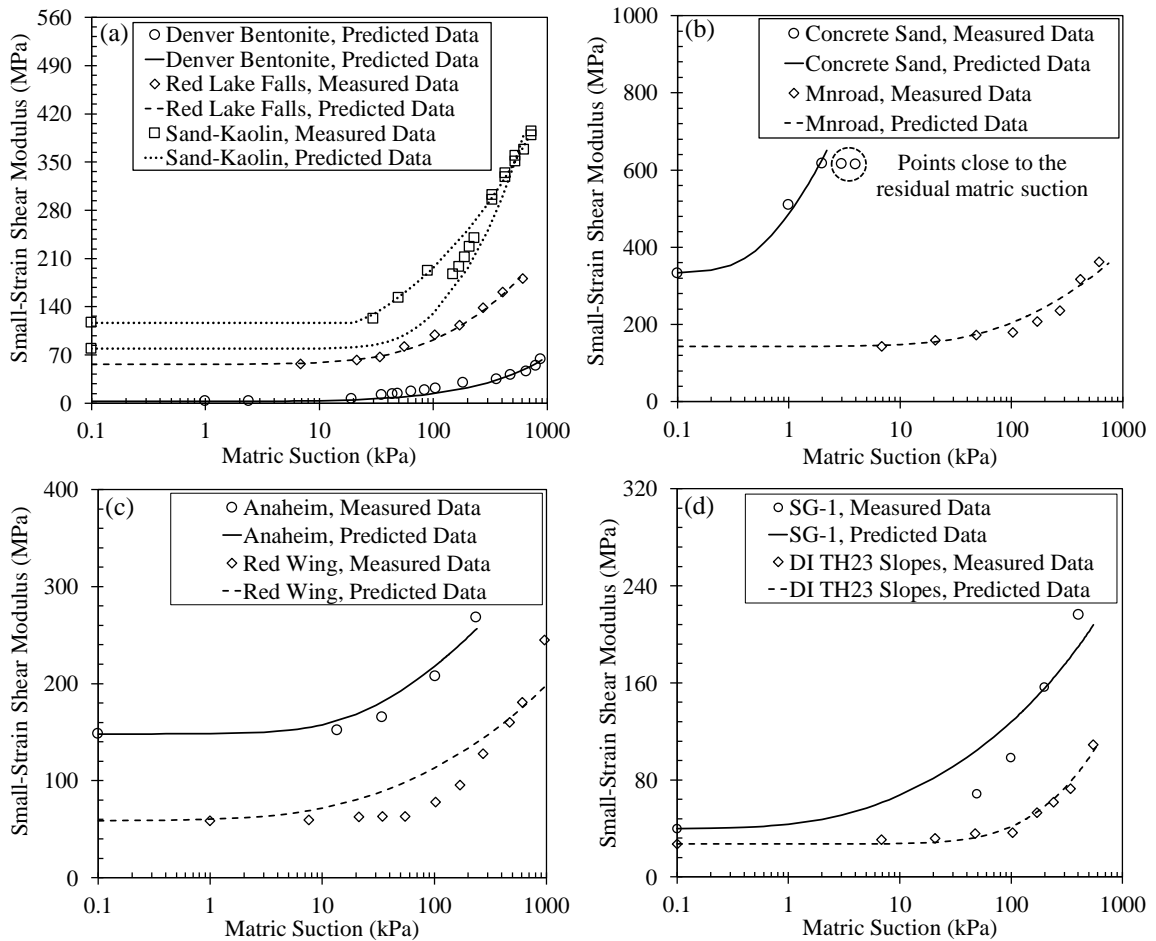


Figure 2.5 Measured and predicted small-strain shear modulus values at constant net normal stress: (a) Denver Bentonite, Red Lake Falls Lean Clay-2 and Sand-Kaolin; (b) Concrete Sand and MN Road Lean Clay-1; (c) Anaheim Clayey Sand and Red Wing Silt ; (d) SG-1 and DI TH23 Slopes Fat Clay

The predicted small-strain shear modulus data well matched the actual values for all soils. Note that two measured small-strain shear modulus values for the Concrete Sand (Picornell and Nazarian, 1998) soil did not match the predicted data. These points corresponded to matric suctions very close to the residual point. As mentioned earlier,

matric suction has almost no effect on the mechanical behavior of the unsaturated soil at suction values close to residual point. The mechanics of the proposed model does not allow for a decrease in the small-strain shear modulus with increase in matric suction. Thus, the measured small-strain shear modulus values that corresponded to these two points were excluded during predicting process. The prediction performance of the proposed model is not influenced by the type of the soil as the model is compatible to the SWCC of each soil. In all cases, the small-strain shear modulus increases with increasing suction, as expected. However, the range of applied suction varies from soil to soil. The fine-grained materials (e.g. clay soil samples) were evaluated over a wider range of suction than the coarse-grained materials. The reason is attributed to the residual suction of fine materials that normally is greater than those of the coarse soils, which allows the small-strain shear modulus measurement over higher magnitudes of matric suction. Considering Denver Bentonite sample, the small-strain shear modulus varies from 2 MPa at saturated state to almost 70 MPa at the maximum applied suction. This indicates an enormous ratio or normalized shear modulus for this soil. The model provides a reasonable prediction over the applied matric suctions, which in turn indicates applicability of the model over a wide variation of the small-strain shear modulus. In case of Sand-Kaolin sample, the small-strain shear modulus data were appropriately estimated along a drying and wetting cycle. The model has been established on the SWCC and hence is capable of estimating the small-stain shear modulus of unsaturated soils over both drying and wetting processes by means of the corresponding SWCC.

Table 2.4 tabulates the coefficients of determination ( $R$ ), net normal stress, and model parameters respective to the modified SWCC (Equation 2.9) and the proposed small-strain shear modulus prediction model (Equation 2.10) for all nine soils. In terms of  $R^2$ , satisfactory predictions were attained for the First group of soils studied under the constant net normal stress. Regarding tabulated data in Table 2.4, the difference between  $m_i$  and  $m$  in most cases is minimal and varies from 0.04 for Red Lake Falls Lean Clay-1 to almost 0.5 for Red Wing Silt sample. The amount of difference is directly proportional to the distance between the air entry point of the modified SWCC and G-capillary point of the normalized shear modulus data, as well as difference between the slope of the normalized shear modulus data and slope of the SWCC. For Red Lake Falls Lean Clay-1 sample, the

two mentioned points almost perfectly line up. However, there is a noticeable distance between air entry point of the modified SWCC and G-capillary point of the normalized shear modulus data for Red Wing Silt sample. In terms of the slopes, difference between the slope of the SWCC and slope of the normalized shear modulus data for Red Lake Falls Lean Clay-1 sample was smaller than the corresponding difference for the Red Wing Silt sample.

Table 2.4 Fitting parameters for the modified SWCCs and small-strain shear modulus equation

Soil Name	$p$ (kPa)	$e_i$	Equation 2.9				Equation 2.10	$R^2$
			$\psi_i$	$\omega_i$	$n$	$m$	$m_i$	
First Group								
Concrete Sand	0.1	0.75	0.03	0.37	2.80	0.32	0.13	0.98
SG-1	0.1	0.31	0.54	0.90	1.29	0.17	0.22	0.86
Anaheim Clayey Sand	35	0.37	1.28	3.98	1.48	0.27	0.13	0.94
Red Wing Silt	35	0.51	2.01	2.02	1.03	0.75	0.24	0.81
MN Road Lean Clay-1	35	0.48	2.90	4.23	1.44	0.24	0.21	0.93
Red Lake Falls Lean Clay-2	35	0.6	2.97	7.94	1.45	0.25	0.29	0.99
DI TH23 Slopes Fat Clay	35	1.15	4.99	121.5	1.77	0.23	0.34	0.98
Denver Bentonite	0.1	2.21	5.87	999.1	2.04	0.11	0.44	0.93
Sand-Kaolin <sup>d</sup>	0.1	0.33	2.65	2.50	2.68	0.18	0.23	0.93
Sand-Kaolin <sup>w</sup>	0.1	0.33	2.15	2.11	46.73	0.002	0.01	1.00
Second Group								
Rock Flour	0.69	0.49	2.00	2.02	23.21	0.02	0.04	0.97
	138	0.39	2.00	2.02	23.21	0.02	0.01	0.99
Completely Decomposed Tuff	110	0.57	2.74	5.96	2.34	0.33	0.16	0.97
	300	0.51	2.74	5.96	2.34	0.33	0.10	0.98
F-75 Silica Sand	3.5	0.61	0.71	1.24	33.82	0.11	0.01	0.90
	12	0.60	0.71	1.24	33.82	0.11	0.01	0.89
Bonny Silt-1 <sup>d</sup>	150	0.53	2.35	2.33	18.04	0.01	0.01	0.98
	200	0.53	2.35	2.33	18.04	0.01	0.003	0.95
Bonny Silt-1 <sup>w</sup>	150	0.53	1.19	0.99	8.46	0.01	0.002	0.97
	200	0.53	1.19	0.99	8.46	0.01	0.001	0.97

Table 2.4 (continued)

Third Group								
Bonny Silt-2	40	0.85	3.28	6.72	1.78	0.37	0.20	0.95
	600	0.63	3.28	6.72	1.78	0.37	0.12	0.97
	900	0.57	3.28	6.72	1.78	0.37	0.18	0.98
Bonny Silt-3	125	0.66	1.82	2.67	3.41	0.08	0.03	0.97
	175	0.65	1.82	2.67	3.41	0.08	0.02	0.97
	225	0.64	1.82	2.67	3.41	0.08	0.02	0.99
Ottawa sand	0.1	0.56	0.81	12.26	3.03	0.58	0.24	0.90
	6.9	0.56	0.81	12.26	3.03	0.58	0.22	0.92
	17.3	0.56	0.81	12.26	3.03	0.58	0.24	0.88
	34.5	0.56	0.81	12.26	3.03	0.58	0.28	0.97

### 2.5.3 Performance of the Proposed Model at Various Net Normal Stresses

The performance of the proposed model in predicting the small-strain shear modulus of unsaturated soils at varying net normal stress and matric suction is assessed herein using the Second group of soils presented in Table 2.3. Also, fitting parameters associated with the Gallipoli et al. (2003) equation are presented on the Table 2.3. Note that these parameters correspond to the original SWCC.

Upon modifying the original SWCC, the small-strain shear modulus was predicted (using Equation 2.10) over various net normal stresses,  $P$ , as a function of void ratio. The prediction performance of the proposed methodology for the Second group of soils is shown in Figure 2.6. For the evaluation samples, the predicted small-strain shear modulus data at the original and secondary net normal stresses matched the measured data very well. For the F-75 Silica Sand, the small-strain shear modulus changed almost at the same rate in both net normal stresses such that the final normalized shear modulus in the original and secondary net normal stresses is almost identical (at  $P = 3.5$  kPa,  $G_{0,unsat} / G_{0,sat}$  is  $23.9/19.8 = 1.21$  and at  $P = 12$  kPa  $G_{0,unsat} / G_{0,sat}$  is  $23.9/26.9 = 1.2$ ). The reason is attributed to minor volumetric changes with net normal stress.



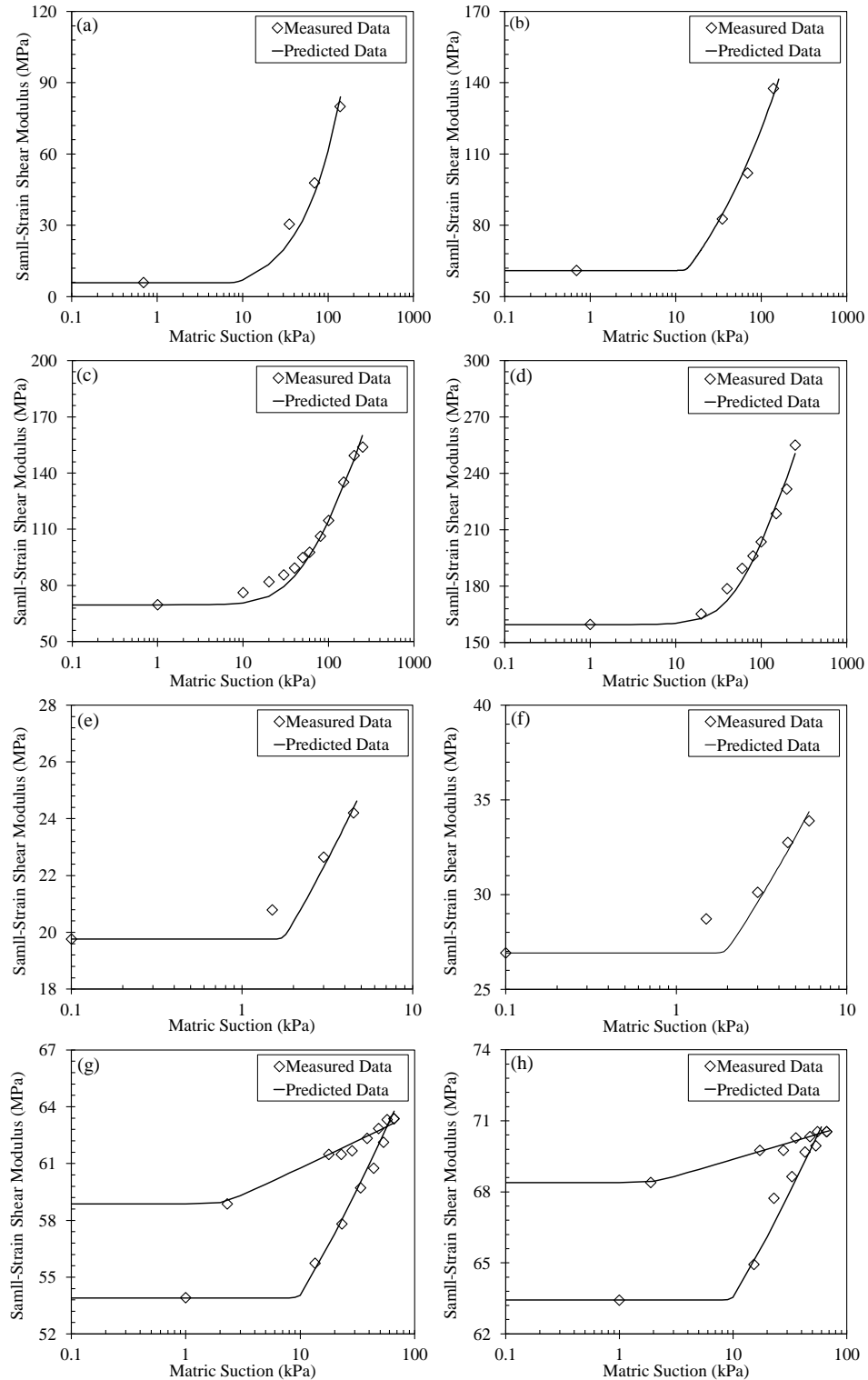


Figure 2.6 Measured and predicted small-strain shear modulus data for four literature soils at several net normal stresses, (a) Rock Flour at  $P = 0.69$  kPa, (b) Rock Flour at  $P = 138$  kPa, (c) Completely Decomposed Tuff at  $P = 110$  kPa, (d) Completely Decomposed Tuff at  $P = 300$  kPa, (e) F-75 Silica Sand at  $P = 3.5$  kPa, (f) F-75 Silica Sand at  $P = 12$  kPa, (g) Bonny Silt-1 at  $P = 150$  kPa, (h) Bonny Silt-1 at  $P = 200$  kPa

The advantage of the proposed methodology is highlighted as the difference between the original net normal stress and secondary net normal stresses increases. As discussed earlier, the small-strain shear modulus is predicted based on the modified SWCC, which was essentially derived from the original SWCC. Also, the original SWCC varies with net normal stress, which inherently causes a change in the modified SWCC as well. Thus, a modified SWCC is required for each net normal stress. In general, the process of measuring the original SWCC at various net normal stresses requires a great amount of time. Regarding the SWCC adjustment, the modified SWCCs at a secondary net normal stress is generated based on the modified SWCC corresponding to the original net normal stress. Thus, the methodology presented within this study do not require any SWCC measurement with net normal stress change. The difference between the original net normal stress and the secondary net normal stress is 50 kPa, almost 137 kPa and 190 kPa for the Bonny Silt-1, Rock Flour and Completely Decomposed Tuff, respectively. In these cases, the predicted small-strain shear modulus data were very close to the measured values. This performance illustrates the applicability of the proposed methodology for wide ranges of net normal stresses.

An interesting feature related to the Bonny Silt-1, Rock Flour and Completely Decomposed Tuff samples is the change of the highest value of the small-strain shear modulus with net normal stress. For the Rock Flour sample at net normal stress of 0.69 kPa, the small-strain shear modulus changes from 5.9 MPa to 80 MPa which is equivalent to a peak normalized shear modulus of 14. However, the maximum normalized shear modulus at net normal stress of 138 kPa is around 2.3 ( $137.6 / 61$ ). The same behavior is observed for the Bonny silt-1 and Completely Decomposed Tuff in which the maximum normalized shear modulus at the secondary net normal stress is smaller than the maximum normalized shear modulus at the original net normal stress. This difference can be explained based on the effect of consolidation stress (net normal stress) on volumetric strain of the soil and consequently the tension force between solid particles and water molecules. Regarding the Young (1805) principle, void ratio reduction induced by elevated net normal stress leads to an increase in solid-water tension, which retards the water desorption process. Due to this phenomenon, for a given soil and over a specific matric suction interval (e.g. 0 to 100 kPa), a lesser amount of water is drained at higher net normal

stress than at a lower net normal stress. Therefore, the change of effective degree of saturation,  $\Delta S_e$  at higher net normal stress is less than the change of effective degree of saturation at lower net normal stress. As discussed earlier, suction stress varies with respect to effective degree of saturation and matric suction,  $\Delta \sigma^s = \Delta S_e \cdot \Delta(u_a - u_w)$ . Thus, at the same suction interval the suction stress change would be smaller for a higher net normal stress. In addition, the change of small-strain shear modulus is directly proportional to the suction stress change,  $\Delta G_{0,unsat} \propto \Delta \sigma^s$  (this functionality is directly equivalent to the change of normalized shear modulus with suction stress,  $\Delta G_{0,unsat} / G_{0,sat} \propto \Delta \sigma^s$ , as all small-strain shear modulus data are divided by a constant small-strain shear modulus value). Therefore, it can be deduced that the change of the normalized shear modulus with suction would be smaller at higher net normal stress than at a lower net normal stress. That is why the peak value of the normalized shear modulus varies with net normal stress change.

Values of the net normal stresses, parameters related to the modified SWCCs (Equation 2.9) and the small-strain shear modulus prediction model (Equation 2.10), as well as  $R^2$  for all four soils are presented on Table 2.4. The obtained  $R^2$  values show reasonable prediction performance for all cases. Consider the F-75 Silica Sand, the value of  $m_i$  did not significantly change with net normal variation. The meaning of this observation is that a slight increase of net normal stress from 3.5 to 12 kPa caused minimal change in the structure of the soil with load (i.e. minimum load-dependent volume change). In this case, the modified SWCC of the F-75 Silica Sand at net normal stress of 12 kPa is almost identical to the modified SWCC at 3.5 kPa. Therefore, using the same value of  $m_i$  over both net normal stresses leads to satisfactory prediction results. For the other literature soils, due to significant variation in net normal stress and hence the modified SWCCs, the value of  $m_i$  slightly changes with net normal stress.

#### 2.5.4 Performance of the Proposed Model at Constant Suction

The prediction performance of the proposed methodology (Equation 2.10) at constant suction was assessed using measured small-strain shear modulus data from the

Third Group of the soils, (Khosravi et al. 2018a; Khosravi et al. 2016; Takkabutr 2006). The soil samples include Bonny Silt and Ottawa Sand. It should be noted that the Bonny Silt sample was prepared at two different initial void ratios. Thus, each soil sample was able to be evaluated separately. The Bonny Silt sample prepared at an initial void ratio of 0.85 was denoted as Bonny Silt-2. The second Bonny Silt sample was prepared at an initial void ratio of 0.66 and was identified as Bonny Silt-3. For the Third Group soils, the fitting parameters governing the original SWCC are tabulated in Table 2.3.

The small-strain shear modulus measurement was conducted over a constant suction but varying net normal stresses. Having the small-strain shear modulus over various net normal stresses predicted, the small-strain shear modulus data were extracted at constant suctions. The selected suctions for Bonny Silt-2, Bonny Silt-3 and Ottawa Sand are 50, 60 and 70 kPa, respectively. The small-strain shear modulus data based on the constant matric suction and over a range of net normal stress is illustrated in Figure 2.7.

The Bonny Silt samples underwent a wide range of net normal stresses, while the Ottawa Sand was subjected to a narrow net normal stress ranging from 0 to 35 kPa. As can be observed, the measured small-strain shear modulus increases with net normal stress in all samples. The reason behind of this ascending trend can be described in accordance to the effect of the net normal stress on the void ratio reduction, and in turn elevation of the small-strain shear modulus (See Equation 2.4).

Regarding the estimated small-strain shear modulus, the developed models indicates a suitable prediction performance for all samples under constant suction condition. This in turn shows the applicability of the proposed methodology for a constant suction. Table 2.4 presents fitting parameters associated with each equation and  $R^2$  values obtained from the prediction.

The maximum difference between the  $m_i$  and  $m$  for the third group of soils presented in Table 2.4 is around 0.3. Considering all data tabulated on Table 2.4, difference between the  $m_i$  and  $m$  mostly varies from 0 to 0.3. Thus, it can be concluded that the difference between the  $m_i$  and  $m$  lays in this range, as  $m_i - m \leq 0.3$ .

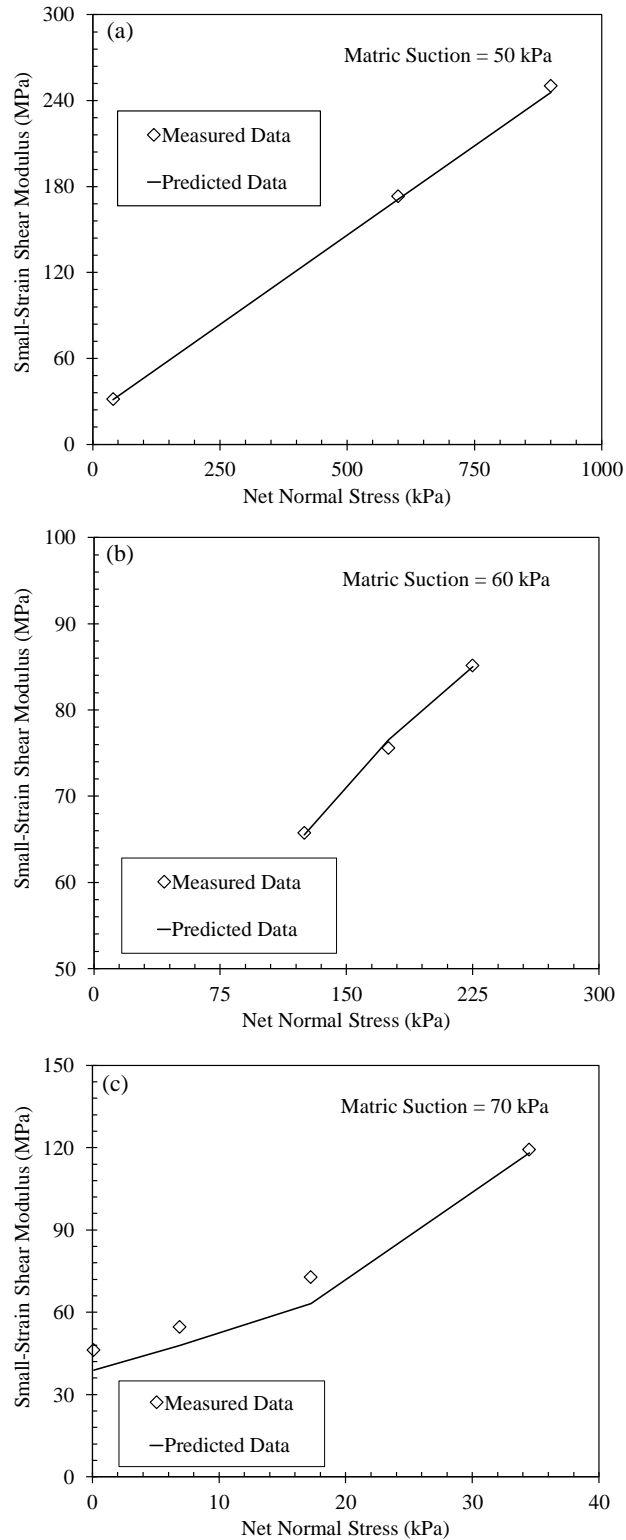


Figure 2.7 Measured and predicted small-strain shear modulus for three literature soils at several matric suctions. (a) Bonny Silt-2 at matric suction = 50 kPa and initial void ratio = 0.85 (b) Bonny Silt-3 at matric suction = 60 kPa and initial void ratio = 0.66, c) Ottawa Sand at matric suction = 70 kPa

### 2.5.5 Sensitivity of the Proposed Model to the Parameter $m_i$

Parameter  $m_i$  is the key parameter of the model determining the prediction performance of the model. Along with this section, the sensitivity of the model to the value of parameter  $m_i$  is investigated by giving three values to this parameter. For this purpose, DI TH23 Slopes Fat Clay and Bonny silt-2 were selected as the evaluation soils. Initially, the small-strain shear modulus was predicted by a value of the  $m_i$  (denoted as initial  $m_i$  parameter) that produces the best prediction result. Then, the prediction was repeated twice by changing parameter  $m_i$  to two values (denoted as secondary  $m_i$  parameters), such that the difference between new  $m_i$  parameters and the initial one lays in a range of  $\pm 0.05$ . Figure 2.8 illustrates prediction results obtained by each value of the parameter  $m_i$ . As should be expected, any change of parameter  $m_i$  from the initial value would impact the predictability of the model. The shown data indicate that the prediction performance is slightly sensitive to the value of parameter  $m_i$  for Bonny silt-2 sample. This can be confirmed by the minimal distance between the prediction curve generated by the initial  $m_i$  and the prediction curve created by each secondary  $m_i$  parameter. In case of the DI TH23 Slopes Fat Clay, the predicted small-strain shear modulus values are close to the measured values, except that the final small-strain shear modulus which the difference between the predicted and measure value increases. However, the overall prediction performance delivered by both secondary  $m_i$  parameters is quite satisfactory.

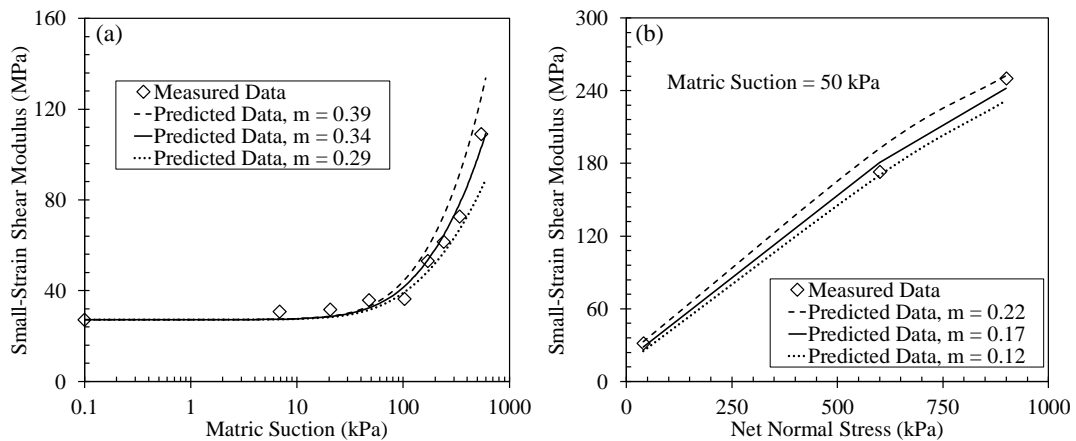


Figure 2.8 Evaluate sensitivity of the proposed model to the value of parameter  $m_i$ . (a) DI TH23 Slopes Fat Clay, (b) Bonny Silt-2

## **Constitutive Model for Describing the Fully Coupled Hydro-Mechanical Behavior of Unsaturated Soils**

### 3.1 Introduction

The unsaturated state is characterized by the existence of a gaseous phase interacting with a liquid phase inside the voids. The mechanical behavior of an unsaturated soil is described by the air-water differential pressure, referred to as suction. As a soil is subjected to greater magnitude of suction, the wetted area of contact between the soil particles decreases (Vanapalli and Fredlund 1999). This phenomenon contributes to the changes in the skeleton stress and thus changes to the mechanical behavior of the unsaturated soil as well (Han and Vanapalli, 2016; Ahmed and Bryson, 2019).

Unsaturated soil constitutive models are generally extensions of saturated soil constitutive models. Such extensions are performed by considering net normal stress and suction as stress state variables for describing the mechanical and hydraulic behavior of the unsaturated soils (Zhou et al., 2012). An example of this extension is the Barcelona Basic Model (BBM) proposed by Alonso et al. (1990). This model is an extension of the Modified Cam Clay Model and serves as a basis for a multitude of unsaturated soil constitutive models (e.g. Kohgo et al., 1993; Wheeler and Sivakumar, 1995; Bolzon et al., 1996; Cui and Delage, 1996; Wheeler, 1996; Gens 1996; Dangla et al., 1997; Jommi, 2000; Vaunat et al., 2000; Tang and Graham, 2002; Loret and Khalili, 2002; Gens et al., 2006; Gallipoli et al., 2003a; Wheeler et al., 2003; Sheng et al., 2004; Santagiuliana and Schrefler, 2006; Sun et al., 2007a; Sun et al., 2007b). The available constitutive models generally have the ability to simulate some basic mechanical behavior of the unsaturated soil, such as volumetric deformation under isotropic stress and stress-strain relationship under anisotropic stress over a constant suction. However, most models lack the capability to precisely simulate: (i) the change of the yield stress with suction, (ii) the deformation of a soil over the drying process, and (iii) the soil volume change as soil transitions from a saturated state to an unsaturated state (Sheng et. al, 2008a).

Sheng et al. (2008a) developed a model to address the aforementioned issues. The model, referred as SFG, formulates the volumetric strain based on independent stress and

suction variables. The model then incorporates isotropic hardening laws to develop the loading-collapse yield surfaces. The hysteresis behavior of the soil is expressed as a function of volumetric deformation that is associated with suction and stress, as well as water content-suction relationship that is defined by soil-water characteristic curve (SWCC). The shear strength of the soil is estimated based on yield surface equation. An incremental stress-strain relationship is derived by imposing a consistency condition on yield function. Solving the equation leads to the introduction of a plastic multiplier that governs the plastic volumetric strain and the plastic shear strain.

Available constitutive models for unsaturated soils normally employ a loading-collapse yield curve, denoted herein as the yield curve, to describe change of preconsolidation (yield) stress with suction. Many constitutive laws in literature (e.g. Vaunat et al., 2000; Tang and Graham, 2002) assume that the preconsolidation stress increases with an increase in suction. However, the SFG model assumes that yield stress increases with decreasing suction up to the air entry suction,  $s_{ae}$ , and increases with increasing suction thereafter. This behavior is more rational. In addition, the SFG approach generates a more precise yield curve for nonconsolidated soils, (e.g. drying a non-consolidated slurry soil, and wetting an initially unsaturated soil). Existing models assume that normal consolidation lines are linear at a constant suction (for suction  $> 0$  kPa). However, several experimental data in literature (e.g. Cunningham et al, 2003; Lloret et al, 2003) show that normal consolidation lines are curved at a constant suction. In the SFG model, associating volumetric deformation with independent stress and suction functions contributes to curvature of the normal consolidation lines in void ratio-logarithmic mean stress space. However, the water content-volume change relationship was described in form of a power function in which the power coefficient ranged from 0 to 1. This variation adds uncertainty to the predictability of the model. Therefore, the hydraulic component of the SFG model must be redefined.

Until now, few researchers have successfully applied SFG model to predict incremental stress-strain behavior of unsaturated soils over the shearing process. This is attributed to the complexity of the stress-strain equation, as well as several parameters (e.g. small-strain shear modulus,  $G_0$ ) that need to be measured in advance. The small-strain shear modulus is a key parameter used for describing elastic shear strain of the soil with respect



to the stress. Many researchers (Ng and Yung, 2008; Hoyos et al., 2011; Khosravi and McCartney, 2012; Heitor et al., 2013; Oh and Vanapalli, 2014; Hoyos et al., 2015; Dong et al., 2016; Khosravi et al., 2018b) have proposed models to formulate the small-strain shear modulus of unsaturated soils as a function of net normal stress and suction. Some of these models only predict the small-strain shear modulus over the drying condition with respect to suction increase, while a group of models adopts separate equations for the wetting and drying conditions. However, each of these models is highly dependent on the various empirical equations that are only valid for that model. Thus, the geotechnical discipline lacks a general framework that can predict the small-strain shear modulus of unsaturated soils over various suctions and net normal stresses.

This current study pursues three major goals: (i) redefine the hydraulic component of the original SFG model to generate a more reliable function for describing water content-volumetric change (ii) redefine the elastic shear strain component of the SFG model based on a new shear modulus equation that consider volume change during wetting and drying, (iii) utilize the modified model to predict incremental stress-strain and water content-stress state behavior of unsaturated soils over shearing phase. The modified-SFG model can be considered as a combination of the original SFG model and the redefined equations. Therefore, the proposed model will follow the same principles that were applied by Sheng et al. (2008a) to develop SFG model, as well as basic fundamentals applied by the authors to redefine the hydraulic and elastic shear strain components of the original model.

## 3.2 An Overview of the Original SFG Model

### 3.2.1 Volumetric Strain

Consider a normally consolidated soil subjected to an isotropic consolidation pressure, incremental volumetric strain,  $d\varepsilon_v$  of an unsaturated soil with respect to stress and suction variation is calculated as follows,

$$d\varepsilon_v = \frac{de}{1+e} = \frac{\lambda_{vp}}{1+e} \frac{d\bar{p}}{\bar{p}+s} + \frac{\lambda_{vs}}{1+e} \frac{ds}{\bar{p}+s} \quad (3.1a)$$

$$d\varepsilon_v^e = \frac{de}{1+e} = \frac{\kappa_{vp}}{1+e} \frac{d\bar{p}}{\bar{p}+s} + \frac{\kappa_{vs}}{1+e} \frac{ds}{\bar{p}+s} \quad (3.1b)$$

$$d\varepsilon_v^p = \frac{de}{1+e} = \frac{\lambda_{vp} - \kappa_{vp}}{1+e} \frac{d\bar{p}}{\bar{p}+s} + \frac{\lambda_{vs} - \kappa_{vs}}{1+e} \frac{ds}{\bar{p}+s} \quad (3.1c)$$

where  $d\varepsilon_v^e$  and  $d\varepsilon_v^p$  are elastic and plastic volumetric strain, respectively;  $e$  is void ratio;  $\kappa_{vp}$  is slope of the normally consolidated line associated with the unloading-reloading segment, and is replaced by  $\lambda_{vp}$  for the virgin compression portion of the normally consolidated line;  $\bar{p} = p - u_a$  is mean net normal stress,  $p$  is mean stress and  $u_a$  is pore-air pressure;  $S$  is suction;  $\kappa_{vs}$  is a parameter governing swelling-recompression behavior induced by suction change, and is replaced by  $\lambda_{vs}$  if the change of suction leads to a virgin compression. Since  $\kappa_{vp}$  and  $\lambda_{vp}$  describe volumetric deformation induced by isotropic stress, it is assumed that these parameters would be independent of suction. Thus,  $\kappa_{vp}$  and  $\lambda_{vp}$  remain constant for a typical unsaturated soil over several magnitudes of suction. This outstanding feature contributes to prediction of volumetric-isotropic stress of the soil over several suctions by using only one value of  $\kappa_{vp}$  and  $\lambda_{vp}$  that can be easily estimated from one isotropic consolidation test at saturated state. It is noted that other unsaturated constitutive models, such as the Refined Barcelona Basic Model (Hoyos and Pérez-Ruiz, 2012) require different values of  $\lambda_{vp}$  for each suction. In contrast to the  $\kappa_{vp}$  and  $\lambda_{vp}$  parameters, the magnitude of  $\kappa_{vs}$  and  $\lambda_{vs}$  is a function of suction. Sheng et al. (2008a) introduced a point on the SWCC that is identified as saturation suction,  $S_{sa}$ . The point is used as a reference to separate the saturated state from the unsaturated one. In the definition of saturation suction, the  $\lambda_{vs}$  parameter is defined as a function of suction as,

$$\kappa_{vs} = \begin{cases} \kappa_{vp} & s < s_{sa} \\ \kappa_{vp} \frac{s_{sa} + 1}{s + 1} & s \geq s_{sa} \end{cases} \quad (3.2)$$

Analogous to  $\kappa_{vs}$ , the value of parameter  $\lambda_{vs}$  is controlled by suction in the same manner. The saturation suction,  $s_{sa}$  normally equals air entry suction,  $s_{ae}$ . Introducing Equation 3.2 into the Equation 3.1 and integrating leads to mathematical expressions that describe soil volume change for various load and suction conditions, including mean net normal stress changes under constant suction or suction changes under constant mean net normal stress. In the SFG model, if a soil is initially dried to a suction beyond the saturation suction, and then subjected to isotropic loading, the deformational behavior of the soil will be plastic, hence the volumetric behavior of the soil is only governed by  $\lambda_{vp}$  and  $\lambda_{vs}$  (Zhou and Sheng, 2009). The reason behind of this behavior will be explained in subsequent sections. The main goal of this paper is to model incremental stress-strain behavior of the soils under loading. Thus, it is preferred to use a differential form of volumetric strain (Equation 3.1) for this research.

### 3.2.2 Yield Curve and Hardening Laws

Projection of the yield curve in  $\bar{p} - s$  space can be formulated based on the volumetric strain equation (Equation 3.1) coupled with the hardening laws. The preconsolidation stress, as defined by Henshall (1996), is a border in stress space between elastic and plastic behavior. Therefore, the soil sample does not experience any plastic volumetric change before preconsolidation stress. Since all volume change of the soil is recoverable before and up to the preconsolidation stress, the soil undergoes no plastic volumetric strain. Setting Equation 3.1c equal to zero, the following expression is derived,

$$\left(\lambda_{vp} - \kappa_{vp}\right) \frac{d\bar{p}}{\bar{p}_y + s} + \left(\lambda_{vs} - \kappa_{vs}\right) \frac{ds}{\bar{p}_y + s} = 0 \Rightarrow \frac{d\bar{p}_y}{ds} = -\frac{\lambda_{vs} - \kappa_{vs}}{\lambda_{vp} - \kappa_{vp}} \quad (3.3)$$

where  $\bar{p}_y$  is the preconsolidation stress. Equation 3.3 gives the change of the preconsolidation stress,  $d\bar{p}_y$  with respect to the suction variation,  $ds$ . The equation may

be rearranged based on the saturation suction by introducing Equation 3.2 into the Equation 3.3. Then, the projection of the preconsolidation surface in  $\bar{p} - s$  space can be modeled via conducting mathematical integration on the rearranged equation, along specified intervals. Setting the preconsolidation stress interval from  $\bar{p}_{y0}$  to  $\bar{p}_y$  and suction interval from 0 to  $S$  then integrating over the mentioned intervals, the following equations are derived for estimating preconsolidation stress based on the suction,

$$\bar{p}_y = \begin{cases} \bar{p}_{y0} - s & s < s_{sa} \\ \bar{p}_{y0} - s_{sa} - (s_{sa} + 1) \ln \frac{s + 1}{s_{sa} + 1} & s \geq s_{sa} \end{cases} \quad (3.4)$$

Setting the integration interval from  $(0, 0)$  to  $(\bar{p}_0, s)$  and reperforming the integration leads to,

$$\bar{p}_0 = \begin{cases} -s & s < s_{sa} \\ -s_{sa} - (s_{sa} + 1) \ln \frac{s + 1}{s_{sa} + 1} & s \geq s_{sa} \end{cases} \quad (3.5)$$

Equation 3.5 defines the yield curve for a soil that was never consolidated under saturated state (slurry soil). An area is formed between  $\bar{p}_0$  and  $\bar{p}_y$  curves, that corresponds to initial elastic zone. However, the soil experiences irrecoverable (plastic) deformation as the magnitude of the applied stress exceeds the initial preconsolidation stress. To describe deformational behavior of the soil in plastic zone, a hardening law and plastic volume change must be reapplied. Upon passing preconsolidation stress, plastic volumetric strain would not equal zero, thus Equation 3.3 is not valid. In addition, sequential yield surfaces are generated at successive preconsolidation stresses. Under constant suction, the term governing the effect of suction change,  $ds$ , on volumetric strain becomes ineffective, hence it is eliminated from Equation 3.1c. Accordingly, the plastic volumetric strain is redefined as,

$$d\varepsilon_v^p = \frac{de^p}{1+e} = \frac{(\lambda_{vp} - \kappa_{vp})}{1+e} \frac{d\bar{p}_y}{\bar{p}_y + s} \quad (3.6)$$

Equation 3.6 indicates that the evolution of preconsolidation stress,  $\bar{p}_y$ , is function of suction. If the soil is isotropically loaded to plastic yielding at different suction levels, a new yield curve is generated that represents a contour of total plastic volumetric change. This means that total plastic volumetric change will be the same when every points on the current yield curve,  $\bar{p}_y$ , is loaded to a new yield curve  $\bar{p}_{yn}$  under constant suction (Sheng et al., 2008a). Thus, the following equivalent relation can be drawn,

$$\int_{\bar{p}_y}^{\bar{p}_{yn}} (\lambda_{vp} - \kappa_{vp}) \frac{d\bar{p}_y}{\bar{p}_y + s} = \int_{\bar{p}_{y0}}^{\bar{p}_{yn0}} (\lambda_{vp} - \kappa_{vp}) \frac{d\bar{p}_y}{\bar{p}_y + 0} \quad (3.7)$$

Imposing the integral on the above equation leads to the following expressions that give yield stresses greater than initial preconsolidation stress,  $\bar{p}_y$ .

$$\bar{p}_{yn} = \begin{cases} \bar{p}_{yn0} - s & s < s_{sa} \\ \frac{\bar{p}_{yn0}}{\bar{p}_{y0}} \left[ \bar{p}_{y0} + s - s_{sa} - (s_{sa} + 1) \ln \frac{s+1}{s_{sa}+1} \right] - s & s \geq s_{sa} \end{cases} \quad (3.8)$$

If the soil is dried from the current yield curve under a constant mean net normal stress,  $\bar{p}$  the projection of yield curve is defined by the following equations:

$$\bar{p} = 1 \Rightarrow s_{yn} = \begin{cases} \frac{1}{\frac{1}{s_y + 1} - \frac{1}{s_{sa} + 1} \ln \frac{\bar{p}_{yn0}}{\bar{p}_{y0}}} - 1 & \bar{p} \leq \bar{p}_{y0} - s_{sa} \\ \frac{s_{sa} + 1}{1 - \ln \frac{\bar{p}_{yn0}}{\bar{p} + s_{sa}}} - 1 & \bar{p}_{yn0} - s_{sa} \geq \bar{p} > \bar{p}_{y0} - s_{sa} \\ \bar{p}_{yn0} - \bar{p} & \bar{p} > \bar{p}_{yn0} - s_{sa} \end{cases} \quad (3.9a)$$

$$\bar{p} \neq 1 \Rightarrow s_{yn} = \begin{cases} \frac{A\bar{p} - 1}{1 - A} & \bar{p} \leq \bar{p}_{y0} - s_{sa} \\ \frac{B\bar{p} - 1}{1 - B} & \bar{p}_{yn0} - s_{sa} \geq \bar{p} > \bar{p}_{y0} - s_{sa} \\ \bar{p}_{yn0} - \bar{p} & \bar{p} > \bar{p}_{yn0} - s_{sa} \end{cases} \quad (3.9b)$$

where,

$$A = \left( \frac{\bar{p}_{yn0}}{\bar{p}_{y0}} \right)^{\frac{\bar{p}-1}{s_{sa}+1}} \frac{s_y + 1}{s_y + \bar{p}}, \quad B = \left( \frac{\bar{p}_{yn0}}{\bar{p} + s_{sa}} \right)^{\frac{\bar{p}-1}{s_{sa}+1}} \frac{s_{sa} + 1}{s_{sa} + \bar{p}}$$

### 3.2.3 Shear Strength

Fredlund et al. (1978) proposed the following mathematical relationship to describe shear strength of unsaturated soils with respect to the stress and suction.

$$\tau = \left[ c' + (\sigma_n - u_a) \tan \phi' \right] + \left[ s \tan \phi^b \right] = \bar{c} + (\sigma_n - u_a) \tan \phi' \quad (3.10)$$

where  $\tau$  is the shear strength,  $c'$  is the effective cohesion and is usually zero unless the soil is cemented,  $\phi'$  is the effective friction angle that can be obtained from saturated condition,  $\sigma_n$  is the normal stress on the failure plane,  $\bar{c}$  is apparent cohesion and  $\phi^b$  is the frictional angle due to suction. Equation 3.10 gives shear strength of saturated soil, if  $\phi^b$  is set to  $\phi'$ . Sheng et al. (2008a) formulated shear strength of the unsaturated soils according to the preconsolidation stress function. In elastoplastic models, the shear strength of an unsaturated soil is usually embodied in the apparent tensile strength function,  $\bar{p}_0$  (Sheng et al., 2008b). The apparent cohesion,  $\bar{c}$  in the SFG model is defined as

$$\bar{c} = -\bar{p}_0 \tan \phi' \quad (3.11)$$

Inserting Equation 3.5 into the Equation 3.11 yields,

$$\bar{c} = \begin{cases} s \tan \phi' & s < s_{sa} \\ \left[ s_{sa} + (s_{sa} + 1) \ln \frac{s+1}{s_{sa}+1} \right] \tan \phi' & s \geq s_{sa} \end{cases} \quad (3.12)$$

Combining Equation 3.10 with Equation 3.12 formulates the shear strength of unsaturated soils as a function of the suction and net normal stress.

$$\tau = \begin{cases} s \tan \phi' + (\sigma_n - u_a) \tan \phi' & s < s_{sa} \\ \left[ s_{sa} + (s_{sa} + 1) \ln \frac{s+1}{s_{sa}+1} \right] \tan \phi' + (\sigma_n - u_a) \tan \phi' & s \geq s_{sa} \end{cases} \quad (3.13)$$

### 3.2.4 Incremental Stress-Strain Over Shearing Phase

A crucial feature of the SFG model involves describing incremental relationship between the stress and strain. For an unsaturated soil subjected to isotropic loads, the stress-strain relationship only is governed by the suction and net normal stress. However, mechanical behavior of unsaturated soils in the shearing stage is controlled by suction, net normal stress and the anisotropic load termed the deviatoric stress,  $q$ . The stress-strain model must describe the mechanical behavior of the soil in both saturated and unsaturated conditions for continuity across degree of saturation extents. Mechanical response of an unsaturated soil in  $q - p$  space can be described by an ellipse, referred to as yield surface. If the Modified Cam Clay (MCC), model is used as the base model for the saturated soil, then the elliptic yield surface can be extended to the suction axis as follows (Sheng et al., 2008b),

$$f = q^2 - M^2(\bar{p} - \bar{p}_0)(\bar{p}_{yn} - \bar{p}) = 0 \quad (3.14)$$

where  $f$  is yield surface function; and  $M$  is slope of critical state line in  $q - p$  space. Equation 3.14 reverts to Modified Cam Clay model at zero suction (saturation condition), since  $\bar{p}_0$  becomes zero (Equation 3.5). Due to an anisotropic load, a soil sample would undergo both volumetric and shear strains, at shearing stage. In addition, soil samples experiences both elastic and plastic volume changes. Thus, there are four strain components associated with the shearing phase, as elastic volumetric strain,  $d\varepsilon_v^e$ , plastic volumetric strain,  $d\varepsilon_v^p$ , elastic shear strain,  $d\varepsilon_s^e$  and plastic shear strain,  $d\varepsilon_s^p$ . In terms of elastic components,  $d\varepsilon_v^e$  is estimated from Equation 3.1a and  $d\varepsilon_s^e$  is computed as a function of deviatoric stress,  $q$  and small-strain shear modulus,  $G_0$ .

$$d\varepsilon_s^e = \frac{dq}{3G_0} \quad (3.15)$$

It should be noted that the value of small-strain shear modulus corresponds to the end of the consolidation process or initiation of shear phase. Contrary to elastic strain components, the increments of plastic strains need to be estimated by associated flow rule.

Sheng et al. (2008a) proposed the following equations for describing plastic strain components.

$$d\varepsilon_v^p = \Lambda \frac{\partial f}{\partial \bar{p}} ; d\varepsilon_s^p = \Lambda \beta \frac{\partial f}{\partial q} \quad (3.16a,b)$$

where  $\Lambda$  is plastic multiplier. Imposing consistency condition on yield function, leads to definition of  $\Lambda$ , as

$$\Lambda = \frac{-1}{\frac{\partial f}{\partial \bar{p}} \frac{\partial f}{\partial \bar{p}_y} \frac{\partial \bar{p}_y}{\partial \varepsilon_v^p}} \left[ \frac{\partial f}{\partial \bar{p}} d\bar{p} + \frac{\partial f}{\partial q} dq + \left( \frac{\partial f}{\partial \bar{p}_0} \frac{\partial \bar{p}_0}{\partial s} + \frac{\partial f}{\partial \bar{p}_y} \frac{\partial \bar{p}_y}{\partial s} \right) ds \right] \quad (3.17)$$

Parameter  $\beta$  in Equation 3.16 is defined by Alonso et al, (1990) as follows,

$$\beta = \frac{M(M-9)(M-3)}{9(6-M)} \left[ \frac{1}{1 - \frac{\kappa_{vp}}{\lambda_{vp}}} \right] \quad (3.18)$$

A full description of incremental volumetric and shear strains of the soil under triaxial/shearing load are presented in the following expressions,

$$d\varepsilon_v = \frac{\kappa_{vp}}{1+e} \frac{d\bar{p}}{\bar{p}+s} + \frac{\kappa_{vs}}{1+e} \frac{ds}{\bar{p}+s} + \Lambda \frac{\partial f}{\partial \bar{p}} \quad (3.19a)$$

$$d\varepsilon_s = \frac{dq}{3G_0} + \Lambda \beta \frac{\partial f}{\partial q} \quad (3.19b)$$

To describe elastic component of shear strain, the magnitude of small-strain shear modulus must be available in advance. The small-strain shear modulus changes proportionally with net normal stress and suction, therefore it must be measured for each set of suction and net normal stress. Generally, measurement of small-strain shear modulus is a time-consuming and skill-demanding procedure. Thus, any methodology that can estimate the small-strain shear modulus of unsaturated soils with respect to net normal stress and suction may be greatly contributive.



### 3.3 Modified-SFG Model

#### 3.3.1 Hysteresis Behavior

Sheng et al. (2008a) introduced a hysteresis component to model change of water content with respect to suction. It was assumed that wetting and drying SWCCs mirror each other, as shown on Figure 3.1. As an approximation, SWCC may be divided into three linear segments with respect to different suction intervals. Each linear segment has a slope that governs changing rate of effective degree of saturation,  $S_e$  with respect to suction. The effective degree of saturation is defined as,

$$S_e = \frac{S_r - S_{r,res}}{1 - S_{r,res}} \quad (3.20)$$

where  $S_r$  is a degree of saturation and  $S_{r,res}$  is degree of saturation corresponding to residual suction,  $S_{res}$ . In  $S_e - \ln s$  space, incremental changes in effective degree of saturation with suction can be quantified as follows.

$$S_e = -J \cdot \ln s \xrightarrow{\text{Derivation}} dS_e = -J \frac{ds}{s} \quad (3.21)$$

where  $J$  represents slope of a linear segment that corresponds to a specific suction interval.

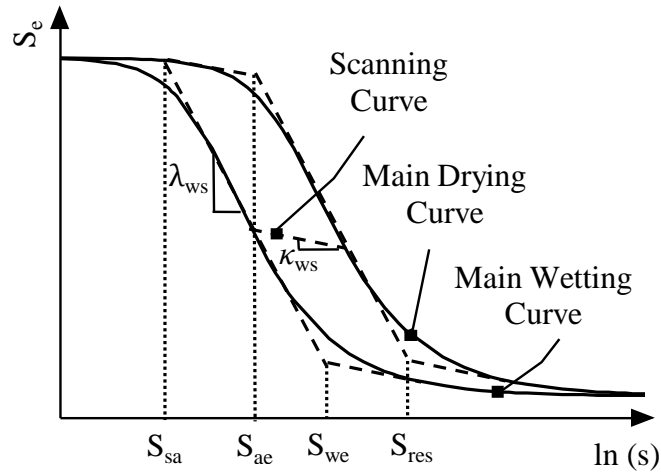


Figure 3.1 Degree of saturation versus suction

Due to variation of desaturation/absorption rate with suction range, slope of each segment is defined as a function of suction interval, as follows

$$J = \begin{cases} 0 & s < s_{sa} \\ \kappa_{ws} & s_{sa} \leq s < s_{ae} \\ \lambda_{ws} & s_{ae} \leq s < s_{res} \\ \kappa_{ws} & s_{res} \leq s \end{cases} \quad (3.22)$$

where  $s_{ae}$  and  $s_{we}$  are air entry suction and water entry suction, respectively. The wetting process may be interpreted based on wetting SWCC that is controlled by water entry suction,  $s_{we}$ . Thus, Equation 3.22 is also valid for wetting process. It should be noted that all scanning curves are assumed to be parallel and have a slope of  $\kappa_{ws}$ . Normally, the effective degree of saturation-suction relationship is described based on  $\log s$ , thus, Equation 3.21 can be converted to the following form, in  $S_e - \log s$  space,

$$S_e = -J \cdot \log s \xrightarrow{\text{Derivation}} dS_e = \frac{-J}{\ln(10)} \frac{ds}{s} \quad (3.23)$$

As suggested by Masin (2010), water content of unsaturated soils is controlled by both suction and void ratio. Therefore, Equation 3.23 may not be able to fully describe the hydraulic behavior of the unsaturated soils. Sun et al. (2007b) proposed an equation that formulates increment in the degree of saturation with respect to both suction change and volume change. Their model takes the following form and can be considered as a modified version of the Equation 3.23.

$$dS_e = -\frac{J}{\ln(10)} \frac{ds}{s} - Kde \quad (3.24)$$

where  $K = \lambda_{se}$ . Parameter  $\lambda_{se}$  is the slope of a line that defines degree of saturation versus void ratio under constant suction. Therefore, the parameter  $\lambda_{se}$  must be available before conducting prediction process. Obviously, the parameter  $\lambda_{se}$  is estimated based on known values of degree of saturation and void ratio, while the objective of this study is to predict both degree of saturation and void ratio. Thus, the approach proposed by Sun et al. (2007b) would not be applicable to this study. Sheng and Zhou (2011) modified the original

SFG hysteresis component in accordance to the framework established by Sun et al. (2007b), Equation 3.24. In their approach, parameter  $K$  is redefined as,

$$K = \frac{S_r}{e} (1 - S_r)^m \quad (3.25)$$

where  $m$  is a fitting parameter ranging from 0 to 1. A full description of hysteresis model proposed by Sheng and Zhou (2011) can be expressed as,

$$dS_r = -\frac{J}{\ln(10)} \frac{ds}{s} - \frac{S_r}{e} (1 - S_r)^m de \quad (3.26)$$

Defining Equation 3.26 in terms of effective degree of saturation yields,

$$dS_e = -\frac{J}{\ln(10)} \frac{ds}{s} - \frac{[S_e(1 - S_{r,res})] + S_{r,res}}{e(1 - S_{r,res})} \left(1 - \{[S_e(1 - S_{r,res})] + S_{r,res}\}\right)^m de \quad (3.27)$$

In this case, the only values needed are effective degree of saturation and void ratio at the beginning of the loading phase. Sheng and Zhou (2011) did not provide any methodology for determining the exact value of parameter  $m$ . Sensitivity of prediction performance to the value of this parameter will be evaluated later. The main purpose of using the parameter  $K$  is to describe change of effective degree of saturation with respect to void ratio variations. Thus,  $K$  is a coefficient that can be defined as  $K = \partial S_e / \partial e$ . To estimate parameter  $K$ , partial derivation must be applied to an equation that formulates effective degree of saturation based on the void ratio. Gallipoli et al. (2003b) proposed an SWCC equation that includes both suction and void ratio to predict absorption and desorption behaviors of the unsaturated soils. Gallipoli et al. (2003b) developed their model based on van Genuchten (1980) SWCC equation. This model addresses water content-matric suction relationship at a constant void ratio. The van Genuchten model (1980) has the following form, as

$$S_e = \left[ 1 + \left( \frac{s}{\alpha} \right)^n \right]^{-m} \quad (3.28)$$

where  $\alpha$ ,  $n$  and  $m$  are fitting parameters reflecting the air entry value, the slope at the inflection point of the SWCC, and the curvature of the SWCC near the residual point, respectively. The Gallipoli et al. (2003b) model assumed that the shift in the SWCC could

be quantified by replacing the  $\alpha$  parameter of the van Genuchten (1980) model with an equivalent term as,  $\alpha = \omega/e^\psi$ . The Gallipoli et al. (2003b) model is given as,

$$S_e = \left[ 1 + \left( \frac{e^\psi s}{\omega} \right)^n \right]^{-m} \quad (3.29)$$

where  $n$  and  $m$  are the van Genuchten (1980) fitting parameters;  $\psi$  and  $\omega$  are model parameters mostly govern air entry change with void ratio change and the location of the SWCC as a function of the current void ratio, respectively. Imposing partial derivation to Equation 3.29 based on void ratio leads to another definition of parameter  $K$ , as follows,

$$K = \frac{\partial S_e}{\partial e} = \frac{-mn\psi \left[ 1 + \left( \frac{e^\psi s}{\omega} \right)^n \right]^{-m-1} \cdot \left( \frac{e^\psi s}{\omega} \right)^n}{e} \quad (3.30)$$

Taking Equation 3.29 into account, Equation 3.30 is rewritten as,

$$K = \frac{\partial S_e}{\partial e} = \frac{mn\psi \cdot S_e^{\frac{m+1}{m}} \cdot \left( 1 - S_e^{\frac{-1}{m}} \right)}{e} \quad (3.31)$$

Imputing Equation 3.31 into Equation 3.24, the hydraulic behavior of the soil as a function of both matric suction and void ratio can be quantified by an expression given as,

$$dS_e = -\frac{J}{\ln(10)} \frac{ds}{s} - \left[ mn\psi \cdot S_e^{\frac{m+1}{m}} \cdot \left( 1 - S_e^{\frac{-1}{m}} \right) \right] \frac{de}{e} \quad (3.32)$$

Equation 3.32 applies SWCC to predict hydraulic behavior of the soil with respect to the applied load. The equation is independent of any fitting parameter (except that the SWCC parameters) and can be considered as an alternative to the Sheng and Zhou (2011) approach. The ability of the Equation 3.32 and Sheng and Zhou (2011) approach in predicting hydraulic behavior of unsaturated soils with respect to the applying stress is evaluated through a preliminary performance assessment.

Data used for the preliminary performance assessment was obtained from Sharma (1998). The sample in that study was prepared by mixing 20 percent of bentonite with 80 percent of kaolin (by mass), then compacting the mixture to a vertical stress equal to 400 kPa. Under constant suction of 200 kPa, the sample was subjected to a consolidation test that included several cycles of loading, unloading and reloading. The soil yielded at a mean net normal stress around 40 kPa. The estimated consolidation indices at saturated state associated with loading and unloading/reloading segments were  $\lambda_{vp} = 0.46$  and  $\kappa_{vp} = 0.09$ . Since the suction remained constant during consolidation process,  $ds = 0$ , parameters  $\lambda_{vs}$ ,  $\kappa_{vs}$  and  $J$  were excluded for the simulations. Consolidation behavior of the soil was simulated using Equation 3.1. The predicted and measured consolidation data are presented on Figure 3.2a. For all individual segments, the predicted data sufficiently fit the experimental data.

The predicted values of void ratio were used along with Equations 3.27 and 3.32 to evaluate the accuracy of these equations in simulating hydraulic behavior of the soil (Figure 3.2b). As explained earlier, parameter  $m$  varies over a range between 0 to 1. For more complete evaluation, three values including 0, 0.5 and 1 were selected for  $m$ . The best prediction results were achieved when the parameter  $m$  was set to 0. In this case, Equation 3.27 gives the best simulation performance as the predicted data almost perfectly fit the measured data over all loading, unloading and reloading segments. In accordance to Equation 3.32, the prediction performance is satisfactory, but slightly less accurate than Equation 3.27 when  $m = 0$ . However, any changes in value of  $m$  causes noticeable impact on prediction performance of the Equation 3.27. When  $m$  is set to 0.5 and 1, Equation 3.27 becomes unable to simulate hydraulic behavior of the soil beyond the initial preconsolidation stress (around 40 kPa). Thus, the Sheng and Zhou (2011) model is highly sensitive to the parameter  $m$ . Due to this fact, the Sheng and Zhou (2011) approach would not be a unique solution for estimating hydraulic behavior of the soils over loading phase. On the other hand, Equation 3.32 gave a reasonable prediction performance without using any fitting parameter. Hence, it can be deduced that Equation 3.32 is more reliable than the Equation 3.27 and can be considered as a unique solution for simulating hydro-mechanical behavior of unsaturated soils. Based on preliminary simulations conducted,  $m_{opt}$  is from

1.1 to 1.2 if hydraulic path corresponds main wetting curve (such as this example). This exactly adopts a case study performed by Gallipoli et al. (2003b), in which the  $m_{ny}$  was approximately equal to 1.13. However, the  $m_{ny}$  must be set to a value smaller than 1 if hydraulic path adopts scanning curve. This case normally is seen in soils that are dried to a given matric suction, then subjected to isotropic/triaxial stress (see section 3.3.1). Redefinition of stress-hydraulic relationship imposes the first modification to the original SFG model.

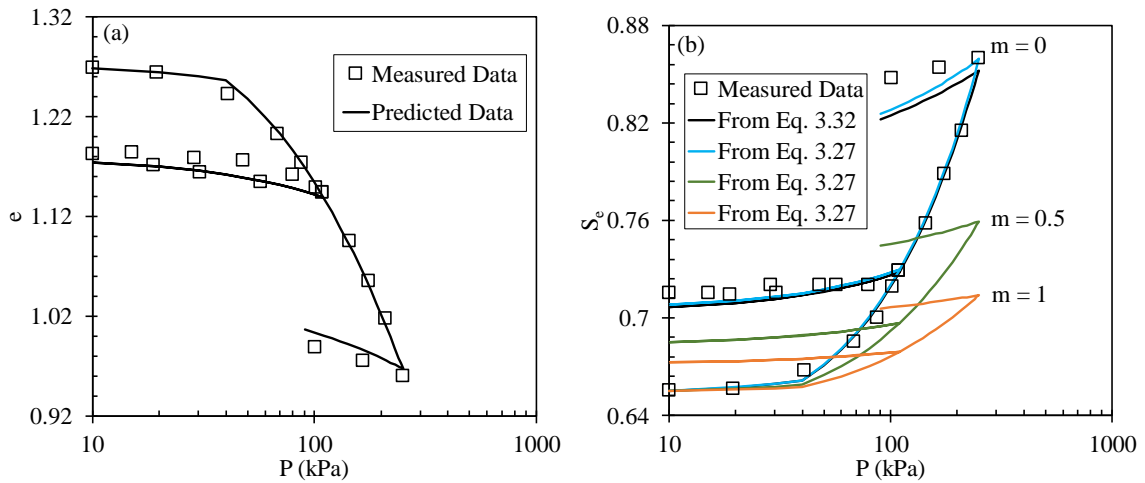


Figure 3.2 Simulation of hydro-mechanical behavior of an unsaturated soil, (a) isotropic deformation under  $s = 200$  kPa, (b) effective degree of saturation with respect to mean net normal stress

### 3.3.2 Shear Modulus Model

Diversity of the small-strain shear modulus predictive models in literature essentially indicates lack of a unique framework for describing the small-strain shear modulus of the unsaturated soils over various stress and state conditions. Accordingly, a robust and reliable scheme was developed for predicting the small-strain shear modulus with respect to changes in suction and net normal stress. As discussed earlier, a change in suction leads to a change in skeleton stress, and hence, the shear modulus of the soil. Thus, mechanical behavior of the unsaturated soil, similar to water content, is function of applied suction. For instance, with an increase in suction, water content decreases, while the small-strain shear modulus increases as a result of the enhanced skeleton stress. This reveals an inverse relationship between the SWCC and the small-strain shear modulus, which was set as the fundamental of the developed model. Change of the small-strain shear modulus with

suction was studied in terms of the ratio between small-strain shear modulus at a specific suction,  $G_{0,unsat}$  and small-strain shear modulus at the saturated state,  $G_{0,sat}$ . This ratio was denoted as normalized shear modulus,  $G_{0,unsat}/G_{0,sat}$ . The inverse relationship between SWCC and normalized shear modulus curve was evaluated using three literature soils including a clay, a silt (Figure 3.3) and a sand.

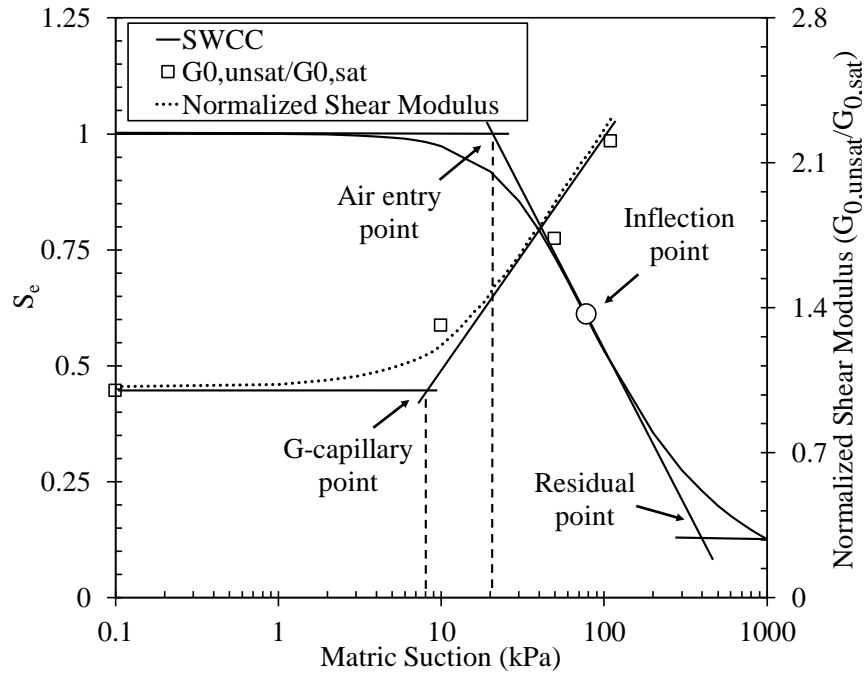


Figure 3.3 SWCC and normalized shear modulus curve for silty soil

Preliminary study revealed that the curve associated to the small-strain shear modulus data (termed as normalized shear modulus curve) do not exactly mirror SWCC, as shown on the Figure 3.3. A break point can be detected on each curve. The break point associated with SWCC is air entry point. The break point on the normalized shear modulus curve was arbitrary called G-capillary point. As illustrated on the Figure 3.3, the air entry point and G-capillary point do not align, such that the G-capillary point is at wet side (left) of the air entry point. Upon passing the air entry and G-capillary points, SWCC and normalized shear modulus curve have also different slopes. Thus, the normalized shear modulus curve does not mimic the SWCC.

Due to the distance between the air entry point and G-capillary point and difference between slope of curves, a direct estimation of the small-strain shear modulus as a function of SWCC is difficult. Thus, the original SWCC must be subjected to a modification/shifting

process in order to reduce the distance between air entry point and the G-capillary point. Also, the difference between the slope of the normalized shear modulus data and SWCC must be reduced through an offsetting process. Since G-capillary point locates at the left side of the original SWCC, the shifting direction must be towards the left. The SWCC shifting distance is proportional to the distance between the air entry point of the original SWCC and the G-capillary point of the normalized shear modulus curve. However, the exact location of the G-capillary point is unknown, therefore the exact shifting distance is also unknown. The only determinable parameters are air entry point and inflection point of the original SWCC. Thus, the modified/shifted SWCC can only be performed using air entry and inflection points of the original SWCC.

The Gallipoli et al. (2003b) model (Equation 3.29) can generate SWCC over various net normal stresses, thus can be considered as a general equation for SWCC definition. Based on the model, location of air entry point is related to parameters  $\psi$  and  $\omega$  and the slope (after air entry point) and curvature of the SWCC are respectively correlated to parameters  $n$  and  $m$ . Regarding the purpose of the SWCC modification, which shifts the location of the air entry point of the SWCC, parameters  $\psi$  and  $\omega$  would be the only controlling parameters in SWCC modification process.

The SWCC modification was conducted through three steps as; 1) recognize the inflection point of the original SWCC (Figure 3.3), 2) estimate the exact value of air entry point of the original SWCC using the inflection point of the original SWCC found from previous step, 3) assume that the inflection point of the shifted/modified SWCC is equal to the air entry point of the original SWCC. Then, keep parameters  $n$  and  $m$  constant and systematically change parameters  $\psi$  and  $\omega$  such that generate a SWCC passing through the assumed point. The SWCC modification process was applied on the three mentioned literature soils. In all cases, the SWCC modification decreased the distance between the air entry point and G-capillary point, which in turn improved inverse relationship between the SWCC and normalized shear modulus curve. This facilitates a direct estimation of the small-strain shear modulus by means of the SWCC. Having SWCC modified, Equation 3.29 takes a new form as,



$$Se_i = \left[ 1 + \left( \frac{e_i^{\psi_i} s}{\omega_i} \right)^n \right]^{-m} \quad (3.33)$$

where  $Se_i$  is effective degree of saturation,  $\psi_i$  and  $\omega_i$  are fitting parameters of the modified SWCC which are different from  $\psi$  and  $\omega$  in value,  $n$  and  $m$  are fitting parameters of the modified SWCC equal to the original parameters in value. The entire modified SWCC can be created by inputting arbitrary suctions into the Equation 3.33.

To develop the small-strain shear modulus prediction model, two key factors must be considered as; (1) analogies and dissimilarities between the modified SWCC and normalized shear modulus curve, (2) the effect of each fitting parameter on the shape of the modified SWCC. The modification process enhances alignment of the air entry point of the SWCC and G-capillary point of the normalized shear modulus curve. Likewise, slope of curves and their concavity are also different. The modified SWCC model (Equation 3.33) can be simply inverted by changing the sign of power coefficient,  $m$  with leaving its magnitude unchanged. Also,  $\psi_i$ ,  $\omega_i$  and  $n$  are kept constant in both sign and magnitude. Eventually, the proposed small-strain shear modulus prediction model takes a form as following.

$$X = \frac{G_{0, \text{unsat}}}{G_{0, \text{sat}}} = \left[ 1 + \left( \frac{e_i^{\psi'_i} s}{\omega_i} \right)^{n_i} \right]^{m_i} \quad (3.34)$$

To draw a clear distinction between the modified SWCC equation (Equation 3.33) and the small-strain shear modulus prediction equation (Equation 3.34), parameters  $\psi_i$ ,  $n$  and  $m$  were intentionally changed to  $\psi'_i$ ,  $n_i$  and  $m_i$ . SWCC modification shifts the air entry point of the SWCC towards the G-capillary point of the normalized shear modulus data, but the modification does not exactly align these points. Thus, the value of  $\psi'_i$  is not exactly equal  $\psi_i$ . In addition, the slope of the SWCC and normalized shear modulus are different as well. To predict the normalized shear modulus, there is no option but setting  $\psi'_i$  equal to the  $\psi_i$  and  $n$  equal to  $n_i$  then changing  $m_i$  to compensate for the difference

between both  $\psi'_i$  and  $\psi_i$  and between  $n$  and  $n_i$ . The prediction performance of the developed model was evaluated using data extracted from Ng et al. (2009). The sample is denoted as Completely Decomposed Tuff (CDT) with 72 percent of silt-sized particles by weight. The test specimens were fabricated through compaction such that the initial void ratio of samples was around 0.63. Then, specimens were subjected to isotropic consolidation process, followed by small-strain shear modulus measurement over various suctions. Table 3.1 presents the applied net normal stresses,  $R^2$  and fitting parameters associated with Equations 3.33 and 3.34.

Table 3.1 Parameters used to predict the small-strain shear modulus under varying net normal stress

Soil Name	$\bar{p}$ (kPa)	$e_i$	Equation 3.33				Equation 3.34	$R^2$
			$\psi_i$	$\omega_i$	$n$	$m$	$m_i$	
CDT	110	0.57	2.74	5.96	2.34	0.33	0.16	0.97
	300	0.51	2.74	5.96	2.34	0.33	0.10	0.98

For the discussed test conditions, the measured and predicted normalized shear modulus data over a series of matric suctions are illustrated on Figure 3.4. Consider a given model that gives precise prediction results for few numbers of measured data. The reliability of the model would be validated if the number of measured points increases and the model still provides satisfactory prediction. Thus, the number of measured data can be used as an indicator to assess the real precision of a prediction model. A noticeable feature associated with the Figure 3.4 is the substantial numbers of the small-strain shear modulus measurements, as well as accurate prediction results provided by the model. Therefore, consistency of the proposed methodology to predict the small-strain shear modulus under varying net normal stress and suction is established.

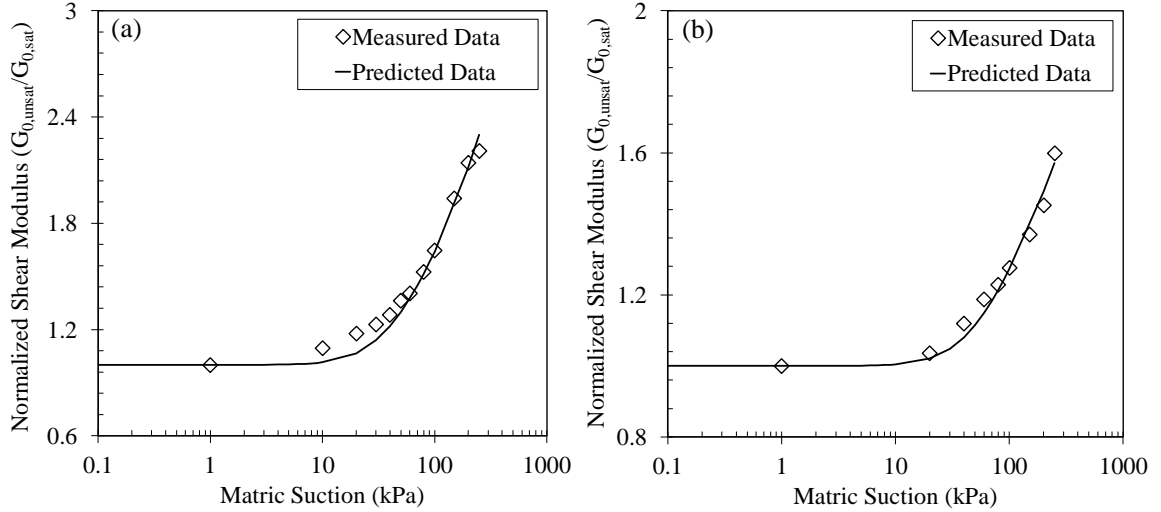


Figure 3.4 Measured and predicted normalized shear modulus data for the Completely Decomposed Tuff at, (a)  $\bar{p} = 110$  kPa and (b)  $\bar{p} = 300$  kPa

Reasonable prediction performance offered by the proposed model enhances the possibility of predicting the small-strain shear modulus term,  $G_0$  of the elastic shear strain component (Equation 3.15) over different net normal stresses. In this regard, Equation 3.15 is redefined with respect to Equation 3.34 and yields,

$$d\varepsilon_s^e = \frac{dq}{3G_{0,\text{sat}} \cdot \left[ 1 + \left( \frac{e_i \psi'_i s}{\omega_i} \right)^{n_i} \right]^{m_i}} \quad (3.35)$$

Value of  $s$  corresponds to the suction at equilibrium state and  $e_i$  corresponds to void ratio at the end of consolidation. Formulating elastic shear strain with respect to shear modulus equation imposes great modification to the SFG model, as there is no need to measure the small-strain shear modulus. Therefore, the incremental stress-strain relationship of the unsaturated soils over shearing phase can be quickly interpreted at different suctions and net normal stresses. Accordingly, stress-strain equation used for simulating mechanical behavior of unsaturated soils over shearing phase is summarized as following.

$$d\varepsilon_v = \frac{\kappa_{vp}}{1+e} \frac{d\bar{p}}{\bar{p}+s} + \frac{\kappa_{vs}}{1+e} \frac{ds}{\bar{p}+s} + \Lambda \frac{\partial f}{\partial \bar{p}} \quad (3.36a)$$

$$d\varepsilon_s = \frac{dq}{3G_{0,\text{sat}} \cdot \left[ 1 + \left( \frac{e_i^{\psi_i s}}{\omega_i} \right)^{n_i} \right]^{m_i}} + \Lambda \beta \frac{\partial f}{\partial q} \quad (3.36b)$$

Redefining the elastic component of the shear strain imposes the second modification to the original SFG model. Coupling redefined stress-hydraulic equation with the redefined stress-strain equation leads to generation of the modified-SFG model.

The applicability of the redefined hydraulic equation in predicting stress-hydraulic behavior of the soil over consolidation phase was validated before. The capability of the modified-SFG model for predicting stress-strain and stress-hydraulic behaviors of unsaturated soils over shearing phase is evaluated in the subsequent section. The procedure of hydro-mechanical simulations via modified-SFG model is established from the state condition. Specifically, several modeling parameters of the modified-SFG model (e.g. yield stress) are directly affected by the suction. For a soil undergoing suction change before the shearing stage, the modified-SFG initially serves to estimate the change of the yield stress with respect to suction variation. Figure 3.5 shows various loading-collapse/yield curves associated with a given specimen.

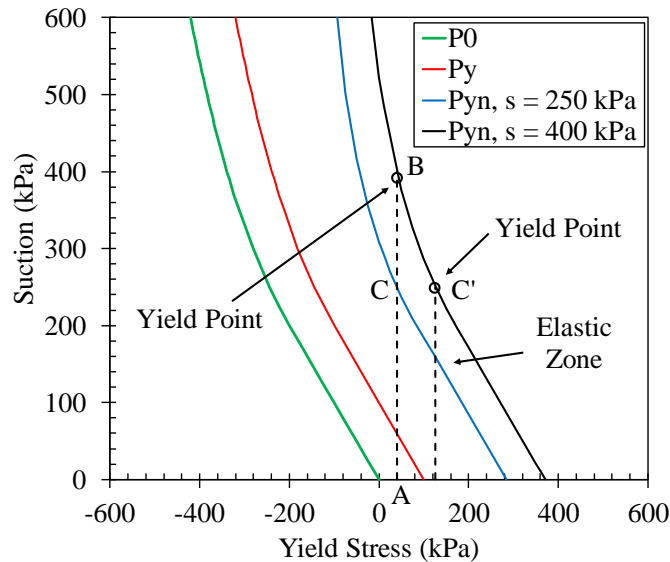


Figure 3.5 Change of preconsolidation stress with suction

The soil sample is initially consolidated under a load of 40 kPa at the saturated state. Thus, the first state of the specimen corresponds to Point A in the Figure 3.5. Then, a suction equal to 400 kPa is applied to the sample that leads to formation of a loading-

collapse curve (generated by Equation 3.9) associated with the suction of 400 kPa. The secondary state of the soil is on Point B, which is located on the yield stress. At this point, applying any stress greater than 40 kPa causes plastic deformation. On the other hand, before exerting any stress, a suction reduction to 250 kPa results in a loading-collapse curve corresponding to suction of 250 kPa. The wetting process causes a state shift from Point B to Point C. An area formed between the loading-collapse curves which is essentially an elastic zone. In this case, the yield stress of the specimen would be equal to a stress corresponding to Point C'. If the soil sample is subjected to any stress at Point C, it would express elastic behavior with stress increase, up to the Point C'. Therefore, the hydrologic variation or suction change before shearing stage directly affects the yield stress of unsaturated soils and thus deformational behavior of the soils. Depending on the state of the soil, either in elastic or plastic zone, different associated parameters ( $K_{vp}$  or  $\lambda_{vp}$ ) must be used for simulations. This example clearly shows how the simulating procedure and governing parameters are controlled by the suction variation.

### 3.3.3 Performance Evaluation of the Modified-SFG model Over Shearing Phase

The methodology of using the modified-SFG model to predict incremental stress-strain-hydraulic behavior of unsaturated soils over the shearing phase was verified using some literature data. The developed equations were fitted to three experimental tests for verification purposes. The selected tests had been conducted on two soils, Pearl Clay (Gao et al., 2018) and Speswhite Kaolin (Sivakumar, 1993). The index properties of the verification soils are given in Table 3.2. The soils utilized for this research were subjected two different testing conditions in terms of net normal stress. The Pearl Clay was subjected to only one net normal stress before shearing phase. The Speswhite Kaolin sample was tested under two consolidation condition, an initial net normal stress and a secondary one. The experimental procedure for each soil is discussed in detail in the subsequent sections.

Table 3.2 Geotechnical index properties for two soils utilized for verification purposes

Reference	PI (%)	Sand (%)	Silt (%)	Clay (%)	MDD (kN/m <sup>3</sup> )	OMC (%)
Sivakumar (1993)	N/A	0	25	75	14.07	28
Gao et al., (2018)	17.5	0	74	26	N/A	N/A

PI = plasticity index; Gs = specific gravity; MDD = maximum dry unit weight (Standard Proctor); OMC = optimum gravimetric moisture content (Standard Proctor).

### 3.3.3.1 Performance of the Modified-SFG Model Under Constant Net Normal Stress

In order to observe effect of matric suction change on shear behavior of unsaturated soils, Gao et al (2018) performed a triaxial compression test on unsaturated compacted Pearl Clay. The size of specimen was 38 mm in diameter and 76 mm in height. Soil specimen had an average void ratio equal to 1.0 that corresponded to dry density of 1355 kg/m<sup>3</sup>. Test specimen was prepared by compaction in a mold at gravimetric water content of about 26 percent, which was obtained by uniformly spraying water over the dry powdered Pearl Clay. The specimen was statically compacted in five layers. The average initial suction of specimen after the compaction was about 110 kPa, that was measured by the axis translation technique. The triaxial test was performed in three steps including equalization at a specific suction, isotropic loading at a constant suction and finally shearing to a critical state. Soil sample studied in this section was initially equalized (dried) at matric suction of 150 kPa. Then, sample was subjected to isotropic consolidation load of 200 kPa. Stress path for triaxial test is shown on Figure 3.6, where  $q$  is deviatoric stress,  $\bar{p}$  is mean net stress, and  $s$  is suction. Point A corresponds to initial state of specimens after compaction, while Point B represents equalization points. The specimen was tested according to path ABCD.

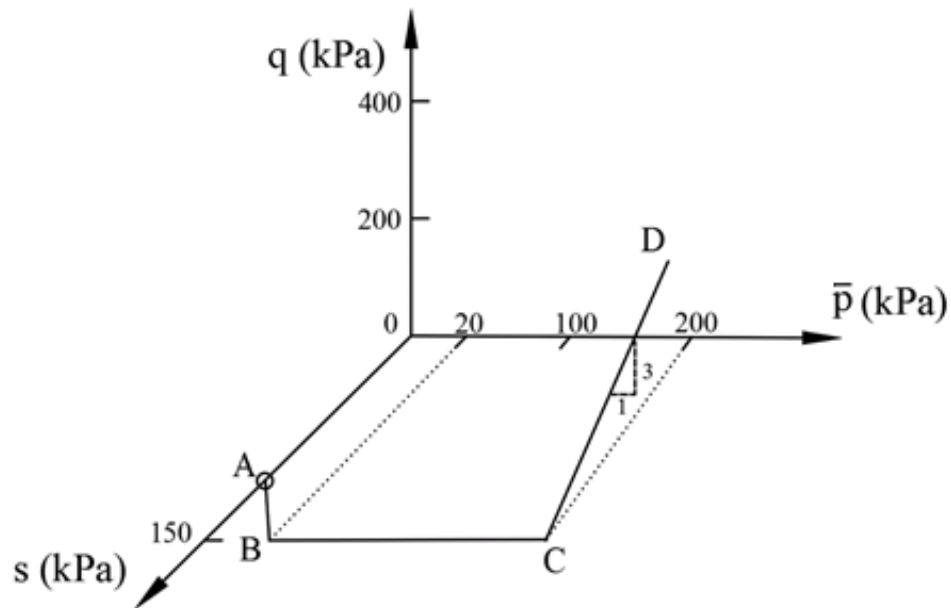


Figure 3.6 Stress paths for triaxial shear tests on Pearl Clay

The values of simulation parameters that were used to predict the stress-strain and stress-hydraulic behaviors of the Pearl Clay are tabulated in Table 3.3. The parameters are  $\kappa_{vp}$  to estimate the elastic volumetric strains induced by deviatoric stress changes (Equation 3.36a);  $\lambda_{vp}$  is used with  $\kappa_{vp}$  to calculate  $\beta$  in Equation 3.18;  $\psi$ ,  $n$  and  $m$  are fitting parameters of the SWCC to describe hydraulic behavior of the soil with respect to loading (Equation 3.32);  $e_i$ ,  $\psi'_i$ ,  $\omega_i$  and  $m_i$  are fitting parameters of the small-strain shear modulus term in the elastic shear strain expression (Equation 3.35); and  $M$  is the slope of the critical state line in the  $q - \bar{p}$  plane (Equation 3.14). In addition, the sample had the initial state values of  $e = 0.93$  and  $S_e = 73.8$  percent that correspond to the beginning of the shear stage. It should be noted that the second term in volumetric strain expression (Equation 3.36a) and the first term in Equation 3.32 become zero at constant suction condition,  $ds = 0$ . Thus, parameters  $\kappa_{vs}$  and  $J$  are excluded for the simulations.

Table 3.3 Parameters used for simulating hydro-mechanical behavior of Pearl Clay

$\kappa_{vp}$	$\lambda_{vp}$	$s_{sa}$	$\psi$	$n$	$m$	$e_i$	$\psi'_i$	$\omega_i$	$n_i$	$m_i$	$M$
0.03	0.05	20	6.1	11.8	0.01	0.93	6.23	46.12	1.63	0.61	1.16

Measured and predicted results of triaxial compression test on compacted Pearl Clay are shown in Figure 3.7. In the figure,  $\varepsilon_v$ ,  $\varepsilon_s$ , and  $\varepsilon_a$  are the volumetric strain, shear strain, and axial strain, respectively. The modified-SFG model give a decent description of the stress-strain and stress-hydraulic behavior of unsaturated compacted Pearl Clay under constant suction during shearing phase. This fact reveals the reliability of the proposed model to describe mechanical and hydraulic behavior of unsaturated soils under constant matric suction and constant net normal stress.

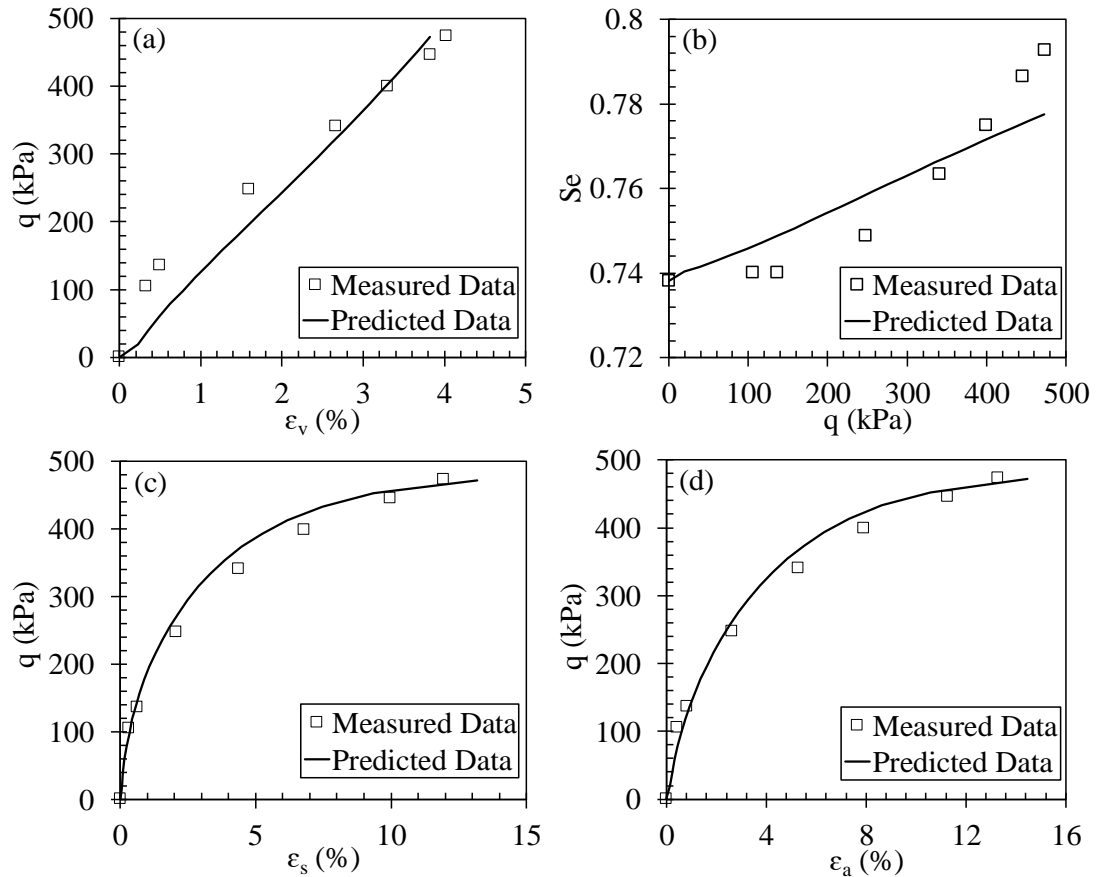


Figure 3.7 Measured and predicted results of triaxial compression test on Pearl Clay, (a) volumetric strain versus deviatoric stress, (b) deviatoric stress versus effective degree of saturation, (c) shear strain versus deviatoric stress, (d) axial strain versus deviatoric stress

### 3.3.3.2 Performance of the Modified-SFG Model Under Varying Net Normal Stress

Sivakumar (1993) conducted two triaxial compression experiments on Speswhite kaolin using a suction controlled triaxial cell. Soil specimens were statically compacted at a water content of 25 percent (4 percent dry of Proctor optimum) and a dry density of 1200 kg/m<sup>3</sup>. The vertical compaction force was 700 kPa, which corresponded to initial suction of 700 kPa. The samples were initially subjected to a wetting process at a constant mean net stress of 50 kPa from the as-compacted suction to a suction of 300 kPa. No collapse behavior was observed during this initial equalization (Sivakumar, 1993), which indicates that the soil had not reach the yield surface and, hence, the soil locates inside the initial elastic zone. The equalization stage was followed by isotropic loading at a constant value of suction and then some form of suction-controlled shearing to a critical state. Soil samples studied in this section were subjected to isotropic consolidation loads equal to 100 kPa and



150 kPa. Stress paths for the triaxial tests are shown on Figure 3.8. Point A represents the initial state of specimens after compaction. The first and the second specimens were tested according to path ABCD and ABEF, respectively. The initial void ratio of the first and the second specimens at the beginning of the shear stage was 1.19 and 1.14, respectively.

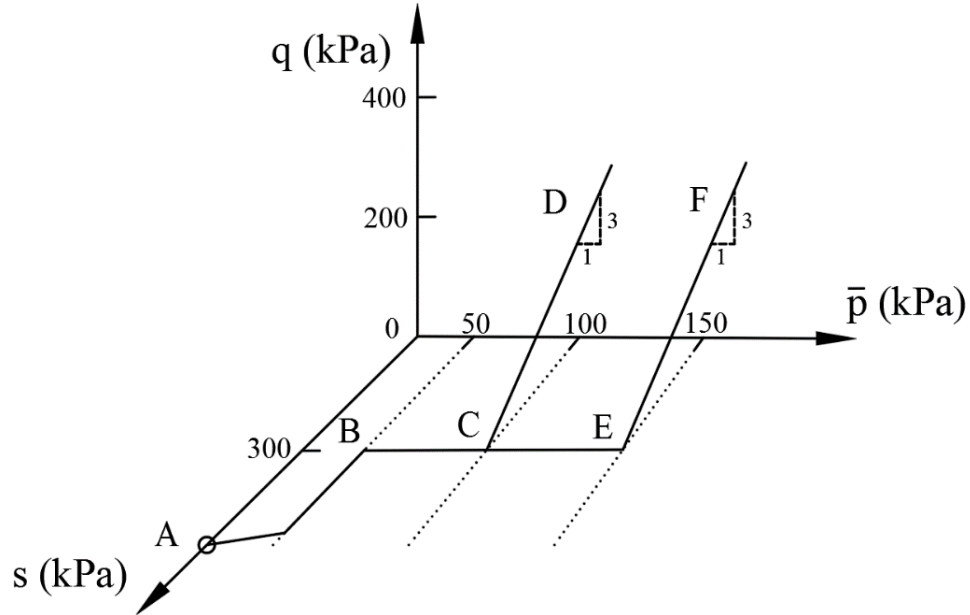


Figure 3.8 Stress paths for triaxial shear tests on Speswhite kaolin

The values of constitutive parameters used in simulations are summarized in Table 3.4. Equations utilized to describe hydro-mechanical behavior of the Pearl Clay are also valid for Speswhite Kaolin.

Table 3.4 Model parameters used for simulating hydro-mechanical behavior of Speswhite Kaolin

$\bar{p}$ (kPa)	$\kappa_{vp}$	$\lambda_{vp}$	$s_{sa}$	$\psi$	$n$	$m$	$\psi'_i$	$\omega_i$	$n_i$	$m_i$	$M$
100	0.02	0.16	60	8.27	5.67	0.02	3.26	10.53	5.67	0.02	0.85
150	0.02	0.16	60	8.27	5.67	0.02	3.26	10.53	5.67	0.02	0.85

Figures 3.9 and 3.10 show the measured and predicted results of triaxial compression tests on compacted Speswhite kaolin under drained condition, i.e., with the net normal stress and suction being controlled and the strains and water content being measured. For sample consolidated to net stress of 100 kPa, the initial state values of  $e = 1.19$  and  $S_e = 61\%$ , were observed at the beginning of the shear stage. Sample subjected to

isotropic load of 150 kPa had initial state values of  $e = 1.14$  and  $S_e = 62.7\%$ . These values were used as the initial values in predictions.

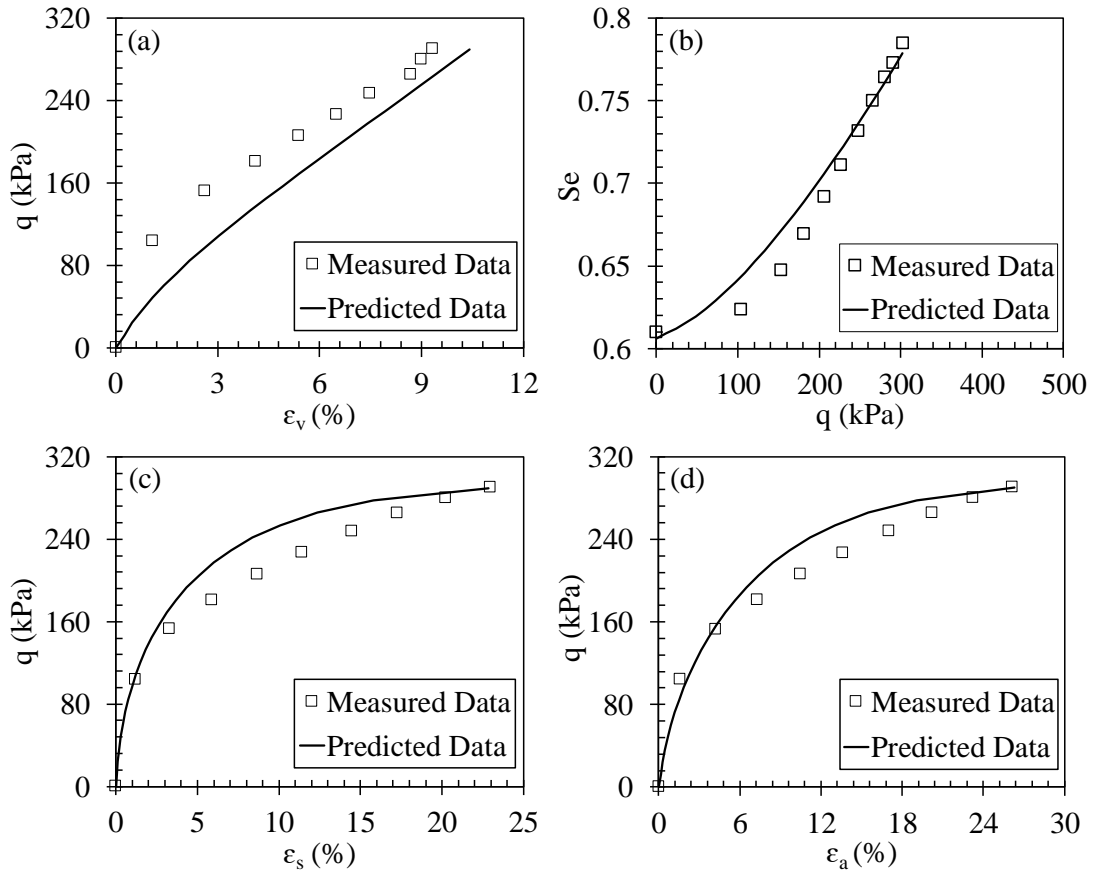


Figure 3.9 Measured and predicted results of triaxial compression test on Speswhite kaolin consolidated to  $p = 100$  kPa. (a) Volumetric strain versus deviatoric stress, (b) Deviatoric stress versus effective degree of saturation, (c) Shear strain versus deviatoric stress, (d) Axial strain versus deviatoric stress

The test and predicted results show that the strain and hydraulic components of the soil increases with deviatoric stress. Soil sample undergoes compaction and deformation under the shear stress, and hence, it experiences volumetric and shear strain over triaxial loading. Any volumetric strain causes a decrease in void ratio. Since the matric suction is constant, the change of effective degree of saturation is only affected by change of void ratio (Equation 3.32). Thus, a decrease in void ratio leads to an increase in effective degree of saturation. The modified-SFG model provides satisfactory predictions of the stress-strain and stress-hydraulic behaviors of Speswhite kaolin (consolidated to  $\bar{p} = 100$  kPa) during triaxial compression.

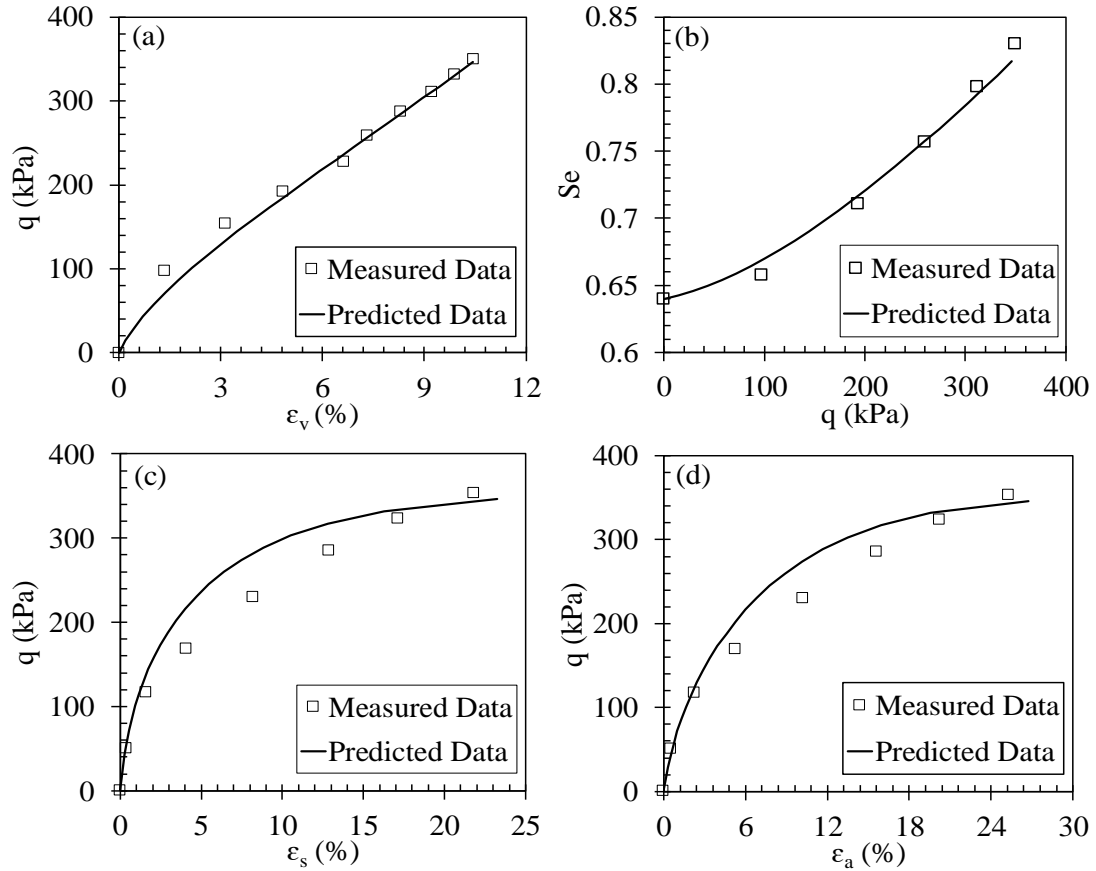


Figure 3.10 Measured and predicted results of triaxial compression test on Speswhite kaolin consolidated to  $p = 150$  kPa. (a) Volumetric strain versus deviatoric stress, (b) Deviatoric stress versus effective degree of saturation, (c) Shear strain versus deviatoric stress, (d) Axial strain versus deviatoric stress

Mechanical and hydraulic behavior of the sample consolidated to  $\bar{p} = 150$  kPa is very similar to the previous sample in which the same stress-strain and stress-hydraulic trends can be observed. However, the shear strength of the sample consolidated to  $\bar{p} = 150$  kPa is higher than the sample consolidated to  $\bar{p} = 100$  kPa. This result is consistent with the effect of consolidation load on soil compaction, and hence the elevation of soil strength (Budhu, 2008). In this case, the modified-SFG model also sufficiently simulates hydro-mechanical behavior of the Speswhite kaolin sample.

## **Prediction of Coupled Hydro-Mechanical Behavior of Unsaturated Soils Based on Seasonal Variations in Hydrologic Conditions**

### 4.1 Introduction

Hydrological variations induced by seasonal rainfall and evapotranspiration events causes variation soils' state from saturated to residual. For an unsaturated soil, a change in the degree of saturation causes significant changes in hydro-mechanical properties (Lo Presti et al., 2018; Pham et al., 2019). The close link between the hydrologic and mechanical properties of unsaturated soils can be explained based on suction stress (Lu et al., 2010). The concept of suction stress is used to describe the change of skeleton stress arising from the physicochemical forces and capillarity under variable water content conditions (Kurimoto et al., 2017; Khosravi et al., 2018b). Therefore, suction stress controls the mechanical behavior of unsaturated soils (shear strength/small-strain shear modulus) in terms of matric suction (pressure head) and degree of saturation. Generally, climatic conditions subject soils to cyclic drying and wetting, hence, causes periodic changes in suction stress. Therefore, the mechanical behavior of the soil is also influenced by cyclic wetting and drying.

Currently, most investigations have focused on the effect of hydrologic variations on the shear strength of unsaturated soils (e.g. Zhou and Sheng, 2016; Zhang et al., 2018; Mpawenayo and Gerard, 2019). Before reaching the final strength, the soil experiences incremental volumetric change/deformation due to change of hydrologic conditions. However, shear strength prediction models provide no data about the incremental deformation of the soils. In addition, having a real-time insight into hydrologic-driven incremental deformations of the soil can inform of probable failure, and hence contribute more effective hazard management (Baum et al., 2010).

Incremental deformation of a soil is generally simulated by constitutive models. Numerous models have been developed for describing hydro-mechanical behavior of unsaturated soils (e.g. Gallipoli et al., 2003a; Santagiuliana and Schrefler, 2006; Sun et al., 2007a). However, the majority of models lack the ability to address some significant aspects of unsaturated soils such as; (i) the change of the yield stress with matric suction,

(ii) deformation of slurry soil over drying process, and (iii) transition from saturated state to unsaturated state. Sheng et al. (2008a) developed a constitutive model, referred to as the SFG model, that has been shown to be highly flexible in modelling hydro-mechanical behavior of unsaturated soils. The model is capable of using hydrologic data as inputs and yielding hydro-mechanical behavior of unsaturated soils as outputs.

Surface water infiltration resulting from seasonal climatic events (i.e. rainfall and evapotranspiration) directly governs hydrologic behavior of the soil, and thus controls the hydro-mechanical characteristics of the soil. Rainfall and evapotranspiration mechanisms cause downward and upward infiltrations, respectively. Water infiltration through subsurface is modeled based on the assumption that the water flow is either steady (constant rate) or transient (rate varying). Steady state flow models ignore nonlinear dependence of the pore water response to rainfall/evapotranspiration, and thus make unreliable patterns of hydrologic data within the soil's body (Batlle-Aguilar, and Cook, 2012; Godt et al., 2012). Thus, transient infiltration models are preferable for describing water flow inside the unsaturated regime.

Presently, no constitutive model has been developed for describing real-time hydro-mechanical behavior of unsaturated soils as a function of hydrologic variations. Lack of a clear understanding of the hydrological-driven deformational behavior of a soil may lead to catastrophic failure and fatalities. The main objective of this paper was to apply the SFG model with hydrologic data and predict hydro-mechanical behavior of unsaturated soils as a function of seasonal rainfall/evapotranspiration events. This methodology provides a real-time description of all deformations corresponding to the hydrologic variations. However, the SFG model showed substantial uncertainty to simulate hysteresis behavior of the unsaturated soils. Also, the model uses a constant small-strain shear modulus to estimate elastic shear strain of the soil. Since the small-strain shear modulus changes with hydrologic conditions and overburden pressure, using a constant small-strain shear modulus leads to unrealistic simulation results. Thus, the original SFG model was modified in terms of hysteresis and elastic shear strain equations to become suitable for the purpose of this study. As a secondary objective, this study developed a transient infiltration model to predict long-term hydrologic characteristics of unsaturated soils by use of only small

amount of in-situ hydrologic data. This model is highly contributive in such cases where long time measurement of the hydrologic data is not feasible.

## 4.2 Framework Used for Developing Modified-SFG Model

The modified-SFG model reformulates the equations related to hysteresis and elastic shear strain of the original model. The basic equations in original SFG model that govern volumetric strain, plastic shear strain, yield stress and shear strength can be found in Sheng et al. (2008a). In this current paper, only the procedures for modifying the equations that govern hysteresis and elastic shear strain are presented.

### 4.2.1 Modifying Hysteresis Function

Water content dependence to matric suction is normally addressed by the soil-water characteristic curve (SWCC). As pointed out by Masin (2010), water content or degree of saturation is controlled by both matric suction (i.e. negative pressure head) and void ratio. Sun et al. (2007b) proposed a general formulation of degree of saturation,  $S_r$  in terms of changes in pressure head and void ratio,  $e$ .

$$dS_r = -J \frac{d|h|}{|h|} - K de \quad (4.1)$$

where  $J$  is slope of the desaturation section of the SWCC that is synonymous to the rate of water content change with pressure head,  $h$ ;  $K$  is a parameter that governs changes in degree of saturation due to void ratio variation. Sheng and Zhou (2011) set Equation 4.1 as the general form of the hysteresis function for the original SFG model. Sheng and Zhou (2011) defined the  $K$  parameter as,

$$K = \frac{S_r}{e} (1 - S_r)^\beta \quad (4.2)$$

where  $\beta$  is a fitting coefficient varying between 0 and 1. Substituting Equation 4.2 into Equation 4.1 gives a complete description of the hysteresis function used in the original SFG model.

$$dS_r = -J \frac{d|h|}{|h|} - S_r (1 - S_r)^\beta \frac{de}{e} \quad (4.3)$$

The performance of Equation 4.3 is extremely sensitive to the value of  $\beta$ . Small perturbations of  $\beta$  result in significant changes in performance thus making Equation 4.3 unreliable. For this study, hysteresis was addressed by re-evaluating Equation 4.1. The  $K$  parameter serves to define changes of degree of saturation based on the changes in void ratio. Hence,  $K$  is mathematically expressed as,  $K = \partial S_r / \partial e$ . The  $K$  parameter can be estimated by taking the partial derivative of an equation that correlates changes in degree of saturation to the changes in void ratio. Gallipoli et al. (2003b) proposed a SWCC model that estimates degree of saturation with respect to changes in pressure head and void ratio. The model was established based on the van Genuchten (1980) SWCC model, which governs change of degree of saturation with pressure head under a constant void ratio. The van Genuchten (1980) model is expressed as,

$$S_r = S_{r,res} + (S_{r,sat} - S_{r,res}) \left[ 1 + (\alpha |h|)^n \right]^{-m} \quad (4.4)$$

where  $S_{r,res}$  and  $S_{r,sat}$  are residual and saturated degree of saturation, respectively;  $n$  and  $m$  are fitting parameters associated with the slope of the transition region and curvature of the SWCC, respectively ( $m = 1 - 1/n$ );  $\alpha$  is fitting parameter corresponding to air entry pressure head, which controls the location of the SWCC. To consider the effect of void ratio change on SWCC, Gallipoli et al. (2003b) redefined parameter  $\alpha$  as  $\alpha = \omega / e^\psi$ . The Gallipoli et al. (2003b) model is expressed as,

$$S_r = S_{r,res} + (S_{r,sat} - S_{r,res}) \left[ 1 + \left( \frac{\omega |h|}{e^\psi} \right)^n \right]^{-m} \quad (4.5)$$

where  $\psi$  and  $\omega$  are fitting parameters that determine the position of air entry pressure head (essentially location of SWCC) with respect to the void ratio. Taking the partial derivative of Equation 4.5 with respect to the void ratio yields a new description of the  $K$  parameter as,

$$K = \frac{\partial S_r}{\partial e} = \frac{-mn\psi \left[ 1 + \left( \frac{\omega |h|}{e^\psi} \right)^n \right]^{-m-1} \cdot \left( \frac{\omega |h|}{e^\psi} \right)^n \cdot (S_{r,sat} - S_{r,res})}{e} \quad (4.6)$$

Rewriting Equation 4.6 based on Equation 4.5 yields,

$$K = \frac{\partial S_r}{\partial e} = \frac{mn\psi \left[ 1 - \left( \frac{S_r - S_{r,res}}{S_{r,sat} - S_{r,res}} \right)^{\frac{-1}{m}} \right] \cdot \left( \frac{S_r - S_{r,res}}{S_{r,sat} - S_{r,res}} \right)^{\frac{m+1}{m}} \cdot (S_{r,sat} - S_{r,res})}{e} \quad (4.7)$$

Introducing Equation 4.7 into Equation 4.1,

$$dS_r = -J \frac{d|h|}{|h|} - \left[ mn\psi \left[ 1 - \left( \frac{S_r - S_{r,res}}{S_{r,sat} - S_{r,res}} \right)^{\frac{-1}{m}} \right] \cdot \left( \frac{S_r - S_{r,res}}{S_{r,sat} - S_{r,res}} \right)^{\frac{m+1}{m}} \cdot (S_{r,sat} - S_{r,res}) \right] \frac{de}{e} \quad (4.8)$$

A verification analysis of Equation 4.8 using data reported by Sharma (1998) showed the equation was more reliability than Equation 4.3 in describing hysteresis behavior. Thus, Equation 4.8 was adopted for the modified-SFG model.

#### 4.2.2 Modifying Elastic Shear Strain Component

The elastic shear strain component,  $d\varepsilon_s^e$  in the original SFG model is governed by deviatoric stress,  $q$  and the small-strain shear modulus,  $G_0$  as,

$$d\varepsilon_s^e = \frac{dq}{3G_0} \quad (4.9)$$

The small-strain shear modulus of Equation 4.9 is represented as a static value. However, variations in hydrologic conditions are typically accompanied by suction stress change. Thus, the small-strain shear modulus will change with changing hydrologic conditions. For this study, a fully coupled hydro-mechanical description of the small-strain shear modulus was developed based on the inverse relationship between the SWCC and the small-strain shear modulus. The changing trend of the small-strain shear modulus with pressure head is addressed by a ratio between the small-strain shear modulus at a particular pressure head,  $G_{0,unsat}$  and the small-strain shear modulus at zero pressure head  $G_{0,sat}$ . The ratio is referred to as the normalized shear modulus,  $G_{0,unsat}/G_{0,sat}$ . Primary studies revealed that the air entry point of the SWCC and the break point on the normalized shear modulus curve, denoted herein as the G-capillary point, do not align. The SWCC is thus shifted to better align the two curves. Also, the slope of the normalized shear modulus data is



different from the slope of SWCC. Thus, this difference must be offset. It should be noted that the slope of SWCC and the normalized shear modulus curve corresponds to the parameter  $n$ .

The Gallipoli et al. (2003b) model provides a SWCC over various net normal stresses with respect to void ratio. As previously discussed, the location of the air entry point is governed by  $\psi$  and  $\omega$ . Thus, to better align the air entry point and G-capillary point, the values of  $\psi$  and  $\omega$  must be changed. To modify/shift the SWCC, initially the air entry point of the original SWCC is determined. Then, inflection point of the shifted/modified SWCC is assumed to be equal to the air entry point of the original SWCC. The  $n$  and  $m$  are kept constant while  $\psi$  and  $\omega$  are changed as to create a SWCC that passes through the inflection point of the shifted/modified SWCC. It is noted that the shifting process decreases distance between the air entry point and G-capillary point but does not exactly line up these two points. The modified SWCC equation is formulated as,

$$S_r = S_{r,res} + (S_{r,sat} - S_{r,res}) \left[ 1 + \left( \frac{\omega_i |h|}{e^{\psi_i}} \right)^n \right]^{-m} \quad (4.10)$$

Since  $\psi$  and  $\omega$  are changed for the SWCC modification process, they are renamed  $\psi_i$  and  $\omega_i$ . The inverse relationship between the modified SWCC and normalized shear modulus curve essentially indicates different concavity of the curves. The modified SWCC, as a shifted version of the original SWCC, concaves downward. In contrast, the normalized shear modulus curve has an upward concavity. Hence, the modified SWCC can be inverted by changing the sign of the power coefficient,  $m$  while keeping its value unchanged. The values and signs of the other parameters remain constant during this transformation. Thus, the predictive small-strain shear modulus model is derived from Equation 4.10.

$$f = \frac{G_{0,unsat}}{G_{0,sat}} = \left[ 1 + \left( \frac{\omega_i |h|}{e^{\psi_i}} \right)^{n_i} \right]^{m_i} \quad (4.11)$$

To make a distinction between the modified SWCC equation and the normalized shear modulus prediction equation, parameters  $\psi_i$ ,  $n$  and  $m$  are changed to  $\psi'_i$ ,  $n_i$  and  $m_i$ . Parameter  $m_i$  is changed to compensate difference between parameters  $\psi_i$  and  $\psi'_i$  and

between  $n$  and  $n_i$ . Equation 4.11 allows for the small-strain shear modulus to be predicted at different net normal stresses and pressure heads. Hence, the small-strain shear modulus term,  $G_0$  of elastic shear strain component (Equation 4.8) can be predicted by the proposed model. Accordingly, Equation 4.8 is redefined based on the small-strain shear modulus equation, as

$$d\varepsilon_s^e = \frac{dq}{3 \cdot G_{\max,0} \cdot \left[ 1 + \left( \frac{\omega_i |h|}{e^{w'_i}} \right)^{n_i} \right]^{m_i}} \quad (4.12)$$

Equation 4.12 was adopted in the modified-SFG model. Now, real-time hydro-mechanical behavior of an unsaturated soil can be described as a function of net normal stress and hydrologic variations by incorporating hydrologic data with the modified-SFG model.

#### 4.3 Modeling Hydro-Mechanical Behavior of Unsaturated Soils by Means of the Modified-SFG Model

Hydro-mechanical description of the unsaturated soils as a function of hydrologic events initially requires rainfall and evapotranspiration data, which are obtained from field measurements.

##### 4.3.1 Field Methodology and Hydrologic Observations

Field measurements were conducted on two sites in different physiographic locations of the Kentucky. The Doe Run site was located in Erlanger, Kentucky, above the Bullock Pen Creek in northern Kentucky. The monitored site had an average slope of 13 degrees and the length of the downslope axis was around 52 m (Crawford and Bryson, 2018). The Herron Hill site was located in Tollesboro, Kentucky in the Knobs physiographic region (McDowell, 1986), west of the Cumberland Escarpment. The average slope was around 16 degree and downslope axis was approximately 153 m. Figure 4.1 shows the locations of the monitoring sites. The red dots in the figures represent the locations of the test pits containing the hydrologic sensors. The sensors consisted of a nested pair of volumetric water content and water potential (i.e. matric suction) sensors at upper and lower depths. The areas enclosed by yellow irregular shapes represent the

locations of the upslope and downslope test pits. For this study, only data related to the upslope test pits are presented.

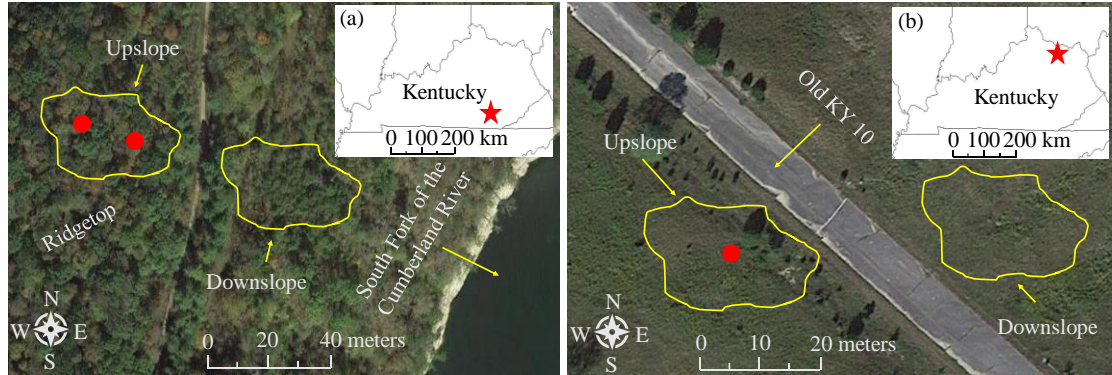


Figure 4.1 Overview of monitoring sites, (a) Doe Run, (b) Herron Hill

Long-term hydrologic data were collected over a period of 2 years that represents regular climatic changes within unsaturated zone. The hydrologic data including rainfall intensity and duration, volumetric water content and water potential were collected as the daily average values. At near-saturated state, the measurements from the water potential sensors remained around 9 kPa (equivalent to -0.92 m of pressure head), which was the manufacturer’s stated limit of sensor measurement. The depths of the volumetric water content and water potential sensors in the upslope pits are presented in Table 4.1.

Table 4.1 Depth of hydrologic sensors at the Doe Run and Herron Hill sites

Site	Sensor type	Upper sensor depth (cm)	Lower sensor depth (cm)
Doe Run	Volumetric water content	30	70
	Water potential	30	65
Herron Hill	Volumetric water content	90	-
	Water potential	100	-

Table 4.2 presents the geotechnical properties of the soils at each site. The Unified Soil Classification System (USCS) showed that the soils at the sites were generally silt and lean clay. These soils are generically referred to as colluvium.

Table 4.2 Geotechnical properties of the monitoring sites

Site	Sample Depth (cm)	$w_n$ (%)	LL (%)	PI (%)	USCS
Doe Run	70	41.2	45.2	27	CL
Herron Hill	120	26	44	18	ML

$w_n$  = natural water content;  $LL$  = liquid limit;  $PI$  = plasticity index.

Several cycles of drying-wetting-saturation were observed at study sites. Since the hysteresis equation in the modified-SFG model (Equation 4.8) was defined based on the degree of saturation, water content is described by the degree of saturation for consistency throughout this study. Figure 4.2 shows variation of the degree of saturation and pressure head at the Doe Run and Herron Hill sites along with daily and cumulative rainfall. Generally, sensors nested closer to ground surface gave quicker responses to the rainfall events. Referring to Doe Run (Figure 4.2b), cyclic drying and wetting occasions induced by seasonal variations caused considerable fluctuations in the data collected from the shallower depth. However, the data fluctuation decreased with an increase in depth of the sensor. It should be noted that the noticeable gap observed in data recorded at Herron Hill site (Figure 4.2d) is attributed to temporary malfunction of the measuring devices.

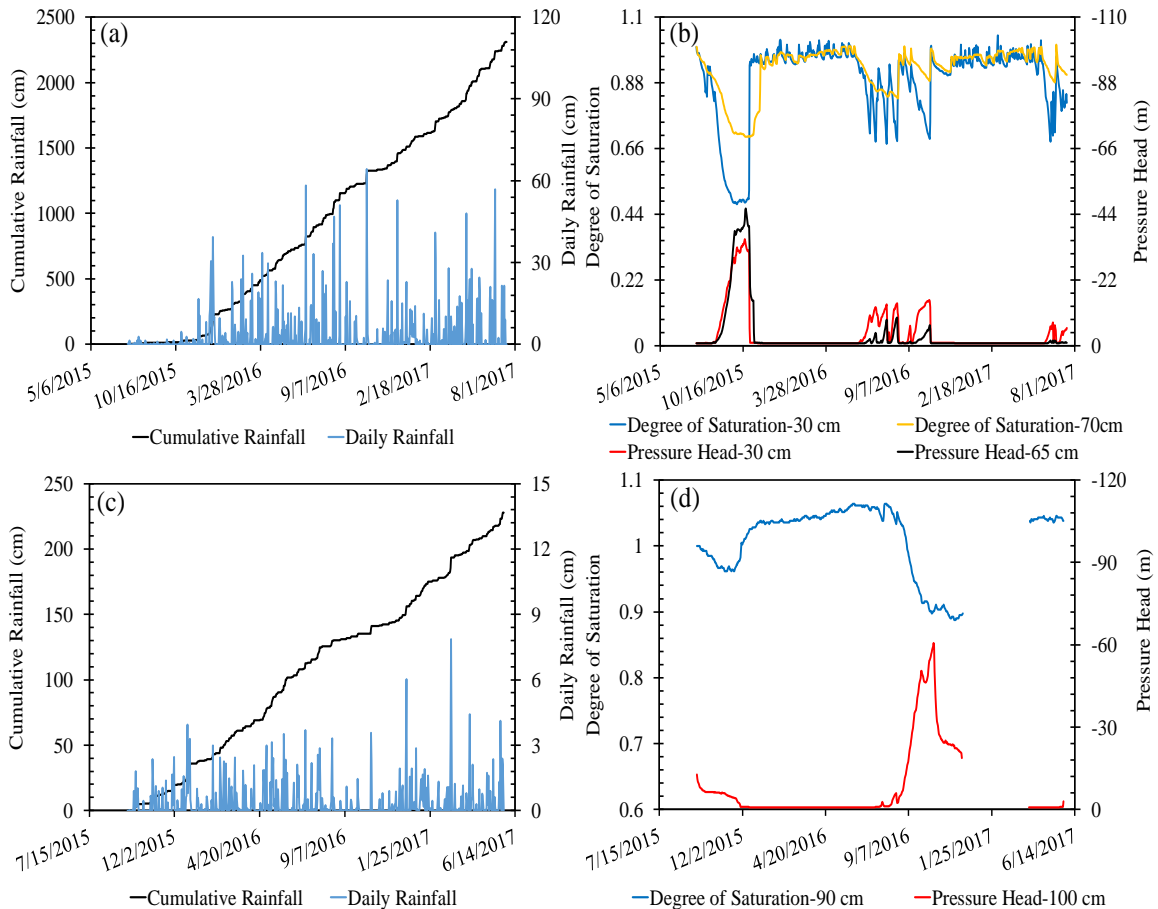


Figure 4.2 Seasonal hydrologic-rainfall data for monitoring sites, (a) cumulative and daily rainfall at Doe Run, (b) degree of saturation and pressure head at Doe Run, (c) cumulative and daily rainfall at Herron hill, (d) degree of saturation and pressure head at Herron hill

As explained earlier, the mechanical behavior of a soil is influenced by both pressure head and degree of saturation. These two parameters are controlled by rainfall and evapotranspiration events at a site. Moreover, the response of a soil to an applied load can be describe by the modified-SFG model. Thus, coupling field hydrologic data with the modified-SFG model provides real time data for the simultaneous responses of the soil to both hydrological variation and applied load. The modified-SFG model predicts mechanical behavior (i.e. stress-strain-hydraulic behavior) of unsaturated soils under a constant pressure head. However, hydrologic events induce pressure head change. Thus, to describe the entire hydro-mechanical behavior of a soil system, multiple hydro-mechanical behavioral curves at several constant pressure heads must be generated. A change in pressure head leads to a transition from one curve to another. The subsequent example presents the incorporation of the modified-SFG model with hydrologic data obtained from field monitoring for simulating hydro-mechanical behavior of unsaturated soils in tandem.

#### 4.3.2 Hydro-Mechanical Simulation

This study considered the hydraulic and deformational behavior of the Herron Hill site for a period of 44 days. The pressure head and degree of saturation data correspond to the depth of 100 cm. A short drying period from 7/31/2016 to 9/11/2016 was selected for the simulation. During the selected time frame, the measured pressure head ranged from 0 m to -25.04 m that corresponded to a degree of saturation from 1 to 0.911. The stress-strain and stress-hydraulic behavior of the Herron Hill slope was simulated using the modified-SFG model. The initial values of parameters used for the model are tabulated in Table 4.3. The  $\kappa_{vp}$  and  $\lambda_{vp}$  parameters are used to predict volumetric strains;  $\psi$ ,  $n$  and  $m$  give the hydraulic behavior of the soil as a function of void ratio change (Equation 4.8);  $\psi'_i$ ,  $\omega_i$ ,  $n_i$  and  $m_i$  estimate the small-strain shear modulus term in the elastic shear strain equation (Equation 4.10); and  $M$  is the slope of the critical state line in the  $q:p$  plane.

Table 4.3 Value of parameters used for hydro-mechanical simulations

$\kappa_{vp}$	$\lambda_{vp}$	$\psi$	$n$	$m$	$\psi'_i$	$\omega_i (m^{-1})$	$n_i$	$m_i$	$M$
0.01	0.1	17.00	1.03	0.03	1.30	0.38	1.15	0.13	0.85

It was assumed that the soil was normally consolidated. In the environment/field, a particular soil is consolidated under the overburden pressure (load exerted from upper layers), which is controlled by moist unit weight and depth of the soil. The moist unit weight of the soil varies with degree of saturation. For this study, the moist unit weight of the soil during the mentioned time frame varied from 19.16 to 19.52 kN/m<sup>3</sup>. This variation corresponded to an average overburden pressure equal to 19.34 kPa (1.97 m). Likewise, the void ratio of the soil at the saturated state was around 0.715.

As explained earlier, several sets of hydrologic data were obtained for the monitoring period. These data varied in small increments, hence conducting hydro-mechanical simulations for all hydrologic data sets lead to generation of several curves that were hardly distinguishable. For a better illustration, the hydro-mechanical simulations were conducted only on five data points. The selected pressure head values included 0 m, -2.63 m, -5.41 m, -15.04 m and -25.04 m that respectively, corresponded to degree of saturations equaled to 1, 0.983, 0.971, 0.942 and 0.911.

To describe mechanical response of the Herron Hill slope to hydrologic variation, initially, stress-strain behavior at a specific constant pressure head (e.g. -25.04 m) was simulated. This process yields different deformational components (volumetric, shear and axial strains) over a range of deviatoric stress from zero to a maximum value which corresponds to the shear strength. The behavioral curves resulting from this process illustrate the mechanical behavior of the soil at only one pressure head and degree of saturation. For other sets of hydrologic data, the same simulation procedure was applied, and the corresponding mechanical curves were obtained. The simulation curves generated for all sets of hydrologic data can be used as deformation paths as they illustrate all possible combinations of loading and hydrologic conditions. In other words, the entire mechanical behavior of the soil will change within the obtained curves as a function of loading and hydrologic variations. The simulated mechanical behaviors of Herron Hill site along the specified drying period are presented on Figure 4.3.

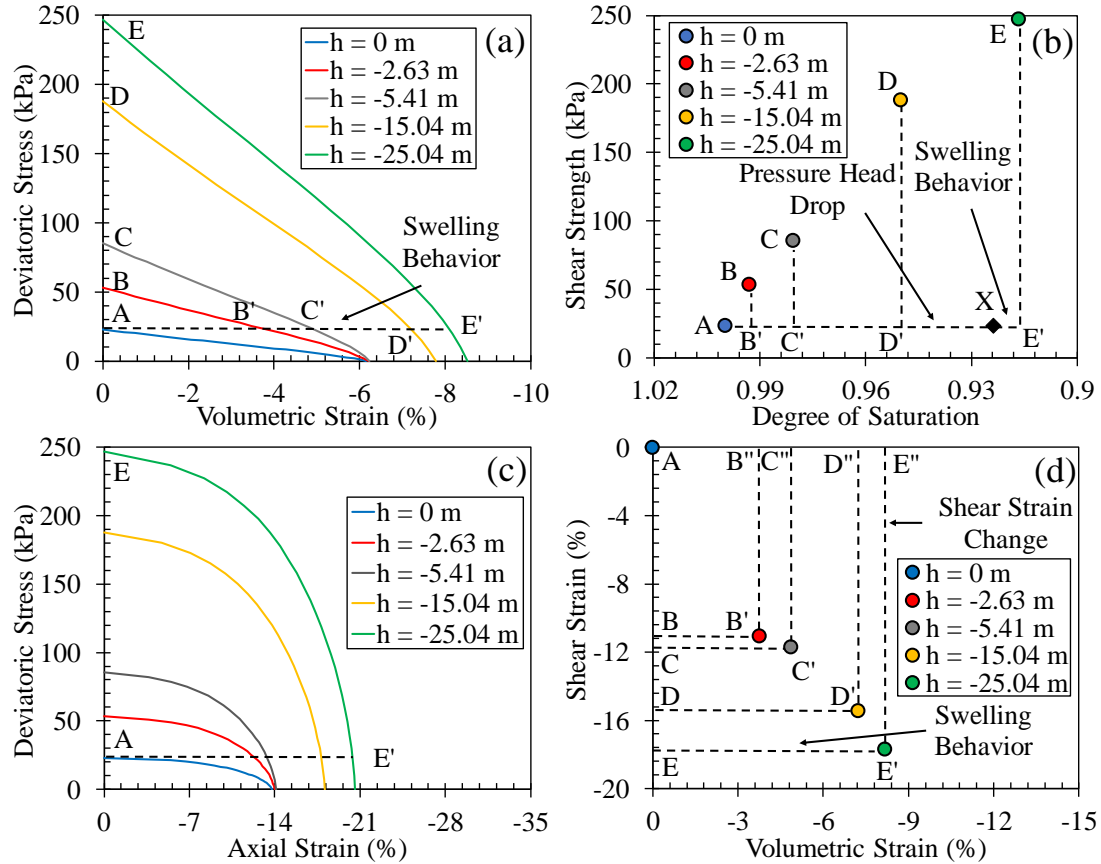


Figure 4.3 Simulated hydro-mechanical behavior of the Herron Hill, (a) volumetric strain versus deviatoric stress, (b) degree of saturation versus shear strength, (c) axial strain versus deviatoric stress, (d) volumetric strain versus shear strain.

As previously explained, the soil undergoes a drying process along the specified time frame. The initial state of the soil corresponds to a pressure head of 0 m (Point A in the Figure 4.3). The shear strength values,  $\tau_f$  over several hydrologic conditions corresponds to Points A, B, C, D, and E. As proposed by Lu and Likos (2006), suction stress increases with pressure head reduction. Due to direct link between the shear strength and suction stress, the shear strength also elevates with pressure head drop. This hypothesis is confirmed based on the Figure 4.3a and Figure 4.3c, in which the shear strength of the Herron Hill slope increased incrementally from 23 kPa at a pressure head of 0 m (Point A) to 247 kPa at a pressure head of -25.04 m (Point E).

The initial increase in shear strength corresponded to a change from Point A to B that was attributed to a pressure head reduction from 0 m to -2.63 m. However, the change in shear strength would not have occurred along a constant void ratio. Any decreases in pressure head causes a process of void ratio increase, referred to as swelling behavior

(Alonso et al., 1990; Sheng, 2011). It should be noted that the studying hillslope is initially at zero pressure head and zero volumetric strain. The purpose of simulation is to investigate the change of hydro-mechanical behavior of the slope relative to the initial state. Regarding volumetric strain equation,  $\varepsilon_v = (e_{\text{initial}} - e_{\text{secondary}}) / e_{\text{initial}}$  and swelling phenomenon, gradual increases in void ratio relative to initial void ratio causes the volumetric strain to continuously decrease. Since the initial volumetric strain is zero, the successive volumetric strains become negative.

Volumetric strain due to pressure head drop can be quantified by drawing a horizontal line starting from Point A and ending at Point B' (Figure 4.3a). The volumetric strain induced by swelling phenomenon equals the distance from A to B'. With a decrease in pressure head, the shear strength increases (e.g. from A to B, from B to C, etc.) while volumetric strain keeps decreasing (e.g. from A-B' to A-C', from A-C' to A-D', etc.). When the pressure head reaches the final value (-25.04 m), the volumetric strain of the soil stops. In this case, the final shear strength of the soil would be around 247 kPa and the amount of volumetric strain is equal to the distance between Points A and E'. The Herron Hill slope experienced a total volumetric strain of -8.16 percent during the drying process. This amount of volumetric strain corresponds to an axial strain of -20.41 percent (line A-E' in Figure 4.3c). Each increment of volumetric strain caused by the swelling behavior corresponds to an increment of shear strain, as illustrated on Figure 4.3d. As discussed previously, a pressure head decrease from an initial value to -2.63 m causes a volumetric strain equal to length of line A-B' (almost -3.76 percent). The shear strain corresponding to this amount of volumetric strain would be equal to length of line B'-B'' in Figure 4.3d. The shear strain incrementally decreases with a reduction in pressure head up to -25.04 m (Point E'), where the final shear strain of the slope would be around -17.69 percent (length of line E'-E'').

In terms of hydraulic behavior, a change in pressure head from 0 m to -2.63 m leads to a decrease in degree of saturation equivalent to the distance between A and B' (Figure 4.3b). The change of degree of saturation is attributed to two phenomena; (i) void ratio increase due to swelling, and (ii) water desorption induced by pressure head decrease. Contribution of each phenomenon on the reduction of the degree of saturation can be estimated by Equation 4.8 and volumetric strain during swelling process. For instance,



volumetric strain from Point D' to Point E' was about -0.94 percent, (Figure 4.3a). Also, the change of void ratio was directly proportional to the volumetric strain. Thus, the change of void ratio,  $de$  can be calculated from volumetric strain, -0.94 percent. Imputing differential void ratio,  $de$  into the Equation 4.8 yields a change in the degree of saturation,  $dS_r$ , due to a change in void ratio. This approach estimates the second component of Equation 4.8. The volumetric strain of -0.94 percent caused a change in the degree of saturation of about 0.007. The total change of degree of saturation from D' to E' is about 0.033. Thus, subtracting the total change of degree of saturation (0.033) from the change in the degree of saturation due to volumetric strain (0.007) gives the change of degree of saturation induced by pressure head drop (0.026). The degree of saturation of the soil only due to pressure head decrease is around 0.924 (Point X in Figure 4.3b), which is obtained by subtracting degree of saturation at Point D' (0.95) from the change of degree of saturation due to the pressure head drop (0.026). The swelling phenomenon causes the degree of saturation further decreases from 0.924 to 0.917 (Point E'). The ultimate state of the soil corresponds to pressure head equal to -25.04 m, which is inferred by Point E' on Figure 4.3b. Along the drying process, the total change in the degree of saturation is almost 0.08, which is equivalent to the length of line A-E'.

Normally, the factor of safety (FOS) is utilized to assess stability of a given slope. The FOS is defined as the ratio of the shear strength to driving stress, both acting along slip surface of the slope but in opposite directions. A FOS greater than unity implies a stable slope and failure of a given slope is assumed to occur if the FOS drops below unity. Thus, a state of limit equilibrium exists where  $FOS = 1$ . As previously mentioned, the shear strength values over several hydrologic conditions corresponds to Points A, B, C, D, and E in Figure 4.3. The driving stress,  $\tau_d$  is defined as,

$$\tau_d = \gamma Z \sin \delta \quad (4.13)$$

where  $\gamma$  is moist unit weight of the soil;  $Z$  is depth of slip surface;  $\delta$  is inclination angle of the slope. Figure 4.4 shows the change of factor of safety with degree of saturation, which indeed is synonymous to pressure head variation. For the study period, the moist unit weight of the soil varied from 19.16 to 19.52 kN/m<sup>3</sup>. The depth and inclination angle of the slip surface was assumed to remain unchanged during lifetime of the slope.

Therefore, the magnitude of the driving stress exhibited negligible changes (from 5.28 to 5.38 kPa) with degree of saturation/pressure head change. Thus, any change in the FOS was mostly due to a change in the shear strength. To calculate the FOS, an average value of 5.33 kPa was considered for the driving stress.

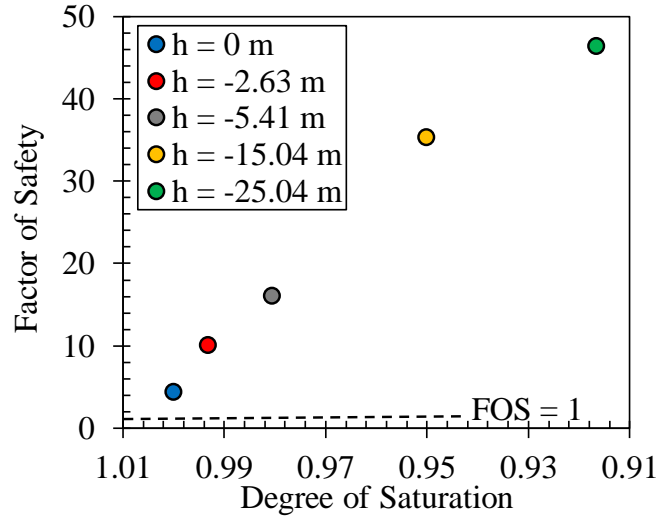


Figure 4.4 Changes in factor of safety with a reduction in degree of saturation at the Herron Hill site

In Figure 4.4, the FOS at the saturated state was almost 4.31 ( $\tau_f/\tau_d = 23/5.33$ ). For the final shear strength of the soil at pressure head of -25.04 m, the FOS was around 46.33 ( $\tau_f/\tau_d = 247/5.33$ ). Therefore, continues reduction in pressure head/degree of saturation induced by evapotranspiration causes a dramatic increase in FOS (Figure 4.4).

The presented example illustrates the great possibility of estimating incremental hydraulic and mechanical characteristics of unsaturated slopes at various hydrologic conditions. The integration of the modified-SFG model with the hydrologic data provides real-time FOS information for a hillslope with respect to seasonal events. When used with reliable predictions of hydrological data, the proposed methodology allows for predictions of slope deformations and stability and hence facilitates the development of timely and effective stabilization strategies.

#### 4.4 Framework Used for Developing an Infiltration Model

A real-time description of the hydro-mechanical behavior of an unsaturated site/slope is driven by a reasonable approximation of the seasonal variations of the

hydrologic characteristics for a slope system. Rainfall and evapotranspiration act as positive and negative surface fluxes for a slope system, causing water to move downward or upward in the soil. Because steady state flow is typically not achieved during cyclic wetting (i.e. rainfall) and drying (i.e. evapotranspiration) events, transient infiltration models are most appropriate to describe the seasonal variations in the hydrologic behavior.

#### 4.4.1 Transient Infiltration

One-dimensional transient infiltration through an unsaturated medium is described by a nonlinear partial differential equation developed by Richards (1931), as

$$\frac{\partial \theta}{\partial t} = \frac{\partial}{\partial z} \left[ K_{un} \cdot \left( \frac{\partial h}{\partial z} + \cos \varphi \right) \right] - S \quad (4.14)$$

where  $\theta$  is volumetric water content;  $t$  is time;  $z$  is soil depth;  $K_{un}$  is unsaturated hydraulic conductivity;  $h$  is pressure head;  $\varphi$  is the angle between the flow direction and the vertical axis;  $S$  is the sink or source term. Several numerical approximations of Equation 4.14 (e.g. Yang et al., 2017; Gowdish and Munoz-Carpena, 2018; Duong et al., 2019) have been presented for modeling transient infiltration. The Hydrus software (Simunek et al., 2018) is finite element tool widely utilized to describe the transient infiltration of unsaturated soils under various climatically conditions (e.g. Fan et al., 2018; Li et al., 2019; Kirkham et al., 2019). Thus, the Hydrus software was used in this study to simulate hydrologic characteristics of the unsaturated soils with respect to rainfall and evapotranspiration events. Benson et al. (2014) reported correlations between fitting parameters of van Genuchten (1980) SWCC model and physical properties of the soils. Thus, the van Genuchten (1980) model was used for the infiltration analysis. The van Genuchten (1980) SWCC model in terms of volumetric water content,  $\theta$  is similar to the function previously presented for degree of saturation (Equation 4.4) given as,

$$\theta = \theta_r + (\theta_s - \theta_r) \left[ 1 + \alpha |h|^n \right]^{-m} \quad (4.15)$$

In addition, van Genuchten (1980) hydraulic conductivity,  $K_{un}$ , function was used as well, which is defined as,

$$K_{un} = K_s \left( \frac{\theta - \theta_r}{\theta_s - \theta_r} \right)^l \left[ 1 - \left( 1 - \left( \frac{\theta - \theta_r}{\theta_s - \theta_r} \right)^{\frac{1}{m}} \right)^m \right]^2 \quad (4.16)$$

where  $\theta_s$  is the saturated volumetric water content;  $\theta_r$  is the residual volumetric water content;  $m$  is the fitting parameter from the van Genuchten (1980) SWCC model;  $K_s$  is the saturated hydraulic conductivity;  $l$  is a pore-connectivity parameter.

#### 4.4.2 Simulation of Infiltration Process

A secondary objective of this paper was to develop a transient infiltration model to describe real-time hydrologic features of the unsaturated soils as a function of rainfall/evapotranspiration events. The implication is the model would include elements of hysteresis such as a main drying curve and main wetting curve and several scanning curves enclosed between the main curves. As an example, seasonal hydrologic data and the corresponding in-situ SWCC for Doe Run at depth of 30 cm is shown in Figure 4.5. Figure 4.5 is typical of the other study sites. For all study sites, the maximum drying point (i.e. the lowest volumetric water content observed during the monitoring period) was greater than the residual volumetric water content.

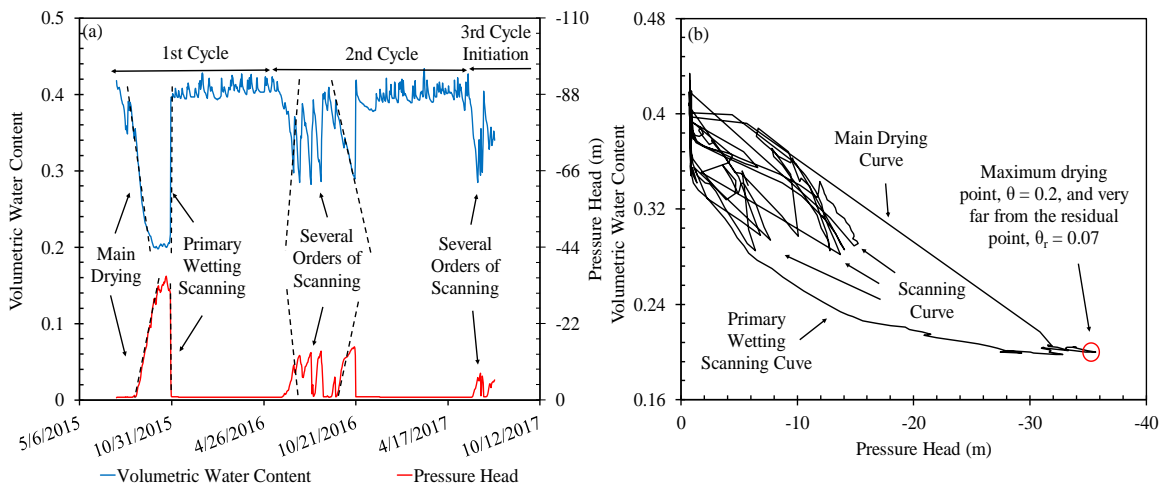


Figure 4.5 Hydrologic data for Doe Run at depth of 30 cm, (a) seasonal volumetric water content and pressure head (b) in-situ SWCC

Although it is assumed that the SWCC behavior can be adequately described using the van Genuchten (1980) model, the expectation is there are distinct fitting parameters for

the main drying curve, main wetting curve, and the scanning curves (wet-to-dry and dry-to-wet). Thus, there are a possibility of four sets of fitting parameters. The fitting parameters for the SWCC are commonly obtained by using an optimization routine between the predicted (Equation 4.15) and measured data. While the presented study cases provided an abundance of measured data, in-situ measurements of both volumetric water content and water potential (i.e. matric suction) are not common at most field sites. This study hypothesized that different behaviors of the SWCC are correlated to each other, and hence their fitting parameters are proportionally related to each other. The goal was to simulate the hydrologic behavior due to an entire seasonal variation using one set of fitting parameters.

It was observed in Figure 4.5a that all drying curves tended to have very similar slopes of inclination and all wetting curves tended to have very similar inclinations. Also observed, the slopes of the wetting curves seem to be very similar to those of the drying curves. These phenomena indicate that different parts of volumetric water content and pressure head plot were proportionally correlated to each other. Thus, the fitting parameters of the different curves of the SWCC may be scaled from the fitting parameters of one curve of the SWCC.

As explained previously, the slope and curvature of the SWCC are controlled by the  $n$  parameter of van Genuchten (1980) model. Since different segments of volumetric water content and pressure head curves were inclined very similarly (Figure 4.5), the  $n$  parameter of several curves was assumed to be identical. Several researchers (e.g. Kool and Parker, 1987; Zhou et al, 2012) suggested that the  $\alpha$  parameter of the drying and wetting scanning curves can be scaled from the main drying and main wetting curves, respectively. These researchers also suggested the  $\alpha$  parameter of the main wetting curve was correlated to the  $\alpha$  parameter from the main drying curve. Thus, the  $\alpha$  and  $n$  parameters of the main drying curve was used to estimate the  $\alpha$  and  $n$  parameters of various parts of the SWCC, and hence simulate the entire seasonal hydrologic data. The  $\alpha$  and  $n$  parameters of main drying curve are estimated by fitting the Equation 4.15 to in-situ volumetric water content and pressure head data. In this approach, the only required measured data were those corresponding to the main drying curve. The  $\alpha$  and  $n$  parameters obtained through this process are denoted as  $\alpha_{fit}$  and  $n_{fit}$ .

Regarding Equations 4.15 and 4.16, in addition to  $\alpha_{fit}$  and  $n_{fit}$ , parameters  $K_s$ ,  $l$ ,  $\theta_s$  and  $\theta_r$  are also required to can conduct hydrological simulation. Value of  $K_s$  corresponding to the location and depth of a given soil can be found on soil databases. Parameter  $l$  is assumed to be 0.5 in the original study of Mualem (1976). Thus, 0.5 is accepted for  $l$ . Saturated volumetric water content,  $\theta_s$  corresponds to the initial point of the main drying curve and residual volumetric water content,  $\theta_r$ , varies within a small range from 0.07 to 0.11.

Referring to the simulation approach,  $\alpha$  and  $n$  parameters of different parts of SWCC will be scaled from  $\alpha$  and  $n$  parameters of the main drying curve. Consequently, before simulating the entire hydrologic data, it is essential to assess the ability of hydraulic parameters ( $\theta_s$ ,  $\theta_r$ ,  $K_s$ ,  $l$ ,  $\alpha_{fit}$  and  $n_{fit}$ ) in simulating hydrologic data of the main drying segment as a function of rainfall and evapotranspiration events. As a prime evaluation,  $\theta_s$ ,  $\theta_r$ ,  $K_s$ ,  $l$ ,  $\alpha_{fit}$  and  $n_{fit}$  associated with Doe Run at depth of 30 cm were imputed inside the Hydrus along with daily rainfall and evapotranspiration data and the pressure head and volumetric water content were predicted for main drying segment. This process is termed as direct simulation since all parameters were imputed inside the software without any change. Having simulation completed, the predicted results did not suitably match the actual data. This phenomenon clearly indicates  $\alpha_{fit}$  and  $n_{fit}$  may not be able to perform satisfactory simulations, thus they must be optimized.

The Hydrus software offers a useful technique by which the hydraulic parameters are optimized systematically such that the predicted results match the measured results with a reasonable degree of precision. This process is denoted as inverse simulation. The inverse estimation of  $\alpha$  and  $n$  was conducted over pressure head data corresponding to main drying period. Upon inverse simulation, the Hydrus software yields predicted/simulated pressure head with optimized  $\alpha$  and  $n$ . It should be noted that the value of  $\theta_s$ ,  $\theta_r$ ,  $K_s$  and  $l$  were kept constant during inverse simulation. The  $\alpha$  and  $n$  parameters optimized

through inverse simulation of pressure head are denoted as,  $\alpha_{opt,h}$  and  $n_{opt,h}$ . The inverse simulated and in-situ data are illustrated on Figure 4.6.

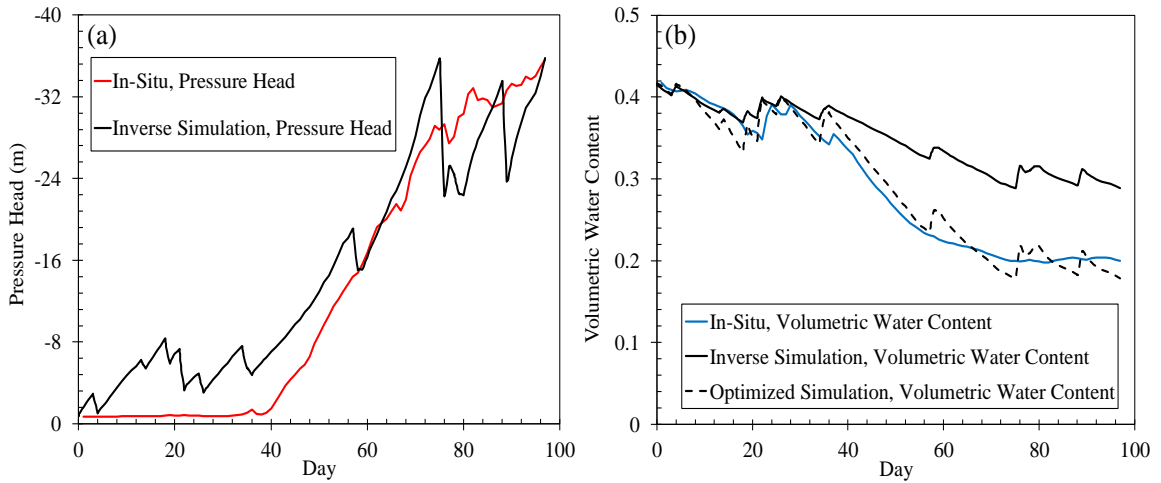


Figure 4.6 Simulated and in-situ data along main drying segment for Doe Run at depth of 30 cm, (a) inverse simulation of pressure head, (b) inverse and optimized simulation of volumetric water content

The Hydrus software utilizes optimized SWCC fitting parameters,  $\alpha_{opt,h}$  and  $n_{opt,h}$  along with Equation 4.15 to predict the volumetric water content over main drying segment. However, volumetric water content curve simulated by  $\alpha_{opt,h}$  and  $n_{opt,h}$  does not closely match the actual results (Figure 4.6, b). To improve the simulation performance associated with the volumetric water content,  $\alpha_{opt,h}$  and  $n_{opt,h}$  were imputed into the Equation 4.15 and systematically optimized till the difference between the predicted and the measured volumetric water content reaches a minimum. Parameters attained through this process are denoted as  $\alpha_{opt,\theta}$  and  $n_{opt,\theta}$ . Prediction results associated with  $\alpha_{opt,\theta}$  and  $n_{opt,\theta}$  generates a prediction curve named as optimized simulation (Figure 4.6, b). This curve highly fits the measured volumetric water content, and hence improves the simulation conducted by inverse method.

As discussed previously, different segments of hydrologic data will be described as a function of main drying curve, in which  $\alpha$  and  $n$  parameters of different segments will be scaled from  $\alpha$  and  $n$  associated with the main drying curve. For main drying curve, the inverse simulation yields much more precise prediction than direct simulation, thus the

optimized values of SWCC fitting parameters,  $\alpha_{opt,h}$  and  $n_{opt,h}$ , will be used for scaling process. Obtaining  $\alpha_{opt,h}$  and  $n_{opt,h}$  for each soil based on corresponding main drying curve,  $\alpha$  and  $n$  parameters associated with primary wetting scanning and several order of scanning curves were scaled from  $\alpha_{opt,h}$  and  $n_{opt,h}$ . In case of primary wetting scanning curve, associated  $\alpha$  and  $n$  were attained by multiplying  $\alpha_{opt,h}$  and  $n_{opt,h}$  to a factor of 1.4 and 1, respectively ( $\alpha = 1.4\alpha_{opt,h}$  and  $n = 1n_{opt,h}$ ). For several order of scanning curves, the multiplying factors for  $\alpha$  and  $n$  are respectively 0.3 and 1, as  $\alpha = 0.3\alpha_{opt,h}$  and  $n = 1n_{opt,h}$ . As discussed previously,  $\alpha_{opt,h}$  and  $n_{opt,h}$  do not provide suitable simulation results over volumetric water content data. Thus,  $\alpha$  and  $n$  parameters scaled from  $\alpha_{opt,h}$  and  $n_{opt,h}$  would not lead to an accurate volumetric water content simulation. In this case,  $\alpha$  and  $n$  parameters for volumetric water content simulation must be scaled from  $\alpha_{opt,\theta}$  and  $n_{opt,\theta}$ . Scaling factors used for  $\alpha$  and  $n$  are respectively equal to 0.9 and 1 ( $\alpha = 0.9\alpha_{opt,\theta}$  and  $n = 1n_{opt,\theta}$ ), for primary wetting scanning curves. To simulate volumetric water content for several order of scanning parts, 1.1 and 1 must be set as scaling factors for  $\alpha$  and  $n$  ( $\alpha = 1.1\alpha_{opt,\theta}$  and  $n = 1n_{opt,\theta}$ ), respectively. Scaling factors result in simulated pressure head and volumetric water content over primary wetting scanning and several order of scanning curves for all soils, and thus are general factors for this study. Pressure head and volumetric water content simulations were conducted on individual segments using the corresponding scaled parameters. Finally, the predicted data were linked together, and continuous simulation curves were generated. It should be noted that the measured and predicted volumetric water content data were converted to degree of saturation. The presented methodology for predicting hydrologic data is denoted as infiltration model. Figure 4.7 illustrates the simulated and in-situ pressure head and degree of saturation for study soils at their respective depths.



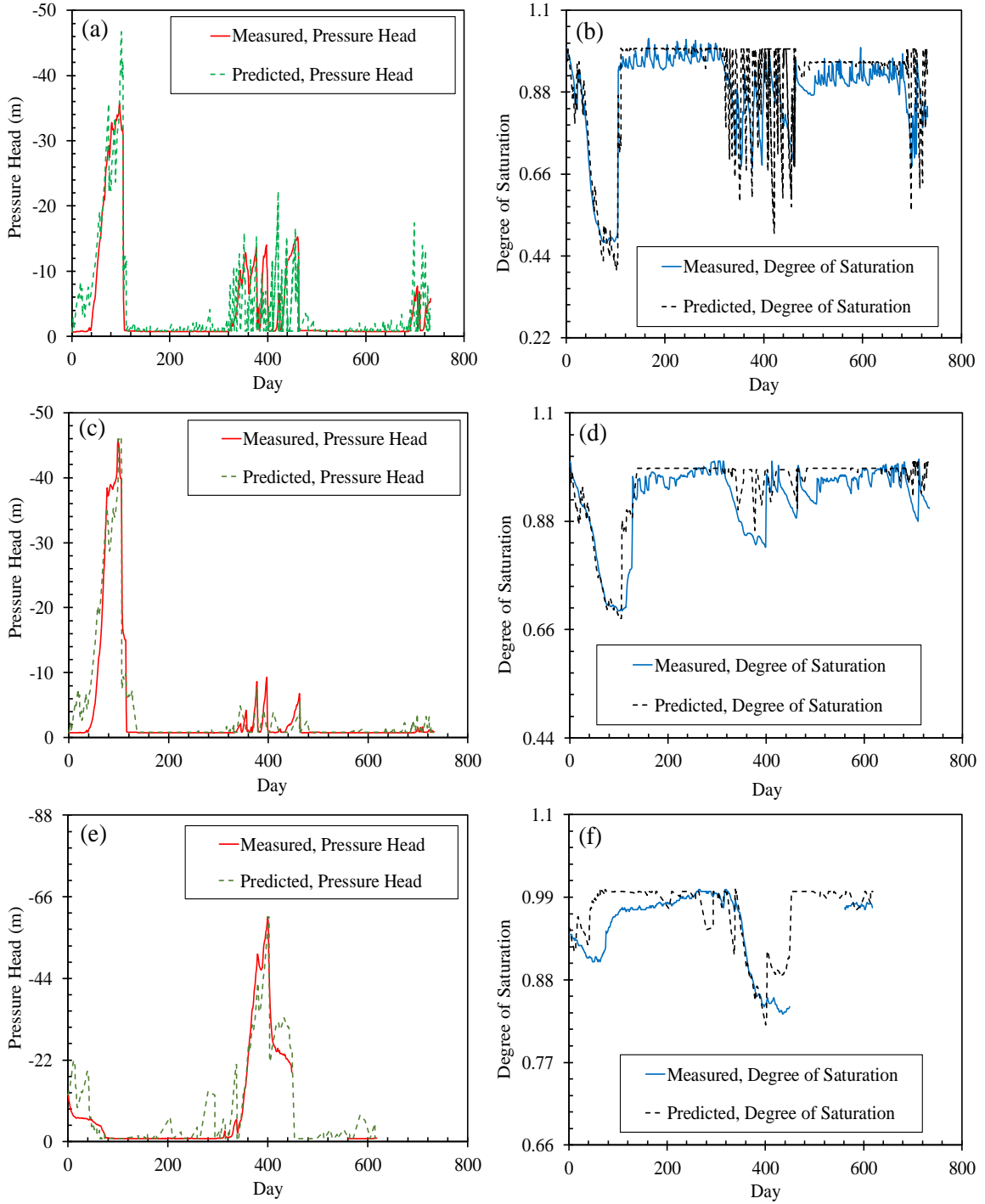


Figure 4.7 Simulated and measured pressure head for monitoring sites, (a) pressure head data for Doe Run at depth of 30 cm, (b) degree of saturation data for Doe Run at depth of 30 cm, (c) pressure head data for Doe Run at depth of 70 cm, (d) degree of saturation data for Doe Run at depth of 70 cm, (e) pressure head data for Herron Hill at depth of 100 cm, (f) degree of saturation data for Herron Hill at depth of 100 cm

The infiltration model shows an appropriate prediction performance in terms of pressure head and degree of saturation over different seasons. In general, most hillslope failures occur along wetting processes induced by rainfall. Since the modified-SFG model uses hydrologic data for simulating hydro-mechanical behavior of the unsaturated slopes, an accurate prediction of the pressure head and degree of saturation along wetting processes can anticipate slope failure in advance. Prediction results firmly confirms applicability of the proposed method in simulating long term hydrologic data using short term hydrologic data. Thus, once hydrologic data are recorded along the summer, the entire hydrologic data over various seasons can be simulated. Table 4.4 presents the optimized and scaled fitting parameters for each monitoring site at respective analysis depths. The name of sites has been shortened to fit inside the table cell. Accordingly, DR and HH stands for Doe Run and Herron Hill, respectively.

Table 4.4 Original hydraulic parameters with optimized SWCC parameters

		Original hydraulic parameters of main drying					Optimized SWCC parameters of main drying for pressure head		Optimized SWCC parameters of main drying for volumetric water content	
Site	Depth (cm)	$\theta_s$	$\theta_r$	$K_s$ (m/day)	$\alpha$ (1/m)	$n$	$\alpha_{opt,h}$ (1/m)	$n_{opt,h}$	$\alpha_{opt,\theta}$ (1/m)	$n_{opt,\theta}$
DR	30	0.42	0.11	0.13	1.12	1.36	0.11	1.36	0.11	2.05
	70	0.46	0.07	0.13	3.77	1.08	0.18	1.18	0.18	1.23
HH	100	0.42	0.07	0.04	0.05	1.15	0.05	1.14	0.05	1.20

Tabulated data for Doe Run at depth of 70 shows the same value of hydraulic conductivity,  $K_s$  for both measurement depths. This equality is mostly attributed to the similar soil texture and particle size distribution over both depths. As discussed earlier, sensors' rate of response to hydrological events varies with depth. Therefore, the SWCC parameters also varies with a change in depth from 30 to 70 cm. Hydraulic conductivity has a minimal value in Herron Hill slope. This site mostly contains fine grain-size particles, that normally cause high solid-water tension force. Thus, water may not be able to easily

pass through void spaces generated within fine-grained soils, and hence the value of hydraulic conductivity for this type of soils is normally small. Due to high tension force, stronger matric suction (or lower pressure head) is required to initiate water drainage from the soil's void spaces. Thereby, the air entry point of fine materials is higher, which is synonymous to lower value of  $\alpha$  parameter. Having hydrologic data simulated, modified-SFG model can be utilized to describe mechanical behavior of the soils based on the predicted hydrologic data.

#### 4.5 Coupled Modified-SFG and Infiltration Model

Applicability of incorporating infiltration model with the modified-SFG scheme for simulating hydro-mechanical behavior of the Herron Hill slope is assessed herein. The same drying period and monitoring time frame selected before are chosen for simulation. The purpose of this selection is to compare simulated results obtained by using the measured hydrologic data with the simulation attained by means of the predicted hydrologic data. Accordingly, pressure head and volumetric water content were predicted using the infiltration model for the same dates. The value of the predicted and measured pressure head and volumetric water content as well as dates of measurement/prediction are presented on Table 4.5.

Table 4.5 Measured and predicted hydrologic data for Herron Hill slope

Date	Pressure head		Degree of Saturation	
	Measured	Predicted	Measured	Predicted
7/31/2016	0	0	1.000	1.000
8/20/2016	-2.63	-1.37	0.983	0.995
8/25/2016	-5.41	-5.02	0.971	0.975
9/4/2016	-15.04	-15.79	0.942	0.932
9/11/2016	-25.04	-25.78	0.911	0.900

For the most data points, predicted pressure head and degree of saturation are very close to the measured results, that validates the predictability of the infiltration model. Therefore, it is expected that using the predicted hydrologic data provides almost the same hydro-mechanical simulations as produced by using the measured hydrologic data. The

predicted pressure head and degree of saturation were imputed inside the modified-SFG model along with the parameters governing stress-strain and stress-hydraulic behavior of the soil. These parameters are tabulated in the Table 4.6. Upon inverse simulation conducted,  $\psi'_i$ ,  $\omega_i$ ,  $n_i$  and  $m_i$  parameters were estimated from  $\alpha$  and  $n$  parameters of the inversed main drying SWCC. Also,  $\psi$ ,  $n$  and  $m$  parameters used for modeling hysteresis behavior of the soil were estimated based on the relationship between inverse main drying and primary wetting scanning. Eventually, the hydro-mechanical behavior of the Herron Hill slope was remodeled for all data points.

Table 4.6 Parameters used to describe hydro-mechanical behavior of the Herron Hill by the predicted hydrologic data

$\kappa_{vp}$	$\lambda_{vp}$	$\psi$	$n$	$m$	$\psi'_i$	$\omega_i (m^{-1})$	$n_i$	$m_i$	$M$
0.01	0.1	5.62	1.14	0.13	1.31	0.39	1.14	0.13	0.85

The hydraulic and mechanical simulations associated with the predicted hydrologic data are illustrated in Figure 4.8 with simulation data obtained by means of the measured hydrologic data. For all data points, the simulation carried out by the predicted hydrologic data suitably match the volumetric strain and axial strain curves obtained from the measured hydrologic data. In most cases, difference between the values of shear strength obtained from the predicted and measured hydrologic data is less than 6 kPa (Figure 4.8b). The only exception is associated with the data point of -2.63 m and its corresponding predicted pressure head, -1.37 m. In this case, difference between the shear strength values is approximately 15 kPa, which still is an acceptable value. This divergence is essentially attributed to the difference between the measured pressure head (-2.63 m) and the predicted pressure head (-1.37 m), which is slightly higher than the corresponding difference for the other data points (e.g. -15.04 m and -15.79 m, -25.04 m and -25.78 m). In terms of shear strain-volumetric strain (volumetric strain due to swelling), values of shear strain obtained from the predicted hydrologic data well match the values calculated by the measured hydrologic data.

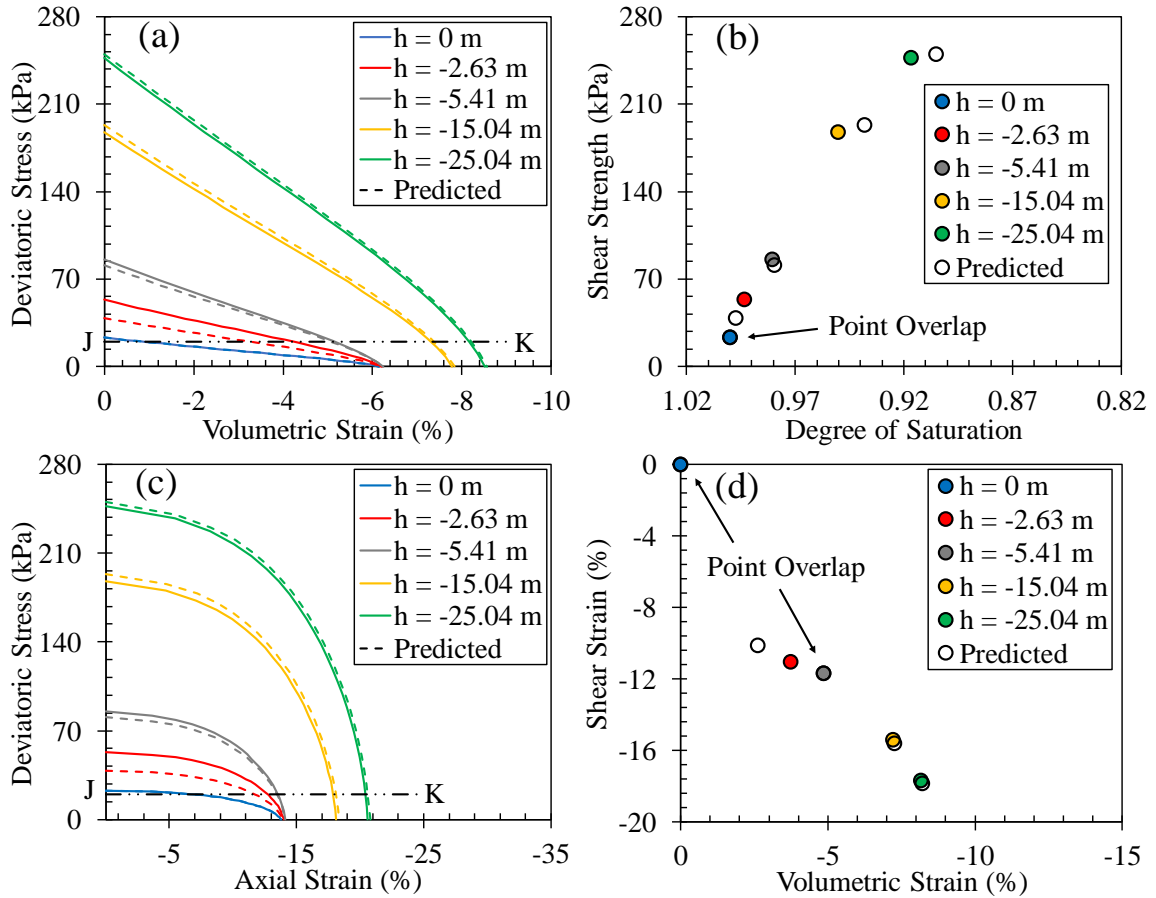


Figure 4.8 Hydro-mechanical behavior of the Herron Hill site simulated by the measured and predicted hydrologic data, (a) deviatoric stress versus volumetric strain, (b) degree of saturation versus shear strength, (c) deviatoric stress versus axial strain, (d) volumetric strain versus shear strain

The coupled infiltration-modified-SFG model can also be utilized to analyze mechanical response of the Herron Hill slope to hydrological variations at a specific deviatoric stress. The intention is to study the change of volumetric and axial strain along the given drying period at a deviatoric stress equal to 20 kPa. This amount of deviatoric stress corresponds to line J-K in Figures 4.8a and 4.8c. The change of volumetric and axial strain with respect to pressure head are illustrated on Figure 4.9. For deviatoric stress equal to 20 kPa, volumetric and axial strain data estimated by the measured and predicted hydrologic data are extracted from Figures 4.8a and 4.8c. Circles inside the Figure 4.9 correspond to the volumetric and axial strain data obtained from the measured pressure heads (i.e. 0, -2.63, -5.41, -15.04, and -25.04 m). Volumetric strain and axial strain data calculated by the predicted pressure heads (i.e. 0, -1.37, -5.02, -15.79, and -25.78 m) have

not been shown as individual points in the figure. However, these points were connected to each other such that a prediction curve was created.

At the mentioned deviatoric stress, the volumetric strain predicted by the measured hydrological data reduces with a decrease in pressure head, which obviously is attributed to the swelling phenomenon. Prediction curve associated with the volumetric strain data reasonably follows volumetric strain data attained from the measured hydrological data. Each increment of the volumetric strain corresponds a specific axial strain. Consequently, the axial strain also decreases with pressure head reduction. In this case, the associated prediction curve satisfactorily matches axial strain values estimated by the measured hydrological data. Minimal difference between the prediction curves and volumetric/axial strain data indicates that the coupled infiltration-modified-SFG model can precisely describe deformational behavior of unsaturated hillslopes over various deviatoric stresses.

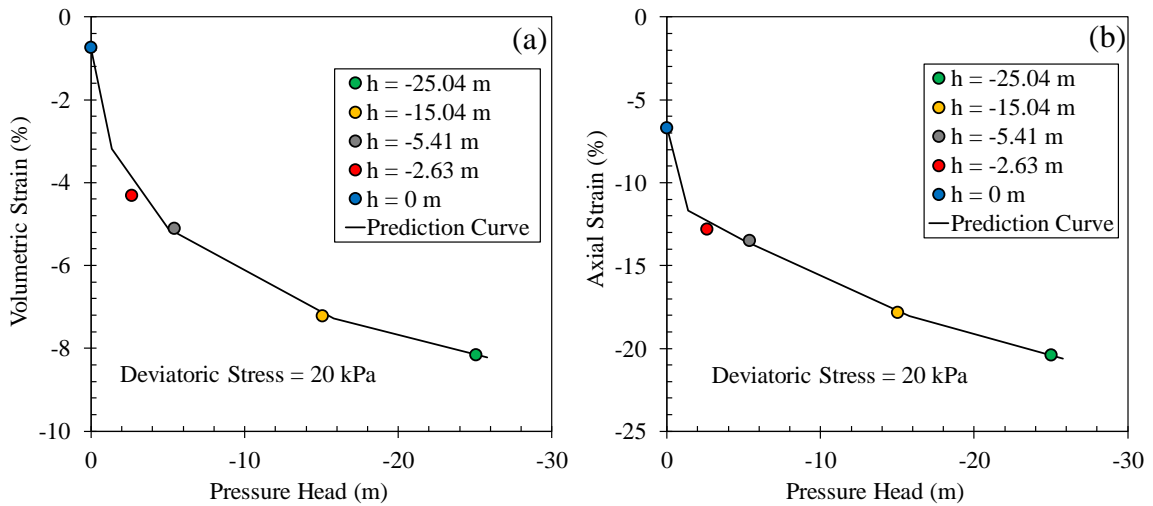


Figure 4.9 Simulated mechanical behavior of Herron Hill slope at a specific deviatoric stress (a) pressure head versus volumetric strain, (b) pressure head versus axial strain

## CHAPTER 5. SUMMARY AND CONCLUSION

The main objective of this study was to provide a robust and suitable constitutive framework that can be used as a predictive tool for describing incremental behavior of the unsaturated soils as a function of variable hydrologic conditions. This study initially proposed a novel methodology to estimate the small-strain shear modulus of unsaturated soils as a function of net normal stress and matric suction. The basis of the predictive model was established on an inverse relationship between the soil-water characteristics curve (SWCC) and the small-strain shear modulus curve. Primary evaluations partly confirmed validity of the proposed hypothesis, while highlighted a need for SWCC modification so that improve the inverse relationship between the SWCC and small-strain shear modulus curve. Net normal stress-induced deformations cause a change in the SWCC. Thus, the modified SWCC was adjusted for the net normal stresses differing from the original stress state. The small-strain shear modulus prediction model was subsequently derived from the modified SWCC. The predictive scheme comprises of four fitting parameters that are estimated from the modified SWCC. The developed model was successfully applied to a series of case studies for various net normal stresses and over a wide range of matric suctions. The proposed approach will reduce the amount of laboratory experiments required to determine the small-strain shear modulus of unsaturated soils. The predictive model also allows real-time values of the small-strain shear modulus with respect to the hydrologic variations.

Likewise, this study presented an elastoplastic constitutive framework, identified as SFG, to describe skeletal deformation and hydraulic characteristics of the unsaturated soils using stress-suction coupled relationship. In comparison with the existing constitutive schemes, the SFG model provides more rational and precise descriptions of the volumetric strain, yield stress and shear strength of the partially saturated soils. However, the model delivers inconsistent and uncertain simulations of the hydraulic-deformation responses. Furthermore, the SFG model postulates a constant value for the small-strain shear modulus to describe elastic shear strain of the soil over triaxial loading. Since the small-strain shear modulus varies with seasonal changes, the original SFG scheme is incompatible to hydrologic variations, and thus incapable of producing the real-time descriptions of the

soils' behavior. The original SFG model was imposed to two modifications. Initially, the hydraulic-deformation relationship was reformed, which yielded more reliable and coherent descriptions of the hydraulic characteristics as a manner of the volumetric changes. Additionally, the predictive model proposed for the small-strain shear modulus was introduced to the original SFG model to facilitate the real-time descriptions of stress-strain behavior of the soils with respect to the hydrologic variations. Reliability of the modified-SFG model was assessed in accordance to different case studies, which indeed represented various hydrologic events. The prediction outcome firmly confirms dependability and coherence of the modified-SFG model in replicating essential stress-strain and hydraulic characteristics of the unsaturated soils.

Along with this study an innovative methodology was developed to produce the long-term hydrologic characteristics of the unsaturated soil as a response to cyclic rainfall and evapotranspiration events. Hydraulic simulations were totally implemented using Hydrus, a finite element hosted software that receives SWCC fitting parameters and hydraulic conductivity as inputs and yields hydraulic characteristic of the soil as output. The software provides numerical solutions to the Richards equation, a firmly established equation governing the transient infiltration phenomenon within the unsaturated regime. General framework of the proposed methodology laid on the correlation between different parts of the hydrologic dataset, which essentially represent different segments of the SWCC. Several wetting and drying events, particularly main and scanning curves were simulated using only SWCC parameters of the main drying event. The proposed infiltration scheme aides to predict the long-time hydrologic dataset using limited amount of in-situ hydrologic data. The methodology provides a possibility of estimating future hydrologic characteristics of a specific site in advance.

This study was finalized through coupling the transient infiltration framework with the modified-SFG model, which results in a robust and steady constitutive model being capable of simulating hydro-mechanical behavior of the unsaturated soils with respect to variations in hydrologic condition. This study equips geotechnical engineers with an invaluable tool to accurately monitor sublayer behavior under various real-time rainfall and evapotranspiration conditions, and therefore contributes more effectual risk management planning.



## APPENDIX A SWCC MODELING

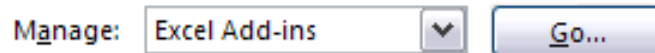
### ***Optimization process to model SWCC based on laboratory results***

Different equations are fitted to experimental results to model a full SWCC for suction values which no laboratory measurements have been conducted for those suctions. Within this study, the measured laboratory data were initially extracted from the literature, then Van Genuchten (1980) equation was fitted to the experimental data to create the entire SWCC. The fitting parameters of the Van Genuchten (1980) equation were obtained using Microsoft Excel Solver, which systematically optimizes the fitting parameters to minimize least square difference between the measured water content and the values predicted by the Van Genuchten (1980) equation.

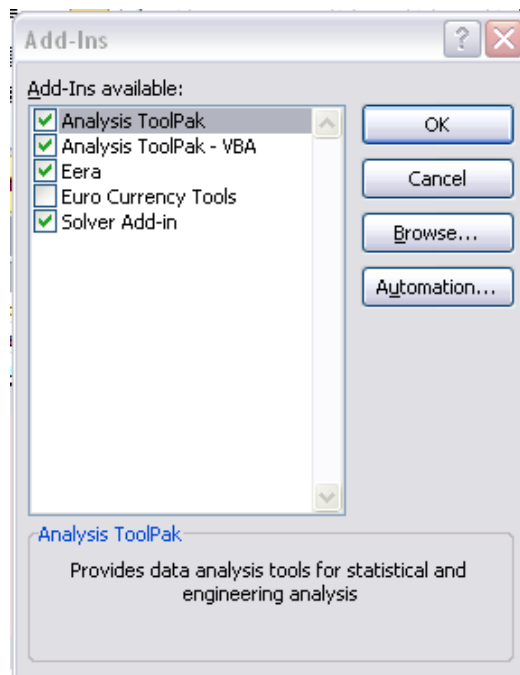
#### **How to install Microsoft Excel Solver**

- **Step 1.** File/Options/Add-In

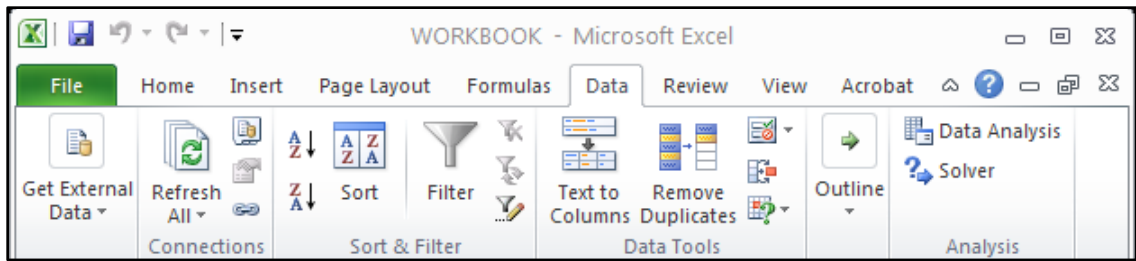
Upon clicking “Add-ins” the following appears



- **Step 2.** Go/Check Solver Add-In/OK



Upon clicking “OK” the Solver will be added under the “Data” tab



**Optimize Procedure**

➤ **Step 1.** Create parameter optimization layout as illustrated on Figure A.1.

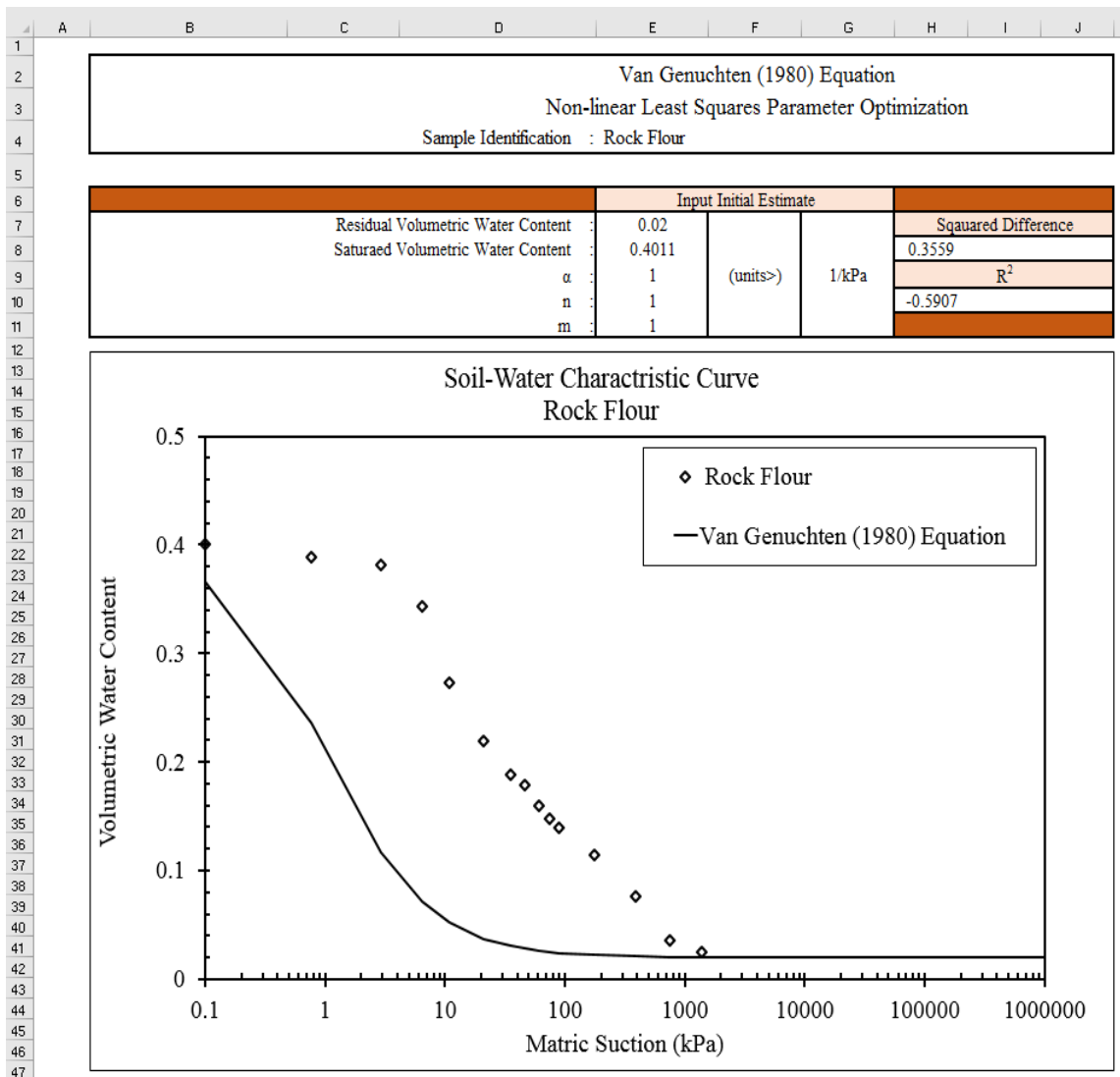


Figure A.1 General spreadsheet of Van Genuchten (1980) optimizer in Microsoft Excel

Based on the Van Genuchten (1980) equation, the required parameters for describing SWCC are: Residual Volumetric Water Content, Saturated Volumetric Water Content,  $\alpha$ ,  $n$  and  $m$ . The initial value of the mentioned parameters is estimated as follows,

- The Residual Volumetric Water Content is determined from SWCC generated by Fredlund and Xing (1994) equation (the model will be presented later).
- The Saturated Volumetric Water Content is equal to the first data point corresponding to the minimum matric suction.
- The fitting parameters  $\alpha$ ,  $n$  and  $m$  are initially guessed, which they are set as unity for Rock Flour sample.

Besides, two more parameters are identifiable on the presented layout that are defined as

- Squared Difference: a statistical factor that evaluates prediction performance of a typical equation, and in particular with the Van Genuchten (1980) equation, it demonstrates how well the predicted volumetric water contents match the measured values. The prediction performance improves with a decrease in Squared Difference, in which the prediction results completely match the actual data at the Squared Difference equal to zero (the ideal value for the Squared Difference).
- $R^2$ : another statistical factor employed for assessing the prediction performance of a typical equation. The best prediction results are attained if the  $R^2$  equals to the unity (the ideal value for the  $R^2$ ).

Note: The value of Residual Volumetric Water Content and Saturated Volumetric Water Content remain unchanged throughout the SWCC generation, while  $\alpha$ ,  $n$  and  $m$  must be systematically changed to minimize and maximize the value of Squared Difference and  $R^2$ , respectively.

The initial values of parameters are inserted into the Van Genuchten (1980) equation and volumetric water content is predicted with respect to a range of matric suction. Figure A.2 illustrates arrays of measured and predicted results, in which the highlighted cells contain measured data obtained from laboratory testing. A remarkable difference is noted between the measured and predicted data that can directly be inferred from the quantified Squared Difference,  $R^2$  and prediction curve (Figure A.1).

	A	B	C	D
48				
49		Test Results		Predicted Results
50		Volumetric Water Content	Matric Suction	Volumetric Water Content
51			(kPa)	
52		0.4011	0.1	0.3665
53		0.3891	0.76	0.2365
54		0.381	2.92	0.1172
55		0.3438	6.48	0.0709
56		0.2731	10.88	0.0521
57		0.2192	20.99	0.0373
58		0.1882	35.65	0.0304
59		0.1785	46.54	0.0280
60		0.1592	60.58	0.0262
61		0.148	73.89	0.0251
62		0.1398	90.22	0.0242
63		0.1144	175.6	0.0222
64		0.0757	389.52	0.0210
65		0.036	754.91	0.0205
66		0.0254	1379.69	0.0203
67			3000	0.0201
68			5000	0.0201
69			10000	0.0200
70			20000	0.0200
71			30000	0.0200
72			40000	0.0200
73			50000	0.0200
74			60000	0.0200
75			70000	0.0200
76			80000	0.0200
77			90000	0.0200
78			100000	0.0200
79			200000	0.0200
80			300000	0.0200
81			400000	0.0200
82			500000	0.0200
83			600000	0.0200
84			700000	0.0200
85			800000	0.0200
86			900000	0.0200
87			1000000	0.0200
88				

Figure A.2 Initial data array of the measured data versus predicted data for optimizing fitting parameters (Note: Bold and highlighted data from laboratory measurements)

Codes defined for calculating Squared Difference and R<sup>2</sup>: (see Figure A.1)

- To calculate Squared Difference, cell H8 is coded as:  
=SUM((B52:B66- D52:D66)^2).
- To calculate R2, cell H10 is coded as:  
=1-(SUM((B52:B66- D52:D66)^2)/SUM((B52:B66-AVERAGE(B52:B66))^2)).

- **Step 2.** Improve prediction performance using solver.

Clicking the “Solver” icon under the “Data” tab, Solver Parameter input window appears in following, as shown on Figure A.3.

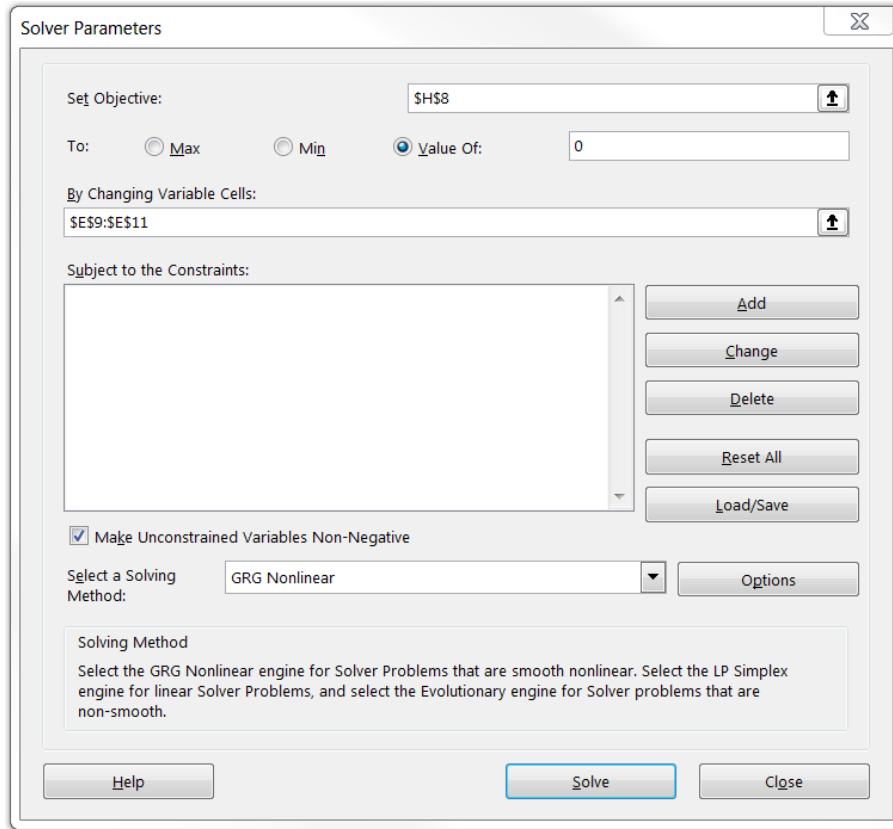


Figure A.3 Microsoft Solver screen for optimizing van Genuchten (1980) equation parameters

- **Step 2A.** Set the location of the Objective value. If the intention is to minimize the Squared Difference, cell H8 is selected, otherwise cell H10 is chosen for maximizing  $R^2$ .
- **Step 2B.** Set the optimization criterion to Min for minimizing Squared Difference, otherwise mark Max for maximizing  $R^2$ .
- **Step 2C.** Determine the variable cells that must be changed to meet the selected criterion. The cells that will be optimized are those corresponding to  $\alpha$ , n and m (E9, E10 and E11).
- **Step 2D.** Optimize the fitting parameters by clicking the “Solve” button.

It should be noted that if a prediction performance results in a Squared Difference close to 0, it automatically results in a  $R^2$  close to 1. Therefore, parameters optimization can be conducted by either minimizing Squared Difference or maximizing  $R^2$ . The process illustrated on the Figure A.3 governs Squared Difference. Upon clicking the “Solve” button, the Solver will optimize parameters  $\alpha$ ,  $n$  and  $m$  by minimizing the squared difference between the measured and predicted volumetric water content values at respective matric suctions. The software systematically changes E9, E10 and E11 till sum of the squared differences in cell H8 iterates to a minimum value. Tabulated and plotted prediction data versus measured data as well as Squared Difference and  $R^2$  are presented on Figure A.4. To generate a smooth SWCC, intermediate suction values were added between actual suctions. Procedure of parameter optimization is the same if the intention is to generate SWCC based on the effective degree of saturation, however the measured volumetric water contents are converted to the effective degree of saturation values.

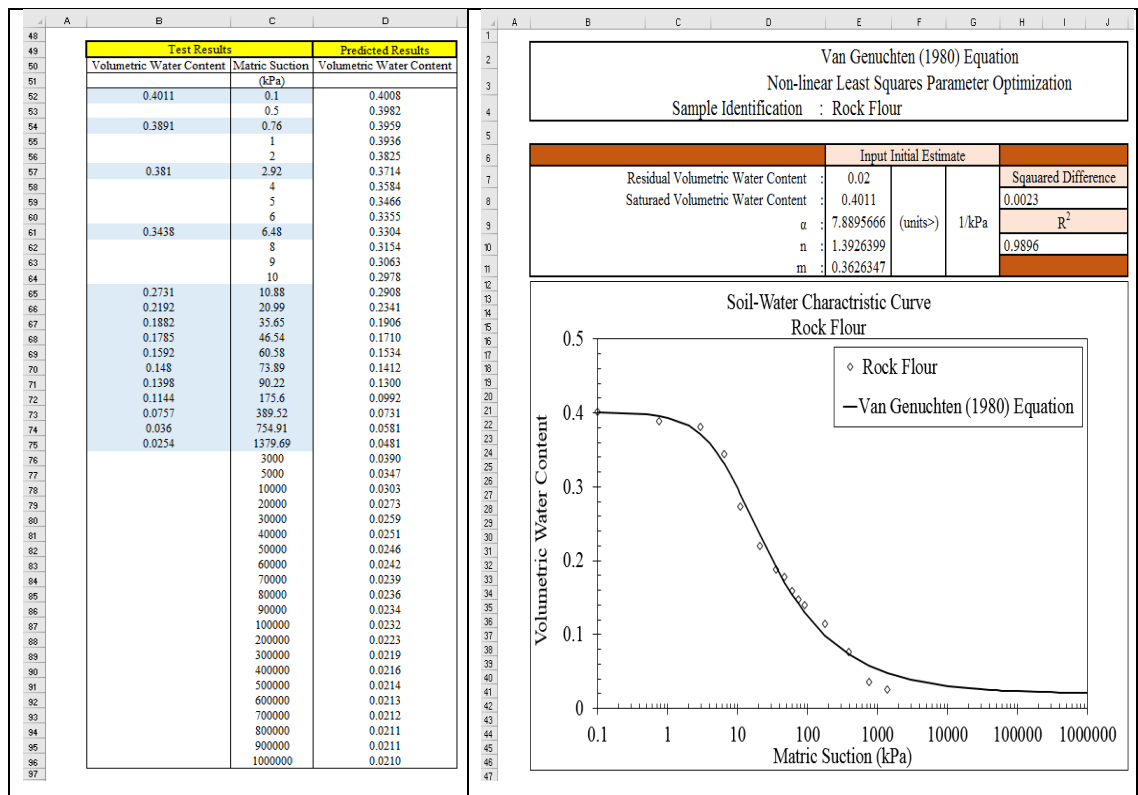


Figure A.4 Van Genuchten (1980) optimizer in Microsoft Excel: (left side) intermediate input data added to create a smooth curve; (right side) measured against predicted values with optimized parameters, Square Difference and  $R^2$

## APPENDIX B SWCCS MODIFICATION



The initial step towards development of shear modulus prediction model was SWCC modification through which the original SWCC was shifted along the matric suction axis, so that diminish divergence between air entry point of SWCC and G-capillary point of normalized shear modulus curve. The entire SWCC transition procedure is given as follows,

- **Step 1.** Determine inflection point of the original SWCC. Figure B.1 shows general layout created for estimating the inflection point.

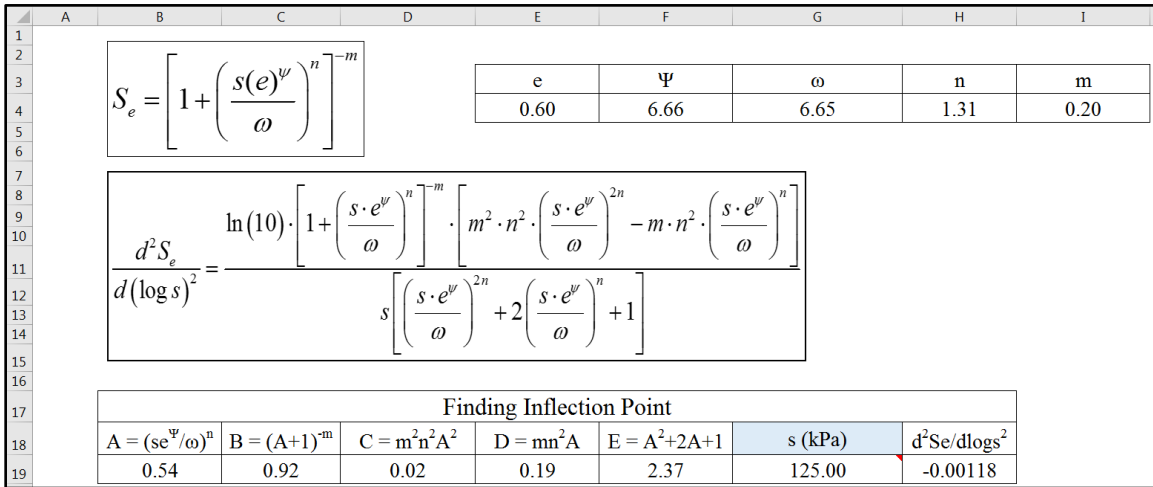


Figure B.1 General spreadsheet of inflection point finder in the Microsoft Excel

- **Step 1A.** Fitting parameters of the original SWCC are estimated based on the procedure explained over the Appendix B. The Gallipoli et al. (2003b) equation was used to define the SWCCs, thus the involving parameters are  $e$ ,  $\psi$ ,  $\omega$ ,  $n$  and  $m$ .
- **Step 1B.** Impose the second derivation on the Gallipoli et al. (2003b) equation.
- **Step 1C.** Set an initial value for matric suction and calculate the value of second derivation of the Gallipoli et al. (2003b) equation.

Codes used for calculating different components of the second derivation of the Gallipoli et al. (2003b) equation (see Figure B.1):

- Cell B19 is coded as:  

$$=((G19*(E4^F4))/G4)^H4$$
- Cell C19 is coded as:  

$$=(B19+1)^(-I4)$$
- Cell D19 is coded as:

$$=(I4^2)*(H4^2)*(B19^2)$$

- Cell E19 is coded as:

$$=I4*(H4^2)*B19$$

- Cell F19 is coded as:

$$=(B19^2)+(B19*2)+1$$

- Cell H19 is coded as:

$$=((LN(10))*C19*(D19-E19))/(F19*G19)$$

➤ **Step 1D.** As a mathematical rule, the second derivation of the equation defining a typical curve is equal to zero at the inflection point. Accordingly, the Microsoft Excel Solver was used to systematically changes the matric section (Cell G19) till the value of the second derivation of the Gallipoli et al. (2003b) equation becomes zero. Thus, open the “Solver” and change the Solver Parameters as follows,

- Set the Objective Cell to cell H19.
- Set the optimization criterion to Value Of 0.
- Select cell G19 as Variable Cell.
- Click the “Solve” button.

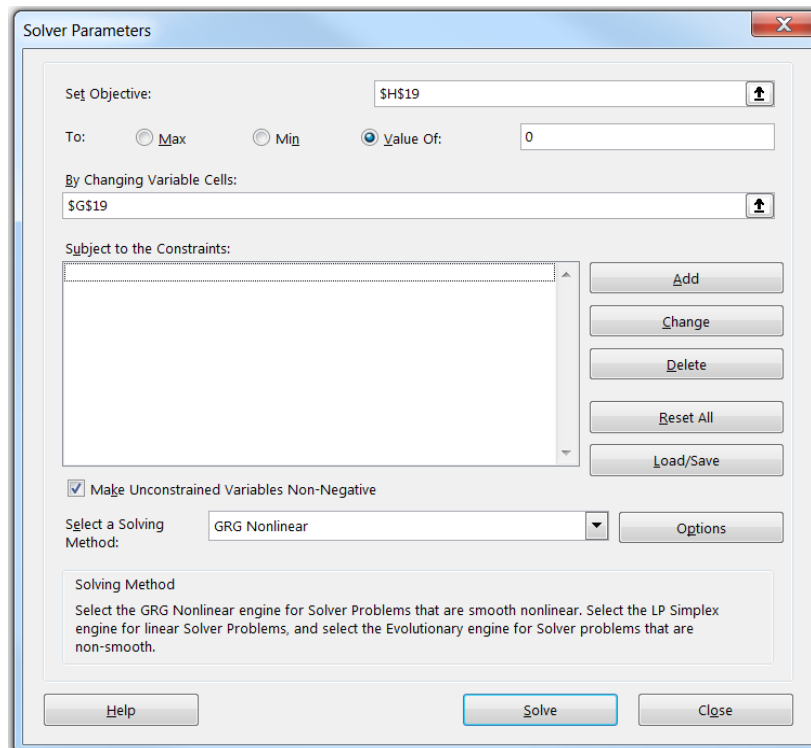


Figure B.2 Microsoft Solver screen for estimating inflection point of the SWCC

Upon clicking the “Solve” button, the Solver will change matric suction (cell G19) till the value of cell H19 approaches 0. Figure B.3 illustrates the optimized value of matric suction, which indeed represent the inflection point of the SWCC.

Finding Inflection Point							
A = (se <sup>ψ</sup> /ω) <sup>n</sup>	B = (A+1) <sup>-m</sup>	C = m <sup>2</sup> n <sup>2</sup> A <sup>2</sup>	D = mn <sup>2</sup> A	E = A <sup>2</sup> +2A+1	s (kPa)	d <sup>2</sup> Se/dlogs <sup>2</sup>	
5.03	0.70	1.73	1.73	36.31	682.87	0.00000	

Value of this cell is now equivalent to the root of second derivation of Gallipoli equation and represents matric suction at inflection point.

Figure B.3 Estimated matric suction at the inflection point

- **Step 2.** Determine the exact value of air entry point of the original SWCC using the inflection point and a line tangent to the SWCC at inflection point.
- **Step 2A.** The first derivation of the SWCC equation gives slope of any line tangent to the curve. Thus, impose the first derivation on the Gallipoli et al. (2003b) equation.
- **Step 2B.** Calculate the slope of the line tangent to the SWCC at inflection point by inputting the matric suction corresponding to the inflection point inside the first derivation of the Gallipoli et al. (2003b) equation (Figure B.4).

$S_e = \left[ 1 + \left( \frac{s(e^\psi)}{\omega} \right)^n \right]^{-m}$					e	ψ	ω	n	m
					0.60	6.66	6.65	1.31	0.20
$\frac{dS_e}{d(\log s)} = -\ln(10) \cdot m \cdot n \cdot \left( \frac{s \cdot e^\psi}{\omega} \right)^n \cdot \left[ \left( \frac{s \cdot e^\psi}{\omega} \right)^n + 1 \right]^{-m-1}$									
Finding Slope of Line Tangent to the SWCC at Inflection Point									
S <sub>inflection</sub> (kPa)	A = -ln(10)mn	B = (se <sup>ψ</sup> /ω) <sup>n</sup>	C = (B+1) <sup>-m-1</sup>	dSe/dlogs (1/kPa)					
682.87	-0.60	5.03	0.12	-0.35					

Figure B.4 Calculate slope of the line tangent to the SWCC at the inflection point

Codes used for calculating different components of the first derivation of the Gallipoli et al. (2003b) equation (see Figure B.4):

- Cell C17 is coded as:  
=(-LN(10))\*I4\*H4
- Cell D17 is coded as:  
=((B17\*(E4^F4))/G4)^H4

- Cell E17 is coded as:  

$$=(D17+1)^{(-I4-1)}$$
- Cell F17 (the slope of the tangent line) is coded as:  

$$=C17*D17*E17$$
- **Step 2C.** Calculate matric suction corresponding to the air entry point. If the tangent line is extended towards the maximum effective degree of saturation, ( $S_e = 1.0$ ), and if it is assumed that a horizontal line can be drawn from the maximum effective degree of saturation, the tangent line and horizontal line intersects at a point corresponding to the matric suction at air entry point. In essence, the slope of tangent line between inflection point and air entry point equals to the ratio of differential effective degree of saturation to differential matric suction. Thus, matric suction at air entry point can be obtained from slope of tangent line at inflection point, maximum effective degree of saturation and effective degree of saturation at inflection point. The estimated matric suction is then used along with the Gallipoli et al. (2003b) equation to calculate effective degree of saturation at the air entry point. Figure B.5 illustrates Excel spreadsheet used for determining the air entry point of the original SWCC.

	A	B	C	D	E	F	G	H
19								
20		e	$\Psi$	$\omega$	n	m		
21		0.60	6.66	6.65	1.31	0.20		
22								
23								
24		$S_e = \left[ 1 + \left( \frac{s(e)^\psi}{\omega} \right)^n \right]^{-m}$			$\log s_{aev} = \log s_{inf} + \frac{1 - S_{e_{inf}}}{Slope_{ti}}$			
25								
26								
27								
28								
29								
30					Intersection Point		Air Entry Point	
31		$S_{inflection}$ (kPa)	$S_{e_{inflection}}$	dSe/dlogs (1/kPa)	log s (kPa)	s (kPa)	s (kPa)	$S_{e_{projected}}$
32		682.87	0.70	-0.35	1.98	95.15	95.15	0.94

Figure B.5 Estimate matric suction corresponding to the air entry point

Codes used for estimating air entry point of original SWCC (see Figure B.5):

- Cell C32 is coded as:  

$$=(1+(((B32*(B21^C21))/D21)^E21))^{(-F21)}$$
- Cell E32 is coded as:  

$$=(\text{LOG}(B32))+((1-C32)/D32)$$
- Cell F32 is coded as:  

$$=10^E32$$

- Cell G32 is coded as:  
=F32
  - Cell H32 is coded as:  
=(1+(((G32\*(B21^C21))/D21)^E21))^(F21)
- **Step 3.** As discussed along with the Chapter 2, the air entry point is always at the left side of the inflection point and the purpose of the SWCC modification is to shift the curve towards the left. Thus, shifting process can be implemented using air entry point of the original SWCC and second derivation of the Gallipoli et al. (2003b) equation, which indeed governs inflection point of the SWCC. Figure B.6 shows general layout created for shifting the SWCC.

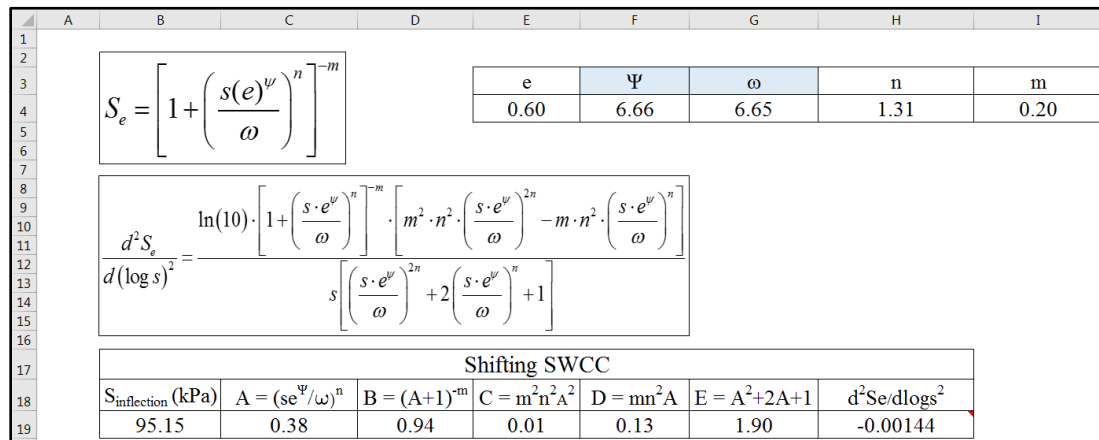


Figure B.6 General spreadsheet used for shifting the original SWCC

- **Step 3A.** Set the inflection point of the shifted SWCC equal to the air entry point of the original SWCC while leaving  $\psi$ ,  $\omega$ ,  $n$  and  $m$  unchanged. Calculate the second derivation of the Gallipoli et al. (2003b) equation at new inflection point. Codes used for computations are as same as those applied over the “Step 1C”. Upon calculations, the second derivation numerically converges to a non-zero value (Figure B.6), however it must become zero at the inflection point.
- **Step 3B.** It should be noted that the modified SWCC is shifted version of the original SWCC, therefore both curves must be parallel and have the same curvature but different air entry point. Regarding correlation between different parts of the SWCC and fitting parameters of the Gallipoli et al. (2003b) equation, the air entry point of the SWCC is addressed by  $\psi$  and  $\omega$ . Thus, apply Solver and change  $\psi$  and  $\omega$  so that the value of second derivation of the Gallipoli et al. (2003b) equation converts to the zero.

In Solver Parameter window, cell H19 is selected as the Objective Cell, the optimization criterion is set to the Value Of 0 and cells F4 and G4 are selected as the Variable Cells. Having the second derivation equal to zero, optimized values for  $\psi$  and  $\omega$  are obtained, as shown on Figure B.7.

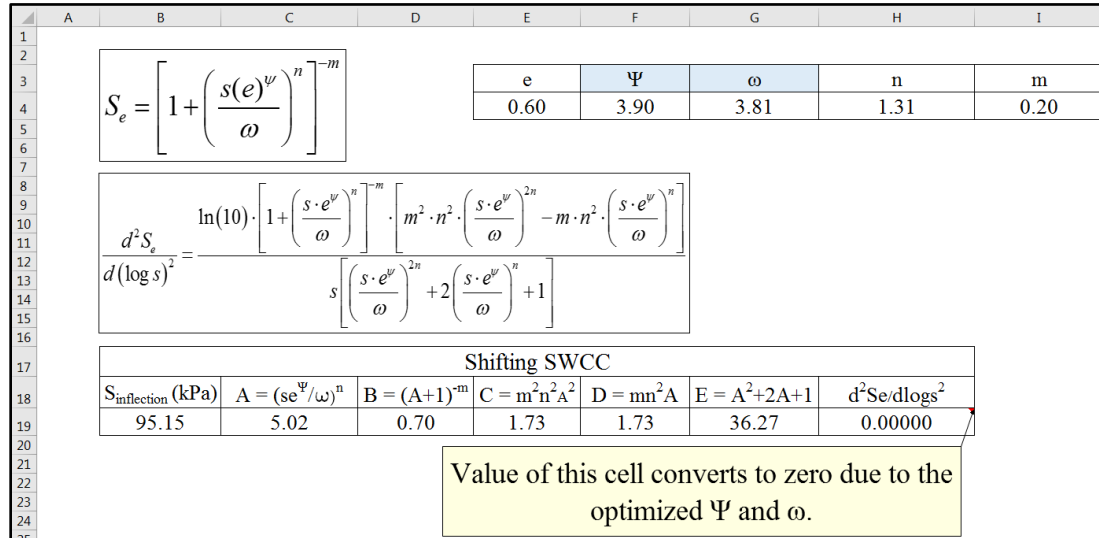


Figure B.7 Optimized parameters for the shifted SWCC

➤ **Step 3C.** Utilize values obtained for parameters  $e$ ,  $\psi$ ,  $\omega$ ,  $n$  and  $m$  along with arbitrary values of matric suction to generate the shifted SWCC. Figure B.8 illustrates the original and the modified/shifted SWCCs for the soils used in this study.

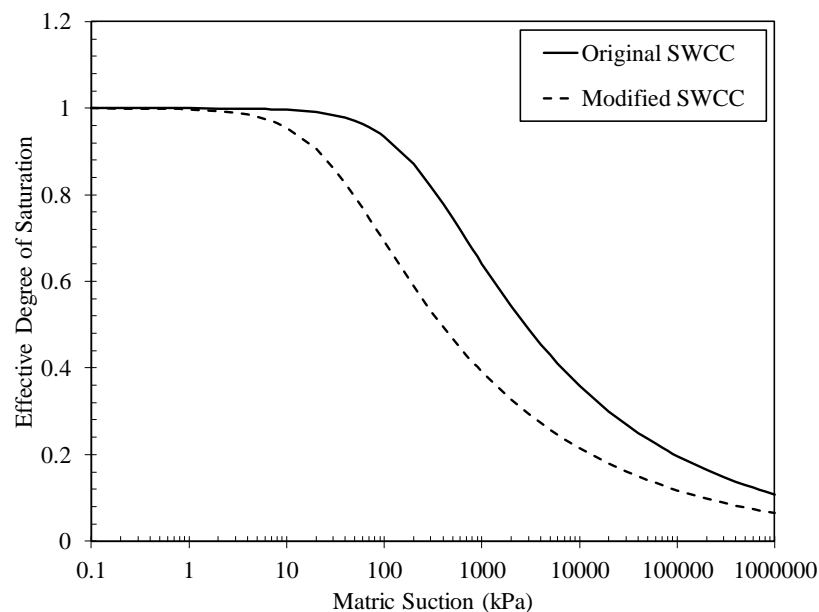


Figure B.8 Original and Modified SWCCs

APPENDIX C SWCCS OF THE LITERATURE SOILS USED FOR VALIDATING  
THE SMALL-STRAIN SHEAR MODULUS MODEL

APPENDIX C.1 ORIGINAL SWCCS

**Original SWCCs for the Soils Tested under a Single Net Normal Stress and over a Range of Suction**

Laboratory and modeled SWCC data for the literature soils tested under only one net normal stress are presented on Figures C.1 and C.2, in which the SWCC data are plotted in terms of the effective degree of saturation and volumetric water content, respectively. The soil samples are referred to as Concrete Sand, SG-1, DI TH23 Slopes Fat Clay, Anaheim Clayey Sand, Mnroad Lean Clay-1, Red Wing Silt, Red Lake Falls Lean Clay-2, and Denver Bentonite that are respectively labeled as the Concrete Sand, SG-1, DI TH23 Slopes, Anaheim, Mnroad, Red Wing, Red Lake Falls, and Denver Bentonite.

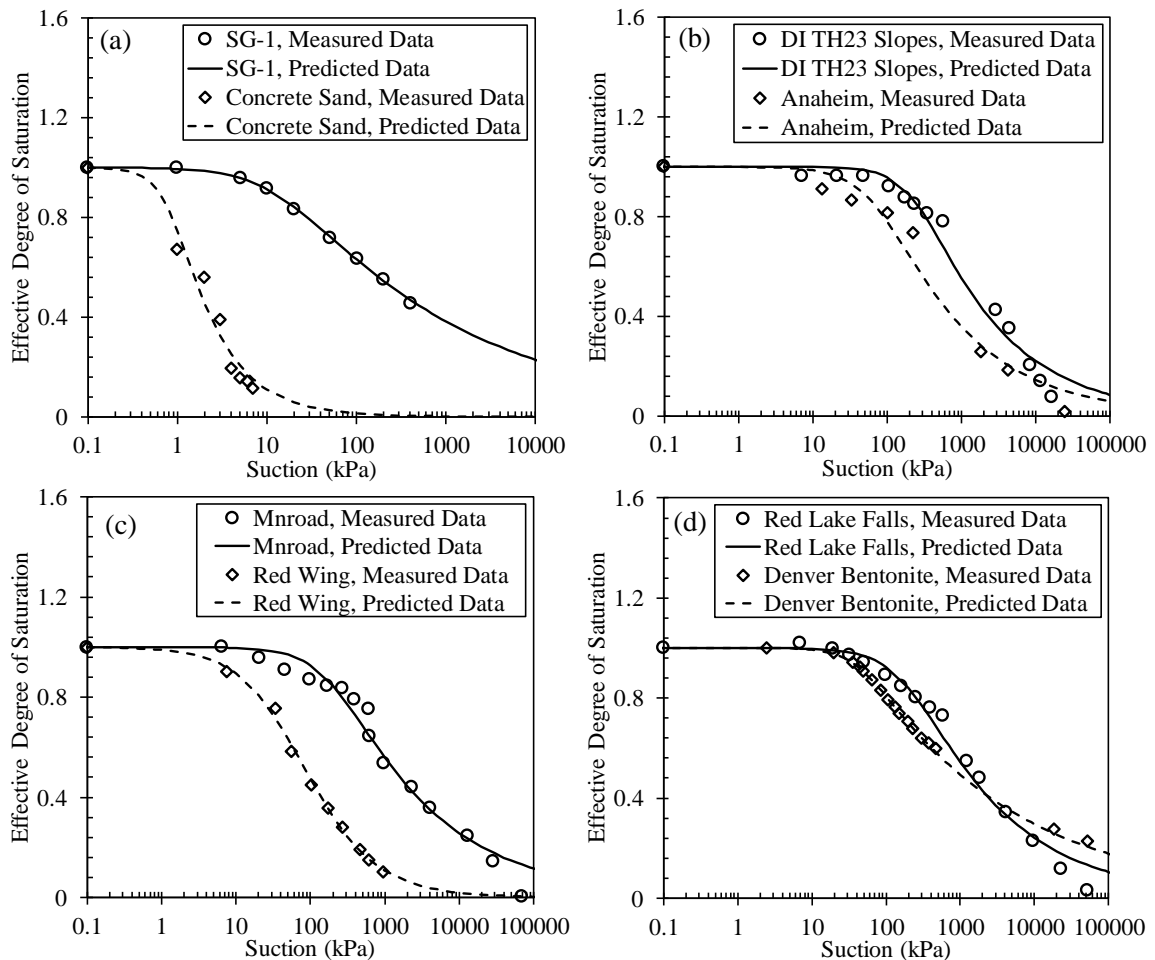


Figure C.1 Laboratory and modeled SWCC data in terms of the effective degree of saturation for the literature soils subjected to the constant net normal stress (a) SG-1 and Concrete Sand; (b) DI TH23 Slopes and Anaheim; (c) Mnroad and Red Wing; (d) Red Lake Falls and Denver Bentonite



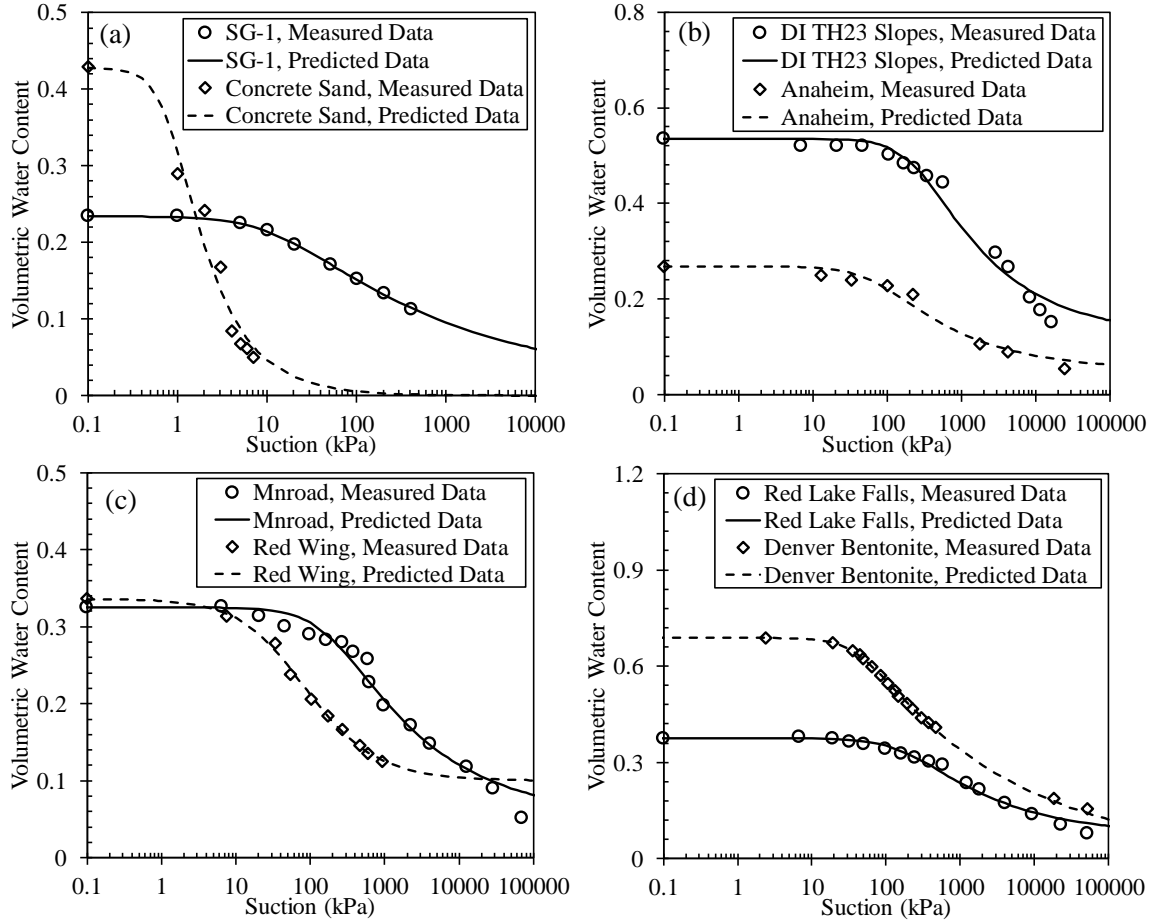


Figure C.2 Laboratory and modeled SWCC data in terms of the volumetric water content for the literature soils subjected to the constant net normal stress (a) SG-1 and Concrete Sand; (b) DI TH23 Slopes and Anaheim; (c) Mnroad and Red Wing; (d) Red Lake Falls and Denver Bentonite

The experimental soil water characteristic data were fitted to the van Genuchten (1980) equation, where the value of the residual volumetric water content was estimated using Fredlund and Xing (1994) model. This equation assumes that the driest state of the soil is at suction equal to  $10^6$  kPa. Fredlund and Xing (1994) model forces the SWCC through the volumetric water content equal to zero and allows estimation of residual volumetric water content by graphical method. The Fredlund and Xing (1994) equation is expressed as,

$$\theta = C(\psi) \frac{\theta_s}{\left\{ \ln \left[ e + (\psi/a)^n \right] \right\}^m} \quad (C.1)$$

where

$$C(\psi) = 1 - \frac{\ln(1 + \psi/\psi_r)}{\ln\left[1 + \left(10^6/\psi_r\right)\right]}$$

$\theta$  = volumetric water content;  $\theta_s$  = saturated volumetric water content;  $a$  = fitting parameter primarily related to the air-entry value;  $n$  = fitting parameter primarily related to transition zone;  $m$  = fitting parameter primarily related to residual water content;  $C(\psi)$  = correction factor related to suction corresponding to residual water content;  $\psi$  = matric suction; and  $\psi_r$  = residual matric suction. The SWCC data for Anaheim Clayey Sand was modeled by Fredlund and Xing (1994) equation as illustrated on Figure C.3. Subsequently, residual volumetric water content for this literature soil can be estimated based on the intersection of two tangent lines on the curve.

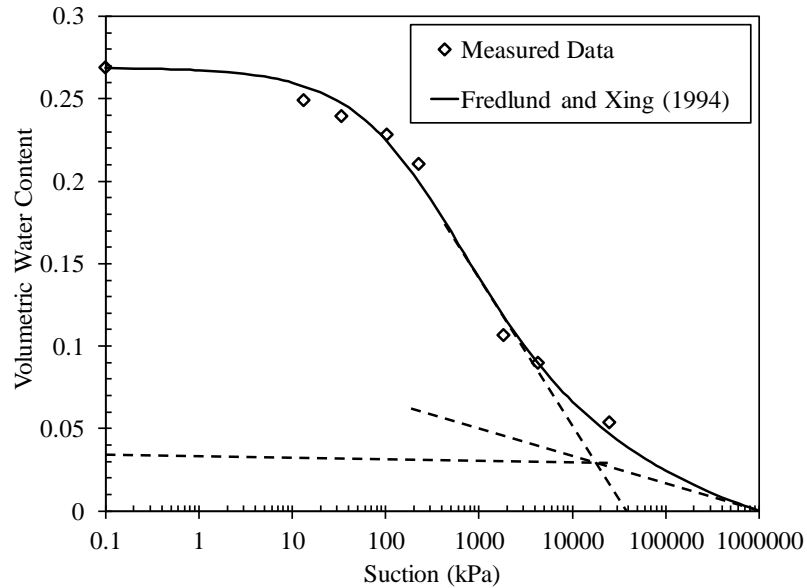


Figure C.3 SWCC modeled by Fredlund and Xing (1994) equation to estimate residual volumetric water content for the Anaheim Clayey Sand

***Original SWCCs for the Soils Tested over Various Net Normal Stresses and Suctions***

For literature soils experiencing various net normal stresses, laboratory and modeled SWCCs in terms of effective degree of saturation and volumetric water content are respectively illustrated on Figures C.4 and C.5. The literature soil samples laying into this category are identified as Rock Flour, Completely Decomposed Tuff and F-75 Silica Sand. It should be noted that the laboratory SWCC data for Rock Flour at net normal stress of 138 kPa was not available.

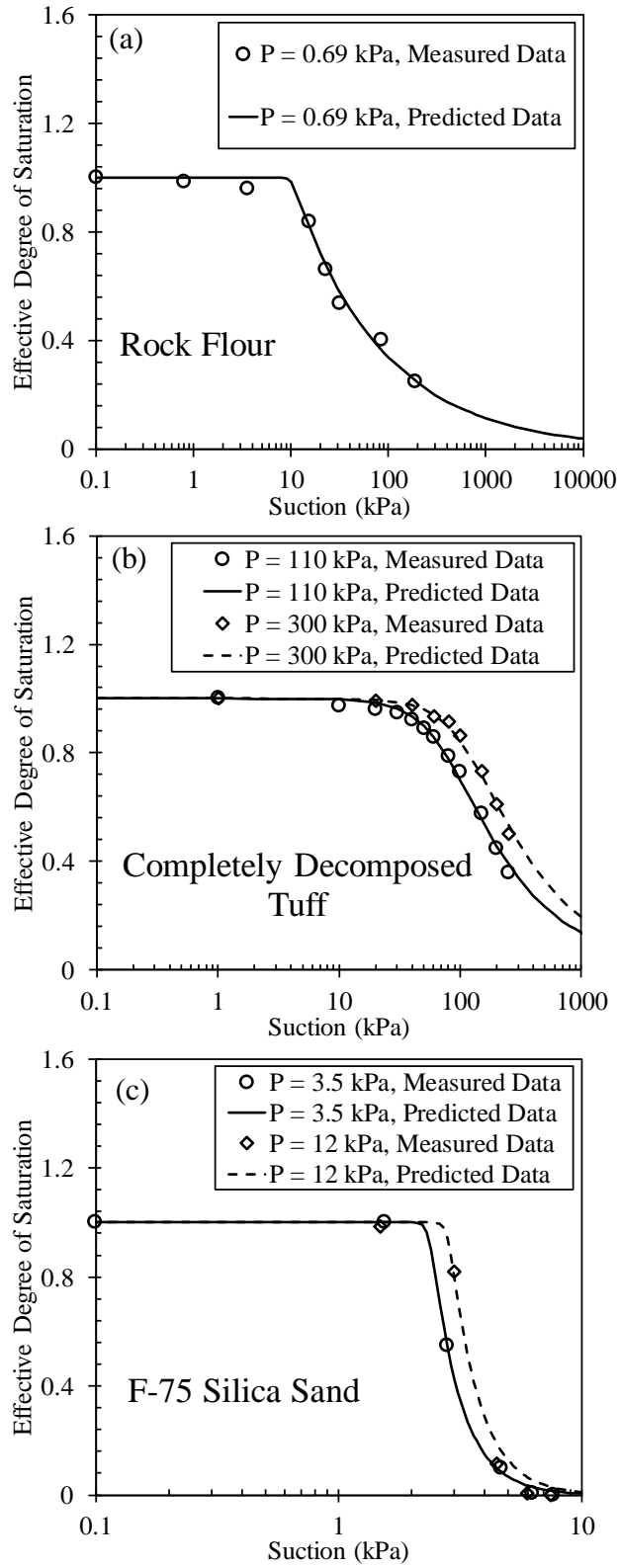


Figure C.4 Laboratory and modeled results associated with the original SWCC based on the effective degree of saturation (a) Rock Flour; (b) Completely Decomposed Tuff; (c) F-75 Silica Sand

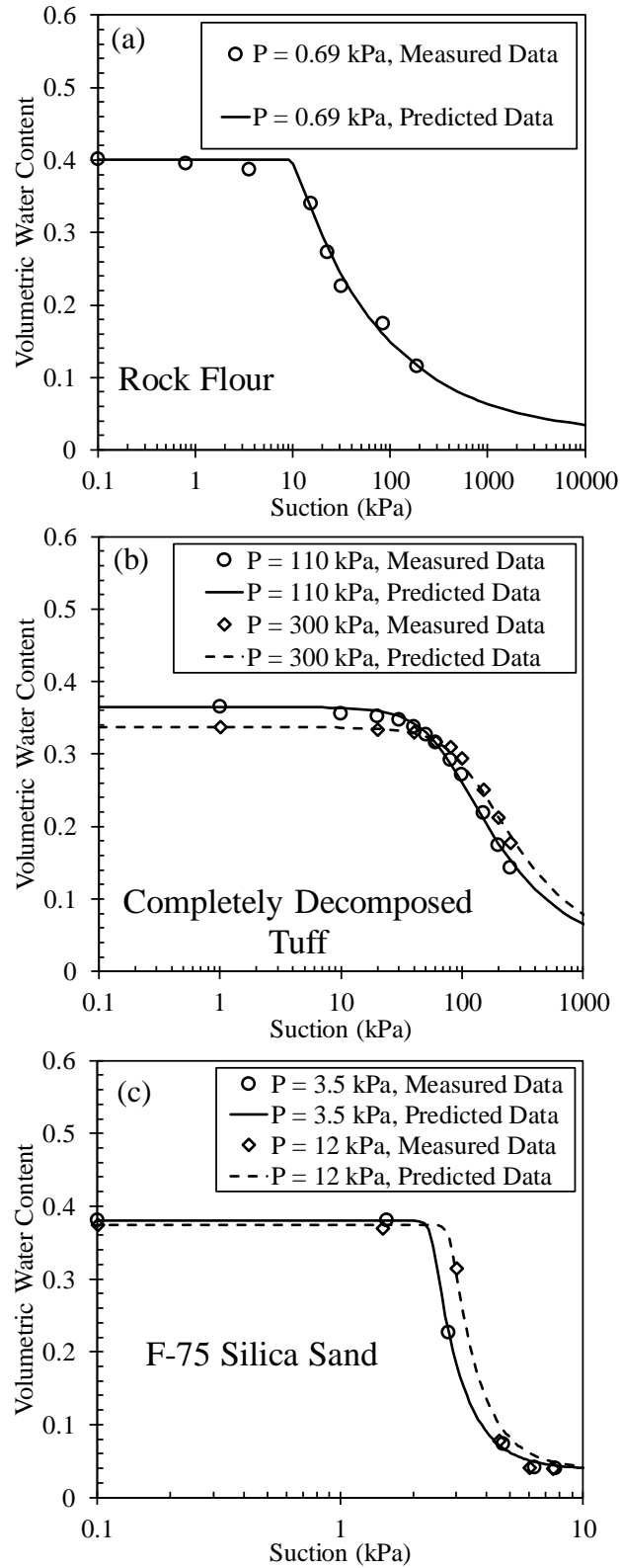


Figure C.5 Laboratory and modeled results associated with the original SWCC based on the volumetric water content (a) Rock Flour; (b) Completely Decomposed Tuff; (c) F-75 Silica Sand

**Original SWCCs for the Soils Tested under a Constant Suction and over a Range of Net Normal Stress**

The last category of case samples governs soils tested under a constant matric suction and varying net normal stresses. Literature soils belonging to this group are Ottawa Sand, Bonny Silt-1 and Bonny Silt-2. Laboratory and modeled SWCCs for these materials in terms of effective degree of saturation and volumetric water content have respectively been shown on Figures C.6 and C.7. Noted that no volumetric water content data was available for Bonny Silt-2.

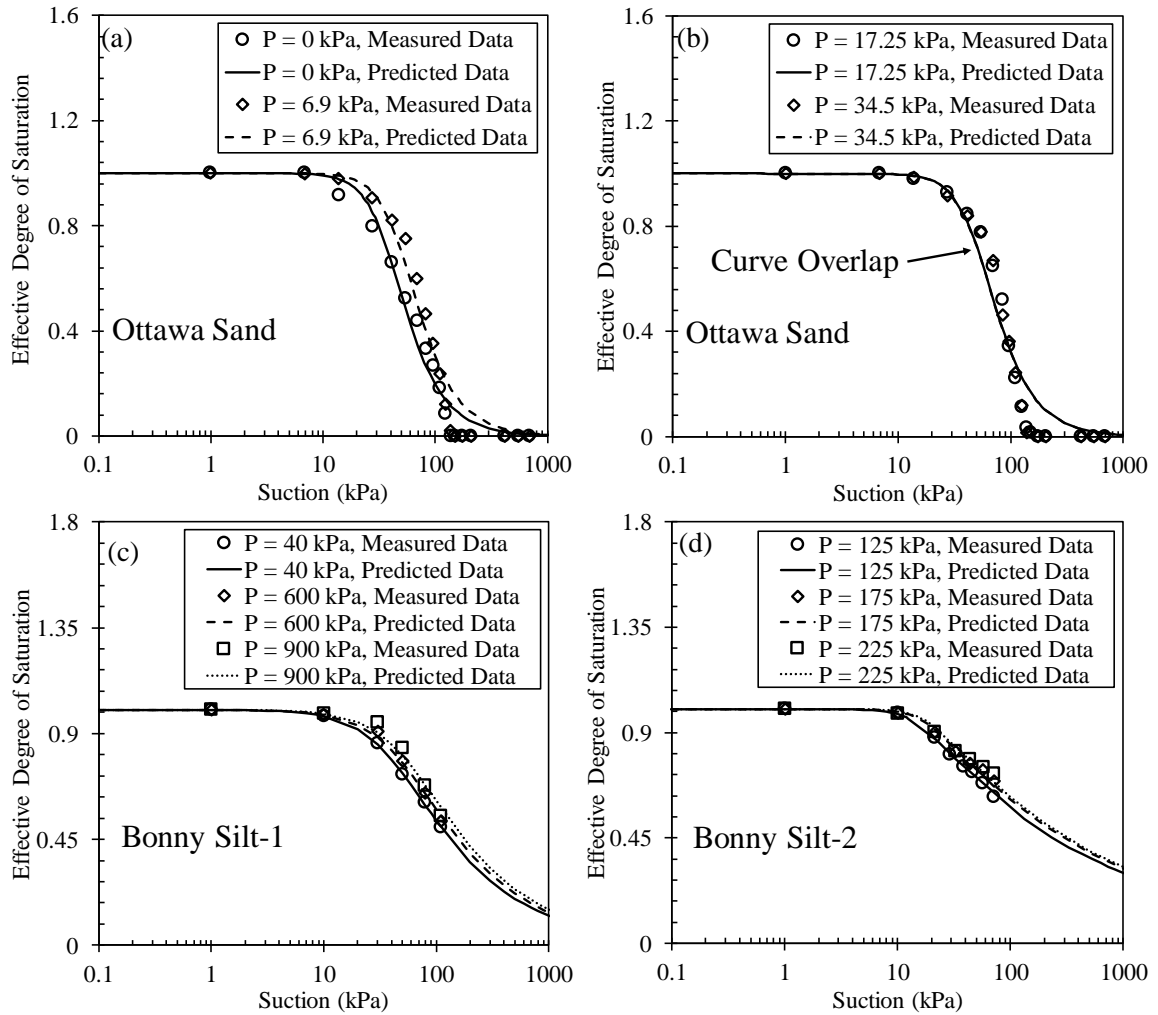


Figure C.6 Laboratory and modeled results associate with the original SWCC based on the effective degree of saturation (a) Ottawa Sand  $P = 0$  kPa and  $P = 6.9$  kPa; (b) Ottawa Sand  $P = 17.25$  kPa and  $P = 34.5$  kPa; (c) Bonny Silt-1; (d) Bonny Silt-2

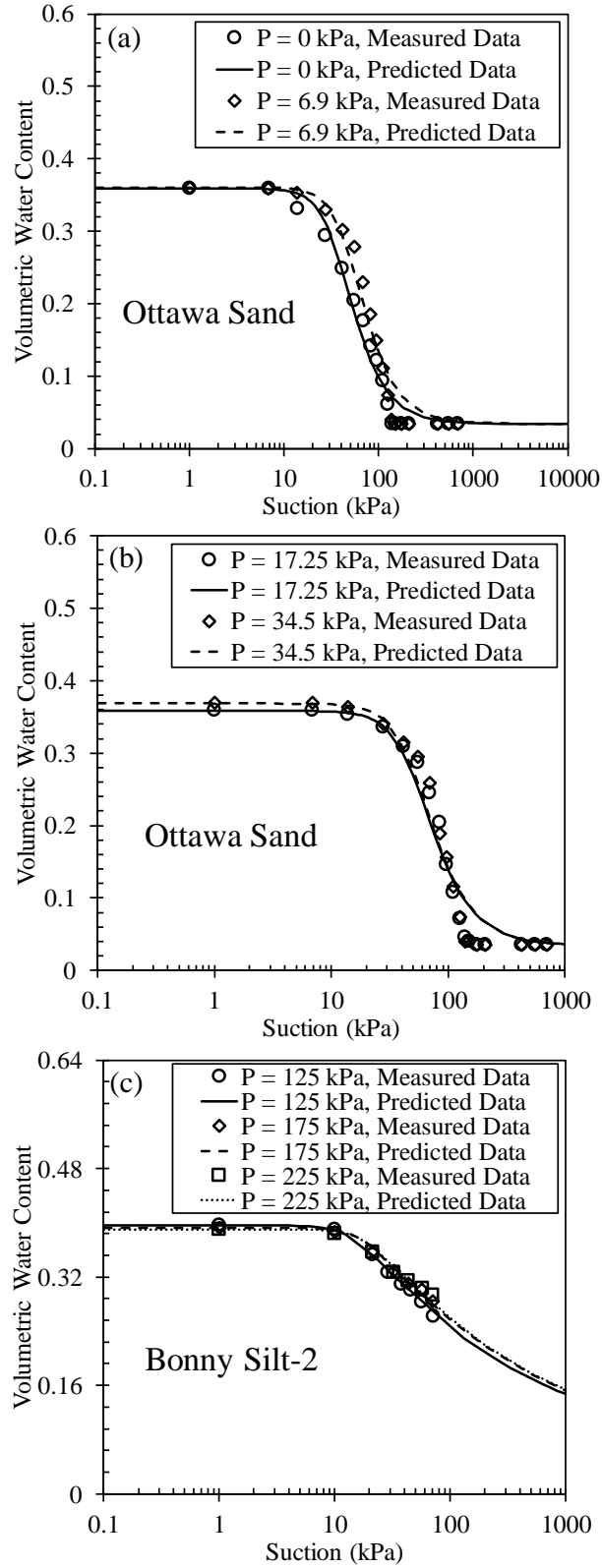


Figure C.7 Laboratory and modeled results associated with the original SWCC based on the volumetric water content (a) Ottawa Sand  $P = 0$  kPa and  $P = 6.9$  kPa; (b) Ottawa Sand  $P = 17.25$  kPa and  $P = 34.5$  kPa; (c) Bonny Silt-2

## APPENDIX C.2 MODIFIED SWCCS

### ***Modified SWCCs for the Soils Tested under a Single Net Normal Stress and over a Range of Suction***

The modified SWCCs in terms of effective degree of saturation and volumetric water content for Concrete Sand, SG-1, DI TH23 Slopes Fat Clay, Anaheim Clayey Sand, Mnroad Lean Clay-1, Red Wing Silt, Red Lake Falls Lean Clay-2, and Denver Bentonite are presented on Figures C.8 and C.9. To better understand the effect of SWCC modification on SWCC shift, the original SWCCs are also shown on the figure.

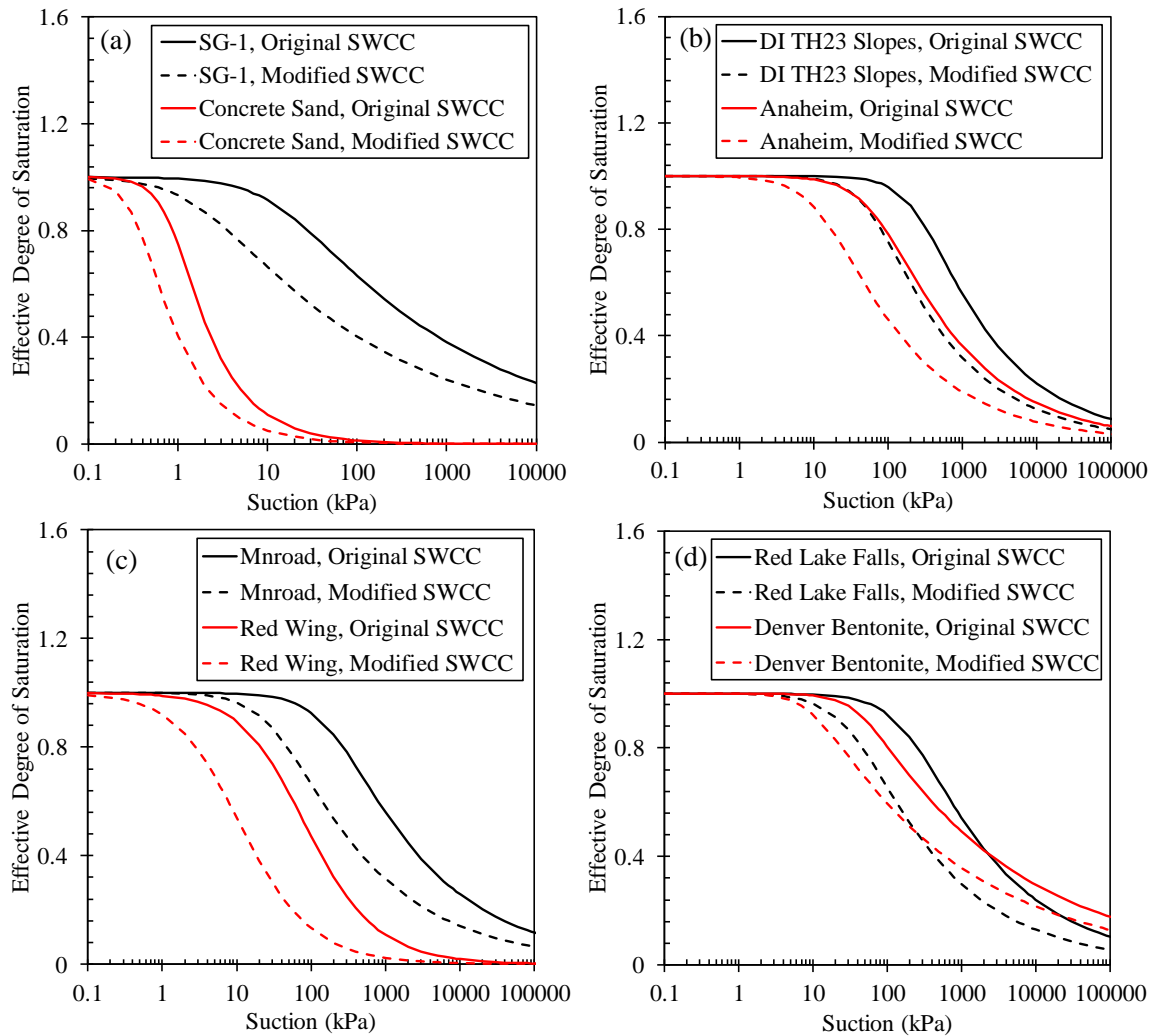


Figure C.8 Original and modified SWCC data in terms of the effective degree of saturation for the literature soils subjected to the constant net normal stress (a) SG-1 and Concrete Sand; (b) DI TH23 Slopes and Anaheim; (c) Mnroad and Red Wing; (d) Red Lake Falls and Denver Bentonite

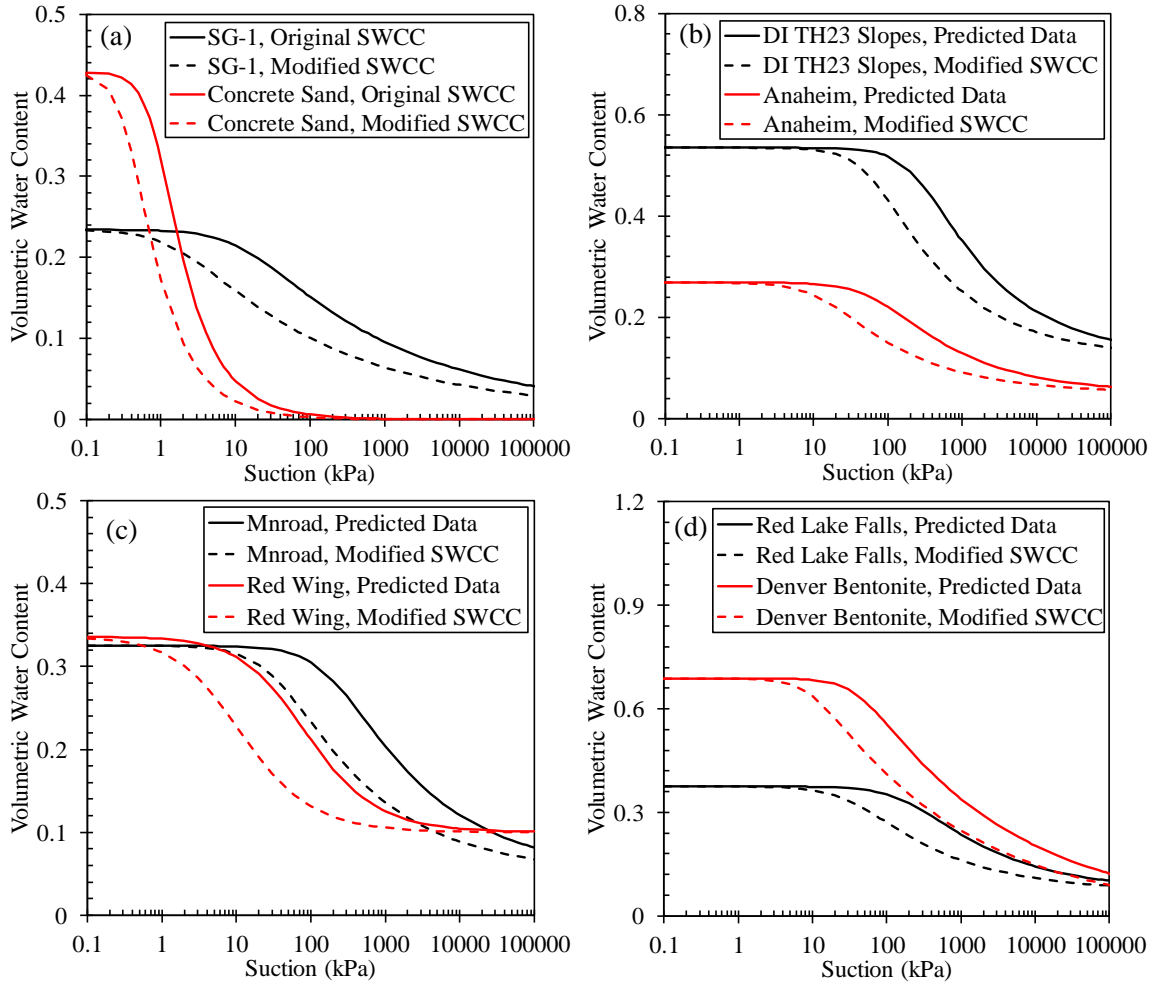


Figure C.9 Original and modified SWCCs in terms of the volumetric water content for the literature soils subjected to the constant net normal stress (a) SG-1 and Concrete Sand; (b) DI TH23 Slopes and Anaheim; (c) Mnroad and Red Wing; (d) Red Lake Falls and Denver Bentonite



*Modified SWCCs for the Soils Tested over Various Net Normal Stresses and Suctions*

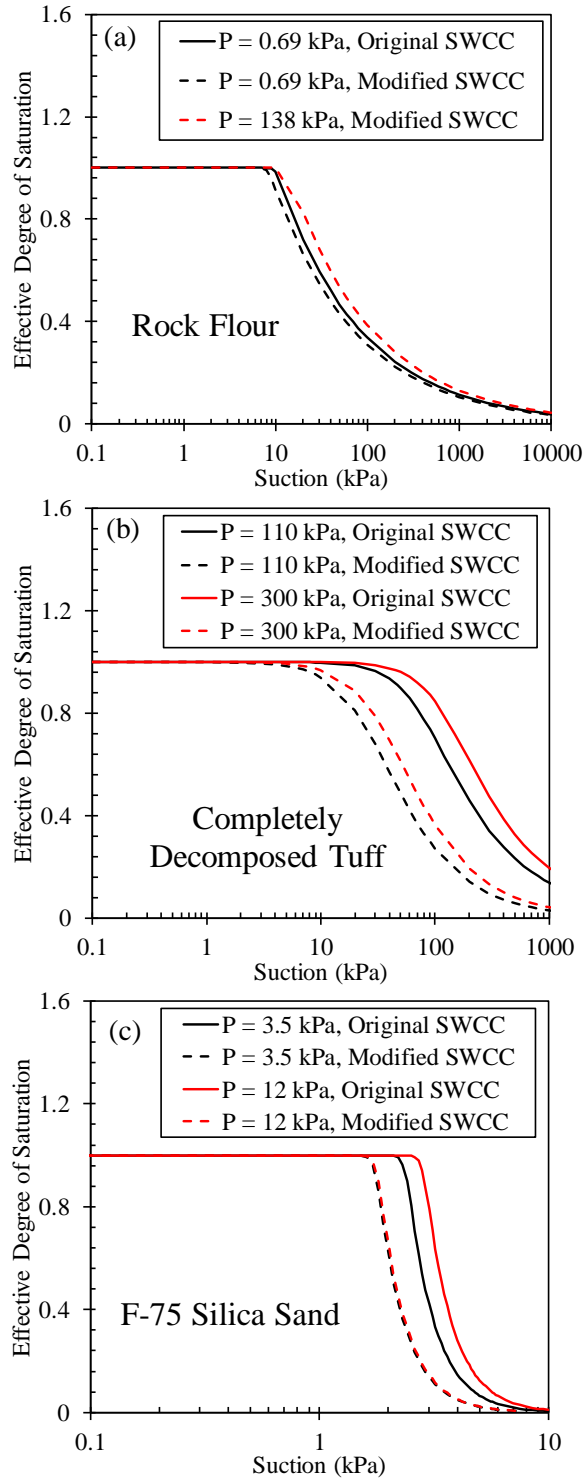


Figure C.10 Original and modified SWCC results based on the effective degree of saturation for soils tested over various net normal stresses and suctions (a) Rock Flour; (b) Completely Decomposed Tuff; (c) F-75 Silica Sand

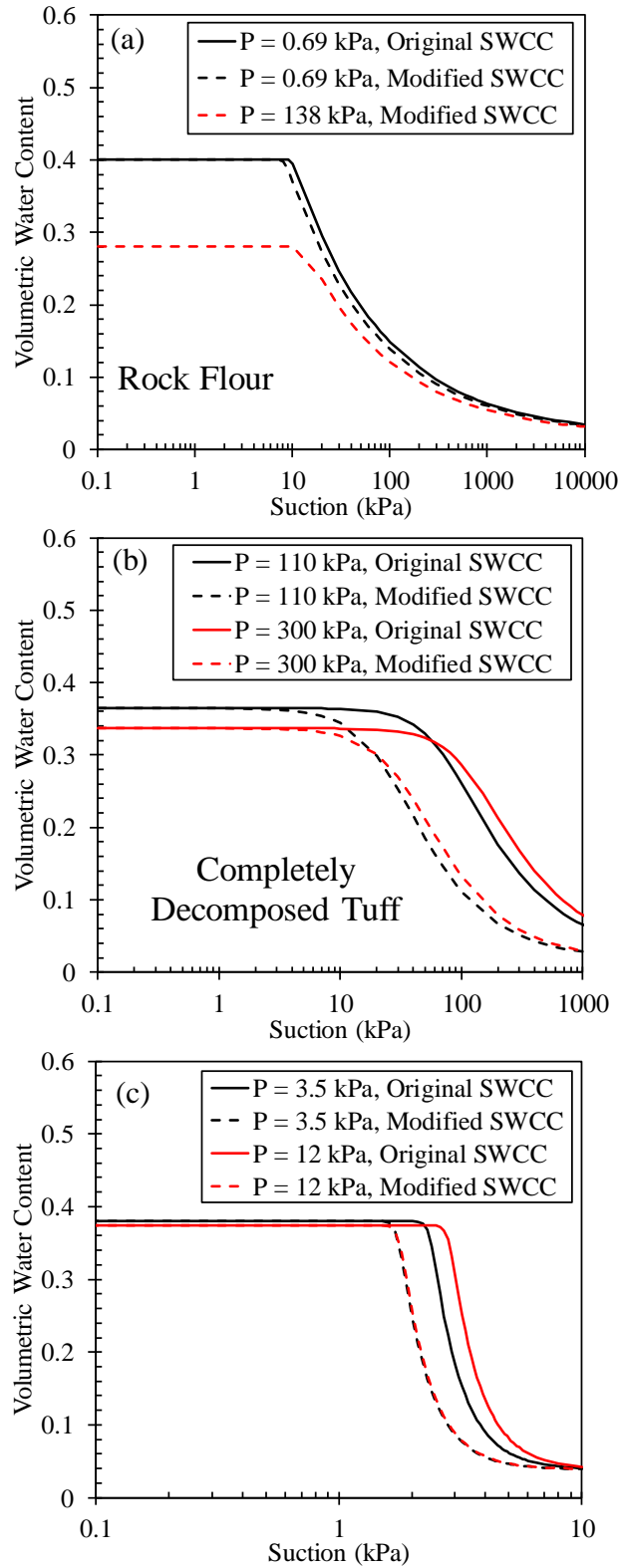


Figure C.11 Original and modified SWCC results based on the volumetric water content for soils tested over various net normal stresses and suctions (a) Rock Flour; (b) Completely Decomposed Tuff; (c) F-75 Silica Sand

**Modified SWCCs for the Soils Tested under a Constant Suction and over a Range of Net Normal Stress**

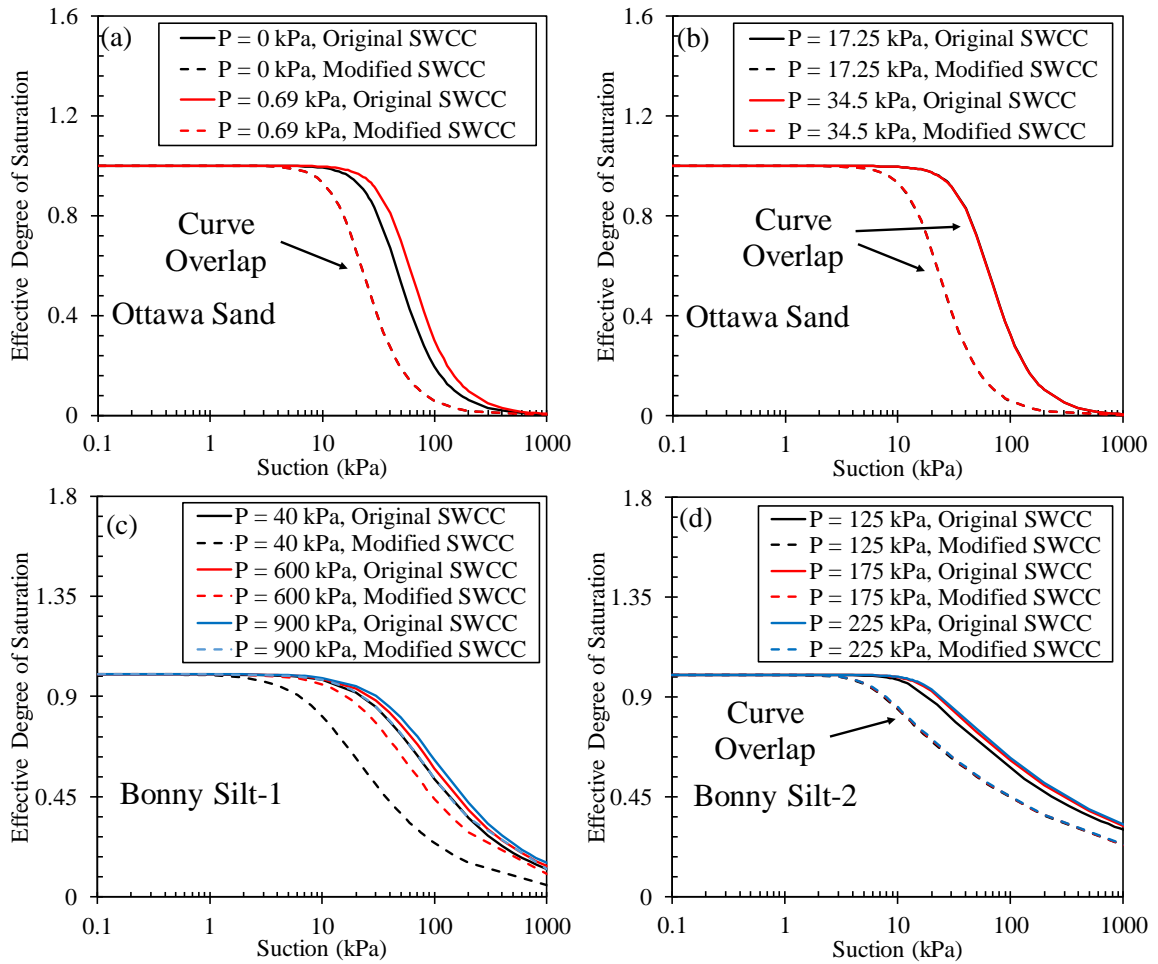


Figure C.12 Original and modified SWCC results based on the effective degree of saturation for soils tested under a constant suction (a) Ottawa Sand  $P = 0$  kPa and  $P = 6.9$  kPa; (b) Ottawa Sand  $P = 17.25$  kPa and  $P = 34.5$  kPa; (c) Bonny Silt-1; (d) Bonny Silt-2

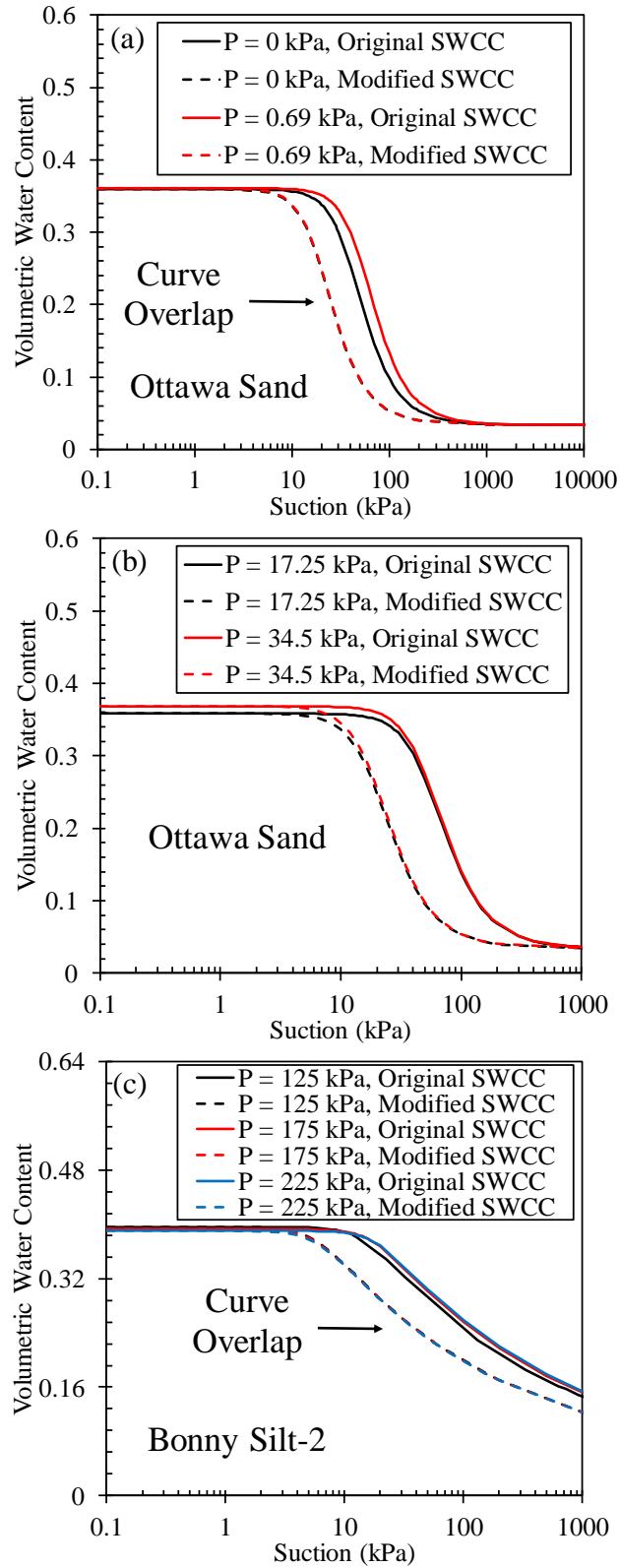


Figure C.13 Original and modified SWCC results based on the volumetric water content for soils tested under a constant suction (a) Ottawa Sand  $P = 0$  kPa and  $P = 6.9$  kPa; (b) Ottawa Sand  $P = 17.25$  kPa and  $P = 34.5$  kPa; (c) Bonny Silt-1; (d) Bonny Silt-2

APPENDIX D SWCCS OF THE LITERATURE SOILS USED FOR VALIDATING  
THE MODIFIED-SFG MODEL

### ***SWCC of the Literature Soil Used for Evaluating Hysteresis Equation of the Modified-SFG Model***

The hysteresis equation of the modified SFG model was confirmed using an expansive soil, which was composed of bentonite and kaolin. The original SWCC is sufficient for simulating hysteresis behavior of the bentonite-kaolin mixture.

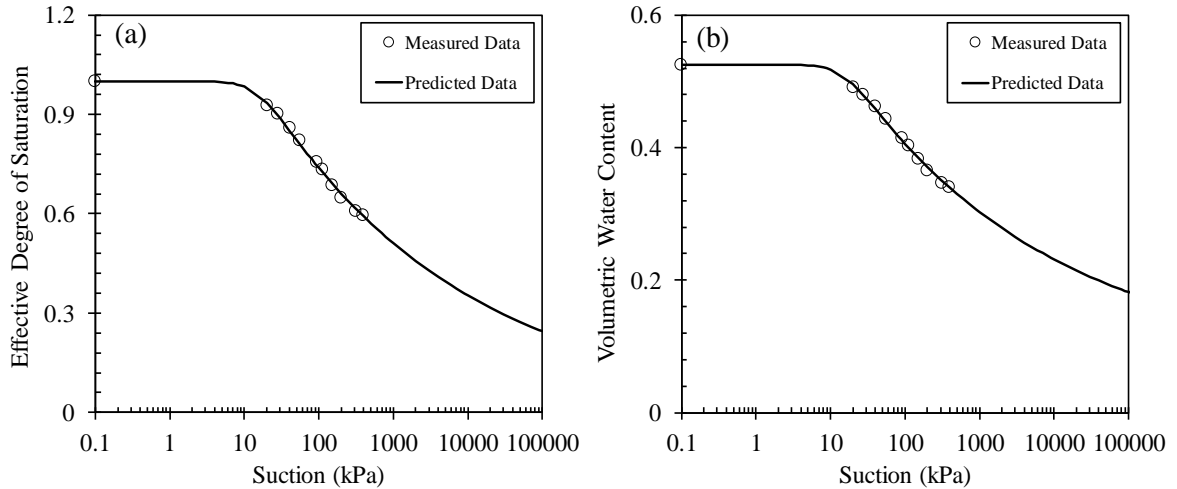


Figure D.1 Original SWCC of literature soil used for evaluating hysteresis equation of the modified-SFG model (a) Effective degree of saturation versus suction; (b) volumetric water content versus suction

### ***SWCC of the Literature Soils Used for Evaluating the modified-SFG Model over Sharing Phase***

Two literature soils, Pearl Clay and Speswhite Kaolin, were utilized in paper two for assessing applicability of the modified-SFG model over sharing phase. The hysteresis and elastic shear strain equations in the modified-SFG model respectively use the original and modified SWCC during simulation process. Thus, for the literature soils, both SWCCs are presented in this section. As a reminder, Pearl Clay soil was dried to suction of 150 kPa and consolidated to an isotopic load equal to 200 kPa, before being sheared. Thus, to estimate the small-strain shear modulus of the soil at the beginning of the shear phase, the modified SWCC derived from original drying SWCC is required. During shear stage, the hydraulic behavior of the soil follows the primary wetting scanning SWCC as the soil locates on the main drying SWCC at the beginning of the shear phase. Therefore, original and modified drying SWCCs and original primary wetting scanning SWCC must be available for simulating hydraulic-strain-stress behavior of the Pearl Clay along shearing

stage. The original and modified SWCCs of the Pearl Clay soil are illustrated on Figures D.2 and D.3, respectively.

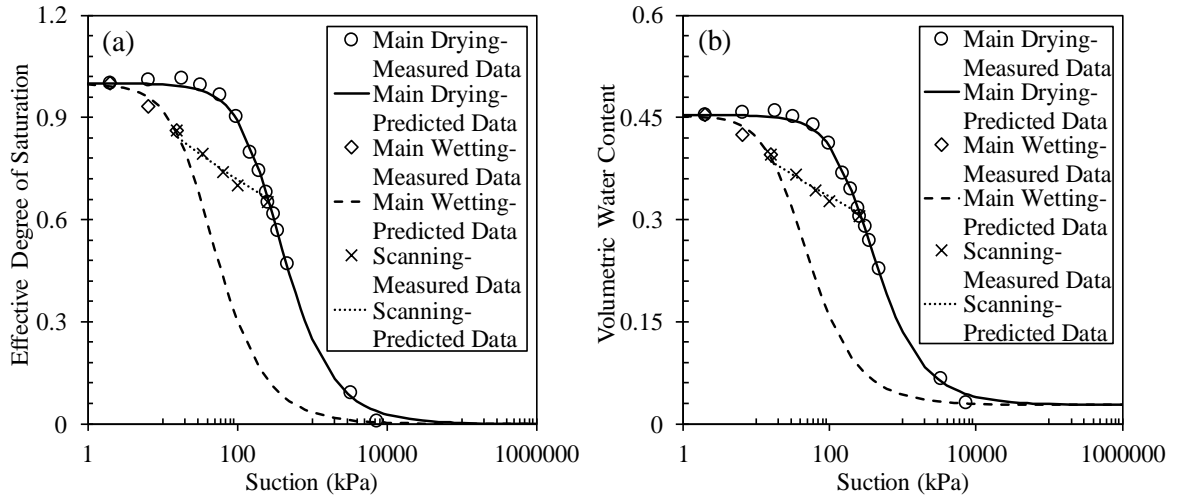


Figure D.2 Original SWCCs of the Pearl Clay soil in terms of main drying, main wetting and primary wetting scanning (a) Effective degree of saturation versus suction; (b) volumetric water content versus suction

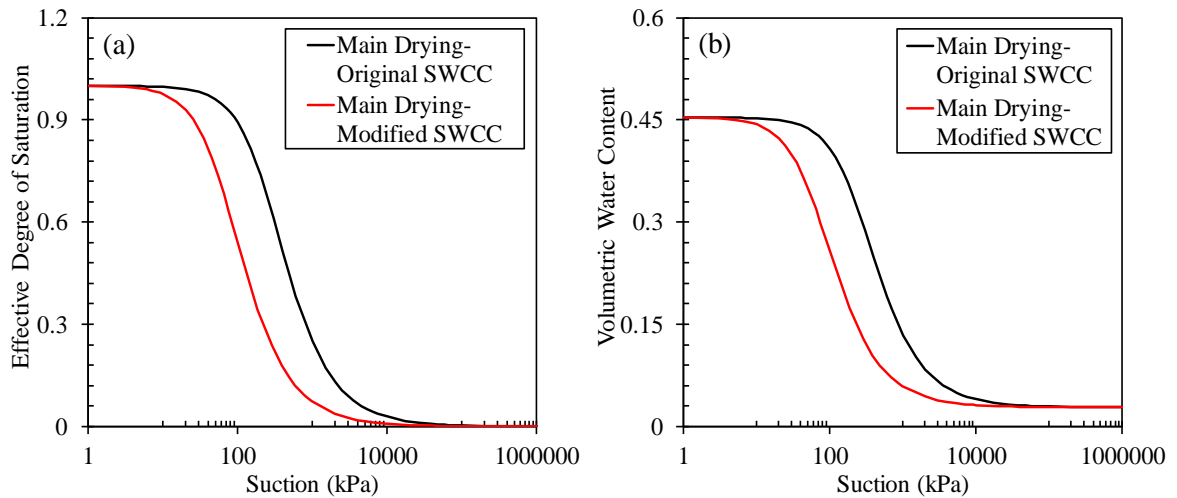


Figure D.3 Original and modified SWCCs of the Pearl Clay corresponding to main drying curve (a) Effective degree of saturation versus suction; (b) volumetric water content versus suction

In case of Speswhite Kaolin, compacted specimens are initially on unsaturated state. The soil samples are later subjected to a wetting process, which is followed by isotropic consolidation and shearing stages. Transition of the soil to wetter state occurs along main wetting SWCC. Thus, the small-strain shear modulus of the soil must be predicted by means of the modified SWCC originated from the original main wetting curve. Also, hydrologic features of the test specimens adopt main wetting curve at the

beginning of the shear stage. Therefore, hydraulic characteristics of the soil as a function of the shearing load changes based on the main wetting curve. In addition, the Speswhite Kaolin was tested under two different confining stresses,  $P$  equal to 100 and 150 kPa. Therefore, the original and modified main wetting SWCCs associated with each confining pressure are required for simulating hydro-mechanical behavior of the Speswhite Kaolin over shearing phase. Figures D.4 and D.5 show the original and modified SWCCs of the Pearl Clay soil in terms of effective degree of saturation and volumetric water content with respect to confining stress,  $P$ .

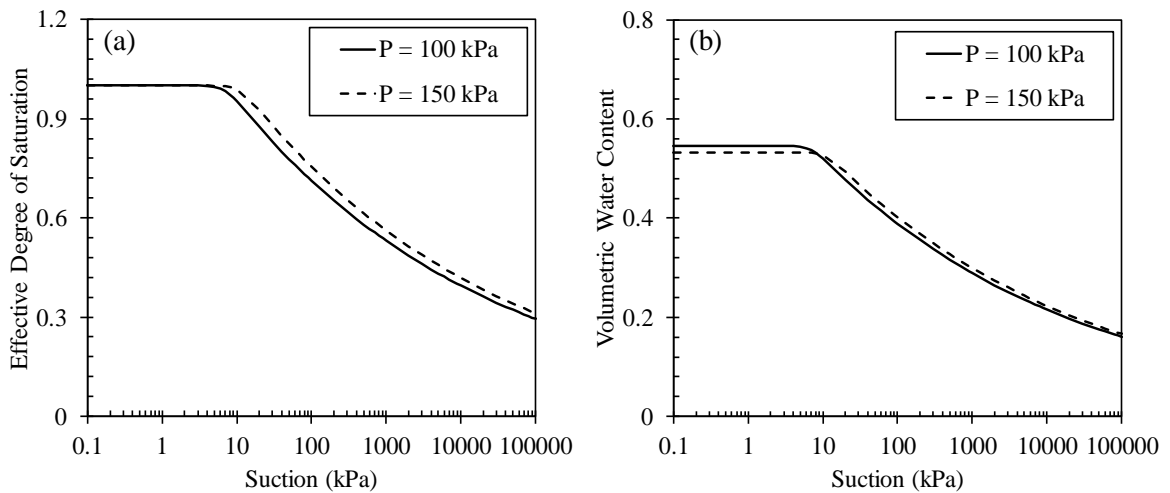


Figure D.4 Original SWCCs of the Speswhite Kaolin soil over various confining stresses (a) Effective degree of saturation versus suction; (b) volumetric water content versus suction

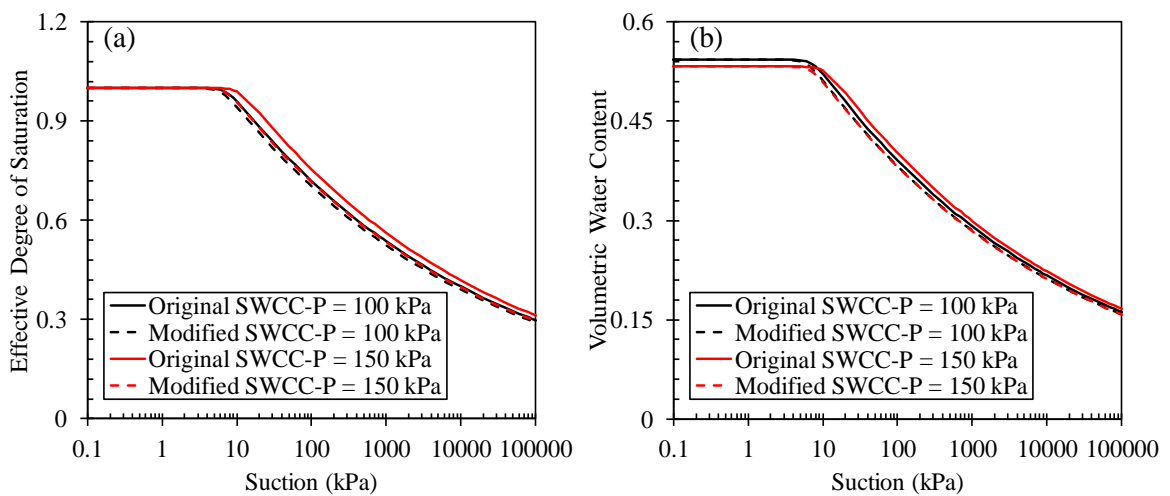


Figure D.5 Original and modified SWCCs of the Pearl Clay with respect to consolidation stresses (a) Effective degree of saturation versus suction; (b) volumetric water content versus suction



APPENDIX E SHEAR WAVE VELOCITY MEASUREMENT USING BENDER  
ELEMENT SYSTEM

The small-strain shear modulus is calculated based on the shear wave propagation velocity through the soils body and moist unit weight of the soil. Bender Element testing is one the most common methods for measuring shear wave velocity through the specimen. Testing procedure associated with the Bender Element is presented in this appendix.

### ***Fundamentals of Bender Element Testing***

The Bender Element system normally is comprised of two Bender Elements, a Master control box and a control and acquisition software. A Bender Element is composed of two thin piezoceramic plates cross-sectionally polarized and firmly bonded together. When a voltage signal is applied, the polarization of the ceramic material and the type of electrical connections permit the elongation of one plate and the shortening of the second plate. The result is a bending displacement which generates a perturbation with a strong shear wave content. This disturbance travels along the specimen such that a similar element at the other end of the specimen receives the mechanical perturbation and generates a voltage. The signal travels a distance between elements and the time difference between the emitted and received signals represents the time of the propagation of the signal (Camacho-Tauta et al., 2012).

The Bender Elements are directly connected to the Master control box, which is responsible for generating and recording the propagated wave. Several types of Master control boxes are available for Bender Element testing that each has different technical specifications, particularly in terms of resolution of data acquisition, sampling rate and data acquisition speed. Master control box manufactured by GDS Instruments is described herein as a typical example. This device provides 16 bit data resolution of the source and receiver signal with a maximum sampling rate of 200 kHz. Also, the maximum voltage acquisition speed achieved by this system is around 2 Mega samples/second.

The Master control box is connected to a computer that runs a control software, which allows for the selection of different source signal types and their control using input parameters for amplitude, period and repeat time. The software also allows for automatic or manual stacking of data to enhance the recorded signal (Walton-Macaulay, 2015). A schematic diagram of a typical Bender Element system is illustrated in Figure E.1.

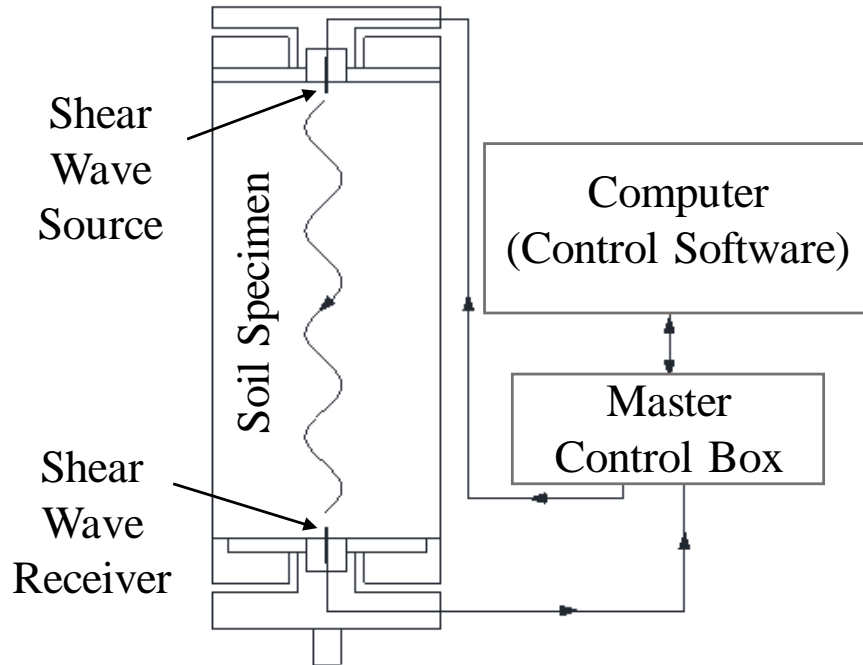


Figure E.1 Configuration of the Bender Element system

The exciting voltage is directly controlled by the software. The amplitude of the voltage is set on a value that causes no plate depolarization. The software also allows us to select waveform signal shapes. Normally, sinusoidal waveform is used for transmitting the shear waves. The shear wave travel time is commonly analyzed based on time and frequency domains. Methods included in time domain category are the Characteristic points (first deflection, first bump/trough, zero crossing, first peak), Cross-correlation and Second arrival. Cross-power spectrum calculation of signals is a method falling into the Frequency domain category (Yamashita et al., 2009). A serious variability is normally identified in travel time data estimated by frequency domain, that is not detected in data analyzed by time domain methods. Thus, time domain methods are more reliable for shear wave travel time calculation and are highly recommended (Yamashita et al., 2007). Figure E.2 shows time-domain characteristic points. Shear wave travel time can be estimated by the control software that can detect all characteristic points.

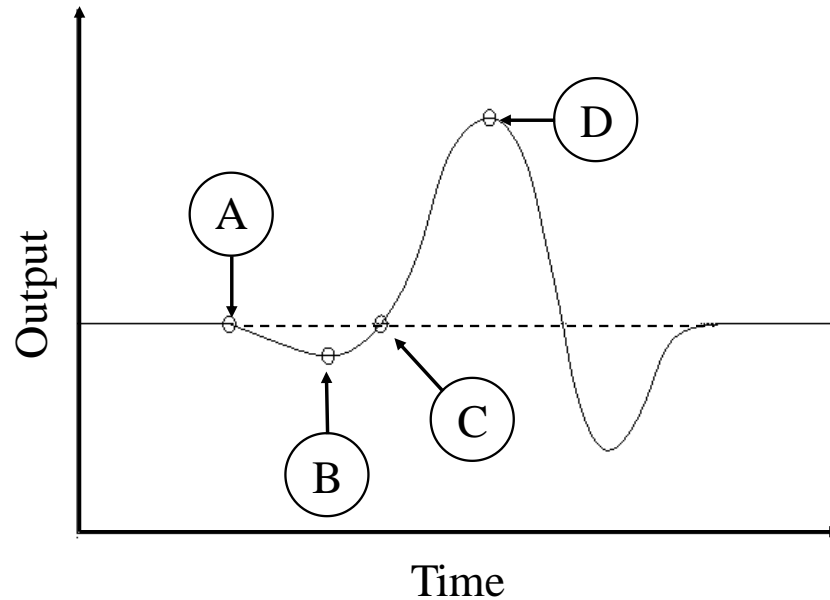


Figure E.2 Idealized received shear wave signal showing the characteristic points (A) first deflection; (B) first trough; (C) zero-crossing; and (D) first peak

Bender Elements are capable of being coupled with different laboratory testing apparatuses, e.g. unsaturated triaxial cell systems. This special feature provides a possibility of measuring the shear wave velocity of a given soil sample over various stress states and state conditions. A series of coupled Bender Element-unsaturated triaxial systems have been manufactured for measuring the shear wave velocity of the unsaturated soils. Along with this appendix, technical features of a coupled Bender Element-unsaturated triaxial device developed by the GDS Instruments is presented. Stress state and state condition of the tested soils are controlled by GDSLAB software, while Bender Element testing is performed by the GDSBES. One set of PC can be used to simultaneously run both GDSLAB and GDSBES.

### *Software Packages Used in Unsaturated Bender Element Testing*

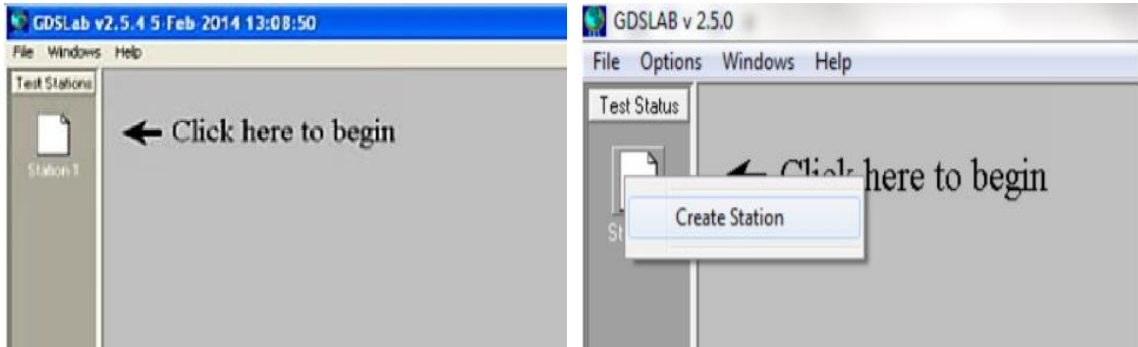
#### **Main Features of GDSLAB Software**

Matric suction regulation and isotropic consolidation are totally automatic processes implemented by use of GDSLAB software.

#### **How to define test steps in GDSLAB software**

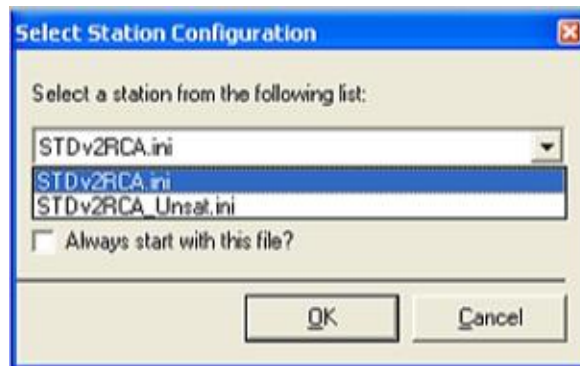
- **Step 1.** Run the software

Figure below shows a schematic of the first window that immediately opens after running the software. A new test is generated by clicking on the “Create Station” Icon. A new test is generated by clicking on the “Create Station” Icon.



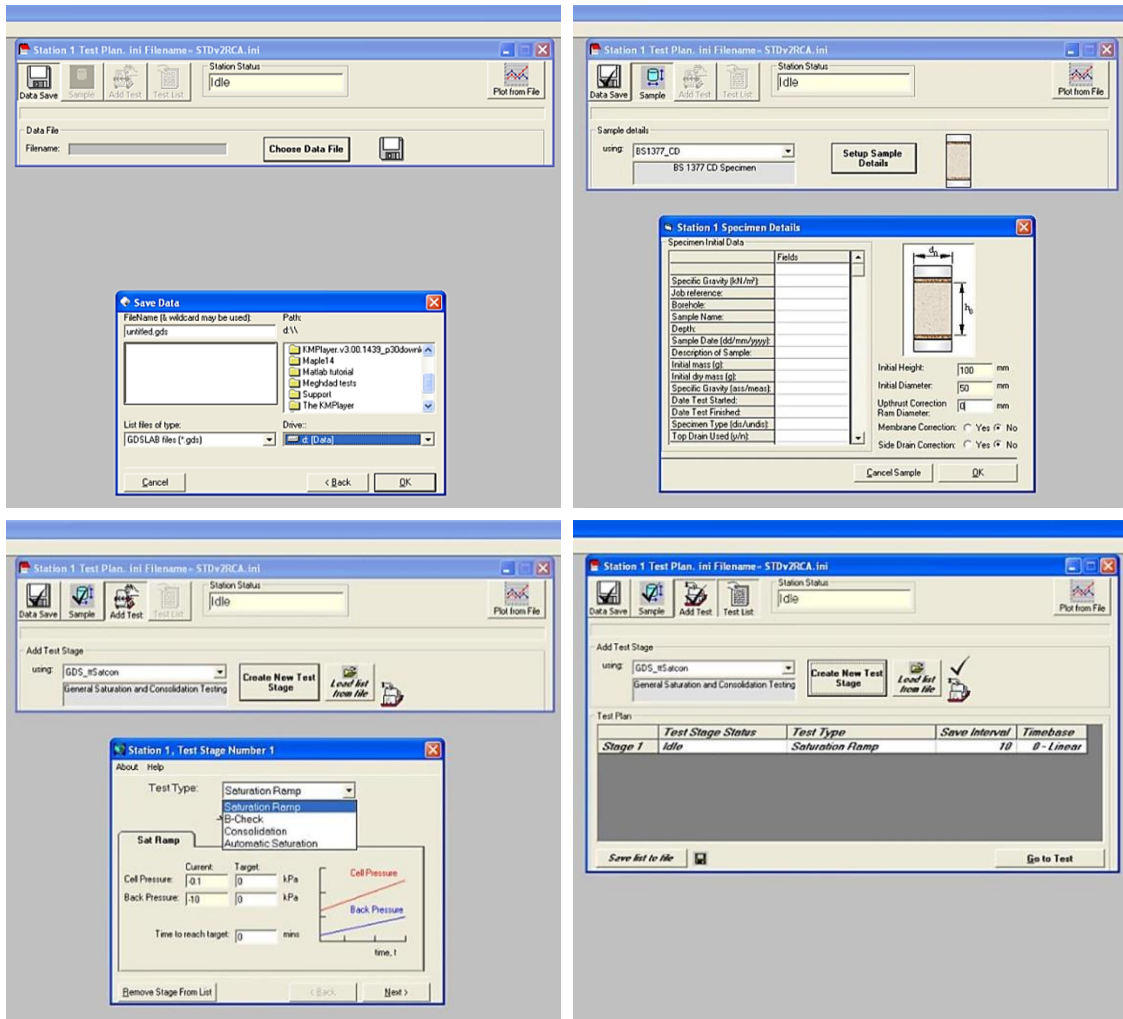
➤ **Step 2.** Select a testing module

Based on the type of the test to be conducted, the software offers two modules as “Sat.ini” for running experiment on the saturated soils and “Unsat.ini” for running test on unsaturated soils.

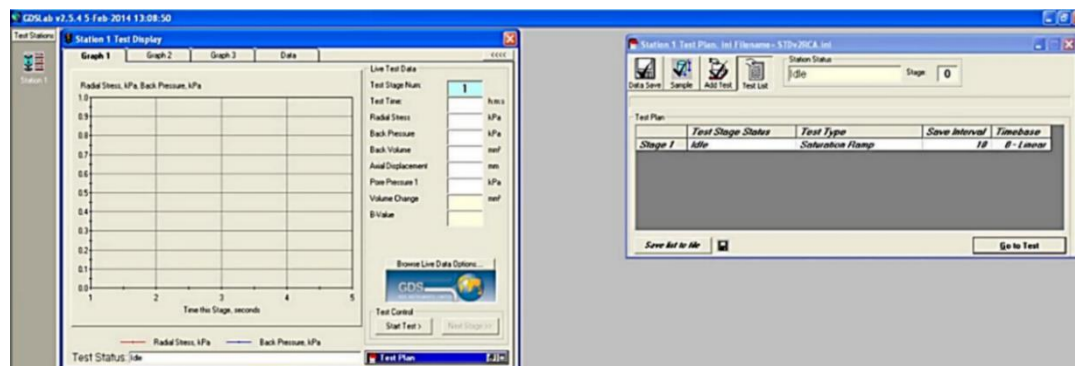


➤ **Step 3.** Define location of the stored data, properties of the specimen and different stages of a test

Upon selecting the desired module, a new window is opened that includes four icons. The first icon, “Data Save” is used to determine the location (filename) and rate of storing data for a specific test. Clicking on “Sample” icon directs user to a table, in which various properties of the specimen including height, diameter, specific gravity of solids and initial dry mass can be inputted. Different individual stages of a test are defined in the “Add Test” section. The last icon, “Test List”, shows all defined stages based on the sequence of implementation along the experiment.



By clicking “Go to Test” button, software directs the user to “Test Display” window that shows the various state and stress parameters (e.g. matric suction and net normal stress) with respect to time.

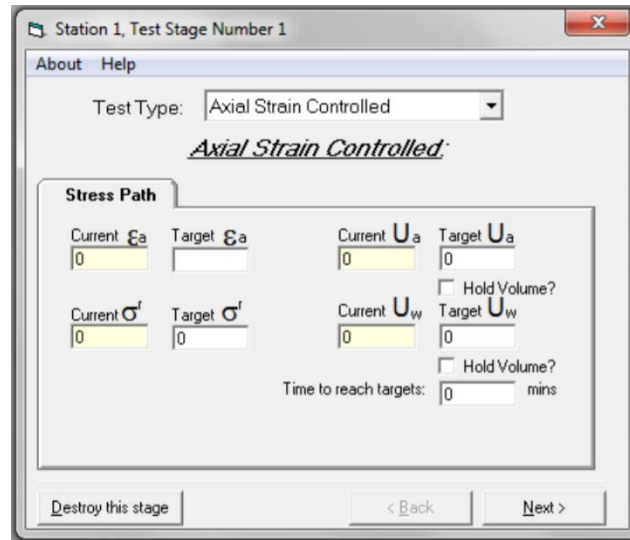


Under the third icon (“Add Test”), several types of modulus have been presented for conducting experiments under various conditions, e.g. triaxial saturated and unsaturated tests under isotropic confining stress. Testing

modules include UNSAT, Advanced Loading, Dynamic Loading, Kzero, Satcon, Standard Triaxial, StressPaths and Triaxial Acquisition. Upon selecting a specific module and clicking on “Create New Test Stage” icon, different test types related to the selected module are displayed. Test types are used to define various stages. The following example explains the procedure of selecting module and test stages as a function of the experiment type. Assume that the intention of running an experiment is to study isotropic deformation of a typical soil under saturated condition. The test must be conducted over two steps, as soil sample will be initially saturated, then subjected to confining stress. The saturation process involves a gradual injection of water to the specimen under a specific pressure till air molecules inside the porous area to be dissolved inside the water. As a general criterion, the saturation state is inferred when the value of Skempton pore water pressure parameter,  $B$  exceeds 0.95. This parameter is defined as the ratio of pore-water pressure change,  $\Delta u$  induced by increasing/decreasing confining stress to the differential confining stress,  $\Delta \sigma$ . The isotropic deformation is synonymous to consolidation process through which soil sample is subjected to equal pressure from different directions. Test types associated with “Satcon” module include “Saturation Ramp”, “B-Check”, “Consolidation”, and “Automatic Saturation”. Thus, the “Satcon” is set as the test module, as the associated test types best meet the requirement of the experiment. Defining test stages based on the sequence of conduction, the initial stage would be “Saturation Ramp”, which is then followed by the “B-Check” and “consolidation” stages.

To run an unsaturated test, the “UNSAT” module is selected to conduct matric suction regulation and consolidation. Test types corresponding to this module include “Axial Stress Controlled” and “Axial Strain Controlled”. For the literature soils utilized in this study, as Bender Element testing was conducted under various consolidation loads, the strain-controlled test is preferable to avoid any axial load on the specimen. In “Axial Strain Controlled” mode, the value of final axial strain is set equal to zero so that the loading ram stay stationary throughout the testing time and thus no axial load is applied on the

specimen. Figure below shows an “Axial Strain Controlled” test stage that can be used to both establish the desired matric suction and perform consolidation process. Setup window associated with this test stage displays current and target axial strain ( $\epsilon_a$ ), pore air pressure ( $u_a$ ), cell pressure ( $\sigma^r$ ), pore water pressure ( $u_w$ ), as well as time required to reach the target values.



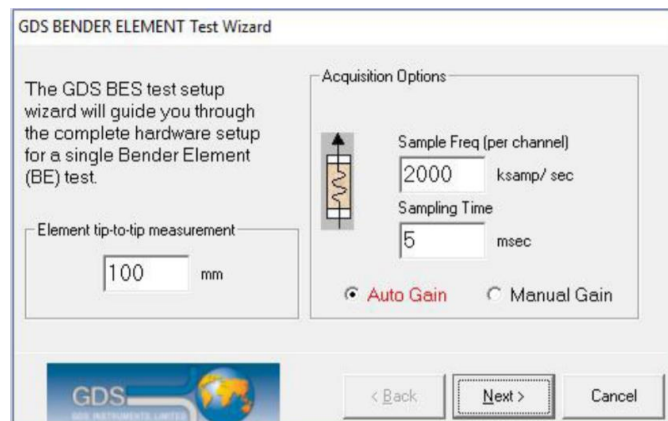
### **Main Features of the GDSBES Software**

To conduct Bender Element testing, the GDSBES software is normally run when the soil sample has reached to the desired net normal stress or matric suction.

### **How to define test steps in GDSBES software**

#### ➤ **Step 1.** Run the GDSBES

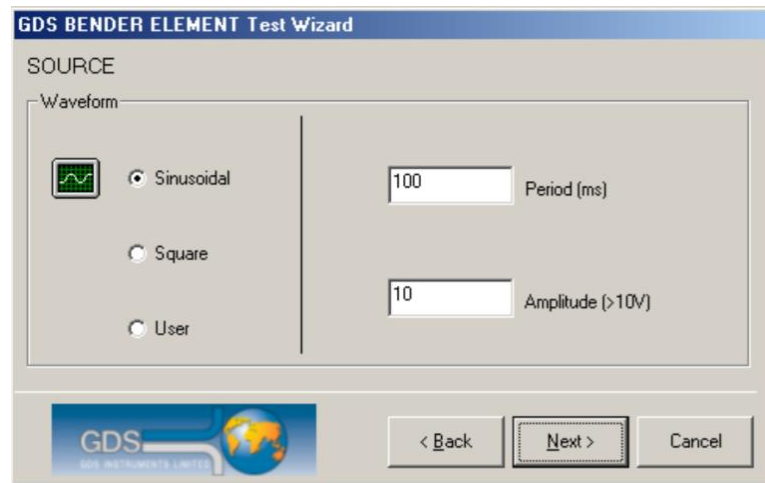
Having the Bender Element software (GDSBES) started, the initial setup screen, “GDS Bender Element Test Wizard” appears.





This screen allows specifying three parameters of the test as height of the specimen, the rate of sampling (which is denoted as “Sample Freq”) and sampling time. Figure above shows test wizard window with the default values defined for the mentioned parameters. Also, the method of data acquisition, either automatically or manually is selected on this screen by marking Auto Gain or Manual Gain. The software uses the height of the sample to calculate the shear wave velocity with this logic that the height of sample is equivalent to the distance between Bender Elements.

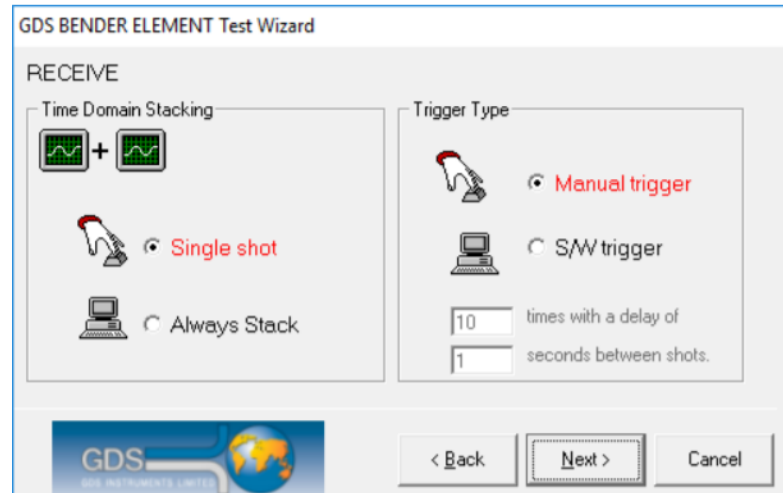
- **Step 2.** Specify type of the experiment and properties of the propagation wave  
The next step involves determining the type of the test (S-wave or P-wave test), the waveform (square or sinusoidal), as well as period/frequency and amplitude of the wave.



Upon pressing “Next” button, the third “Test Wizard” screen pops up.

- **Step 3.** Specify test initiation and data storage method  
Over this screen, time domain stacking options (either “Manual Acceptance” or “Automatic Stacking”) and test initiation type (“Manual Trigger” or “S/W Trigger”) can be selected. If the “Automatic Stacking” option is marked, whenever the shear wave is shot (or a test is repeated), data associated with all emissions are automatically added together and a stack of data is built. However, in “Manual Acceptance”, the user decides which set of data to be stacked. With selection of “Manual Trigger”, the emission is performed only by pressing trigger bottom, however the “S/W Trigger” (which refers to software trigger) allows a number of shots to be automatically

performed with user specified time delay between the shots. It should be noted that the S/W Trigger may can be only used in conjunction with the “Automatic Stacking”.



Once “Next” button is clicked, the main test screen appears.



With all the parameters set up, the test can be initiated by pressing “Trigger” button.

### ***Hardware Package Used in Unsaturated Bender Element Testing***

The coupled Bender Element-unsaturated triaxial apparatus manufactured by the GDS Instruments consists of three standard pressure volume controllers, a data acquisition pad, a load frame machine, a pneumatic pressure controller, a double walled triaxial cell, and the bender element system. The GDS load frame model GDSL50 can run in speed or

displacement control modes, and has a maximum load capacity of 50 kN, which is equivalent to 67443 kips. Figure E.3 illustrates the loading system with an assembled double wall cell mounted on the load frame.



Figure E.3 Load frame and double walled unsaturated triaxial cell

The pressure volume controllers can provide a maximum pressure up to 3 MPa (435 psi) and have a volumetric capacity of 200 ml (12.2 cubic inches) with a resolution of 0.001 ml ( $6.1 \times 10^{-5}$  cubic inches). Each controller can operate as a pressure source for the water and a gauge for reading volumetric changes. Figure E.4 shows three controllers labeled as outer cell, inner cell and pore-pressure, that are responsible for controlling the pressure inside the outer cell, the pressure and volume changes inside the inner cell, and the pore-water pressure within the specimen's body. The water is flowed through the tubes connected to each controller.

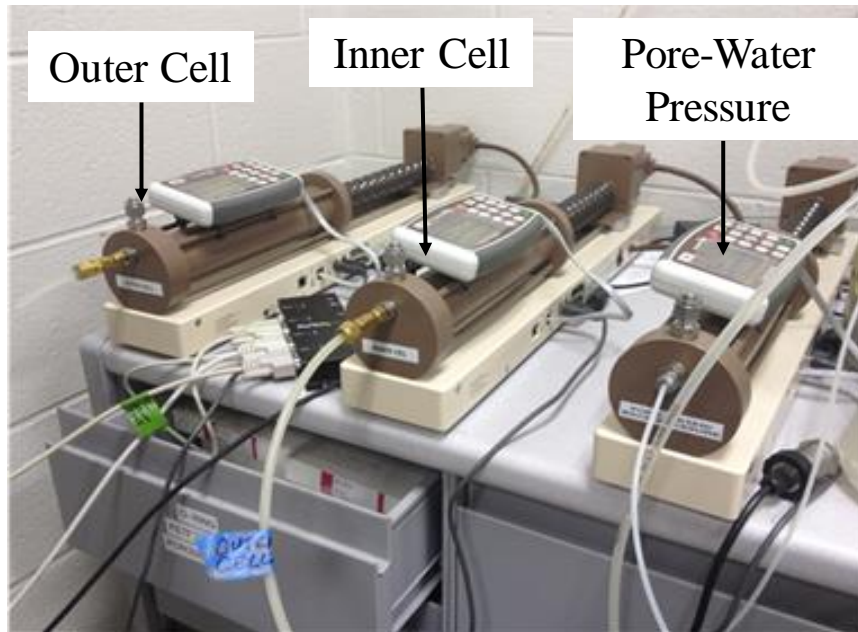


Figure E.4 Pressure volume controllers

The double wall cell refers to as a configuration which includes an inner cell fabricated from Perspex enclosed, an outer cell composed of glass, and reinforcing outer rings. Normally, a singled walled cell undergoes radial creeps over high value of pressure. The purpose of designing a double wall cell is to eliminate this radial creep by setting no pressure difference across the inner cell wall. This configuration yields more precise measurement of the volumetric change of the water inside the inner cell, which is directly attributed to the specimen volume change. The GDS double wall triaxial cell is designed for testing specimens with a diameter of 50 mm (2 inches). A high air-entry porous disk (HAEPD) has been inserted into the base pedestal to separate gaseous phase from the liquid one, and thus maintains a uniform matric suction within the specimen's body.

The Bender Element essentially measures the shear wave velocity with respect to the shear wave travel time over the wave propagation distance. Depending on the configuration of the Bender Elements, the shear wave velocity can be obtained over various directions, vertically and or horizontally. The small-strain shear modulus data utilized in this study were calculated by the shear wave velocity values which were measured along the length of the sample. In this case, Bender Elements were placed into the center of the base pedestal and top caps of the triaxial cells. The Bender Element inside the top cap is

embedded with a porous stone and the Bender Element inserted into the base pedestal is centered on the installed HAEPD as illustrated in Figure E.5.

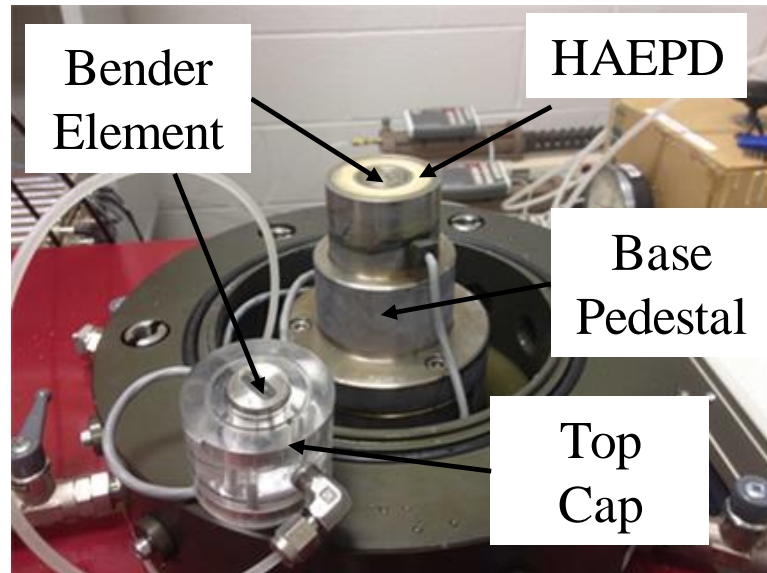


Figure E.5 Bender Element placement into the top cap and base pedestal of an unsaturated triaxial cell

The GDS triaxial system applies an internal and immersible loading mechanism to exert vertical (compression or extension) load to the specimen. The maximum capacity of the loading system is around 8 kN (1800 lbs). A remarkable benefit of an internal loading mechanism is that the load readings are not impacted by the water pressure. Hence, during analyzing the test data, there is no need to make any correction on ram upthrust and friction of the ram. Figure E.6 schematically illustrates the double wall triaxial cell with loading mechanism, and several ports that are inline connected to the corresponding pressure volume controllers. It should be noted that the small-strain shear modulus data of the literature soils all collected at different net normal stresses and matric suctions. This indicates that the specimens have not been subjected to triaxial or shearing loads. However, the modified-SFG model developed in this study is evaluated with respect to the measured stress-strain data obtained from unsaturated triaxial testing. Thus, a brief discussion about the vertical loading mechanism of the GDS triaxial cell sounds to be highly advantageous.

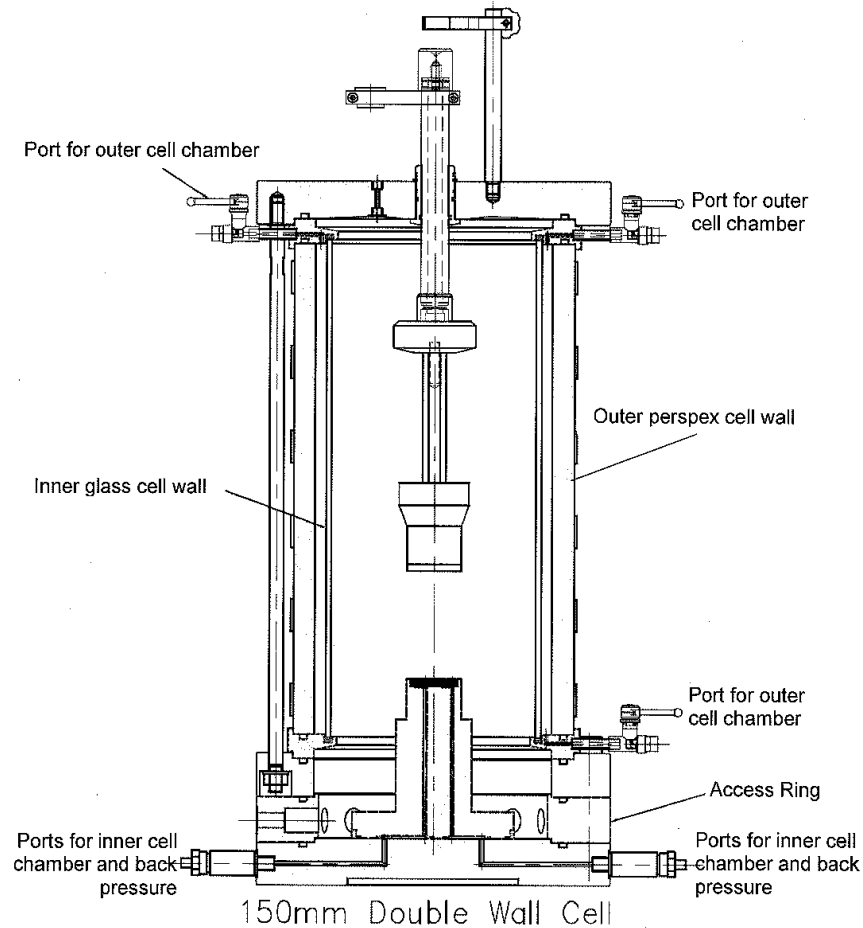


Figure E.6 GDS double wall cell

The desired matric suction is achieved with setting a differential pore-air pressure and pore-water pressure. As discussed earlier, the pore-water pressure controller regulates the magnitude of the pore-water pressure inside the specimen's pores. On the other hand, the pore-air pressure within the soil's body is controlled by the pneumatic pressure controller, which is essentially a control box being able to control 2 channels of air pressure output (Figure E.7). The pneumatic pressure controller is connected to an air house source from an internal port and to the top cap from an external port. The pneumatic pressure controller receives air from the air house, regulates it (based on the desired matric suction), and injects it into the specimen from the external port, inline tube and top cap. The air-pressure regulation is a fully automatic process that is performed by a controlling software.

During a typical experiment, several parts of the triaxial system are connected to a data acquisition system to record and monitor data sets associating with the air pressure, displacement, vertical load, and ambient pressure. In the Figure E.7, the data acquisition system is the top controller box. GDSLAB software receives data from data acquisition device and automatically controls the entire process of a test based on the predetermined testing conditions (e.g. target matric suction and net normal stress). The Bender Element are connected to an associated control box (middle box in Figure E.7) which is controlled by Bender Element software, GDSBES.



Figure E.7 Control boxes for coupled Bender Element-unsaturated triaxial testing: (top) data acquisition system, (middle) Bender Element control box; (bottom) GDS pneumatic pressure controller

The initial step in conducting a Bender Element experiment is to manufacture a testing specimen.

### ***Specimen Fabrication for Bender Element Test***

As discussed earlier, three types of specimens (undisturbed, disturbed and remolded/compacted) are generally utilized for conducting various laboratory experiments. The small-strain shear modulus data of some literature soils used in this study were obtained through running Bender Element tests on the compacted soil samples. Regarding technical features of the GDS Bender Element device, the internal diameter of the testing



specimen must be 50 mm (2 inches), 70 mm (2.8 inch) or 100 mm (4 inch). Along this section, procedure of fabricating a 2-inch diameter specimen is described. Fabrication of a compacted specimen for Bender Element testing is very similar to that for fabricating compacted specimen for SWCC testing, explained in Appendix A. The only difference in fabrication process is that of the number of lifts and their thickness, thus the height of the specimen. It is generally recommended that the height of the specimen must be almost 2.5 times more than its diameter. The compaction process is conducted by means of static compactor/extruder, split mold, pistons and loading frame. To meet the sample size criteria defined by GDS, 2-inch diameter split mold and pistons are selected.

To fabricate a compacted specimen for Bender Element testing, initially a batch mixture of dry soil and water corresponding to the desired dry density and moisture content is prepared. The mixture is stored inside a constant temperature room for around 24 hours such that the mixture has adequate time to reach to the moisture equilibrium state. The compaction is performed by using the compaction system, which consists of static compactor, spacer rings, 2-inch diameter split mold and pistons. The compacted soil for Bender Element testing is fabricated from 4 lifts or layers. Each individual layer of the specimen must have the same dry density that is equal to the final dry density of the specimen. The mass of each portion is determined based on the volume of each layer and the desired dry density. The approximate height of the first compacted layer would be around 36.1 mm (1.42 inches), while the other layers are slightly thinner with an approximate thickness of 28.7 mm (1.13 inches). Upon the equilibrium state achieved, the batch mixture is divided into the 4 portions based on the mass of the mixture required for each lift. Then, the first portion is poured into the mold and compacted without a spacer ring. The second compacted layer is generated by flipping the split mold down, putting a spacer ring under mold, pouring the second portion of the mixture, and raising the hydraulic jack such that the mixture to be compacted inside the split mold. The same process is applied for compacting the rest of the layers by altering the ends of the split mold and using spacer rings. The purpose of using spacer rings is to control the thickness of each layer, and hence bring the dry density of the layer to the desired value. Accordingly, the entire sample would have the uniform dry density. Figure E.8 shows a sequence of steps applied to fabricate a 2-inch diameter compacted specimen.





Figure E.8 Process of fabricating a compacted specimen for unsaturated Bender Element testing

The compacted specimen is extruded from the split mold by means of extruder piston and hydraulic jack. The height and diameter of the specimen fabricated through this process is in average 122.2 mm (4.81 inches) and 50.8 mm (2 inches) respectively, which indicates an approximate height to diameter ratio of 2.4. The compacted specimen is sealed and stored for at least 2 days to avoid moisture loss and allow dissipation of any pressure formed inside the porous areas of the sample.

### ***Bender Element Testing Procedure***

As discussed earlier, to assess the small-strain shear modulus prediction scheme, the measured values of the small-strain shear modulus corresponding to different net normal stresses and matric suctions were used. Due to the direct relation between the small-strain shear modulus and shear wave velocity, it can be deduced that the shear wave velocity was measured over several stress and state paths. For a group of literature cases, the soil specimen was initially subjected to a pre-determined suction, which then isotropically compressed by a specific net normal stress. Having specimen reached the equilibrium state, the Bender Element/Resonant Column test was performed. However, other group of utilized soils was initially consolidated, then dried to a specific suction, and finally were subjected to Bender Element/Resonant Column testing. Depending on the type of the test and regardless stress and state paths, the shear wave velocity of all samples was measured based on the same Bender Element/Resonant Column testing procedure. Since this section totally focuses on the Bender Element testing, only testing procedure associated with the Bender Element is described.

A coupled Bender Element-unsaturated triaxial cell system can be used to measure the shear wave velocity over both saturated and unsaturated states. Prior running a Bender Element test, HAEPD is saturated over three sequential steps as Purging; Bottom-up; and Top-down.

➤ **Step 1.** Purging

The purging is a process through which the air is removed from cavity locating under the HAEPD. Initially, one end of the tube connected to the pore-water pressure volume controller is submerged under the surface of de-aired water inside a beaker. Subsequently, water is run through the tube till no air bubble coming out of the tube. In this case, the tube is fully purged of the air. The tube later is connected to the pore-water pressure port-1 locating on the base of the triaxial system (Figure E.9). Then, a tube is connected to the other pore-water pressure port on the base, and it is dipped below the surface of a beaker of de-aired water. At this stage both pore-water pressure ports are closed. First, the valve associated with the port-2 is opened, then pressure volume controller is set to generate a low pressure equal to 25 kPa. Finally, the pore-water pressure port-1 is opened to allow water passing through the cavity. Consequently, air bubbles entrapped inside the cavity are flowed out of the system. The air purging process is inferred as complete when no more air bubble is expelled from the tube that is connected to the pore-water pressure port-2.

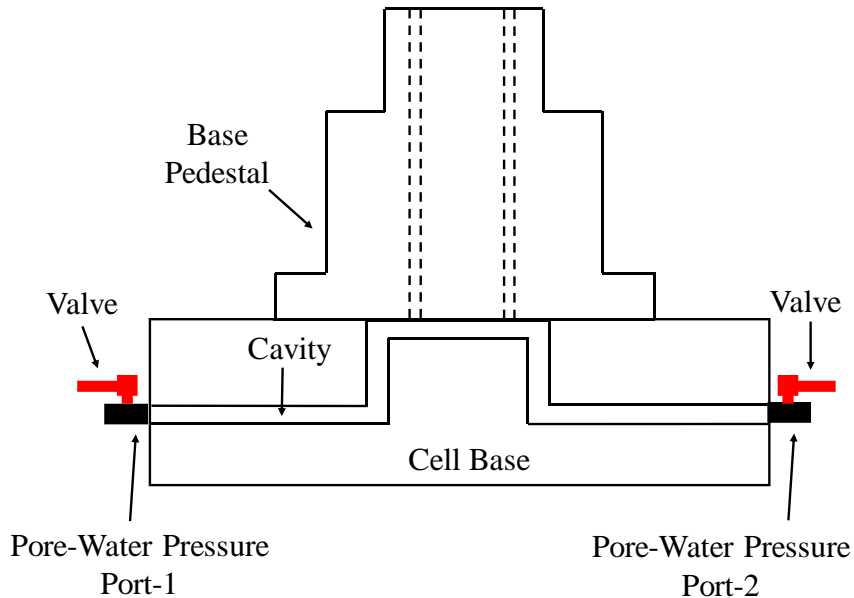


Figure E.9 A schematic of base pedestal

➤ **Step 2.** Bottom-up

The purpose of running bottom-up approach is to remove air molecules from the HAEPD. This process is conducted by applying a low pressure to underside of the HAEPD such that water gradually passes through the pores of the HAEPD and eject air from the system. Having cavity purged of the air, the valve corresponding to the pore-water pressure port-2 is close while the other valve is still open. In this case, the pressure of the water filling the cavity is 25 kPa, which is enough for passing the water through the HAEPD. The pressure is kept constant for at least 1 day such that a pond of water is formed on the surface of HAEPD. Finally, the cavity is depressurized by decreasing the pressure to 0 kPa and both pore-water pressure ports are closed. Figure E.10 shows a saturated HAEPD upon completing bottom-up approach.



Figure E.10 Water pond formed on the surface of HAEPD through bottom-up process

➤ **Step 3.** Top-down

Along with top-down approach, the HAEPD is pressurized in normal direction to ensure removal of any air molecule remaining in the system. This process commences with assembling cells, which is followed by filling inner and outer cells by the de-aired water. Then, inner and outer pressure volume controllers are connected to their corresponding ports on the base of the cell by means of the connecting tubes. Subsequently, both cells are pressurized to 500 kPa. The tube connected to the pore-water pressure port-2 is submerged under the surface of the de-aired water inside a beaker, then the valve corresponding to the pore-water pressure port-2 is opened. The pressurized water flows downward from the inner cell into the HAEPD, passes through the cavity and connecting tube, and is collected inside the beaker.

Upon saturating the HAEPD, the next step towards running an unsaturated Bender Element test is to mount the compacted specimen on the device. To avoid sample adherence to the top cap and base pedestal and thus loss of soil sample, one filter paper is used at each end of the sample. Also, one Bender Element has been inserted inside the top cap and base pedestal for creating and receiving shear wave signals. As shown on the Figure E.5, the flange of Bender Elements is not level with the surface of the top cap and base pedestal. Thus, each filter paper is cut in its center so that accommodate the flange. To make a perfect contact between the soil sample and Bender Elements, a small cut equal to the length of the Bender Element flange is made on each end of the specimen. Then, the compacted sample is mounted on the filter paper on the base pedestal and is pressed unto the flange of the bottom Bender Element. Then, a latex membrane is placed on a vacuum model and stretched open by connecting the mold to a vacuum source. The stretched membrane is inserted over the specimen as shown on the Figure E.11. with removal of the vacuum mold, a filter paper, a porous stone and top cap are placed on the specimen. The flange of the top Bender Element is placed inside the cut made at the top of the sample such that the Bender element comes into a perfect contact with the specimen and align with the bottom Bender Element. The specimen is completely sealed by the latex membrane with use of several rubber O-rings that firmly hold the membrane against top cap and base pedestal.



Figure E.11 Process of mounting an unsaturated specimen on the triaxial device

The process of sample mounting is finalized by placing the inner and outer cells over the specimen, bracing cells with use of steel bars, and extending load rod into the inner cell such that sits on the top cap. The shear wave velocity of the literature soils was measured over a constant suction test through which the magnitude of suction is remained unchanged along the entire test. In this procedure, the pore-water and pore-air controllers regulate the associated pressures within the specimen such that the differential air-water pressure to stay constant throughout the test. During a constant suction test, both air and water are allowed to drain. The constant suction test is conducted over two stage, suction equilibrium and isotropic consolidation that each stage can be performed firstly. Along with this section, the process of suction equilibrium is explained initially. To conduct Bender Element testing over multiple suctions and net normal stresses, initially the specimen is saturated, then is subjected to the desired suctions and net normal stresses.

Upon mounting the specimen on the cell, the inner and outer cells are filled by de-aired water. Then, the soil sample is subjected to a small radial/confining pressure with the aim of holding membrane on the surface of the specimen. Accordingly, inner cell pressure volume controller is set to generate a radial pressure between 3 and 8 kPa. It should be noted that a pressure differential of no more than  $\pm 30$  kPa between the two sides of the inner cell is required throughout testing. Doing so will protect the inner cell wall from over pressurizing in either direction. Therefore, the outer cell pressure volume controller is set to provide the same magnitude of pressure as generated by the inner cell.

An increase in radial stress causes water drainage from the specimen. This water must be collected by the pore-water pressure volume controller as specimen is connected to this controller from base pedestal. Prior increasing the radial stress, the pore-water pressure volume controller is set on the drained mode, which allows the controller to self-adjust its volume for collecting the water expelled from the specimen. At this stage of the testing, the equilibrium state is inferred when volumetric change of the pore-water pressure volume controller reaches a minimum.

As discussed earlier, the pressure and volume of the water inside the specimen is controlled by the pore-water pressure volume controller. Also, the top cap is connected to the pneumatic pressure controller for transmitting regulated air into the specimen. Thus, the soil sample can only be saturated from the bottom, which indeed indicates one-way

saturation process. Due to the low permeability of the HAEPD, the saturation is quite slow and may take several days or weeks. The saturation process can be speeded up by means of a three-way connector equipped with a valve on each outlet. The connecting tube of the pore-water pressure volume controller is connected to the inlet of the three-way connector, as shown on Figure E.12. One outlet of the three-way connector is connected to the pore-air pressure port (let's call it outlet-1) that goes to the top cap (i.e. the pneumatic pressure controller is not connected to the pore-air pressure port at this stage) and the other outlet is connected to the pore-water pressure port (let's call it outlet-2) that goes to the base pedestal. This configuration significantly reduces the amount of time required for saturation, as the water is flowed into the sample from both top and bottom end.

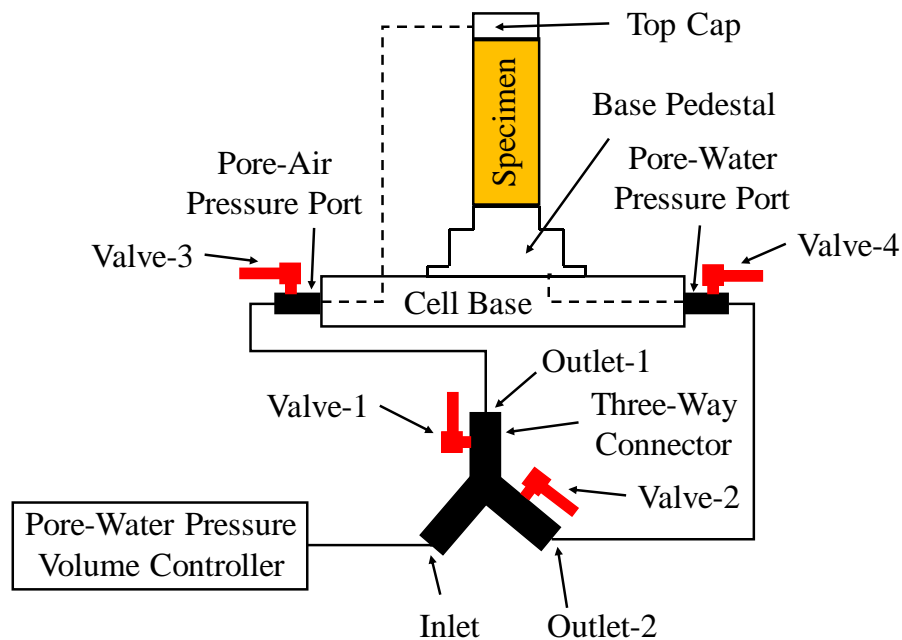


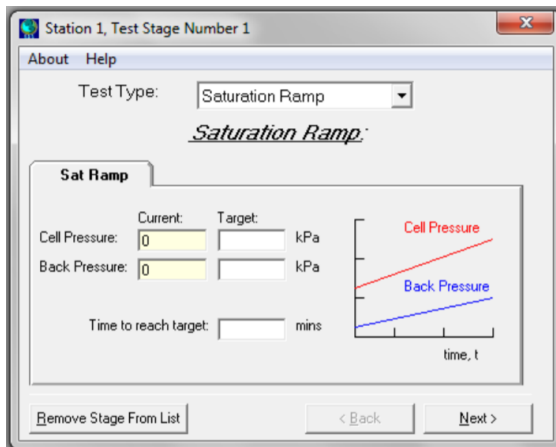
Figure E.12 Two-way saturation circuit

Having the saturation circuit assembled, the “Satcon” is selected as the testing module and “Saturation Ramp” is set as the first testing stages. For each testing stage, an associated setup screen is displayed upon selecting the stage. The window corresponding to the “Saturation Ramp” (Figure E.13) shows the current Cell Pressure (that is identical to inner cell pressure) and Back Pressure (which is supplied and controlled by the pore-water pressure volume controller). The setup screen also allows for selecting the target (final) Cell Pressure and Back Pressure as well as time required to reach to the target pressure values. The target Cell Pressure is set to a value slightly higher than the target value of the

Back Pressure to minimize sample consolidation induced by the differential Cell and Back pressure. Upon selecting the desired pressure values and starting the test, the Cell Pressure and Back Pressure gradually increase till meet the target values at the specified time.

At the end of “Saturation Ramp”, a “B-Check” stage is defined to measure the parameter B and thus evaluate sample saturation. The associated screen setup for “B-Check” stage is shown on Figure E.13 In this screen, the current Cell Pressure and Back Pressure are displayed which correspond to the target values defined in the “Saturation Ramp” stage. The differential Cell Pressure is set by imputing an arbitrary value into the field associated with the “Target Cell Pressure”. Once the stage is implemented, the pore-water pressure volume controller is switched to the undrained mode (i.e. the piston is hold stationary) and Cell Pressure increase to the specified value. The pore-water pressure within the specimen increases with an increase in Cell Pressure and recorded by a sensor installed inside the pore-water pressure volume controller. Eventually, the B parameter is calculated as a function of differential pore-water pressure and differential Cell Pressure. As a general criterion, the saturation state is inferred if the obtained value for B parameter be equal and greater than 0.95. Otherwise, a new “saturation Ramp” stage is added to the list of test stages in order to increase Cell Pressure and Back pressure to facilitate sample saturation. Accordingly, the B value is measured at the end of secondary “Saturation Ramp” stage. The process of defining new “Saturation Ramp” and “B-Check” stages continues till the specimen reaches to the saturation state.

(a)



(b)

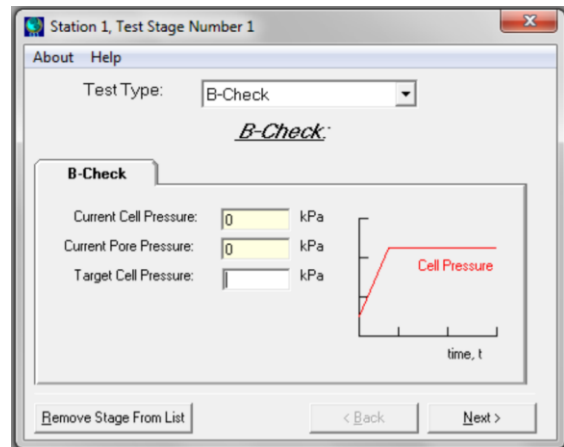


Figure E.13 Required stages for saturating specimen, (a) “Saturation Ramp”, (b) “B-Check”



Once the value of B parameter meets the discussed criterion, the Bender Element software is run, and test parameters are inputted inside the associated fields as previously discussed. With pressing “Trigger” Bottom on Bende Element test screen, an input signal is sent to the Bender Element located inside the top cap. The shear wave generated via input signal travels along the length of the sample. When the shear wave is received by the bottom Element, test results are displayed in form of two sinusoidal graph with time in x-axis and the voltage of the output signal in y-axis (Figure E.14). The red graph corresponds to excitation created by the source Element and the green one is response trace from the receiving Element. If the data is noisy, the signal is resent and manually stacked by clicking on “Re-Trigger” and “ADD TO STACK” bottom, respectively. This process greatly enhances clearance of the obtained data.

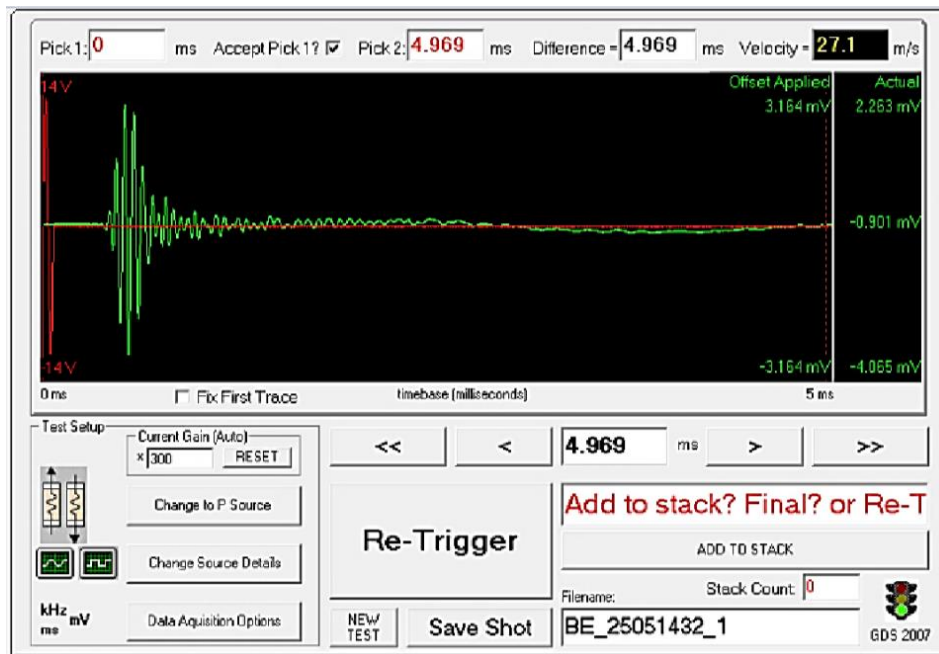


Figure E.14 Bender Element Test Screen after running a test (Payan, 2017)

Upon result exhibition on the test screen, the shear wave travel time can be estimate from the time characteristics points shown earlier on the Figure E.2. As two examples, the process of determining the shear wave propagation time by means of zero-crossing and first peak methods is discussed heroin. Considering results shown on Figure E.15, zero-crossing and first peak points respectively correspond to point “A” and “B” on the response trace (green graph). In zero-crossing method, distance between the start of the excitation and point “A” yields the shear wave propagation time. Based on the first peak method, a



distance from first peak of the emitted signal (on red graph) to point B corresponds to the shear wave travel time. The shear wave velocity is estimated from the length of the specimen and shear wave propagation time. Then, the small-strain shear modulus of the soil at saturated or near saturated state is calculated by Equation 2.3.

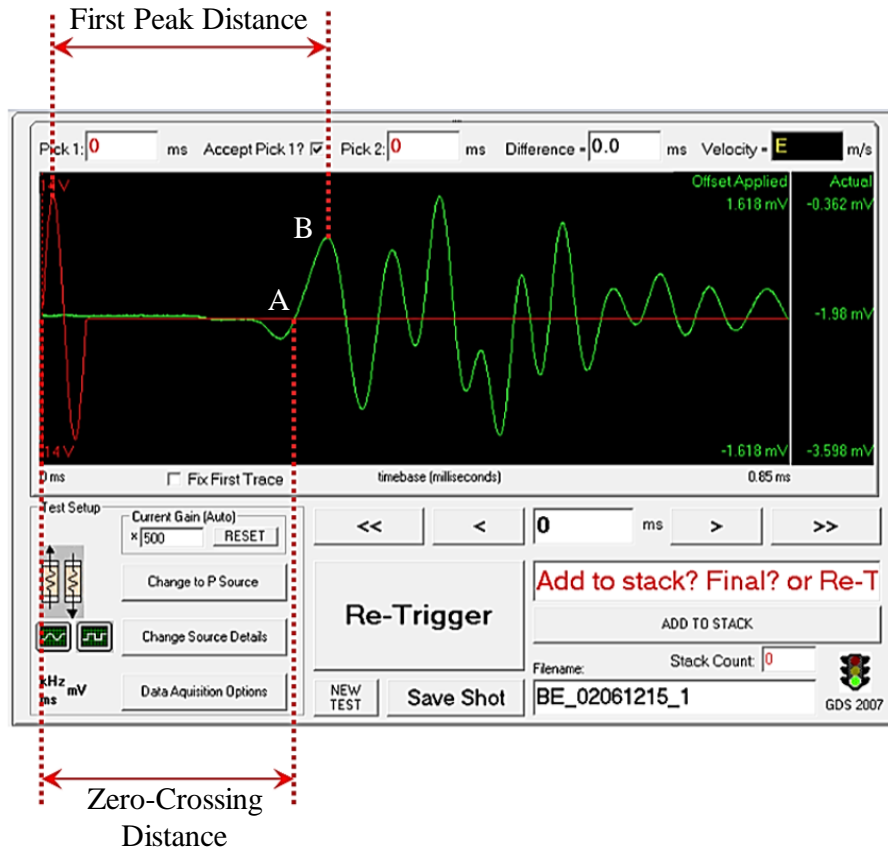


Figure E.15 Estimation of Shear wave travel time using zero-crossing and first peak methods (GDS Instruments, 2017)

To obtain shear wave velocity of the same specimen under unsaturated state, the saturated sample must be subjected to matric suction more than zero, more specifically to a pore-air pressure greater than the current pore-water pressure. In this regard, initially, the valves 3 and 4 at the pore-air and pore-water pressure (Figure E.16) are closed so that avoid any decline in pore-water pressure. The current Back Pressure is reduced to zero by defining a new “Saturation Ramp” stage, in which the value of target Back Pressure is set to zero. It should be noted that the target value selected for the Cell Pressure would be equal to the current Cell Pressure. At this stage of the test, the tube linking the pore-air pressure port to outlet-1 is disconnected from pore-air pressure port and outlet of the

pneumatic pressure controller is connected to the pore-air pressure port. Now, the pore-water pressure controller is only connected to the pore-water pressure port. Figure E.16 illustrates the new configuration of the testing circuit which is adjusted based on the described procedure.

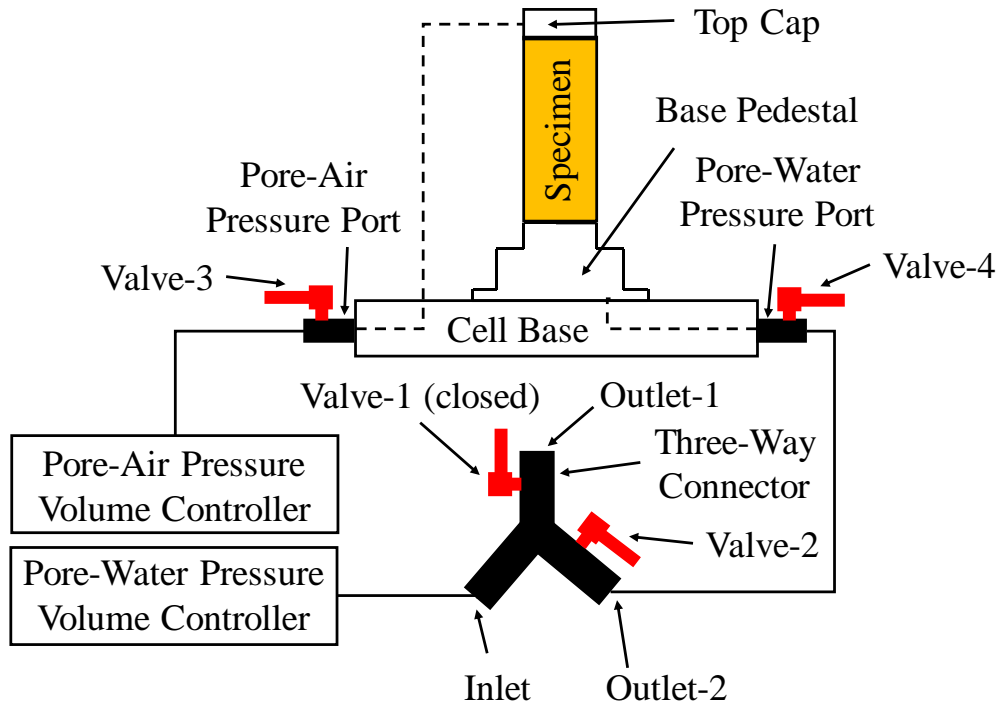


Figure E.16 Testing Circuit configuration for desaturating specimen

With definition of a new “Saturation Ramp” stage, the target Back Pressure is set equal to the value at the end of saturation, then valve-1 is closed (to avoid water drainage for outlet-1) and the stage is implemented. Once “Saturation Ramp” is completed, valve 4 at the pore-water pressure port is opened. Subsequently, an “Axial Strain Controlled” test stage is defined, in which the target pore-air pressure is set to a value such that the difference between pore-air pressure and pore-water pressure to be equal to the desired matric suction. It should be noted that the magnitude of pore-air pressure must be less than Cell Pressure over the entire testing process. Otherwise, the sample would be damaged due to negative confining stress that tends to separate solid particle from each other. Therefore, while defining “Axial Strain Controlled” test stage, the target Cell Pressure is set equal to a value greater than the target pore-air pressure. Once the stage initiates, valve-3 is opened and air is directed into the specimen from top cap. At the end of saturation stage, the

specimen reaches to an equilibrium state, which indicates a uniform pore-water pressure over the entire sample's body. With air injection into the specimen, equilibrium is disturbed due to presence of non-equal pore-pressures inside the specimen. Over time, a three-phase equilibrium is established within the specimen that reveals a uniform matric suction throughout the sample's body. Once again, the Bender Element testing is implemented and the shear wave velocity of the specimen at the initial matric suction is obtained based on the same method used under the saturation state. Then, the small-strain shear modulus is calculated with use of the Equation 2.3.

The successive matric suctions are achieved by simultaneously increasing pore-air pressure and cell pressure in uniform increments (normally 7 kPa per hour) while keeping the pore-water pressure constant. Over this process, difference between cell pressure and pore-air pressure is kept constant to avoid specimen consolidation as the purpose of running Bender Element test at this stage is to study the effect of matric suction on the shear wave velocity of the soil. At each matric suction, shear wave is measured when the equilibrium state is achieved. To obtain the shear wave velocity over various net normal stresses, at a constant matric suction, the cell pressure increases while the pore-air and pore water pressures are remained unchanged. Once specimen reaches to the equilibrium at each net normal stress, the Bender Element testing is performed.

APPENDIX F PREDICTIVE MODELS DEVELOPED FOR THE SMALL-STRAIN  
SHEAR MODULUS OF UNSATURATED SOILS

Several deterministic models have been proposed to predict the small-strain shear modulus of unsaturated soils. These models differ in the frameworks used to describe the variation of the small-strain shear modulus of unsaturated soils with respect to the net normal stress and suction. It is observed that all models use various fitting parameters to estimate the small-strain shear modulus. The fitting parameters represent the influence of individual parameters or the influence of stress state variables on the small-strain shear modulus. The most common approach to estimate the fitting parameters is to optimize the fitting parameters via minimizing the least squared difference between the measured and the predicted values. A summary of the small-strain shear modulus prediction models with type of the testing soil is presented in this section.

➤ **Wu et al. (1984) (fine-grained cohesionless soil)**

$$G_{0,\text{unsat}} = G_{0,\text{unsat}}^{\text{dry}} [1 + H(S_r)]$$

$$H(S_r) = \begin{cases} (a-1) \sin\left(\frac{\pi S_r}{2b}\right) & S_r \leq b \\ (a-1) H_1(S_r) \cdot H_2(S_r) & S_r > b \end{cases}$$

$$H_1(S_r) = 0.5 \left( \frac{S_r - b}{100 - b} \right)^2$$

$$H_2(S_r) = \sin \left[ \frac{\pi}{100 - b} \left( S_r + 50 - \frac{3b}{2} \right) \right] + 1$$

$G_{0,\text{unsat}}^{\text{dry}}$  : small-strain shear modulus of the soil at the driest state

$S_r$  : degree of saturation

$H(S_r), H_1(S_r), H_2(S_r)$  : functions of the degree of saturation

$a$  : maximum value of the  $G_{0,\text{unsat}} / G_{0,\text{unsat}}^{\text{dry}}$

$b$  : optimum degree of saturation which corresponds to the maximum value of the

$G_{0,\text{unsat}} / G_{0,\text{unsat}}^{\text{dry}}$

➤ **Cabarkapa et al. (1999) (quartz silt)**

$$\frac{G_{0,\text{unsat}}}{p_r} = A \left( \frac{p'}{p_r} \right)^n OCR^m$$

$p_r$  : reference pressure

$A, n, m$  : fitting parameters

$p'$  : mean effective stress

$OCR$  : over-consolidation ratio

➤ **Cho and Santamarina (2001) (mixture of kaolinite and glass beads)**

$$G_{0,\text{unsat}} = G_{0,\text{sat}} \left[ 1 + \frac{2\sigma'_{eq}}{(1+K_o)\sigma_v} \right]^{2\beta} \frac{e+G_s}{eS_r+G_s}$$

$G_{0,\text{sat}}$  : small-strain shear modulus of the soil at the saturated state

$\sigma'_{eq}$  : equivalent effective stress induced by the matric suction

$K_o$  : lateral earth pressure coefficient at rest

$\sigma_v$  : vertical effective stress

$\beta$  : empirical parameter

$e$  : void ratio

$G_s$  : specific gravity

➤ **Mancuso et al. (2002) (Compacted silty sand)**

$$\frac{G_{0,\text{sat}}}{p_a} = A \left[ \frac{(p-u_a)}{p_a} \right]^n OCR^m$$

$$\frac{G_{0,\text{unsat}}^{s \leq s_{aev}}}{p_a} = A \left[ \frac{(p-u_a)+s}{p_a} \right]^n OCR^m$$

$$G_{0,\text{unsat}}^{s > s_{aev}} = G_{0,\text{unsat}}^{s_{aev}} \left\{ (1-r) \exp[-\alpha(s-s_{aev})] + r \right\} \quad s > s_{aev}$$

$A, n, m$  : fitting parameters

$p-u_a$  : mean net normal stress

$p_a$  : atmospheric pressure

$s$  : matric suction

$s_{aev}$  : matric suction corresponding to air entry point

$\alpha$  : parameter that controls rate of increase of soil stiffness with matric suction

$r$  : ratio of  $G_{\max}^{s_{aev}}$  to threshold value of  $G_{\max}$

➤ **Inci et al. (2003) (SC, CL, CH)**

$$G_{0,\text{unsat}} = 625 \frac{OCR^\mu}{0.3 + 0.7e^2} \sqrt{p_a \sigma'_0}$$

$\mu$  : fitting parameter

$\sigma'_0$  : effective overburden stress

➤ **Mendoza et al. (2005) (Kaolinite Clay)**

$$G_{0,\text{unsat}} = 13300 \frac{(2.3 - e)^\kappa}{1 + e} [\ln(s)]^{1.35}$$

$\kappa$  : fitting parameter

➤ **Takkabutr (2006) (Sand, Clay)**

$$\frac{G_{0,\text{unsat}}}{\sigma_r} = A \sigma_r^B \left[ s^{C \exp(D\sigma_r)} \right] \exp(E \cdot s)$$

$A, B, C, D, E$  : fitting parameters

$\sigma_r$  : confining stress

➤ **Vassallo et al. (2007) (Clayey, Slightly Sandy Silt)**

$$\frac{G_{0,\text{unsat}}}{f(e) p_a} = A \left( \frac{p - u_a}{p_a} \right)^n OCR^m \cdot H \left( \frac{s_o}{s} \right) + F(s)$$

$$H \left( \frac{s_o}{s} \right) = (1 - \bar{r}) \exp \left[ -\bar{\beta} \left( \frac{s_o}{s} - 1 \right) \right] + \bar{r}$$

$A, n, m$  : fitting parameters

$H, F$  : functions of matric suction

$s_o$  : maximum past matric suction

$\bar{r}$  : Defines the maximum possible effect on stiffness of the distance between the current stress state and the SI surface

$\bar{\beta}$  : Controls the rate of increase of stiffness with the distance between the current stress state and Suction Increase surface

➤ **Ng et al. (2009) (ML)**

$$G_{0,unsat}^{ij} = C_{ij}^2 F(e) \left( \frac{\sigma_i - u_a}{p_r} \cdot \frac{\sigma_j - u_a}{p_r} \right)^n \left( 1 + \frac{s}{p_r} \right)^{2b}$$

$$F(e) = \frac{[f(e)]^2 (G_s + S_r e)}{1 + e} \rho_w$$

$C_{ij}$ : inherent material constant related to (ij) plane

$n, b$ : fitting parameters

$\sigma_i - u_a$ : net normal stress along the i plane

$\sigma_j - u_a$ : net normal stress along the j plane

$f(e)$ : void ratio function equaling to  $e^{-x}$

$\rho_w$ : mass per unit of volume of water

➤ **Sawanguriya et al. (2008) (CL, ML, SC)**

$$G_{0,unsat} = \left( w \frac{E}{E_{std}} \cdot \frac{w_{opt}}{w_{opt, std}} \right) [\alpha \log(s) - \beta]$$

$w$ : gravimetric water content

$E$ : compaction energy achieved by enhanced or reduced Proctor effort

$E_{std}$ : compaction energy achieved by standard Proctor effort

$w_{opt}$ : optimum moisture content obtained from enhanced or reduced Proctor effort

$w_{opt, std}$ : optimum moisture content obtained from standard Proctor effort

$\alpha, \beta$ : fitting parameters

➤ **Alramahi et al. (2008) (Sand, Silt)**

$$G_{0,unsat} = \rho \alpha \left( \frac{\sigma - u_a}{\sigma_{ref}} \right)^{2\beta} \left( 1 + S_r \frac{s}{\sigma - u_a} \right)^{2\beta_{unsat}}$$

$\rho$ : mass per unit of volume of soil

$\alpha$ : fitting parameter

$\sigma - u_a$ : net normal stress



$\sigma_{ref}$  :reference stress equal to 1 kPa

$\beta, \beta_{unsat}$  :experimentally determined exponent that depends on the soil type

➤ **Sawangsuriya et al. (2009) (CL, ML, CH, SC)**

$$G_{0,unsat} = \frac{A}{0.3+0.7e^2} (\sigma - u_a)^n + C\Theta^\kappa s$$

$$G_{0,unsat} = \frac{A}{0.3+0.7e^2} [(\sigma - u_a) + \Theta^\kappa s]^n$$

$A, n, C, \kappa$  : fitting parameters

$\Theta$  : normalized volumetric water content,  $\theta/\theta_s$

$\theta$  : volumetric water content

$\theta_s$  : volumetric water content at saturated state

➤ **Khosravi and McCartney (2009) (SC, SL, Silty Sand, Kaolinite Clay)**

$$G_{0,unsat} = \frac{A \cdot p_a^n}{0.3+0.7e^2} \left[ \frac{\sigma - u_a}{p_a} + \left( \frac{s_{aev}}{p_a} + 1 \right) \ln \left( \frac{s}{p_a} + 1 \right) \right]^n$$

$A, n$  : fitting parameters

➤ **Khosravi et al. (2010) (Silica Sand)**

$$G_{0,unsat} = \frac{A}{0.3+0.7e^2} [(\sigma - u_a) + (S_e \cdot s)]^n$$

$$G_{0,unsat} = \frac{A}{0.3+0.7e^2} [(\sigma - u_a) + s]^n$$

$A, n$  : fitting parameters

$S_e$  : effective degree of saturation,  $\frac{S_r - S_{r,res}}{S_{r,sat} - S_{r,res}}$

$S_{r,res}$  : residual degree of saturation

$S_{r,sat}$  : saturated degree of saturation

➤ **Biglari et al. (2011) (CL)**

$$G_{0,unsat} = A p_a^{1-n} [(\sigma - u_a) + (S_r \cdot s)]^n OCR^m f(e) h(S_r)$$

$$h(S_r) = 1 - \alpha \left\{ 1 - \exp \left[ \beta \frac{f(s)(1 - S_r)}{f(s)} \right] \right\}$$

$A, n, m, \alpha, \beta$ : fitting parameters

$h(S_r)$ : a function of degree of saturation

$f(s)$ : function of suction which depends on the size of the grains and on the value of the water surface tension

➤ **Khosravi and McCartney (2012) (Bonny Silt)**

$$G_{0,\text{unsat}} = Ap_a \left[ \frac{p_c}{p-u_a} \exp\left(\frac{\Delta e^p}{\lambda-\kappa}\right) \right]^m \left[ \frac{p-u_a}{(p-u_a)+(S_e \cdot s)} \exp(\beta[S_{e,i}-S_e]) \right]^n \left[ \frac{(p-u_a)+(S_e \cdot s)}{p_a} \right]^D$$

$A, D$ : effective stress dependency parameters

$n, m, \beta$ : hardening parameters

$\lambda, \kappa$ : slopes of isotropic compression curves

$p_c$ : pre-consolidation stress

$\Delta e^p$ : plastic change in void ratio

$S_{e,i}$ : initial effective degree of saturation

➤ **Heitor et al. (2013) (SP-SC)**

$$\frac{G_{0,\text{unsat}}}{G_{0,\text{sat}}} = Ae^{-x} \left[ \frac{(p-u_a) + (s \cdot S_r^\kappa)}{p_a} \right]^n$$

$$A = a \left[ \frac{S_{r,\text{max}}}{S_r} - 1 \right]^b$$

$\kappa$ : a parameter related to plasticity index

$a, b$ : empirical parameters

$S_{r,\text{max}}$ : maximum saturation defined as the degree of saturation line asymptote

➤ **Oh and Vanapalli (2014) (Sand, SP, SW/Data in literature)**

$$G_{0,\text{unsat}} = G_{0,\text{sat}} \left[ 1 + \zeta \cdot \frac{s}{p_a} \cdot S_r^\xi \right]$$

$\zeta, \xi$ : fitting parameters

➤ **Wong et al. (2014) (Different materials and tests from literature)**

$$G_{0,\text{unsat}} = Ap_r^{1-n} e^{-m} \left[ (p - u_a) + (S_r^{\gamma/\lambda_p} \cdot s) \right]^n S_r^{-k/\lambda_p}$$

$A, n, m, k, \lambda_p$  : fitting parameters

$\gamma$  : a constant equal to -0.55 according to Khalili and Khabbaz (1998)

➤ **Dong et al. (2016) (Different soils both in literature and their study)**

$$G_{0,\text{unsat}} = G_{0,\text{sat}} \left( \frac{1}{S_e} \right)^{9.6n-6} \cdot \left[ \frac{(p - u_a) + (s \cdot S_e)}{p_a} + 1 \right]^{\gamma_o}$$

$n$ : fitting parameter of the Van Genuchten (1980) SWCC equation

$\gamma_o$  : empirical fitting parameter

➤ **Han and Vanapali (2016) (Different soils in literature)**

$$G_{0,\text{unsat}} = G_{0,\text{sat}} + \left[ (G_{0,\text{unsat}}^{\text{ref}} - G_{0,\text{sat}}) \frac{s}{s_{\text{ref}}} \left( \frac{S_r}{S_{r,\text{ref}}} \right)^{\xi} \right]$$

$s_{\text{ref}}$  : reference matric suction

$G_{0,\text{unsat}}^{\text{ref}}$  : small-strain shear modulus at reference matric suction

$S_{r,\text{ref}}$  : reference degree of saturation

$\xi$  : fitting parameter

➤ **Khosravi et al. (2018b) (Silica Sand)**

$$G_{0,\text{unsat}} = \frac{A_{\text{sat}}}{0.3 + 0.7e^2} \left[ 1 + \kappa (s \cdot S_e)^\beta \right] \left[ (p - u_a) + (s \cdot S_e) \right]^{N_{\text{sat}}}$$

$A_{\text{sat}}, \kappa, \beta, N_{\text{sat}}$  : fitting parameters

➤ **Ngoc et al. (2019) (SC)**

$$G_0 = \frac{p_r}{0.3 + 0.7e^2} \left[ a \left( \frac{\sigma - u_a}{p_r} \right)^n + b \left( \frac{s \cdot S_r}{p_r} \right)^m + c (1 - S_r)^k \right]$$

$a, n, b, m, c, k$  : fitting parameters

APPENDIX G ACQUIRING HYDRAULIC AND MECHANICAL DATA  
ASSOCIATED WITH THE SHARING STAGE

The applicability of the modified-SFG model in describing stress-hydraulic-strain behavior of the unsaturated soil over shearing phase was evaluated with respect to several case studies. The same apparatus used for Bender Element testing, GDS, can be utilized for running unsaturated triaxial test. A full triaxial experiment consist of three stages as suction regulation, isotropic consolidation and triaxial shearing. Having suction regulation and consolidation performed, a new test stage is defined, in which the value of the final strain and time to reach to the failure are specified. When vertical load is exerted, pore-air and pore water pressure increase. Both air-water and pore-water controllers are set on the drained mode, hence air and water can be drained out of the sample due to the excess pore-air pressure and pore-water pressure. The associated controllers adjust their volume to collect the expelled air and water. The strain rate must be set to a value such that excess pore-air and pore water pressure generated from the vertical load have enough time to be dissipated and hence the matric suction remains unchanged during the shearing phase. As suggested by Ong (1999), strain rates between 0.009 and 0.081 %/min results in constant matric suction over shearing stage.

Upon starting the stage, the bottom platen moves up based on the defined strain rate while the load ram (resting on top of the sample) is stationary. Thus, specimen is steadily compressed between the bottom pedestal and load ram and compression load gradually increases till soil sample reaches to the failure point. The magnitude of the deviatoric stress is calculated from the recorded load and corrected area of the specimen. The volumetric strain of the specimen corresponds to the amount of water flowing back to the inner cell pressure volume controller from the inner cell. Void ratio at each increment of the deviatoric stress is directly obtained from the sample volumetric change. The amount of water dissipated from the sample is monitored by the pore-water pressure volume controller. The recorded values are later used with the calculated void ratio to estimate the change of degree of saturation with deviatoric stress. The incremental axial strain is calculated based on the ratio of the incremental change of the sample's height to the initial height of the sample. Finally, the shear strain is obtained as follows,

$$\varepsilon_s = \varepsilon_a - \frac{\varepsilon_v}{3} \quad (I.1)$$

where  $\varepsilon_s$ ,  $\varepsilon_a$  and  $\varepsilon_v$  are shear strain, axial strain and volumetric strain, respectively.

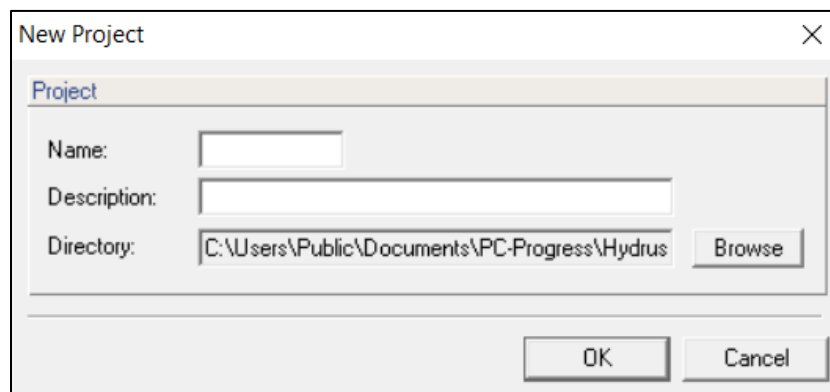
## APPENDIX H HYDRUS SOFTWARE

Several versions of Hydrus software are available for simulating water, heat and solute transport in one-two-and three-dimensional unsaturated media. Hydrus 1-D was utilized along with this study to model hydrological variations within the unsaturated zone over various seasons. The main screen of the software contains two sections, as “Pre-processing” and “Post-processing”, that each of which include several subsections. Type of simulation (water, heat or solute movement), geometry of the soil layer, time characteristics of hydrological events, hydraulic equation used for simulation, water flow condition and pressure head distribution in soil profile are all specified along pre-processing steps. Simulation results (e.g. change of pressure head and volumetric water content with time) are collected in different subsections of the Post-processing. As a reminder, this study involved optimizing hydraulic parameters of the main drying portion of the in-situ SWCC by inverse simulation option offered by the Hydrus. Also, hydrological data associated with the other portions of the in-situ SWCC were simulated based on the direct simulation method. Step by step procedure of conducting simulation by each method is presented in this Appendix.

### ***Inverse simulation***

➤ **Step 1.** Define a new project

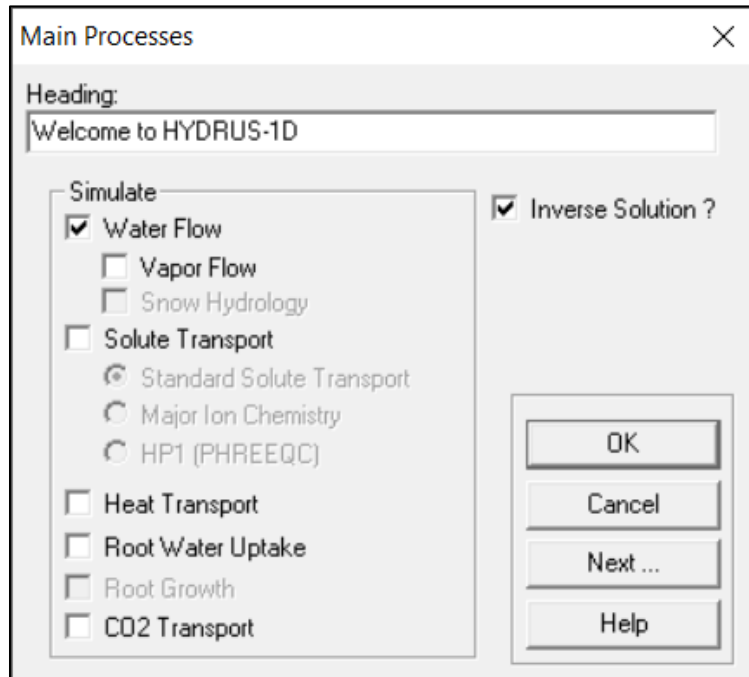
Once the software is run, name and location of the project is specified in the screen shown below.



➤ **Step 2.** Determination of the main process and simulation method

With clicking on “Main Process” tab under “Pre-processing” section, “Water Flow” is marked as the intention is to model water infiltration. Also, the method of simulation,

either direct or inverse, is selected over this screen. Thus, the box associated with the “Inverse Solution” is checked.

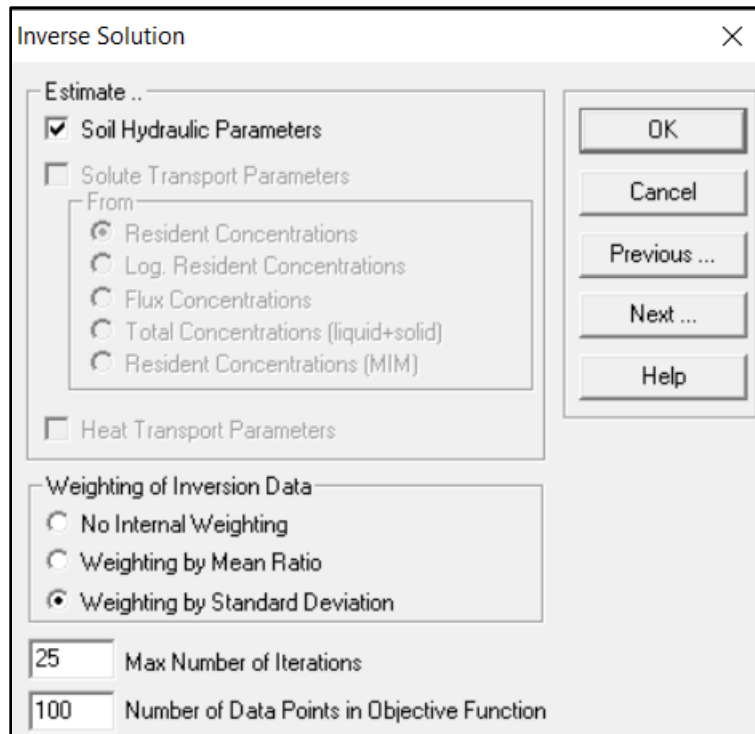


Following with clicking on the Next button, “Inverse Solution” screen appears.

➤ **Step 3.** Specify what parameters to be optimized

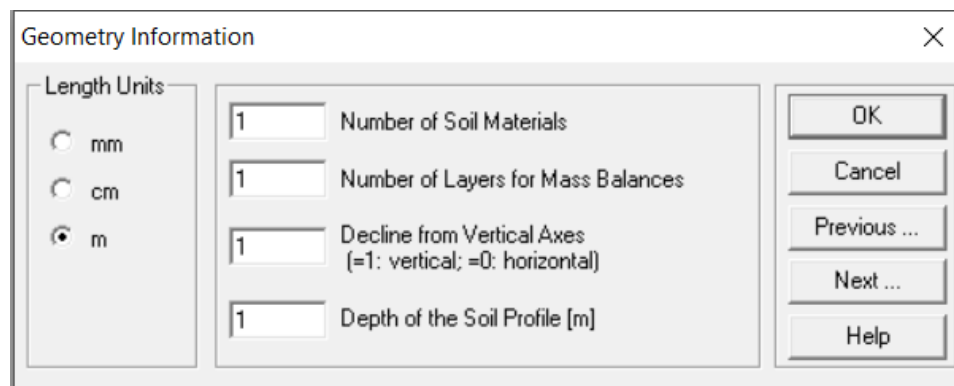
Since the “Water Flow” was selected in previous step, the software is automatically set to estimate “Soil Hydraulic Parameters”. Also, the user determines the method of “Weighting of Inversion Data”. Three options are offered by the software, as “No Internal Weighting”, “Weighting by Mean Ratio” or “Weighting by Standard Deviation”. Upon selecting “No Internal Weighting” option, users must manually set weights for data points in the “Data for Inverse Solution” screen. In case of selecting either “Weighting by Mean Ratio” or “Weighting by Standard Deviation”, the software computes either means or standard deviations of various data (e.g. pressure heads, volumetric water contents, etc.), and then adjust the weights correspondingly. Afterwards, the number of iterations is specified such that if zero is selected as the number of iterations, the software performs direct simulation. Finally, the “Number of Data Points in Objective Function” is specified which corresponds to the total number of the measured data.





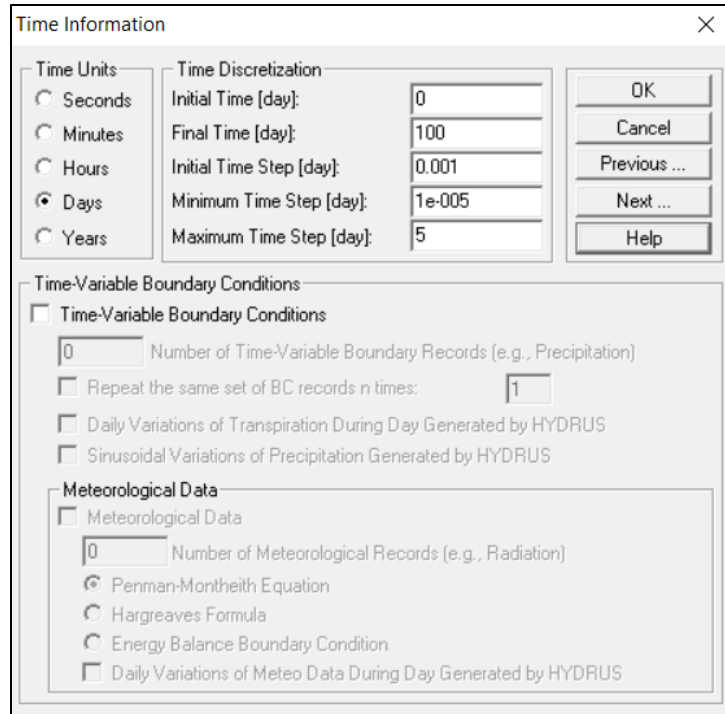
- **Step 4.** Set geometrical characteristics of the studying site

Geometry information screen allows user to specify the length unit to be used throughout the simulation, number of materials existing within the soil layer, inclination of the soil profile (either vertical or horizontal) and the depth of the soil layer.



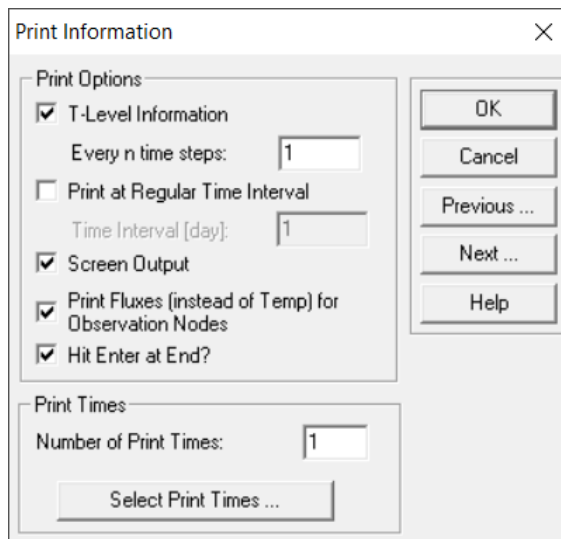
- **Step 5.** Define time characteristics

The third subsection of the “Pre-processing”, “Time Information” screen, is used for defining time unit throughout of the calculations, start and end of the simulation (e.g. initial and last day) and how the time to be discretized.



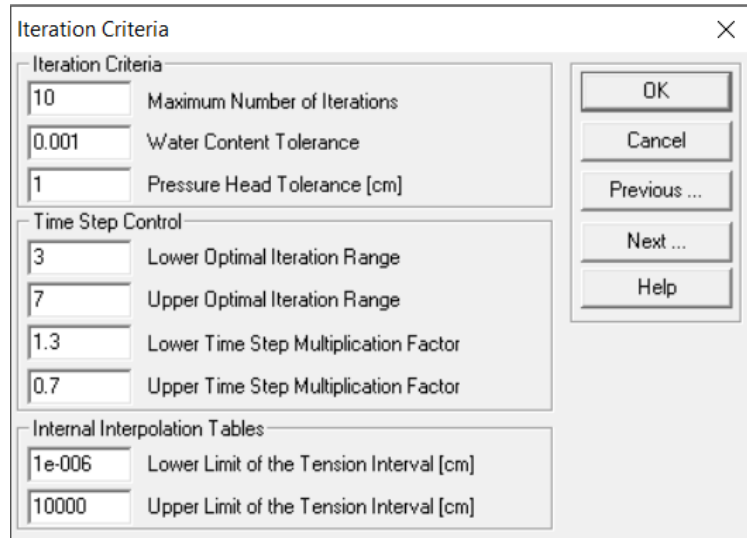
➤ **Step 6.** Input print information

“Print Information” is the fourth screen, where the user decides how often the results to be printed, either on regular time intervals or at pre-determined times.



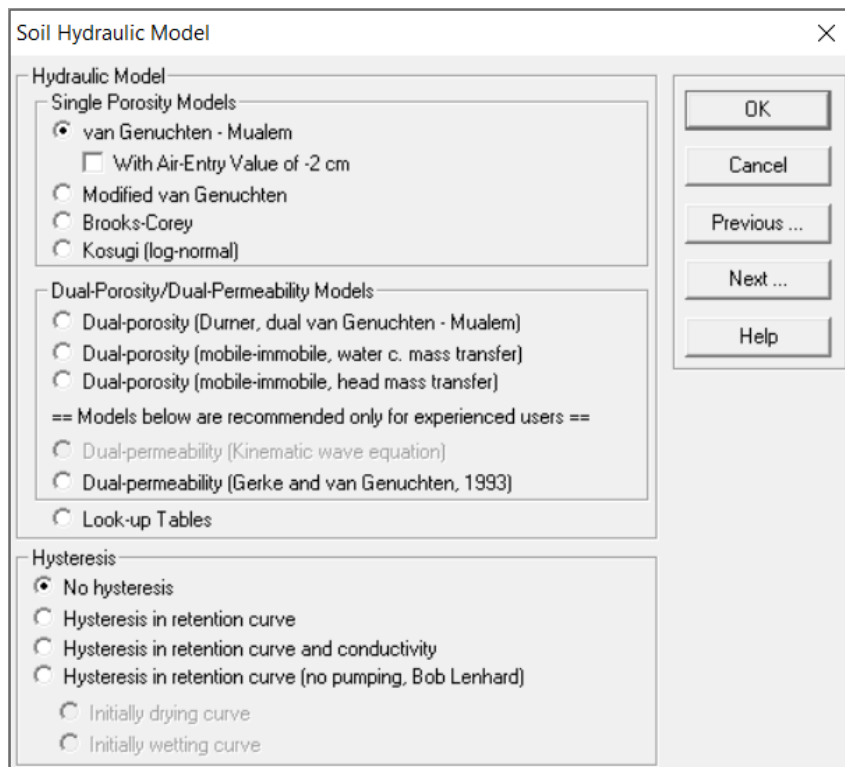
➤ **Step 7.** Set water flow iteration criteria

The process of providing numerical solution to the Richards equation is controlled by the iteration criteria specified in “Water Flow-Iteration Criteria” screen. Default values defined by the software for “Iteration Criteria”, “Time Step Control” and “Internal Interpolation Tables” are recommended to be left unchanged (Simunek et al., 2018).



➤ **Step 8.** Select hydraulic model

Upon clicking on “Water Flow-Soil Hydraulic Property Model” screen, software offers various models that can be utilized for describing hydrologic characteristics of the soil (pressure head and volumetric water content). A typical unsaturated soil exposing to seasonal hydrological variations may reveal hysteresis in retention curve and hydraulic conductivity. Over “Hysteresis” section, the user would specify the hysteresis condition of the site soil.



➤ **Step 9.** Input hydraulic parameters and set constrain to optimization

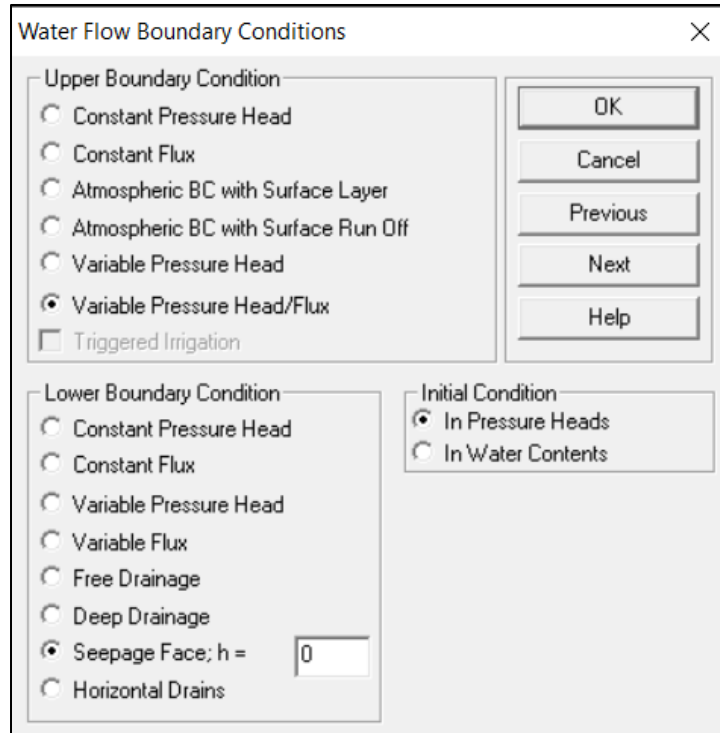
The initial values of the fitting parameters associated with the hydraulic model selected in the previous step are inputted into the corresponding boxes shown on “Water Flow Parameters” screen. It is recommended to use the hydraulic parameters obtained by fitting selected model to the measured hydrological data. If no hydrogel data is available, the user can estimate fitting parameters based on the soil type or physical properties of the soil. Hydraulic parameters needed to be optimized are specified by marking the appropriate box. Also, the user can set parameter constraint for optimization by defining a minimum and maximum value for each selected parameter. During optimization process, the value of the selected parameter (s) can vary within the range defined by the minimum and maximum values. If zero is inputted as the minimum and maximum values, the associated parameter is considered as unconstrained and can accept any value. Furthermore, unmarked parameters are kept unchanged during inverse simulation.

	Qr	Qs	Alpha	n	Ks	l
<b>Initial Estimate</b>	0.07	0.43	3.6	1.1	0.2496	0.5
<b>Minimum Value</b>	0	0	4	1.2	0	0
<b>Maximum Value</b>	0	0	3	1.05	0	0
<b>Fitted ?</b>	<input type="checkbox"/>	<input type="checkbox"/>	<input checked="" type="checkbox"/>	<input checked="" type="checkbox"/>	<input type="checkbox"/>	<input type="checkbox"/>

Soil Catalog for Initial Estimate:

➤ **Step 10.** Specify water flow boundary conditions

Water flow condition at the top and bottom ends of the soil profile is selected in “Water Flow Boundary Conditions”. Several factors such as pressure head and water flux conditions at the ground surface, location of the water table and drainage condition at the end of the soils column directly determine the upper and lower boundary conditions. In the “Initial Condition” box, the user can select if the initial condition of the water flow is defined based on the pressure head or the volumetric water content. For this study “Variable Pressure Head/Flux” and “Seepage Face” were respectively set as upper and lower boundary conditions.



After clicking on “Next”, the software directs user to “Variable Boundary Conditions” subsection

➤ **Step 11.** Input data associated with time and flux

The “Time Variable Boundary Conditions” screen consists of five different sets of data, as Time, time-dependent flux at the ground surface “Flux top”, absolute value of the minimum allowable pressure head at the ground surface “HCritA”, time-dependent pressure head at the ground surface “hTop”, and an variable for selecting if pressure head or flux is used “KodTop” (-1 for flux and +1 for pressure head). Depending on the number of data points specified in Step 3, the software defines the equal number of time data points (inside the first column of the “Time Variable Boundary Conditions” screen). Then, user inputs magnitude of the flux at the ground surface, corresponding to each time point. Default value of the “HCritA” is 1000 m, which was also used over simulations in this study. During field measurement, only time-dependent rainfall data were collected, hence no data associated with the pressure head at ground surface “hTop” are available., In this case, the time-dependent pressure heads “hTop” was left unchanged (the default value is zero) and the value of “KodTop” was set to -1 for all time data points. Accordingly, the software performs computation by only using flux at the surface.

	Time [days]	FluxTop [m/days]	hCritA [m]	hTop [m]	KodTop
1	1	0.004572	1000	0	-1
2	2	0.00508	1000	0	-1
3	3	0.004572	1000	0	-1
4	4	-0.012954	1000	0	-1
5	5	0.004064	1000	0	-1
6	6	0.00381	1000	0	-1
7	7	0.00508	1000	0	-1
8	8	0.004572	1000	0	-1
9	9	0.00508	1000	0	-1
10	10	0.004318	1000	0	-1
11	11	0.00381	1000	0	-1
12	12	0.003302	1000	0	-1
13	13	0.004318	1000	0	-1
14	14	-0.00508	1000	0	-1

Buttons: OK, Cancel, Previous ..., Next ..., Help ..., Add Line, Delete Line, Default Time

➤ **Step 12.** Input data for inverse solution

This step requires the user to input measured data at the observation point (in-situ data at a specific depth). These data will be used by the software during the inverse optimization. More clarification, software systematically optimizes the hydraulic parameter such that the value of the predicted data matches the measured data. Five different sets of data must be inputted inside the corresponding boxes in “Data for Inverse Solution” screen. Values of data inserted into the “X”, “Y” and “Position” columns are directly depended on the values selected for “Type”. A table explaining how to select the value of “Type” with respect to the available/measured data can be found in manual of HYDRUS1-D. In this study, the measured values of the pressure head were used for optimizing hydraulic parameters. Thus, the “Type” was set equal to 1 for all data points. Accordingly, time data were inputted inside, the first column, “X”. The actual values of the pressure head corresponding to each time point were inserted into the column “Y”. The fourth column, “Position”, specifies the location of a node corresponding to the depth of data collection. Therefore, 1 is selected for the “Position” as the pressure head measurement was conducted at one depth. “Weight” is the weight associated with a specific data point and was set equal to 1.

Data for Inverse Solution

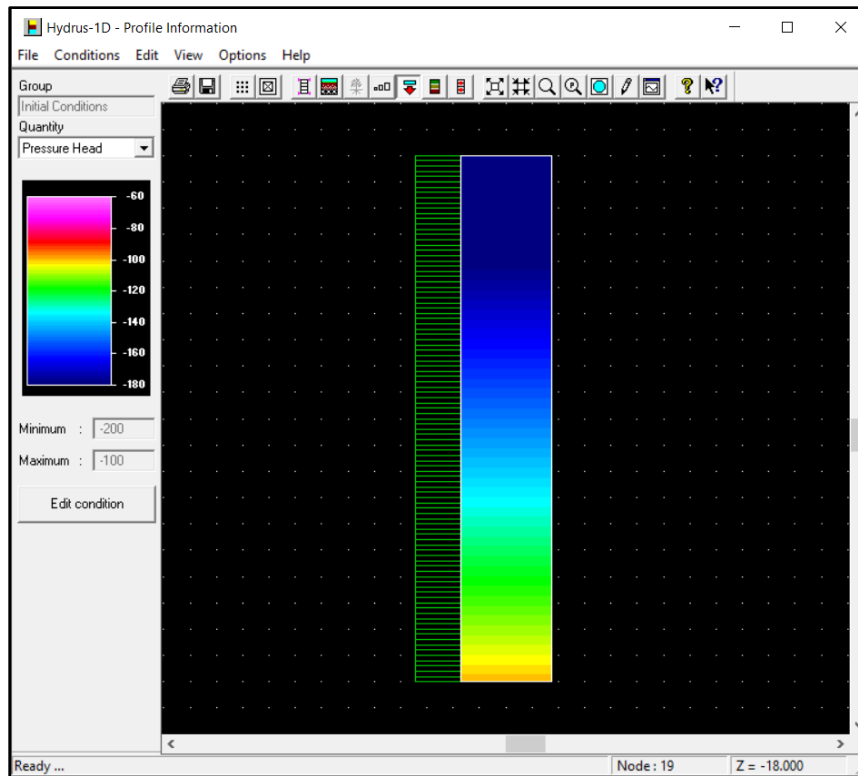
	X	Y	Type	Position	Weight
1	1	-0.73	1	1	1
2	2	-0.74	1	1	1
3	3	-0.74	1	1	1
4	4	-0.75	1	1	1
5	5	-0.75	1	1	1
6	6	-0.75	1	1	1
7	7	-0.75	1	1	1
8	8	-0.75	1	1	1
9	9	-0.75	1	1	1
10	10	-0.75	1	1	1
11	11	-0.75	1	1	1
12	12	-0.76	1	1	1
13	13	-0.76	1	1	1
14	14	-0.76	1	1	1
15	15	-0.76	1	1	1

Show list boxes (not recommended for large data files)

OK  
Cancel  
Previous ...  
Next ...  
Add Line  
Delete Line  
Help ...

➤ **Step 13.** Define soil profile characteristics

Upon clicking on “Soil Profile-Graphical Editor” the soil’s body is shown in form a graphical column, in which the border of layers within the soil’s body (if the studying profile consists of more than one material) and border of sublayers within each layer is specified. Also, the node associated with the depth that pressure head was measured is identified in this column. Regarding the magnitude of the first measured pressure head at the specified node, pressure head at the ground surface and end of the soil profile is defined. It was assumed that the hydrostatic pressure head condition prevails, in which the pressure head changes with depth. Thus, the magnitude of the pressure head at ground surface and end of the soil column were set based on the distance from the node to the ground surface and bottom of the soil profile.



➤ **Step 14.** Review soil profile summary

After closing the “Profile Information” window, the “Soil Profile Summary” screen pops up. This window presents data about depth discretization “z [cm]”, value of pressure head “h [cm]” at the first time point corresponding to each depth, root distribution “Root [1/cm]”, scaling factors (“Axz”, “Bxz”, “Dxz”), and material and layer distributions (Mat and Lay) within the soil’s body.


	z [cm]	h [cm]	Root [1/cm]	Axz	Bxz	Dxz	Mat
1	0	-200	0	1	1	1	1
2	1	-199	0	1	1	1	1
3	2	-198	0	1	1	1	1
4	3	-197	0	1	1	1	1
5	4	-196	0	1	1	1	1
6	5	-195	0	1	1	1	1
7	6	-194	0	1	1	1	1
8	7	-193	0	1	1	1	1
9	8	-192	0	1	1	1	1
10	9	-191	0	1	1	1	1
11	10	-190	0	1	1	1	1
12	11	-189	0	1	1	1	1
13	12	-188	0	1	1	1	1
14	13	-187	0	1	1	1	1
15	14	-186	0	1	1	1	1

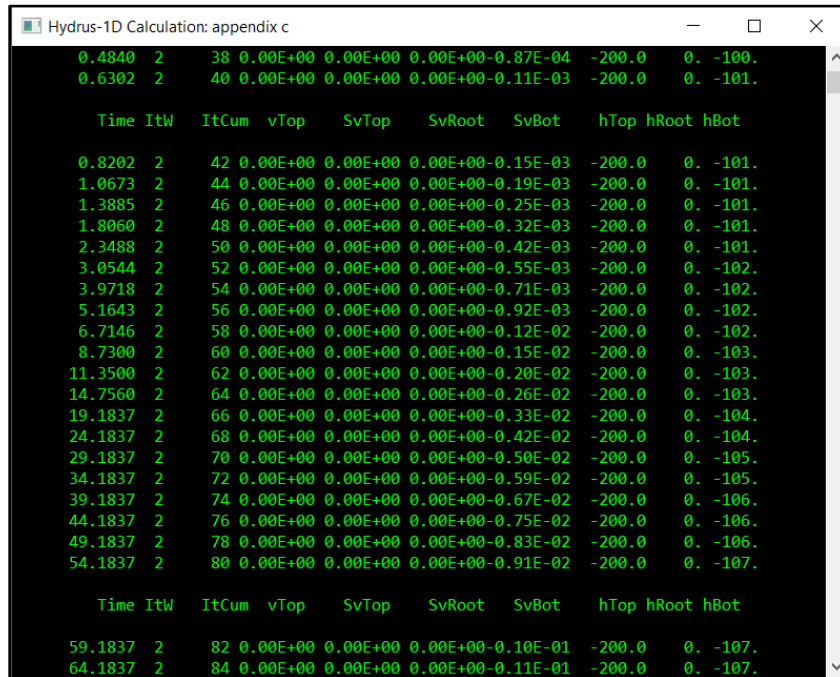
Buttons: Set to Default Values, Set Initial Conditions Equal to Field Capacity, OK, Cancel, Previous, Next, Help



➤ **Step 15.** Run the test

Having checked the tabulated data under the “Soil Profile Summary” screen, the test is

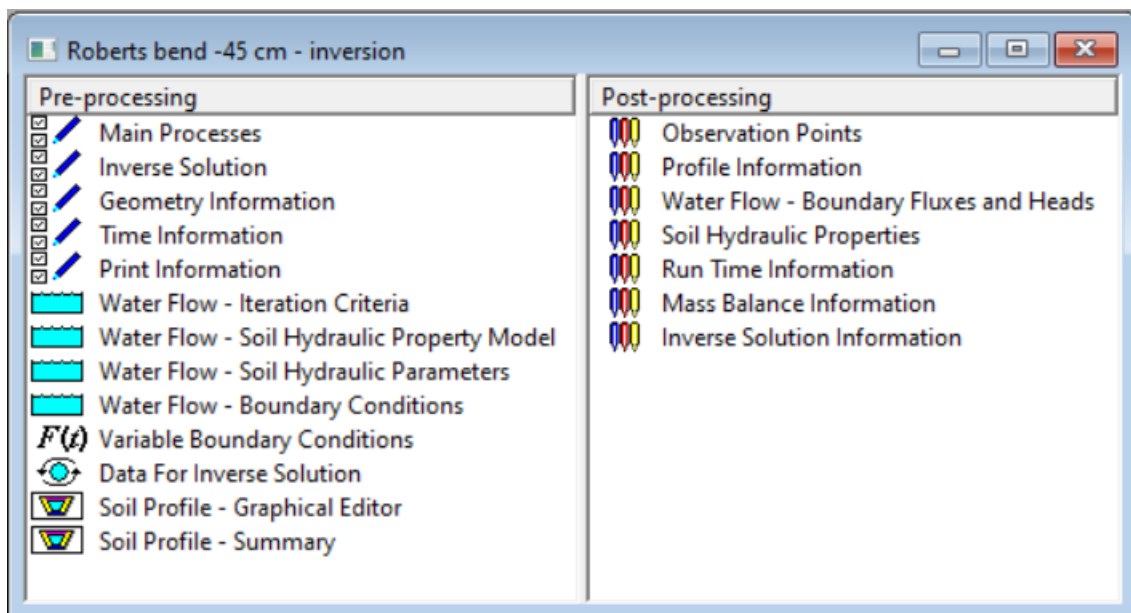
initiated by pressing “Execute HYDRUS” button, . The calculations are performed, with some results shown in a Dos screen.



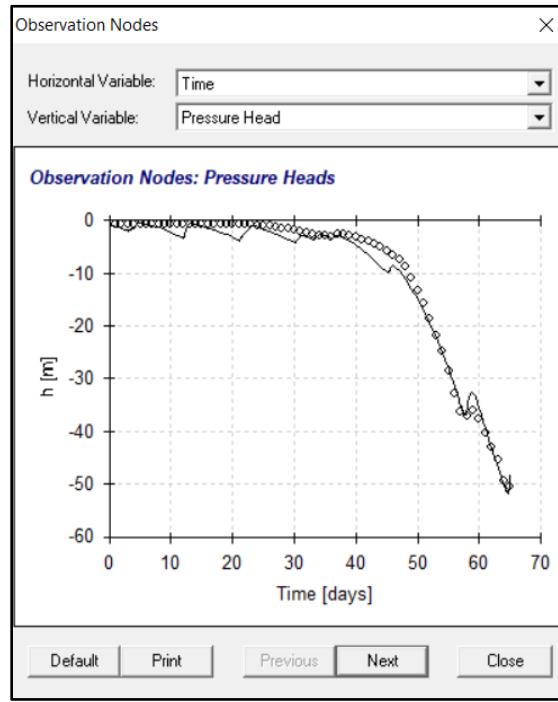
Time	ItW	ItCum	vTop	SvTop	SvRoot	SvBot	hTop	hRoot	hBot
0.4840	2	38	0.00E+00	0.00E+00	0.00E+00	-0.87E-04	-200.0	0.	-100.
0.6302	2	40	0.00E+00	0.00E+00	0.00E+00	-0.11E-03	-200.0	0.	-101.
0.8202	2	42	0.00E+00	0.00E+00	0.00E+00	-0.15E-03	-200.0	0.	-101.
1.0673	2	44	0.00E+00	0.00E+00	0.00E+00	-0.19E-03	-200.0	0.	-101.
1.3885	2	46	0.00E+00	0.00E+00	0.00E+00	-0.25E-03	-200.0	0.	-101.
1.8060	2	48	0.00E+00	0.00E+00	0.00E+00	-0.32E-03	-200.0	0.	-101.
2.3488	2	50	0.00E+00	0.00E+00	0.00E+00	-0.42E-03	-200.0	0.	-101.
3.0544	2	52	0.00E+00	0.00E+00	0.00E+00	-0.55E-03	-200.0	0.	-102.
3.9718	2	54	0.00E+00	0.00E+00	0.00E+00	-0.71E-03	-200.0	0.	-102.
5.1643	2	56	0.00E+00	0.00E+00	0.00E+00	-0.92E-03	-200.0	0.	-102.
6.7146	2	58	0.00E+00	0.00E+00	0.00E+00	-0.12E-02	-200.0	0.	-102.
8.7300	2	60	0.00E+00	0.00E+00	0.00E+00	-0.15E-02	-200.0	0.	-103.
11.3500	2	62	0.00E+00	0.00E+00	0.00E+00	-0.20E-02	-200.0	0.	-103.
14.7560	2	64	0.00E+00	0.00E+00	0.00E+00	-0.26E-02	-200.0	0.	-103.
19.1837	2	66	0.00E+00	0.00E+00	0.00E+00	-0.33E-02	-200.0	0.	-104.
24.1837	2	68	0.00E+00	0.00E+00	0.00E+00	-0.42E-02	-200.0	0.	-104.
29.1837	2	70	0.00E+00	0.00E+00	0.00E+00	-0.50E-02	-200.0	0.	-105.
34.1837	2	72	0.00E+00	0.00E+00	0.00E+00	-0.59E-02	-200.0	0.	-105.
39.1837	2	74	0.00E+00	0.00E+00	0.00E+00	-0.67E-02	-200.0	0.	-106.
44.1837	2	76	0.00E+00	0.00E+00	0.00E+00	-0.75E-02	-200.0	0.	-106.
49.1837	2	78	0.00E+00	0.00E+00	0.00E+00	-0.83E-02	-200.0	0.	-106.
54.1837	2	80	0.00E+00	0.00E+00	0.00E+00	-0.91E-02	-200.0	0.	-107.
59.1837	2	82	0.00E+00	0.00E+00	0.00E+00	-0.10E-01	-200.0	0.	-107.
64.1837	2	84	0.00E+00	0.00E+00	0.00E+00	-0.11E-01	-200.0	0.	-107.

➤ **Step 16.** Post-Processing

Once the computations are completed and “Enter” button is pressed, the simulated data are collected under the “Post-processing” section.



To observe a particular set of simulated results, the associated sub-section is opened, e.g. the measured and predicted pressure head with time at the specified node (depth of measurement) can be found under “Observation Points”.

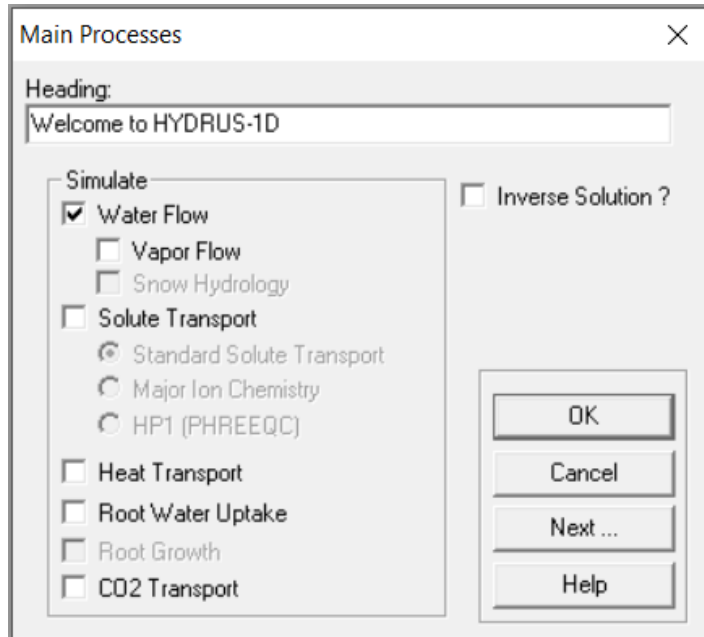


### ***Direct simulation***

In comparison with the inverse simulation method, the main screen of the test in direct simulation method contains less subsections in “Pre-processing” part. In addition, the process of defining some mutual subsections in both methods is exactly the same. Particularly, subsections including “Geometry Information”, “Time Information”, “Print Information”, “Water flow – Iteration Criteria”, “Water flow – Soil Hydraulic Property Model”, “Water flow – Boundary Conditions”, “Variable Boundary Conditions”, and “Soil Profile – Graphical Editor” are defined in the same manner for both direct and inverse simulations. Besides, processes of reviewing data summary, running the test, and observing simulation results are conducted similarly. To avoid redundancy, the mentioned subsections and processes will not be discussed over this part of the appendix.

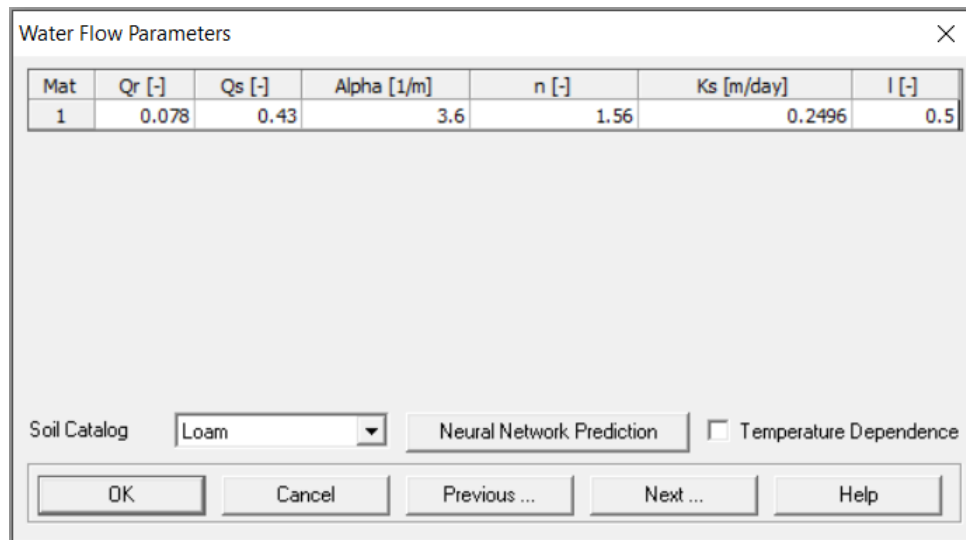
➤ **Step 1.** Determination of the main process and simulation method

Under the “Main Process”, the water flow is marked while the “Inverse Solution” is left unchecked.



➤ **Step 2.** Input hydraulic parameters

Over direct simulation, value of the hydraulic parameters stays constant during the simulation process. To predict hydrologic data of the different segments of the in-situ SWCC, hydraulic parameters associate with each segment were inputted in “Water Flow Parameters” screen.



## REFERENCES

- Ahmed, F. S., and Bryson, L. S. (2019). Influence of Hydrologic Behavior in Assessing Rainfall-Induced Landslides. In *Geo-Congress 2019: Embankments, Dams, and Slopes*. Reston, VA: American Society of Civil Engineers, 194-204.
- Alonso, E. E., Gens, A., and Josa, A. (1990). A constitutive model for partially saturated soils. *Géotechnique*, 40(3), 405-430.
- Aramahi, B., Alshibli, K. A., Fratta, D., and Trautwein, S. (2008). A suction-control apparatus for the measurement of P and S-wave velocity in soils. *Geotechnical Testing Journal*, 31(1), 12-23.
- Atkinson J.H., and Salfors G. (1991) Experimental determination of soil properties. In *Proceedings of the 10th European conference on soil mechanics and foundation engineering*, Florence, Italy. 915-956
- Battle-Aguilar, J., and Cook, P. G. (2012). Transient infiltration from ephemeral streams: A field experiment at the reach scale. *Water Resources Research*, 48(11).
- Baum, R. L., Godt, J. W., and Savage, W. Z. (2010). Estimating the timing and location of shallow rainfall-induced landslides using a model for transient, unsaturated infiltration. *Journal of Geophysical Research: Earth Surface*, 115(F3).
- Benson, C. H., Chiang, I., Chalermyanont, T., and Sawangsuriya, A. (2014). Estimating van Genuchten parameters  $\alpha$  and  $n$  for clean sands from particle size distribution data. In *From Soil Behavior Fundamentals to Innovations in Geotechnical Engineering: Honoring Roy E. Olson*, 410-427.
- Biglari, M., Mancuso, C., d'Onofrio, A., Jafari, M. K., and Shafiee, A. (2011). Modelling the initial shear stiffness of unsaturated soils as a function of the coupled effects of the void ratio and the degree of saturation. *Computers and Geotechnics*, 38(5), 709-720.
- Bittelli, M., Valentino, R., Salvatorelli, F., and Pisa, P. R. (2012). Monitoring soil-water and displacement conditions leading to landslide occurrence in partially saturated clays. *Geomorphology*, 173, 161-173.
- Bolzon, G., Schrefler, B. A., and Zienkiewicz, O. C. (1996). Elastoplastic soil constitutive laws generalized to partially saturated states. *Géotechnique*, 46(2), 279-289.
- Budhu, M. (2008). Soil mechanics and foundations. John Wiley and Sons, Inc.
- Cabarkapa, Z., Cuccovillo, T., and Gunn, M. (1999). Some aspects of the pre-failure behaviour of unsaturated soil. In *Proceedings of the 2nd International Conference on Pre-failure Behavior of Geomaterials*, Turin, Italy. 1, 159-165.

- Camacho-Tauta, J. F., Jimenez Alvarez, J. D., and Reyes-Ortiz, O. J. (2012). A procedure to calibrate and perform the bender element test. *Dyna*, 79(176), 10-18.
- Chang, C. S., Deng, Y., and Yang, Z. (2017). Modeling of minimum void ratio for granular soil with effect of particle size distribution. *Journal of Engineering Mechanics*, 143(9), 04017060.
- Chen, P., Lu, N., Formetta, G., Godt, J. W., and Wayllace, A. (2018). Tropical storm-induced landslide potential using combined field monitoring and numerical modeling. *Journal of Geotechnical and Geoenvironmental Engineering*, 144(11), 05018002.
- Cho, G. C., and Santamarina, J. C. (2001). Unsaturated particulate materials—particle-level studies. *Journal of geotechnical and geoenvironmental engineering*, 127(1), 84-96.
- Crawford, M. M., and Bryson, L. S. (2018). Assessment of active landslides using field electrical measurements. *Engineering Geology*, 233, 146-159.
- Cui, Y. J., and Delage, P. (1996). Yielding and plastic behaviour of an unsaturated compacted silt. *Géotechnique*, 46(2), 291-311.
- Cunningham, M. R., Ridley, A. M., Dineen, K., and Burland, J. B. (2003). The mechanical behaviour of a reconstituted unsaturated silty clay. *Géotechnique*, 53(2), 183-194.
- Dangla, P., Malinsky, L., and Coussy, O. (1997). Plasticity and imbibition-drainage curves for unsaturated soils: a unified approach. In *Proceeding of the 6th International Symposium on Numerical Models in Geomechanics, NUMOG*, Montreal, Quebec, A.A. Balkema, Rotterdam. 141-146.
- Dong, Y. and Lu, N., (2016a). Dependencies of shear wave velocity and shear modulus of soil on saturation. *Journal of Engineering Mechanics*, 142(11), 04016083.
- Dong, Y., and Lu, N. (2016b). Correlation between small-strain shear modulus and suction stress in capillary regime under zero total stress conditions. *Journal of Geotechnical and Geoenvironmental Engineering*, 142(11), 04016056.
- Dong, Y., Lu, N., and McCartney, J. S. (2016). Unified model for small-strain shear modulus of variably saturated soil. *Journal of Geotechnical and Geoenvironmental Engineering*, 142(9), 04016039.
- Dong, Y., Lu, N., and McCartney, J. S. (2018). Scaling shear modulus from small to finite strain for unsaturated soils. *Journal of Geotechnical and Geoenvironmental Engineering*, 144(2), 04017110.
- Duong, T. T., Do, D. M., and Yasuhara, K. (2019). Assessing the Effects of Rainfall Intensity and Hydraulic Conductivity on Riverbank Stability. *Water*, 11(4), 741.

- Fan, Y., Gong, J., Wang, Y., Shao, X., and Zhao, T. (2018). Application of Philip infiltration model to film hole irrigation. *Water Supply*, 19(3), 978-985.
- Fredlund, D. G., and Houston, S. L. (2013). Interpretation of soil-water characteristic curves when volume change occurs as soil suction is changed. *Advances in unsaturated soils*, 1, 15.
- Fredlund, D. G., Morgenstern, N. R., and Widger, R. A. (1978). The shear strength of unsaturated soils. *Canadian Geotechnical Journal*, 15(3), 313-321.
- Gallipoli, D., Gens, A., Sharma, R., and Vaunat, J. (2003a). An elasto-plastic model for unsaturated soil incorporating the effects of suction and degree of saturation on mechanical behaviour. *Géotechnique*, 53(1), 123-136.
- Gallipoli, D., Wheeler, S. J., and Karstunen, M. (2003b). Modelling the variation of degree of saturation in a deformable unsaturated soil. *Géotechnique*, 53(1), 105-112.
- Gao, Y., Sun, D. A., Zhu, Z., and Xu, Y. (2018). Hydromechanical behavior of unsaturated soil with different initial densities over a wide suction range. *Acta Geotechnica*, 1-12.
- GDS Instruments (2017). User's manual for Resonant Column, Bender Elements and StressPath Triaxial.
- Gens, A. (1996). Constitutive modelling: Application to compacted soils. In *Proceedings of the 1st International Conference on Unsaturated Soils*, Paris, France. 3, 1179-1200.
- Gens, A., Sánchez, M., and Sheng, D. (2006). On constitutive modelling of unsaturated soils. *Acta Geotechnica*, 1(3), 137.
- Ghayoomi, M., Suprunenko, G., and Mirshekari, M. (2017). Cyclic triaxial test to measure strain-dependent shear modulus of unsaturated sand. *International Journal of Geomechanics*, 17(9), 04017043.
- Godt, J. W., Baum, R. L., and Lu, N. (2009). Landsliding in partially saturated materials. *Geophysical research letters*, 36(2).
- Godt, J. W., Şener-Kaya, B., Lu, N., and Baum, R. L. (2012). Stability of infinite slopes under transient partially saturated seepage conditions. *Water Resources Research*, 48(5).
- Gowdich, L. C., and Munoz-Carpena, R. (2018). 3DMGAR: A transient quasi-3D point-source Green–Ampt infiltration and redistribution model. *Vadose Zone Journal*, 17(1).
- Han, Z., and Vanapalli, S. K. (2016). Stiffness and shear strength of unsaturated soils in relation to soil-water characteristic curve. *Géotechnique*, 66(8), 627-647.
- Hardin, B. O., and Kalinski, M. E. (2005). Estimating the shear modulus of gravelly soils. *Journal of Geotechnical and Geoenvironmental engineering*, 131(7), 867-875.

- Heitor, A., Indraratna, B., and Rujikiatkamjorn, C. (2013). Laboratory study of small-strain behavior of a compacted silty sand. *Canadian Geotechnical Journal*, 50(2), 179-188.
- Henshall, G. (1996). Improvement in the MATMOD equations for modeling solute effects and yield-surface distortion. *Unified Constitutive Laws of Plastic Deformation*. Academic Press, Inc, 6277 Sea Harbor Dr, Orlando, FL 32887-4900, USA, 1996., 153-227.
- Hillel, D. (1998). Environmental Soil Physics: Fundamentals, applications, and environmental considerations. San Diego, CA, USA: Academic Press.
- Hippley, B. T. (2003). Elastic stiffness of unsaturated soil. PhD thesis, University of Kentucky, USA.
- Hoyos, L. R., and Pérez-Ruiz, D. D. (2012). A refined approach to Barcelona Basic Model using the apparent tensile strength concept. In *Unsaturated Soils: Research and Applications* (pp. 103-110). Springer, Berlin, Heidelberg.
- Hoyos, L. R., Suescun, E. A., and Puppala, A. J. (2011). Small-strain stiffness of unsaturated soils using a suction-controlled resonant column device with bender elements. In *Proceedings of the Geo-Frontiers 2011 Conference*, Dallas, Texas. 4313-4322.
- Hoyos, L. R., Suescún-Florez, E. A., and Puppala, A. J. (2015). Stiffness of intermediate unsaturated soil from simultaneous suction-controlled resonant column and bender element testing. *Engineering Geology*, 188, 10-28.
- Inci, G., Yesiller, N., and Kagawa, T. (2003). Experimental investigation of dynamic response of compacted clayey soils. *Geotechnical Testing Journal*, 26(2), 125-141.
- Jommi, C. (2000). Remarks on the constitutive modelling of unsaturated soils. *Experimental Evidence and Theoretical Approaches in Unsaturated Soils*, 139-153.
- Khosravi, A. (2011). Small strain shear modulus of unsaturated, compacted soils during hydraulic hysteresis. Doctoral dissertation, University of Colorado, Boulder, USA.
- Khosravi, A., and McCartney, J. S. (2009). Impact of stress state on the dynamic shear modulus of unsaturated, compacted soils. In *4th Asia Pacific Conference on Unsaturated Soils*, Newcastle, Australia. 23-25.
- Khosravi, A., and McCartney, J. S. (2012). Impact of hydraulic hysteresis on the small-strain shear modulus of low plasticity soils. *Journal of Geotechnical and Geoenvironmental Engineering*, 138(11), 1326-1333.
- Khosravi, A., Ghayoomi, M., McCartney, J., and Ko, H. Y. (2010). Impact of effective stress on the dynamic shear modulus of unsaturated sand. In *GeoFlorida 2010: Advances in Analysis, Modeling & Design*. 410-419.

- Khosravi, A., Rahimi, M., Gheibi, A., and Mahdi Shahrabi, M. (2018a). Impact of plastic compression on the small strain shear modulus of unsaturated silts. *International Journal of Geomechanics*, 18(2), 04017138.
- Khosravi, A., Salam, S., McCartney, J. S., and Dadashi, A. (2016). Suction-induced hardening effects on the shear modulus of unsaturated silt. *International Journal of Geomechanics*, 16(6), D4016007.
- Khosravi, A., Shahbazan, P., and Pak, A. (2018b). Impact of hydraulic hysteresis on the small strain shear modulus of unsaturated sand. *Soils and Foundations*, 58(2), 344-354.
- Kirkham, J. M., Smith, C. J., Doyle, R. B., and Brown, P. H. (2019). Inverse modelling for predicting both water and nitrate movement in a structured-clay soil (Red Ferrosol). *PeerJ*, 6, e6002.
- Kohgo, Y., Nakano, M., and Miyazaki, T. (1993). Theoretical aspects of constitutive modelling for unsaturated soils. *Soils and foundations*, 33(4), 49-63.
- Kool, J. B., and Parker, J. C. (1987). Development and evaluation of closed-form expressions for hysteretic soil hydraulic properties. *Water Resources Research*, 23(1), 105-114.
- Kurimoto, Y., Kobayashi, S., Tsunemoto, T., and Zhang, F. (2017). Uniaxial compression test of unsaturated masado under constant degree of saturation condition and its modeling. *International Journal of GEOMATE*, 12(31), 83-87.
- Lee, S. H., Seo, W. S., and Kim, D. S. (2007). Evaluation of modulus of unsaturated compacted soils in various matric suctions using modified volumetric pressure plate extractor. In *Proceedings of 60th Canadian Geotechnical Conference*, Ottawa, Canada. 1037-1044.
- Leong, E. C., Rahardjo, H., and Fredlund, D. G. (2003). A comparative study of constitutive models for unsaturated soils. In *Proceedings of 2nd Asian Conference on Unsaturated Soils*, Osaka, Japan. 41-46.
- Li, N., Kinzelbach, W., Li, H., Li, W., and Chen, F. (2019). Decomposition technique for contributions to groundwater heads from inside and outside of an arbitrary boundary: application to Guantao County, North China Plain. *Hydrology and Earth System Sciences*, 23(7), 2823-2840.
- Lloret, A., Villar, M. V., Sanchez, M., Gens, A., Pintado, X., and Alonso, E. E. (2003). Mechanical behaviour of heavily compacted bentonite under high suction changes. *Géotechnique*, 53(1), 27-40.
- Lo Presti, D., Stacul, S., Meisina, C., Bordoni, M., and Bittelli, M. (2018). Preliminary validation of a novel method for the assessment of effective stress state in partially saturated soils by cone penetration tests. *Geosciences*, 8(1), 30.



- Loret, B., and Khalili, N. (2002). An effective stress elastic-plastic model for unsaturated porous media. *Mechanics of Materials*, 34(2), 97-116.
- Lu, N. (2016). Generalized soil water retention equation for adsorption and capillarity. *Journal of Geotechnical and Geoenvironmental Engineering*, 142(10), 04016051.
- Lu, N. and Likos, W.J. (2004). *Unsaturated Soil Mechanics*. John Wiley & Sons, Inc.
- Lu, N., and Godt, J. W. (2013). *Hillslope hydrology and stability*. Cambridge University Press.
- Lu, N., and Kaya, M. (2014). Power law for elastic moduli of unsaturated soil. *Journal of Geotechnical and Geoenvironmental Engineering*, 140(1), 46-56.
- Lu, N., and Khorshidi, M. (2015). Mechanisms for soil-water retention and hysteresis at high suction range. *Journal of Geotechnical and Geoenvironmental Engineering*, 141(8), 04015032.
- Lu, N., and Likos, W. J. (2006). Suction stress characteristic curve for unsaturated soil. *Journal of Geotechnical and Geoenvironmental engineering*, 132(2), 131-142.
- Lu, N., Godt, J. W., and Wu, D. T. (2010). A closed-form equation for effective stress in unsaturated soil. *Water Resources Research*, 46(5).
- Mancuso, C., Vassallo, R., and d'Onofrio, A. (2002). Small strain behavior of a silty sand in controlled-suction resonant column torsional shear tests. *Canadian Geotechnical Journal*, 39(1), 22-31.
- Masin, D. (2010). Predicting the dependency of a degree of saturation on void ratio and suction using effective stress principle for unsaturated soils. *International Journal for Numerical and Analytical Methods in Geomechanics*, 34(1), 73-90.
- McDowell, R. C. (1986). The geology of Kentucky-a text to accompany the geologic map of Kentucky. In: US Geological Survey Professional Paper 1151-H, 76.
- Mendoza, C. E., Colmenares, J. E., and Merchan, V. E. (2005). Stiffness of an unsaturated compacted clayey soil at very small strains. In *Proceedings of International Symposium on Advanced Experimental Unsaturated Soil Mechanics*, Trento, Italy. 199-204.
- Morales, L., Romero Morales, E. E., Jommi, C., Garzón Garzón, E., and Giménez, A. (2015). Ageing effects on the small-strain stiffness of a bio-treated compacted soil. *Géotechnique Letters*, 5(3), 217-223.
- Mpawenayo, R., and Gerard, P. (2019). Prediction of unsaturated shear strength from microstructurally based effective stress. In *E3S Web of Conferences*. 92, 07005. EDP Sciences.

- Mualem, Y. (1976). A new model for predicting the hydraulic conductivity of unsaturated porous media. *Water Resources Research*, 12(3), 513-522.
- Ng, C. W. W., and Yung, S. Y. (2008). Determination of the anisotropic shear stiffness of an unsaturated decomposed soil. *Géotechnique*, 58(1), 23-35.
- Ng, C. W. W., and Zhou, C. (2014). Cyclic behaviour of an unsaturated silt at various suctions and temperatures. *Géotechnique*, 64(9), 709-720.
- Ng, C. W. W., Xu, J., and Yung, S. Y. (2009). Effects of wetting–drying and stress ratio on anisotropic stiffness of an unsaturated soil at very small strains. *Canadian Geotechnical Journal*, 46(9), 1062-1076.
- Ngoc, T. P., Fatahi, B., and Khabbaz, H. (2019). Impacts of Drying-Wetting and Loading-Unloading Cycles on Small Strain Shear Modulus of Unsaturated Soils. *International Journal of Geomechanics*, 19(8), 04019090.
- Oh, W. T., and Vanapalli, S. K. (2014). Semi-empirical model for estimating the small-strain shear modulus of unsaturated non-plastic sandy soils. *Geotechnical and Geological Engineering*, 32(2), 259-271.
- Ong, B. H. (1999). Shear strength and volume change of unsaturated residual soil. Master of Engineering Thesis, Nanyang Technological University, Singapore.
- Payan, M. (2017). Study of small strain dynamic properties of sands and silty sands. Doctoral dissertation, University of New South Wales, Sydney, Australia.
- Perez-Ruiz, D. D. (2009). A refined true triaxial apparatus for testing unsaturated soils under suction-controlled stress paths. Doctoral dissertation, University of Texas, Arlington, USA.
- Pham, K., Kim, D., Lee, I. M., and Choi, H. (2019). Hydraulic-Mechanical Properties of Unsaturated Granite-Weathered Residual Soil in Korea. *Vadose Zone Journal*, 18(1).
- Picornell, M., Nazarian, S. (1998). Effect of soil suction on the low strain shear modulus of soils. In: *Proceeding of the 2nd International Conference on Unsaturated Soil*, Beijing, China. 102-107.
- Richards, L. A. (1931). Capillary conduction of liquids through porous mediums. *Physics*, 1(5), 318-333.
- Rong, W., and McCartney, J. S. (2017), Modeling the Seismic Compression of Unsaturated Sands. In *2nd Pan-American Conference on Unsaturated Soils*, Dallas, Texas. 584-594.
- Santagiuliana, R., and Schrefler, B. A. (2006). Enhancing the Bolzon-Schrefler-Zienkiewicz constitutive model for partially saturated soil. *Transport in Porous Media*, 65(1), 1-30.

- Sawanguriya, A., Edil, T. B., and Bosscher, P. J. (2008). Modulus-suction-moisture relationship for compacted soils. *Canadian Geotechnical Journal*, 45(7), 973-983.
- Sawanguriya, A., Edil, T. B., and Bosscher, P. J. (2009). Modulus-suction-moisture relationship for compacted soils in post compaction state. *Journal of Geotechnical and Geoenvironmental engineering*, 135(10), 1390-1403.
- Schnellmann, R., Rahardjo, H., and Schneider, H. R. (2015). Controlling parameter for unsaturated soil property functions: validated on the unsaturated shear strength. *Canadian Geotechnical Journal*, 52(3), 374-381.
- Sharma, R. S. (1998). Mechanical behavior of unsaturated highly expansive clays. Doctoral dissertation, University of Oxford, Oxford, England.
- Sheng, D. (2011). Constitutive modelling of unsaturated soils: Discussion of fundamental principles. *Unsaturated Soils*, 1, 91-112.
- Sheng, D., and Zhou, A. N. (2011). Coupling hydraulic with mechanical models for unsaturated soils. *Canadian Geotechnical Journal*, 48(5), 826-840.
- Sheng, D., Fredlund, D. G., and Gens, A. (2008a). A new modelling approach for unsaturated soils using independent stress variables. *Canadian Geotechnical Journal*, 45(4), 511-534.
- Sheng, D., Gens, A., Fredlund, D. G., and Sloan, S. W. (2008b). Unsaturated soils: from constitutive modelling to numerical algorithms. *Computers and Geotechnics*, 35(6), 810-824.
- Sheng, D., Sloan, S. W., and Gens, A. (2004). A constitutive model for unsaturated soils: thermomechanical and computational aspects. *Computational Mechanics*, 33(6), 453-465.
- Simunek, J., M. Sejna, H. Saito, M. Sakai, and M. Th. van Genuchten (2018). The HYDRUS-1D Software Package for Simulating the Movement of Water, Heat, and Multiple Solutes in Variably Saturated Media, Version 4.17, *HYDRUS Software Series 3*, Department of Environmental Sciences, University of California Riverside, Riverside, California, USA, pp. 348, 2018.
- Sivakumar, V. (1993). A critical state framework for unsaturated soil. Doctoral dissertation, University of Sheffield, Sheffield, England.
- Sivakumar, V., Kodikara, J., O'hagan, R., Hughes, D., Cairns, P., and McKinley, J. D. (2013). Effects of confining pressure and water content on performance of unsaturated compacted clay under repeated loading. *Géotechnique*, 63(8), 628.
- Sun, D. A., Sheng, D. C., Cui, H. B., and Sloan, S. W. (2007a). A density-dependent elastoplastic hydro-mechanical model for unsaturated compacted soils. *International Journal for Numerical and Analytical Methods in Geomechanics*, 31(11), 1257-1279.

- Sun, D. A., Sheng, D., and Sloan, S. W. (2007b). Elastoplastic modelling of hydraulic and stress–strain behaviour of unsaturated soils. *Mechanics of Materials*, 39(3), 212-221.
- Suradi, M., Fourie, A., Beckett, C., and Buzzi, O. (2014). Rainfall-induced landslides: Development of a simple screening tool based on rainfall data and unsaturated soil mechanics principles, in N . Khalili, *Proceeding 18<sup>th</sup> Annual Conference on Geotechnical Engineering*, Jakarta, Indonesia.
- Suzaki, A., Minato, S., and Ghose, R. (2018). Inversion of soil-water characteristic curve in unsaturated soil embankment using the underlying physics of S-wave and integrated geophysics. In *SEG Technical Program Expanded Abstracts 2018*, 4748-4752. Society of Exploration Geophysicists.
- Takkabutr, P. (2006). Experimental investigations on small-strain stiffness properties of partially saturated soils via resonant column and bender element testing. Doctoral dissertation, University of Texas, Arlington, USA.
- Tang, G. X., and Graham, J. (2002). A possible elastic plastic framework for unsaturated soils with high-plasticity. *Canadian Geotechnical Journal*, 39(4), 894-907.
- Tuller, M., Or, D., and Dudley, L. M. (1999). Adsorption and capillary condensation in porous media: Liquid retention and interfacial configurations in angular pores. *Water Resources Research*, 35(7), 1949-1964.
- Van Genuchten, M. T. (1980). A closed-form equation for predicting the hydraulic conductivity of unsaturated soils. *Soil Science Society of America Journal*, 44(5), 892-898.
- Vanapalli, S.K., and Fredlund, D.G. 2000. Comparison of different procedures to predict unsaturated soil shear strength. In *Advances in Unsaturated Geotechnics, Proceedings of Sessions of Geo-Denver, ASCE*, Denver, Colorado. 195-209
- Vanapalli, S.K., and Fredlund, D.G. (1999). Comparison of empirical procedures to predict the shear strength function for unsaturated soils. *XI Asian Regional Conference, International Society for Soil Mechanics and Foundation Engineering*, Seoul, South Korea, ed. Sung-Wan Hong et al., A. A. Balkema. 1, 93-96.
- Vassallo, R., Mancuso, C., and Vinale, F. (2007). Modelling the influence of stress–strain history on the initial shear stiffness of an unsaturated compacted silt. *Canadian Geotechnical Journal*, 44(4), 463-472.
- Vaunat, J., Romero, E., and Jommi, C. (2000). An elastoplastic hydromechanical model for unsaturated soils. In *Experimental Evidence and Theoretical Approaches in Unsaturated Soils, Proceeding of International Workshop on Unsaturated Soil, 2000*, Trento, Italy, A.A. Balkema, Rotterdam. 121-138.
- Vogel, T., and Cislérova, M. (1988). On the reliability of unsaturated hydraulic conductivity calculated from the moisture retention curve. *Transport in Porous Media*, 3(1), 1-15.

- Walton-Macaulay, C. (2015). Prediction of strength and shear modulus of compacted clays within an unsaturated critical state framework. Doctoral dissertation, University of Kentucky, Lexington, USA.
- Wheeler, S. J. (1996). Inclusion of specific water volume within an elasto-plastic model for unsaturated soil. *Canadian Geotechnical Journal*, 33(1), 42-57.
- Wheeler, S. J., and Sivakumar, V. (1995). An elasto-plastic critical state framework for unsaturated soil. *Géotechnique*, 45(1), 35-53.
- Wheeler, S. J., Sharma, R. S., and Buisson, M. S. R. (2003). Coupling of hydraulic hysteresis and stress-strain behaviour in unsaturated soils. *Géotechnique*, 53(1), 41-54.
- Wong, K. S., Mašin, D., and Ng, C. W. W. (2014). Modelling of shear stiffness of unsaturated fine grained soils at very small strains. *Computers and Geotechnics*, 56, 28-39.
- Wu, S., Gray, D. H., and Richart Jr, F. E. (1984). Capillary effects on dynamic modulus of sands and silts. *Journal of Geotechnical Engineering*, 110(9), 1188-1203.
- Xu, J., and Zhou, C. (2016). A simple model for the hysteretic elastic shear modulus of unsaturated soils. *Journal of Zhejiang University-SCIENCE A*, 17(7), 589-596.
- Yamashita, S., Fujiwara, T., Kawaguchi, T., Mikami, T., Nakata, Y., and Shibuya, S. (2007). International parallel test on the measurement of Gmax using bender elements organized by TC-29. *ISSMGE TC-29 Report*, 1-76.
- Yamashita, S., Kawaguchi, T., Nakata, Y., Mikami, T., Fujiwara, T., and Shibuya, S. (2009). Interpretation of international parallel test on the measurement of Gmax using bender elements. *Soils and foundations*, 49(4), 631-650.
- Yang, K. H., Uzuoka, R., Lin, G. L., and Nakai, Y. (2017). Coupled hydro-mechanical analysis of two unstable unsaturated slopes subject to rainfall infiltration. *Engineering Geology*, 216, 13-30.
- Yang, X., and You, X. (2013). Estimating parameters of van Genuchten model for soil water retention curve by intelligent algorithms. *Applied Mathematics & Information Sciences*, 7(5), 1977.
- Young, T. (1805). An essay on the cohesion of fluids. *Philosophical transactions of the royal society of London*, (95), 65-87.
- Zhang, J., Jiang, T., Wang, X., Liu, C., and Huang, Z. (2018). Influences of Drying and Wetting Cycles and Compaction Degree on Strength of Yudong Silt for Subgrade and Its Prediction. *Advances in Civil Engineering*, 2018.
- Zhou, A. (2011). Constitutive modelling of hydromechanical behaviour of unsaturated soils. Doctoral dissertation, University of Newcastle, Callaghan, Australia.

Zhou, A. N., Sheng, D., Sloan, S. W., and Gens, A. (2012). Interpretation of unsaturated soil behaviour in the stress–saturation space, I: volume change and water retention behaviour. *Computers and Geotechnics*, 43, 178-187.

Zhou, A., and Sheng, D. (2009). Yield stress, volume change, and shear strength behaviour of unsaturated soils: validation of the SFG model. *Canadian Geotechnical Journal*, 46(9), 1034-1045.

Zhou, A., and Sheng, D. (2016). Relating shear strength of unsaturated soils with capillary water retention curve. In *E3S Web of Conferences*. 9, 14010. EDP Sciences.

## VITA

### EDUCATION

University of Kentucky, Lexington, KY December 2014

#### **M.Sc. Mining Engineering**

Azad University, Tehran, Iran December 2007

#### **B.Sc. Mining Engineering**

### RESEARCH EXPERIENCE

University of Kentucky, Lexington, KY Jan 2015 - Present

#### **Graduate Researcher-Civil Engineering**

- Developed a constitutive model to describe real-time hydro-mechanical behavior of unsaturated slopes as a function of seasonal variations. The model contributes to a more effective landslide risk management
- Numerically simulated transient water infiltration within the vadose zone, which led to proposition of a novel methodology for anticipating long-term hydrologic characteristics of partially saturated soils
- Enhanced mechanical properties of collapsible soils using fly ash, investigated consolidation and shear behavior of fly ash-soil mixtures consistent with volumetric fractions of the individual constituents
- Incorporated electrical properties of soils with conventional laboratory techniques, resulting in three predictive models for shales' durability, particle size distribution and unconfined deformation
- Carried out steady-state and transient seepage, as well as stability analyses on embankment dams. Simulations provided pore-water pressure distribution within the dam and values of the factor of safety
- Applied GIS to prepare maps for diverse projects. For instance, performed landslide susceptibility analysis on a densely populated area. The obtained results helped to identify zones requiring stabilization
- Designed and evaluated various engineered earthen structures including shallow and deep foundations, embankments, retaining walls and waste treatment landfills
- Conducted seismic hazard, liquefaction and site response analyses. Investigated seismic stability and permanent displacement of embankments and slopes

University of Kentucky, Lexington, KY Aug 2012 - Dec 2014

#### **Researcher Assistant-Mining Engineering**

- Applied a Programmable Logic Controller (PLC) and embedded microcontroller to automate and control various underground construction and production machines, which resulted in increased output and safety

- Employed 4 advanced coal preparation technologies to separate and recover combustible materials from undesired impurities. Quality of the end product was remarkably improved
- Designed and analyzed mineral processing circuits and operational units, while ensuring compliance of the final product to meet quality specifications

## **PROFESSIONAL EXPERIENCE**

Absa Construction Company, Tehran, Iran

Mar 2008 - May 2012

### **Tunnel Engineer**

- Performed geo-structural numerical modelling analysis on tunnels and underground structures
- Assisted in preparation and modification of reports, specifications and studies for underground projects
- Carried out site inspection and monitoring to track construction progress and ensure conformance to design and safety criteria
- Assisted in mentoring, training, career development and management of junior engineers

Hampa Behineh Consultant Company, Tehran, Iran

May 2007 - Aug 2007

### **Intern-Quarry**

- Fulfilled a multitude of assigned tasks encompassing mine planning, maintenance, optimization of operations and marketing
- Participated in HSE related programs, including safety lectures and site observations

## **TEACHING/LEADERSHIP EXPERIENCE**

University of Kentucky, Lexington, KY

Jan 2016 - Present

### **Teaching Assistant-Civil Engineering**

- Taught Geotechnical laboratory experiments with presenting supplement lectures. Modules included: Field Classification of Soils, Hydraulic Conductivity, Moisture Content, Grain Size Analysis, Atterberg Limits, Proctor Compaction, 1-D Consolidation, Direct Shear and Triaxial Compression
- Instructed AutoCAD to class of ~60 students in weekly laboratory sessions for 7 semesters
- Delivered lectures in 3 core courses including Stability of Earth Slopes, Geotechnical Engineering and Advanced Soil Mechanics.
- Graded written assignments, midterms, and finals
- Held weekly office hours for class of 40 students



**Member and Head of Scientific Society of Mining Engineering Department**

- Organized and executed bi-annual departmental seminars with inviting eminent researchers and leading industry professionals
- Arranged monthly tours to operational mines and ore beneficiation plants for undergraduate students (~40 attendees)
- Edited and co-authored a technical journal with a particular focus on innovations in the mining industry
- Recitation leader for undergraduate students in two courses, as Mine Surveying and Rock Mechanics

**PEER-REVIEWED PUBLICATIONS**

- **Mahmoodabadi, M.**, and Bryson, L. S. Prediction of Coupled Hydro-Mechanical Behavior of Unsaturated Soils Based on Seasonal Variations in Hydrologic Conditions. *Canadian Geotechnical Journal*, Submitted.
- **Mahmoodabadi, M.**, and Bryson, L. S. Constitutive Model for Describing the Fully Coupled Hydro-Mechanical Behavior of Unsaturated Soils. *International Journal of Geomechanics*, Submitted.
- **Mahmoodabadi, M.**, and Bryson, L. S. Direct Application of the Soil-Water Characteristic Curve to Estimate the Shear Modulus of Unsaturated Soils. *International Journal of Geomechanics*, Submitted.
- Bryson, L. S., Kirkendoll, J. S., and **Mahmoodabadi, M.** (2019). A New Rapid Method to Assess the Durability of Shale. *Geotechnical and Geological Engineering*, 37(5), 4135-4150.
- Bryson, L. S., **Mahmoodabadi, M.**, and Adu-Gyamfi, K. (2017). Prediction of Consolidation and Shear Behavior of Fly Ash-Soil Mixtures Using Mixture Theory. *Journal of Materials in Civil Engineering*, 29 (11).

**CONFERENCE PAPERS AND PRESENTATIONS**

- **Mahmoodabadi, M.**, and Bryson, L. S. (2019). Prediction of Unconfined Deformation Behavior of Soils Using Electrical Properties. In *Geo-Congress 2019*, 701-710. With poster presentation.
- **Mahmoodabadi, M.**, and Bryson, L. S. (2018). Prediction of Particle Size Distribution in Clay Using Electrical Conductivity Measurement. In *IFCEE 2018*, 154-164. With oral presentation.
- **Mahmoodabadi, M.** (2015). Multistage Coal Treatment Using Dry-Based Separation Technologies. In *SME Annual Meeting*. Poster presentation.

### **FELLOWSHIPS AND SCHOLARSHIPS**

- PhD Student Summer Research Fellowship, University of Kentucky, Department of Civil Engineering, 2016, 2018 and 2019
- Graduate School Scholarship, University of Kentucky, 2016
- WAAIME Scholarship, Society for Mining, Metallurgy and Exploration, 2013, 2014 and 2015

### **TECHNICAL SKILLS**

- Software: Hydrus, TRIGRS, SEEP/W, ArcGIS, SLOPE/W, PLAXIS, EERA, HELP, FLAC3D, AutoCAD, Matlab, Excel, PowerPoint, Word, Mathcad, LaTeX, TableCurve, CurveExpert, Design-Expert, SAS

### **AFFILIATIONS**

- American Society of Civil Engineers (ASCE)
- Society for Mining, Metallurgy & Exploration (SME)

---

**Majid Mahmoodabadi**